Copyright

by

Steven Kenneth Stanley

2020

The Dissertation Committee for Steven Kenneth Stanley Certifies that this is the approved version of the following dissertation:

Pushing the Limits of Marangoni-driven Patterning

Committee:

Roger T. Bonnecaze, Supervisor

C. Grant Willson

Christopher J. Ellison

Michael Baldea

Nathaniel A. Lynd

Pushing the Limits of Marangoni-driven Patterning

by

Steven Kenneth Stanley

Dissertation

Presented to the Faculty of the Graduate School of
The University of Texas at Austin
in Partial Fulfillment
of the Requirements
for the Degree of

Doctor of Philosophy

The University of Texas at Austin
August 2020

Dedication

Dedicated to my wife, my children, and my parents.

Acknowledgements

I would like to thank Dr. Bonnecaze for his generous support and amazing example to me. He has inspired me to grow as a researcher, engineer, and individual. There have been several major decisions I have faced during my graduate education and his counsel and advice have been invaluable. I would also like to thank Dr. Ellison for his support and collaboration, and I will be forever grateful for his hospitality during my visit to his lab in Minnesota. I would like to thank Dr. Willson for his mentorship and inspiring instruction in lithography. His unique experience and knack for storytelling brought the world of semiconductor engineering to life. I would also like to thank Xing-Fu Zhong and Catherine Frank from Brewer Science Inc. for their support and collaboration. I would also like to thank Dr. Chris Mack, Dr. Michael Baldea, and Dr. Lynd for lending their support, guidance and facilities to my work. And many thanks to my lab mates and collaborators, Saurabh, Gabriel, Yang, Xilan, Tianfei, Soumik, Fardin, Mohamed, Shruti, and Meghali for their support and counsel.

Abstract

Pushing the Limits of Marangoni-driven Patterning

Steven Kenneth Stanley, PhD
The University of Texas at Austin, 2020

Supervisor: Roger T. Bonnecaze

Marangoni-driven patterning (MDP) is a relatively new technique that harnesses surface tension-driven flows to create topography in thin polymer films with potential uses in generating flexible electronics, metamaterials, and functional coatings for light capture, adhesive, and antibiofouling applications. To determine which applications MDP is best suited for, it is important to understand the fundamental limits of achievable pattern pitch and aspect ratio. To date, the maximum reported aspect ratio for MDP is roughly 0.05 and the minimum reported feature pitch is roughly 1.5 μm. To determine how much these metrics could be improved, we perform a numerical analysis to predict the maximum aspect ratio and minimum feature pitch for MDP. Our analysis shows that the maximum aspect ratio is roughly 0.5, which is roughly ten times better than what has been demonstrated to date. We also show that the pattern pitch is fundamentally limited by light-imaging capabilities and engineering constraints.

One issue facing MDP is the leftover residual layer that blocks access to the substrate and necessitates a breakthrough etch for subsequent patterning. To avoid this extra processing step, we investigate the possibility of inducing a dewetting event during MDP, which could expose the underlying substrate during the annealing step and even improve the aspect ratio of the resulting pattern. Through modelling and simulation, we predict the conditions necessary to induce a dewetting event in MDP.

Another issue in MDP is pattern control. When generating two-dimensional shapes like squares, simulations show that the corners and edges of the shape are significantly rounded. To improve pattern quality, we implement an algorithm to optimize the initial exposure to generate more favorable flow patterns and sharper topography. We also experimentally validate this work using a polystyrene polymer system.

Finally, we investigate the root cause of unexpected bias reversal in spin-coated, conformal polymer films. Our model and simulation results show that Marangoni-driven flow could be responsible for this observation.

Table of Contents

List of Tables xiii

List of Figures xviii

Chapter 1: Introduction 1

Chapter 2: Fundamental Limits of Marangoni-driven Patterning 8

2.1 Introduction 8

2.2 Theory And Analysis 11

2.2.1 Model for Marangoni-driven patterning 11

2.2.2 Linear Analysis 15

2.2.3 Nonlinear Analysis 21

2.2.4 Minimum Feature Pitch 29

2.3 Discussion 30

2.4 Conclusion and Future Work 32

Supporting Information 34

S2.1 Table of Polymer Surface Tensions 34

S2.2 Determining the Origin of Difference Between Linear and Nonlinear Solutions 35

S2.3 Simulation Setup for the Case of Step Concentration Profiles 37

Chapter 3: Harnessing Marangoni-driven Patterning to Facilitate Dewetting in Thin Polymer Films 40

3.1 Introduction 40

3.2 Methodology 44

3.2.1 Model for Marangoni-driven patterning 44

3.2.2 Simulation Methodology 48

3.2.3 Feature Evolution and Calculation of Dewetting Contours 49
3.3 Results and Discussion 51
3.3.1 Contour Map Defining Dewetting and Replanarization 51
3.3.2 Comparison to Prior Experiments..53
3.4 Conclusions..57
Chapter 4: Control of Marangoni-driven patterning by an optimized distribution of surface energy 58
4.1 Introduction..58
4.2 Methodology..63
4.2.1 Model for Marangoni-driven patterning 63
4.2.1.1 Geometric and Physical Parameters..65
4.2.1.2 Nondimensionalization 65
4.2.2 Pattern Quality 68
4.2.3 Penalized Area and Feature Height Evolution for the Intuitive Photomask..71
4.3 Photomask Resizing..74
4.4 Pixel-based Exposure Optimization...79
4.4.1 Photomask and Optimization Setup..79
4.4.2 Optimization Results...81
4.5 Conclusions..87
Supporting Information...88
S4.1 Simulation Setup...88
S4.2 Convergence and Conservation Study...89
S4.3 Model Verification...93

S4.4 Calculating the Penalized Area....95

S4.5 Genetic Algorithm Implementation....97

S4.6 Convergence Study for Optimized Photomasks....99

S4.7 Optimized photomasks with corresponding feature profiles and contours....101

S4.8 Effects of Using a Weighted Population Seed....104

Chapter 5: Parameter Estimation and Photoexposure Optimization for a Real Marangoni-driven Pattern System....105

5.1 Introduction....105

5.2 Experimental....110

5.2.1 Materials....110

5.2.2 Methods....110

5.3 Characterization of Polymer Properties....113

5.3.1 Line-Space Experiments....113

5.3.2 Model for MDP....118

5.3.3 Parameter Estimation Method....120

5.3.4 Characterizing Patterns Resulting from an Intuitive Photomask....127

5.4 Optimizing the Photomask....129

5.5 Optimized Photomask Experimental Results....132

5.5.1 Square Shapes Results....137

5.5.2 L-Shapes....144

5.6 Conclusion....147

Supporting Information....148

S5.1 Sensitivity Study....148

S5.2 Long-time Mask Optimization Results for L-Shaped Figures 152

S5.3 All Experimental Feature Contours 153

Chapter 6: Marangoni-driven Bias Reversal in Conformal Polymer Films 160

6.1 Introduction..160

6.2 Experimental Methods And Results 163

6.2.1 Materialsand Polymer Preparation...163

6.2.2 Spin Coating and Annealing 164

6.2.3 Characterization of the Film and Polymer 164

6.2.4 Experimental Results 165

6.3 Theory And Analysis...174

6.3.1 Examining Temperature Variations..174

6.3.2 Examining Solvent Concentration Variations 175

6.3.3 Examining Polymer Concentration Variations 178

6.4 Conclusion 192

Supporting Information...193

S6.1 Viscosity Data and Extrapolation 193

S6.2 Estimating Polymer Self Diffusivity 194

S6.3 Surface Tension Estimation Method 196

S6.4 Thickness reduction for pure PTBSM vs. PS-co-PTBSM 198

Chapter 7: Summary, Outlook, and Future Work...199

7.1 Summary...199

7.2 Outlook for Marangoni-driven Patterning 199

7.3 Future Work..201

References..203

List of Tables

Table 2.1 Experimental conditions and reported feature heights/AR for the literature values reported in Figs. 2.4a and 2.4b. Data extracted from the indicated references. *Values extracted from feature profiles. †Values extracted from maximum recorded peak-to-valley height for given experiment. 27

Table 2.2 Dewetting transition point values, ε_{Min} and associated accuracy for the step and sine function models for $\alpha = \alpha_{\text{Max}} = 2$, $A = A_{\text{Max}} = 10^{-19}$ J, and $\gamma_0 = \gamma_{0\text{Min}} = 10$ mN/m (same as Figs. 2.4ab and 2.5). Corresponding $\Delta h^*_{\text{Nonlin}}$ and $AR_{\text{NonlinMax}}$ are also reported. The maximum aspect ratio observed was for the sine function case at $h_0 = 10$ nm, and is bolded. 29

Table S2.1 Surface tension values for various polymers at 20, 140, and 180°C. Table adapted from Bicerano [27]. Mn is number-average molecular weight, Mw is weight-average molecular weight, Mv is viscosity-average molecular weight, and M is for cases where the type of molecular weight was not provided. 35

Table S2.2 Table shows the dimensionless peak-to-valley height ($\Delta h/h_0$) resulting from solving the linear and nonlinear models under different assumptions. The model assumptions were to include/neglect convection effects and the concentration dependence of capillary forces. In solving the model, the parameters were set to $\varepsilon = 0.3$, $\alpha = 2$, and $V = 5\text{x}10^{-6}$, and $Pe = \infty$. 37

Table 3.1 Physical parameters for system taken from ref. [7]. Air-polystyrene-SiOx Hamaker constant, A, taken from ref. [24]..54

Table 4.1 Physical and geometric parameters used in simulations. Physical parameters taken from Arshad et al. [7] 67

Table 4.2 Penalized area for several square photomask sizes (left-most column) at select dimensionless annealing times and temperatures (Left: T = 120°C, **Right: T = 140°C**). The objective used to calculate the penalized area is a 35x35 μm^2 square. Underlined values indicate the best square photomask among those tested for a given dimensionless annealing time. Note that the 35x35 μm^2 square photomask is the intuitive choice of photomask. Annealing temperature is 120°C for the regular font and 140°C for the bold font. 76

Table S4.1 Comparison of penalized area and pre-etch feature heights using the coarse (1x1 μm^2) and fine (0.5x0.5 μm^2) simulation grid size. The absolute, relative percent difference between the results are provided. 100

Table 5.1 Optimized parameter summary. Sample numbers and associated feature pitch (λ), average initial height ($h_{0\mathrm{Avg}}$) with sample standard deviation, and maximum recorded average peak-to-valley height (Δh_{Max}) are reported. Optimal objective function, *J*, is reported along with optimized variable handles t^*_{Mar}, Pe^*, and κ^*, all reported to three digits. The optimal, primary parameters are provided first in **bold** while the generally sub-optimal, secondary parameters are provided in non-bolded text. *Note that Sample 4 possessed a more optimal solution that was inconsistent with the rest of the 5 μm and 10 μm pitch optimal parameters. For this reason, a different local optimum is reported so as not to skew the parameter averages. Values of $\Delta\Gamma C_0$, μ, and *D* are calculated assuming $\gamma_0 = 32.2$ mN/m as reported in ref. [7]. Average parameter values and corresponding standard deviation of all calculated values are also provided, which helps characterize the sample-to-sample variability seen in experiments. Note that the standard deviation is not a confidence interval. Furthermore, values of $\Delta\Gamma C_0$, μ, and *D* for a similar polystyrene system as determined in ref. [7] at 120°C are also provided along with the resulting values of t^*_{Mar}, Pe^*, and κ^*. 126

Table 5.2 Penalized area and peak-to-valley height data summary for the square target experiments. Standard deviations are provided in parenthesis. The penalized area was averaged for only three of the four squares, excluding the bottom right contour because it was typically smaller than the others. *The optimization for the primary, 10,000 second anneal, 1x1 μm^2 photomask was terminated early after sufficient improvement in the penalized area had been achieved. †Penalized area metrics obtained from only two shapes rather than the usual three so as to exclude a very misshaped pattern...139

Table 5.3 Penalized area and peak-to-valley height data summary for the L-shape target experiments. Standard deviations are provided in parenthesis. The penalized area was averaged for only three of the four shapes, excluding the bottom right contour because it was typically smaller than the others. *Δh measured using only three of the four features. †Penalized area metrics obtained from only two shapes rather than the usual three so as to exclude a very misshaped pattern. 146

Table 6.1 Surface tension, liquid vapor pressure, and normal boiling points for PGME and PGMEA solvents at 25°C and 240°C. Data obtained from reference [64]..176

Table 6.2 Physical parameters used in the simulations and their associated references, where SI stands for the Supporting Information section. Note that α and $\Delta\Gamma$ were varied as part of a parameter sweep between the reported ranges. 186

Table S6.1 Summary of homopolymer surface tension estimates at 240°C obtained through different combinations of correlations. ΔΓ values for each method are provided. 197

List of Figures

Figure 1.1 Schematic of Marangoni-driven patterning carried out using a contact exposure technique. a) Light exposure step in which an equal line-space photomask of periodicity λ is used to selectively expose to UV light the film of initial height, h_0. Exposed areas undergo a chemical reaction and possess a surface energy, or surface tension, of γ_+ while those unexposed areas remain unaffected and possess the nominal surface tension, γ_0. b) Annealing the film above its glass transition temperature causes the polymer film to flow into the exposed regions. The flow is initially strongest at the crossover between the exposed and unexposed regions, resulting double peaks. c) The double peaks eventually merge to form peaks and valleys with a peak to valley height of Δh and an aspect ratio, AR, where $AR = 2\Delta h/\lambda$. d) At long annealing times, the surface tension promoter dissipates due to diffusion effects and capillary forces eventually planarize the film. This figure was published in *Colloids and Surfaces A: Physiochemical and Engineering Aspects*, 603, Stanley, S. K. and Bonnecaze, R. T., Fundamental Limits of Marangoni-driven Patterning, 125217, Copyright Elsevier (2020) and has been adapted to a two-column format..2

Figure 1.2 Photomask, simulated feature, and pattern contour compared to 50x50 μm^2 target. Yellow regions of the photomask are exposed with higher surface tension, whereas dark areas are opaque. The polymer flows towards the center of the exposed, higher surface tension region. Feature profile and contours were taken at an annealing time of 5,000 seconds. The red outline in a) shows the target dimensions. Feature contours are extracted at $h = h_0 = 150$ nm, denoted by the red cut in b). This red cut is for demonstration only and do not represent the dimensions of the target. Note that the features are not drawn to scale, where the pattern pitch is 100 μm and the feature height is in nanometers. 4

Figure 1.3 Depiction of thin films possessing (a) positive and (b) negative bias. Positive bias is characterized by a lower film height in trenched regions with respect to open regions, whereas negative bias is characterized by a higher film height in the trench regions with respect to the open regions. Bias is defined as the difference in film height between the open region and the trench region. 6

Figure 2.1 Schematic of Marangoni-driven patterning carried out using a contact exposure technique. a) Light exposure step in which an equal line-space photomask of periodicity λ is used to selectively expose to UV light the film of initial height, h_0. Exposed areas undergo a chemical reaction and possess a surface energy, or surface tension, of γ_+ while those unexposed areas remain unaffected and possess the nominal surface tension, γ_0. b) Annealing the film above its glass transition temperature causes the polymer film to flow into the exposed regions. The flow is initially strongest at the crossover between the exposed and unexposed regions, resulting double peaks. c) The double peaks eventually merge to form peaks and valleys with a peak to valley height of Δh and an aspect ratio, *AR*, where $AR = 2\Delta h/\lambda$. d) At long annealing times, the surface tension promoter dissipates due to diffusion effects and capillary forces eventually planarize the film. Note that the figures are not necessarily drawn to scale, as films patterned to date are typically several hundreds of nanometers thick and the pattern pitches have ranged from roughly 1-200 μm. 9

Figure 2.2 Feature profiles calculated using the linearized solution for varying a) ε, b) α , and c) *V*. Note that in Fig. 2.2a, there exists a critical value of ε at which the feature touches the substrate. 18

Figure 2.3 Steady-state and dewetting feature profiles as determined by the nonlinear and linear models for the limiting values of α, and αV, where $\alpha = \alpha_{\mathrm{Max}} = 2$ and $\alpha V = \alpha V_{\mathrm{Max}} = 10$. Note that by decreasing the value of ε by ~0.003% from $\varepsilon = 0.31028$ to $\varepsilon = 0.31027$, the film is forced to dewet due to the rapidly increasing van der Waals forces. This transition point defines the minimum value of ε for the nonlinear analysis. Also note that in comparing the linear and nonlinear models for $\varepsilon = 0.31028$, the linear model over predicts the feature height. 23

Figure 2.4 (a) Peak-to-valley height and (b) aspect ratio as a function of pattern periodicity, λ, for given values of h_0, A, γ_0, α, and V. The lines/symbols that terminate at the upper right of each series indicate when $\varepsilon_{\mathrm{Min}}$ is achieved where the film either touches the substrate (linearized model) or is barely stabilized against dewetting (nonlinear model). Experimental observations extracted from various references are also included. The symbol-reference pairs are as follows: ★ = [1], ★ = [7], ★ = [3], ★ = [4], ★ = [6]. Note that the values of h_0, α, A, and γ_0 reported in the figure apply only to the simulation results and not to the experiments. See Table 2.1 for the values used in experiments. 26

Figure 2.5 Aspect ratio as a function of pattern periodicity, λ, for given values of h_0, A, γ_0, α, and V. The symbols that terminate at the upper right of each series indicate when $\varepsilon_{\mathrm{Min}}$ is achieved, except for the step function profiles at $h_0 = 100$ nm and $h_0 = 1000$ nm. 28

Figure S2.1 Comparison of concentration distributions initialized using a sinusoid (black) and smoothed step function (blue). The transition zone is of dimensionless size 0.05 (5% of the full domain length). 38

Figure 3.1 Schematic and possible outcomes of MDP performed using a line-and-space photomask. a) UV light interacts with polymer film in regions unobstructed by the photomask, raising the surface tension in exposed regions. λ is the full-pitch of the equal line-space photomask and λ_{HP} the resulting half-pitch of the surface tension gradient and resulting pattern. h_0 is the initial film thickness. b) Heating the film above its glass transition temperature allows the film to flow into the exposed regions of higher surface tension, resulting in the film being deflected. Initially double peaks form where the gradient is strongest. c) The double peaks eventually merge, and the film height continues to grow. d) If the Marangoni forces are not strong enough, the film will eventually relax back to flat as diffusion erases the surface tension gradient and capillary forces replanarize the film. e) If the film is deflected far enough, van der Waals forces become strong and dewetting occurs. Portions of this figure have been published in *Colloids and Surfaces A: Physiochemical and Engineering Aspects*, 603, Stanley, S. K. and Bonnecaze, R. T., Fundamental Limits of Marangoni-driven Patterning, 125217, Copyright Elsevier (2020). 43

Figure 3.2 a) Normalized concentration profiles and b) normalized film height profiles for a simulation in which the initial concentration was a step function. c) Normalized concentration profiles and d) normalized film height profiles for a simulation in which the initial concentration was a sinusoid. Simulation conditions for all component figures were M, V, = 1, and W = 10....................49

Figure 3.3 a) Normalized concentration profiles and b) normalized film height profiles for a simulation in which the initial concentration was a step function. Simulation conditions for a) and b) were M, V, = 1, and W = 10.7. c) Normalized concentration profiles and d) normalized film height profiles for a simulation in which the initial concentration was a step function. Simulation conditions for c) and d) were M, V, = 1, and W = 10.8. Note that the ~1% increase in the value of W leads to dewetting, which can be seen by comparing b) and d). 50

Figure 3.4 Constant V contours defining the transition from planarization to dewetting. For a given value of V, regions below the contour replanarize while regions above the contour dewet. The validity of the simulation results depends on whether fast vertical diffusion can be assumed, i.e. $W\varepsilon^2/M \leq 0.1$. This borderline is provided for $\varepsilon = 0.01$ (typical of past experiments) and for $\varepsilon = 0.1$ (more general value). Note that for a value of $\varepsilon = 0.1$, the domain is fairly restricted, but for typical experimental conditions in which $\varepsilon = 0.01$, the domain is much less restricted. 52

Figure 3.5 Constant V contours defining the transition from planarization to dewetting. For a given value of V, regions below the contour replanarize while regions above the contour dewet. Assuming silicon oxide as the substrate, experimental values were overlaid with the model predictions, showing that the conditions tested by Arshad et al. would not lead to dewetting.......56

Figure 4.1 Schematic of Marangoni-driven patterning and breakthrough etch. a) Example line-space photomask of periodicity λ and space-width *w* is used to selectively expose the polymer film of initial height h_0 to UV light. The surface energy or tension in the exposed areas (red) increases due to the photochemical reaction, as indicated by the γ_+ symbol. The surface tension in unexposed areas (blue) remains unchanged as indicated by the γ_0 symbol. b) Annealing the film causes the polymer to flow from the unexposed, lower surface tension regions, into the higher surface tension regions. Note the double peaks that form at short times where the gradient in surface tension is greatest. c) Double peaks merge and the surface tension gradient diffuses as indicated by the solid color. Central feature height is indicated by h_c. d) Anisotropic breakthrough etch of height h_e exposes the underlying substrate, leaving features of height h_f and width *CD*. Note that the figures are not drawn to scale as the film height is typically hundreds of nanometers while the feature periodicity is typically tens of microns. 59

Figure 4.2 Repeating 35x35 μm^2 square photomask pattern. Yellow areas represent exposed regions and blue areas represent unexposed regions. The exposed regions of the polymer film possess a higher surface tension relative to the unexposed regions, meaning that fluid will flow into the yellow region......69

Figure 4.3 a,b) Features formed using a 35x35 μm^2 square photomask annealed at 120°C. The pre-etch film height, h/h_0, is indicated by the associated color bars. The red squares in a) and b) help visualize the contour that would result from an anisotropic etch of height h_0. c,d) Feature contours overlaid with the target 35x35 μm^2 square. Notice that the feature corners are significantly rounded. The penalized area, a dimensionless metric for determining feature-target overlap, is also reported with each contour. e,f) Contours of the concentration, C/C_0. Contours levels range from 0 to 1 in intervals of 0.1. The dimensionless annealing times for a,c,e) and b,d,f) were 0.049 and 0.16, respectively. 71

Figure 4.4 a) Penalized area and its component parts vs. scaled annealing time at 120°C and 140°C. b) Normalized feature height vs. scaled annealing time at T = 120°C and T = 140°C. Inset shows that the curves mostly collapse when scaling the feature height by κ. 73

Figure 4.5 a) Intuitive and b) resized photomasks. Red outline overlays the target with the photomask. c,d) Features resulting from annealing at 140°C for t/t_M = 0.16. Red cross-section defines the relevant after-etch contour taken at h_0. e,f) After-etch contour overlaid with the target 35x35 μm^2 square contour. 75

Figure 4.6 a) Penalized area at various annealing times for the intuitive 35x35 μm^2 photomask and the best-performing resized photomasks. b) Fold reduction in penalized area when comparing the penalized areas generated by the intuitive 35x35 μm^2 photomask to the best-performing resized photomasks at each annealing time and temperature. c) Normalized feature height at various annealing times for the intuitive 35x35 μm^2 photomask and the best-performing resized photomasks. d) % reduction in feature height when comparing the feature heights generated by the intuitive 35x35 μm^2 photomask to the best-performing resized photomasks at each annealing time and temperature. 77

Figure 4.7 Normalized feature height over time for various square photomask sizes annealed at 120°C. Note that the smaller square photomask exhibits taller feature heights at early annealing times. The earlier onset of feature decay for the smaller photomask results in shorter features at later times relative to those achieved by larger photomasks. 79

Figure 4.8 Photomask representation. Yellow pixels represent transparent, exposed photomask regions, while the blue areas represent closed photomask region. Note that only one-eighth of the photomask needs to be manipulated due to symmetry (light outline). Also note that the variable domain has been restricted to a subset of the whole domain (bold outline). 80

Figure 4.9 Genetic algorithm convergence plot for optimizations at a) 120°C with fixed annealing times of t/t_M = 0.049, 0.097, 0.16, 0.23, 0.29 and b) 140°C with fixed simulation times of t/t_M = 0.079, 0.16, 0.26, 0.37, and 0.47. The initial point at generation zero for each fixed annealing time reflects the "first order" correction to the intuitive 35x35 μm^2 square photomask (underlined values in Table 4.2). The progression terminates when the photomask population becomes homogeneous. 82

Figure 4.10 a) Optimized photomask for the 120°C optimization at t/t_M = 0.049. The red square depicts the size of the intuitive 35x35 μm^2 square photomask. b) Resulting feature. Note that the feature height is not to scale so as to clearly visualize the feature shape. Red cross-section defines the relevant after-etch contour. c) After-etch contour overlaid with the target 35x35 μm^2 square contour. 84

Figure 4.11 a) Penalized area at various annealing times for the intuitive 35x35 μm^2 photomask and the photomasks optimized using the genetic algorithm. b) Fold reduction in penalized area when comparing the penalized areas generated by the intuitive 35x35 μm^2 photomask to the optimized photomasks at each annealing time and temperature. c) Normalized feature height at various annealing times for the intuitive 35x35 μm^2 photomask and the photomasks optimized using the genetic algorithm. d) % reduction in feature height when comparing the feature heights generated by the intuitive 35x35 μm^2 photomask to the optimized photomasks at each annealing time and temperature. 87

Figure S4.1 Normalized feature height over time calculated using adaptive and constant time stepping methods on simulation grid sizes of 1x1 µm^2 and 0.5x0.5µm^2, respectively. Simulations were performed using square photomasks of size 25x25 µm^2 and 51x51 µm^2 at annealing temperatures of 120°C and 140°C. 90

Figure S4.2 Penalized area over time calculated using adaptive and constant time stepping methods on simulation grid sizes of 1x1 µm^2 and 0.5x0.5µm^2, respectively. Simulations were performed using square photomasks of size 25x25 µm^2 and 51x51 µm^2 at annealing temperatures of 120°C and 140°C. 92

Figure S4.3 Plots showing the progression of relative volume and species loss for square photomasks of size 25x25 µm^2 and 51x51 µm^2 at annealing temperatures of 120°C and 140°C. 93

Figure S4.4 Normalized feature height for the C++ and COMSOL model implementations which were calculated using a 35x35 µm^2 square photomask at an annealing temperature of 120°C. 95

Figure S4.5 Penalized area over time calculated using various grid sizes. Simulations were performed using a square 35x35 µm^2 photomask at an annealing temperature of 120°C. 97

Figure S4.6 Target contour (red) overlaid with feature contours (blue and black) formed using the optimized photomask for conditions $t/t_M = 0.26$ and $T =$ 140°C. The blue contour is that formed using a coarse, 1x1 µm^2 simulation grid, whereas the black, dashed contour is that formed using a fine 0.5x0.5 µm^2 simulation grid. 101

Figure S4.7 Optimized photomasks (left column), resulting feature (middle column), and feature contours (right column) with associated penalized area. Optimizations performed at 120°C for a) $t/t_M = 0.049$, b) $t/t_M = 0.097$, c) $t/t_M = 0.16$, d) $t/t_M = 0.23$, and e) $t/t_M = 0.29$. Note that the feature heights are not to scale not to scale so as to clearly visualize the feature shape. 102

Figure S4.8 Optimized photomasks with overlaid target contour (left column), resulting feature (middle column), and feature contours (right column) with associated penalized area. Optimizations performed at 140°C for a) $t/t_M = 0.079$, b) $t/t_M = 0.16$, c) $t/t_M = 0.26$, d) $t/t_M = 0.37$, and e) $t/t_M = 0.47$. Note that the feature heights are not to scale not to scale so as to clearly visualize the feature shape. 103

Figure S4.9 a) Optimized photomask and overlaid target contour. b) Resulting feature. c) Feature contour and target. Optimization performed at 120°C for using an initial population seed containing a disproportionate amount of 35x35 μm^2 square photomasks. Note that the feature height is not to scale so as to clearly visualize the feature shape. 104

Figure 5.1 Schematic of Marangoni-driven patterning and breakthrough etch. a) Example line-space photomask of periodicity λ and space-width w is used to selectively expose the polymer film of initial height h_0 to UV light. The surface energy or tension in the exposed areas (red) increases due to the photochemical reaction, as indicated by the γ_+ symbol. The surface tension in unexposed areas (blue) remains unchanged as indicated by the γ_0 symbol. b) Annealing the film causes the polymer to flow from the unexposed, lower surface tension regions, into the higher surface tension regions. Note the double peaks that form at short times where the gradient in surface tension is greatest. c) Double peaks merge and the surface tension gradient diffuses as indicated by the solid color. Central feature height is indicated by h_c. d) Anisotropic breakthrough etch of height h_e exposes the underlying substrate, leaving features of height h_f and width CD. Note that the figures are not drawn to scale as the film height is typically hundreds of nanometers while the feature periodicity is typically tens of microns. Figure and caption adapted from S.K. Stanley, C.J. Ellison, R.T. Bonnecaze, Control of Marangoni-driven patterning by an optimized distribution of surface energy, J. Appl. Phys. 127 (2020), with the permission of AIP Publishing. 107

Figure 5.2 Photomask, simulated features, and pattern contours compared to 50x50 μm^2 target. Yellow regions of the photomask are exposed with higher surface tension, whereas dark areas are opaque. The polymer flows towards the center of the exposed, higher surface tension region. Feature profile and contours were taken at an annealing time of 5,000 seconds. The red outline in a) shows the target dimensions. Feature contours are extracted at $h = h_0 = 150$ nm, denoted by the red cut in b). This red cut is for demonstration only and do not represent the dimensions of the target. Note that the features are not drawn to scale, where the pattern pitch is 100 μm and the feature height is in nanometers. Details regarding the simulation will be provided later. 109

Figure 5.3 Reaction diagram for conversion of polystyrene to poly(phenyl acetylene). UV exposure causes a reaction leading to dehydrogenation of the polymer backbone. The pure polystyrene species imparts a surface tension, γ_0, whereas the exposed polymer, now containing some poly(phenyl acetylene), imparts a higher surface tension, γ_+. 112

Figure 5.4 a) Example AFM scan and trace of 10 μm pitch line-space pattern. Low-frequency or linear noise that exists in the trace was reduced using a splining technique. Note that the reported height is only relative and had to be adjusted to an absolute scale by ensuring the volume under the curves was consistent with the initial volume calculated from the initial film thickness, h_{0Avg}. b) Averaged traces and ±1 standard deviation for a similar 10 μm pitch line-space pattern (Sample 1 in Table 5.1) taken at t = 70 seconds. 115

Figure 5.5 Peak-to-valley heights taken from experimental data with ±1 standard deviation. a) Data from 10 μm pitch samples. b) Data from 20 μm pitch samples...117

Figure 5.6 Averaged trace and standard deviation for 20 μm pitch line-space patterns with overlaid simulation profiles. Sample 7 experiment and simulation profiles provided at annealing times a) t = 3 minutes and b) t = 30 minutes. Sample 11 experiment and simulation profiles provided at annealing times c) t = 3 minutes and d) t = 30 minutes. In all cases, blue points represent experimental values with ±1 standard deviation, where red and green points represent simulation data obtained using the primary and secondary parameters in Table 5.1, respectively. Note that good overlap is achieved for the primary parameter set in a) where poor overlap is seen for the secondary parameters. In some cases, though, the secondary parameter set performs well, which makes difficult the task of determining which parameter set is correct. 125

Figure 5.7 Intuitive square and L-shaped photomasks, simulated features, and pattern contours compared to target. a) and d) Photomasks, where yellow regions of the photomask are exposed with higher surface tension and dark areas are opaque. The polymer flows towards the exposed, higher surface tension regions. The red outline shows the target dimensions. b) and e) Feature profile and contours taken at an annealing time of 5,000 seconds. Feature contours are extracted at $h = h_0 = 150$ nm, denoted by the red cut. This red cut is for demonstration only and does not represent the dimensions of the target. Note that the features are not drawn to scale, where the pattern pitch is 100 μm and the feature height is in nanometers. c) and f) Contours extracted at $h = h_0 = 150$ nm compared to target shape. 129

Figure 5.8 Optimized square and L-shaped photomasks with 1x1 μm^2 pixels, simulated features, and pattern contours compared to the corresponding targets. Feature profile and contours taken at an annealing time of 5,000 seconds. The optimized photomasks were obtained through the optimization method using the Sample 8 primary parameters. The red outline in a) and d) shows the target dimensions. The red cut in b) and e) is for demonstration only and does not represent the target dimensions. Feature contours are extracted at $h = h_0 = 150$ nm. Note that the features in b) and e) are not drawn to scale, where the pattern pitch is 100 μm and the feature height is in nanometers. 132

Figure 5.9 Optimized square target photomasks. Ideal (left) and actual photomasks (right) as imaged using an optical microscope. In the ideal images, the yellow regions represent clear, exposed areas, whereas the blue represents opaque areas covered by chrome. In the actual photomask images, the reflective chrome regions are lighter and the darker regions are transparent. The red scalebars in the microscope images correspond to 10 μm. a) Pixels are 1 μm wide. b) Pixels are 2 μm wide. c) Pixels are 4 μm wide. 134

Figure 5.10 Optimized L-shaped target photomasks. Ideal (left) and actual photomasks (right) as imaged using an optical microscope. In the ideal images, the yellow regions represent clear, exposed areas, whereas the blue represents opaque areas covered by chrome. In the actual photomask images, the reflective chrome regions are lighter and the darker regions are transparent. The red scalebars in the microscope images correspond to 10 μm. a) Pixels are 1 μm wide. b) Pixels are 2 μm wide. c) Pixels are 4 μm wide. Note because a photomask with 2 μm wide pixels was seeded into the 1 μm pixel mask optimization, several 2 μm pixels persisted in the 1 μm wide pixel mask. 135

Figure 5.11 Feature height plots (left) and associated photomask pattern (right) used in generating the feature. Results shown are for the a) 50x50 μm^2 square mask, b) 58x58 μm^2 square mask, and the c) optimized mask with 1x1 μm^2 pixels. Samples were annealed for roughly 5,000 seconds. Actual feature contours are shown in red. Target (dashed black) and simulated (solid black) contours were roughly centered around the actual contours. The simulated contours here were obtained using the primary parameter set. The red scale bars in photomask images correspond to 10 μm. Note that point defects were occasionally present that may fall below or above the manually set color bar limits. 138

Figure 5.12 Comparison of penalized areas for the different square target photomasks. The square represents the average value bounded by ±1 standard deviation. In diamonds are the measured values for the corresponding photomasks. 140

Figure 5.13 Peak-to-valley height over time (Δh) for a 50x50 μm^2 square feature as predicted using the primary and secondary parameters. The dashed lines correspond to the Δh predicted using the sample 8 parameters, whereas the upper and lower bounds correspond to the Δh predicted using the sample 5 and sample 11 parameters, respectively. These upper and lower bounds help account for the sample-to-sample variability seen in Fig. 5.5. Experimental Δh values for the 50x50 μm^2 square photomask are overlaid (see Table 5.2). These values fall mainly within the intervals set by the primary parameters, suggesting that the primary parameters are correct. ..143

Figure 5.14 Feature height plots (left) and associated photomask pattern (right) used in generating the feature. Results shown are for the a) 50x25 μm^2 L-shape mask and b) optimized mask with 1x1 μm^2 pixels. Samples were annealed for roughly 5,000 seconds. Actual feature contours are shown in red. Target (dashed black) and simulated (solid black) contours were roughly centered around the actual contours. The simulated contours here were obtained using the primary parameter set. The red scale bars in photomask images correspond to 10 μm. Note that point defects were occasionally present that may fall below or above the color bar limits. 145

Figure 5.15 Comparison of penalized areas for the different L-shape target photomasks. The square represents the average value bounded by ±1 standard deviation. In diamonds are the measured values for the corresponding photomasks...147

Figure S5.1 a) and d) are optimized square photomasks with 1x1 μm^2 pixels obtained using the sample 8 primary parameters and an annealing time of 5,000 seconds. Features and feature-target contours in b) and c) were obtained by simulating feature formation using the sample 11 primary parameters. Features and feature-target contours in e) and f) were obtained by simulating feature formation using the sample 5 primary parameters. The red outline in a) and d) shows the target dimensions. The red cut in b) and e) is for demonstration only and does not represent the dimensions of the target. Feature contours are extracted at $h = h_0 = 150$ nm. Note that the features in b) and e) are not drawn to scale, where the pattern pitch is 100 μm and the feature height is in nanometers. 150

Figure S5.2 a) and d) are optimized square photomasks with 1x1 μm^2 pixels obtained using the Sample 8 primary parameters and an annealing time of 10,000 seconds. Features and feature-target contours in b) and c) were obtained by simulating feature formation using the Sample 11 primary parameters. Features and feature-target contours in e) and f) were obtained by simulating feature formation using the Sample 5 primary parameters. The red outline in a) and d) shows the target dimensions. The red cut in b) and e) is for demonstration only and does not represent the dimensions of the target. Feature contours are extracted at $h = h_0 = 150$ nm. Note that the features in b) and e) are not drawn to scale, where the pattern pitch is 100 μm and the feature height is in nanometers. 151

Figure S5.3 L-shaped photomask with 1x1 μm^2 pixels, simulated feature, and pattern contour compared to the target. Feature profile and contours taken at an annealing time of 12,000 seconds. The optimized photomasks were obtained through the optimization method using the Sample 8 secondary parameters. The red outline in a) shows the target dimensions. The red cut in b) is for demonstration only and does not represent the target dimensions. Feature contours are extracted at $h = h_0 = 150$ nm. Note that the feature in b) is not drawn to scale, where the pattern pitch is 100 μm and the feature height is in nanometers...152

Figure S5.4 Feature height plots (left) and associated photomask pattern (right) used in generating the feature. Results shown are for the a) 50x50 μm^2 square mask and for the optimized masks with b) 1x1 μm^2 pixels, c) 2x2 μm^2 pixels, and d) 4x4 μm^2 pixels. Samples were annealed for roughly 5,000 seconds. Actual feature contours are shown in red. Target (dashed black) and simulated (solid black) contours were roughly centered around the actual contours. The simulated contours here were obtained using the primary parameter set. The red scale bars in photomask images correspond to 10 μm. Note that point defects were occasionally present that may fall below or above the color bar limits. 154

Figure S5.5 Feature height plots (left) and associated photomask pattern (right) used in generating the feature. Results shown are for the a) 50x50 μm^2 square mask and for the optimized masks with b) 1x1 μm^2 pixels, c) 2x2 μm^2 pixels, and d) 4x4 μm^2 pixels. Samples were annealed for roughly 10,000 seconds. Actual feature contours are shown in red. Target (dashed black) and simulated (solid black) contours were roughly centered around the actual contours. The simulated contours here were obtained using the primary parameter set. The red scale bars in photomask images correspond to 10 μm, except in c), where the scale bar is 20 μm. Note that point defects were occasionally present that may fall below or above the color bar limits. 155

Figure S5.6 Feature height plots (left) and associated photomask pattern (right) used in generating the feature. Results shown are for the a) 50x50 μm^2 square mask and for the optimized masks with b) 1x1 μm^2 pixels, c) 2x2 μm^2 pixels, and d) 4x4 μm^2 pixels. Samples were annealed for roughly 6,000 seconds. Actual feature contours are shown in red. Target (dashed black) and simulated (solid black) contours were roughly centered around the actual contours. The simulated contours here were obtained using the secondary parameter set. The red scale bars in photomask images correspond to 10 μm. Note that point defects were occasionally present that may fall below or above the color bar limits. 156

Figure S5.7 Feature height plots (left) and associated photomask pattern (right) used in generating the feature. Results shown are for the a) 50x50 μm^2 square mask and for the optimized masks with b) 1x1 μm^2 pixels, c) 2x2 μm^2 pixels, and d) 4x4 μm^2 pixels. Samples were annealed for roughly 12,000 seconds. Actual feature contours are shown in red. Target (dashed black) and simulated (solid black) contours were roughly centered around the actual contours. The simulated contours here were obtained using the secondary parameter set. The red scale bars in photomask images correspond to 10 μm. Note that point defects were occasionally present that may fall below or above the color bar limits. 157

Figure S5.8 Feature height plots (left) and associated photomask pattern (right) used in generating the feature. Results shown are for the a) 50x25 μm^2 L-shape mask and for the optimized masks with b) 1x1 μm^2 pixels, c) 2x2 μm^2 pixels, and d) 4x4 μm^2 pixels. Samples were annealed for roughly 5,000 seconds. Actual feature contours are shown in red. Target (dashed black) and simulated (solid black) contours were roughly centered around the actual contours. The simulated contours here were obtained using the primary parameter set. The red scale bars in photomask images correspond to 10 μm. Note that point defects were occasionally present that may fall below or above the color bar limits. 158

Figure S5.9 Feature height plots (left) and associated photomask pattern (right) used in generating the feature. Results shown are for the a) 50x25 μm^2 L-shape mask and for the optimized masks with b) 1x1 μm^2 pixels, c) 2x2 μm^2 pixels, and d) 4x4 μm^2 pixels. Samples were annealed for roughly 6,000 seconds. Actual feature contours are shown in red. Target (dashed black) and simulated (solid black) contours were roughly centered around the actual contours. The simulated contours here were obtained using the secondary parameter set. The red scale bars in photomask images correspond to 10 μm. Note that point defects were occasionally present that may fall below or above the color bar limits. 159

Figure 6.1 Depiction of thin films possessing (a) positive and (b) negative bias. Positive bias is characterized by a lower film height in trenched regions with respect to open regions, whereas negative bias is characterized by a higher film height in the trench regions with respect to the open regions. Bias is defined as the difference in film height between the open region and the trench region. 161

Figure 6.2 a) Thermal deprotection reaction in which PS-co-PTBSM forms PS-co-PHOST and gaseous carbon dioxide and isobutylene. Water contact angles show that PHOST subunits impart a higher surface tension compared to PTBSM subunits as indicated by the symbols γ_0 and γ_+. b) Water contact angle on separate polymer films measured at different annealing times. Note the decrease in water contact angle, suggesting an increase in film surface energy over time. Water contact angle data extracted from reference [17]....................166

Figure 6.3 a) Film thickness over several annealing times for samples coated on flat Si-SiOx substrates. Samples were prepared using either PGMEA as the only spin-coating solvent or using a mixture of 40:60 PGME:PGMEA (by weight) as the spin-coating solvent. Thick and thin films were used to determine whether the reaction was thickness dependent. b) Film thickness normalized by the initial film thickness. 168

Figure 6.4 SEM images of trench and open regions for the sample coated on Si-SiOx substrates annealed at 240°C for different times. Trench regions are on the left and open regions are on the right. Scale bars correspond to 100 nm. Note that at *t* = 10 s, the film is notably thicker in the trench regions, as the bias has reversed. 170

Figure 6.5 SEM images of trench and open regions for the sample coated on TiN substrates annealed at 240°C for different times. Trench regions are on the left and open regions are on the right. Smaller scale bars correspond to 100 nm and larger scale bars correspond to 200 nm. Note that at $t = 10$ s, the film is notably thicker in the trench regions, as the bias has reversed. Also note that the bright, thin TiN coating can be distinguished from the original substrate. 171

Figure 6.6 Wide-angle SEM images of trench and open regions for the sample coated on Si-SiOx substrates and annealed at 240°C for different times. At $t = 0$ s (no bake), a dip in height in the trench regions is visible. By $t = 10$ s, a dome is apparent, as significant polymer has flowed into the trench regions. By $t = 60$ s, the dome has relaxed, and the surface appears flatter relative to the 10 s bake. 172

Figure 6.7 Film thickness measured from the substrate (excluding trench depth) in the a) open region and b) trench region over time. c) Film bias over time measured as Bias = h_{Open}-h_{Trench}. 173

Figure 6.8 Diagram of the adjusted film height, $\Phi(x)$, film thickness, $h(x)$, and substrate geometry, $S(x)$. The adjust film height is calculated as $\Phi(x) = h(x) + S(x)$. 180

Figure 6.9 Adjusted film height, $\Phi(x)$, obtained at several times using a five-trench substrate for a) $\Delta\Gamma = 14$ mN/m and $\alpha = 1$, and for b) $\Delta\Gamma = 14$ mN/m and $\alpha = 4$. c) Bias over time for simulated results compared to experimental results featured previously. 187

Figure 6.10 a) Minimum bias calculated/interpolated across a range of ΔΓ and α. Red line denotes the contour at which the minimum bias is zero. Regions to the left of the contour did not reverse in bias, whereas regions to the right did. b) Contours denoting zero bias for the 5-trench and 10-trench geometries. The similarity in contours suggests that adding more trenches to the simulation domain would not greatly affect the results. 188

Figure 6.11 a) Objective, J, calculated/interpolated across a range of ΔΓ and α for the 5-trench geometry. Red contours enclose regions where the simulated bias reversal at t = 10 s is within 10% of that achieved in experiments. b) Comparison of the contours for the 5-trench and 10-trench setups. Note that only a small difference is observed, suggesting that adding more trenches would not greatly affect the results...190

Figure S6.1 Log-viscosity vs. inverse temperature plot for deprotected PS-co-PTBSM sample, which has presumably converted into PS-co-PHOST. Data and Arhenius-like fit are provided..194

Figure S6.2 Log-diffusivity vs. inverse temperature data extracted from reference [65]. Black lines correspond to quadratic fits used to extrapolate out to 240°C. 196

Figure S6.3 Thickness over time for pure PTBSM and PS-co-PTBSM annealed at 225°C on a silicon substrate...198

Chapter 1: Introduction

Marangoni-driven patterning (MDP) is a relatively new technique that harnesses surface tension-driven flows to create topography in thin polymer films [1–8]. The process begins by selectively exposing a photoactive polymer film to UV light, where exposed regions undergo a chemical reaction and experience a change in surface energy/tension. When the polymer is heated above its glass transition temperature after exposure, the surface tension gradients are allowed to act on the now liquid polymer film and cause it to flow into the regions of higher surface tension by way of the Marangoni effect. This flow process generates hill-and-valley topography with peak-to-valley height, Δh and pattern periodicity, λ. By cooling the film below its glass transition temperature, the topography can be locked in place. The magnitude of the topography generated through MDP is primarily limited by diffusion and capillary forces. Initially, Marangoni forces are strong relative to capillary forces, thereby generating the topography. Over time, though, diffusion sufficiently degrades the concentration gradient to the point that capillary forces dampen the feature height and eventually planarize the film. A schematic of MDP using a line-space contact exposure technique is provided in Fig. 1.1. It is worth noting that patterning with “unzipping” polymers is notably similar to MDP. Unzipping polymers with low ceiling temperatures and end caps are kinetically stable, but upon exposure to UV light, bond scission allows for depolymerization when the polymer is heated above the ceiling temperature. In some cases, the exposed polymer can be made to vaporize immediately or upon heating and thereby undergo solvent-free development [9,10], much like in MDP.

MDP possesses several distinguishing processing characteristics relative to other roll-to-roll patterning methodologies. Where photolithography requires developing solvents to develop the latent image, MDP relies solely on heat to develop the pattern. Furthermore, MDP could be made contactless using techniques like maskless lithography [11] inherently avoiding the template contact issues often associated with imprint lithography. In the R2R patterning space, applications for MDP might include generating flexible electronics, metamaterials [12,13], and functional coatings for light capture [14], adhesive [15], and antibiofouling applications [16].

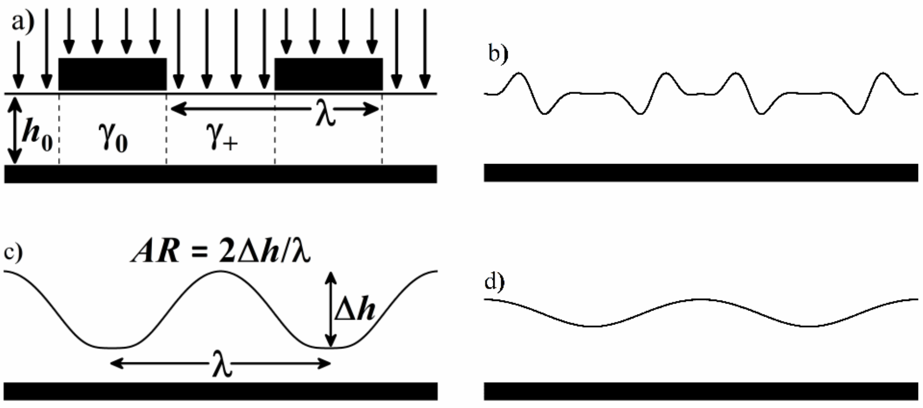

Figure 1.1 Schematic of Marangoni-driven patterning carried out using a contact exposure technique. a) Light exposure step in which an equal line-space photomask of periodicity λ is used to selectively expose to UV light the film of initial height, h_0. Exposed areas undergo a chemical reaction and possess a surface energy, or surface tension, of γ_+ while those unexposed areas remain unaffected and possess the nominal surface tension, γ_0. b) Annealing the film above its glass transition temperature causes the polymer film to flow into the exposed regions. The flow is initially strongest at the crossover between the exposed and unexposed regions, resulting double peaks. c) The double peaks eventually merge to form peaks and valleys with a peak to valley height of Δh and an aspect ratio, AR, where $AR = 2\Delta h/\lambda$. d) At long annealing times, the surface tension promoter dissipates due to diffusion effects and capillary forces eventually planarize the film. This figure was published in *Colloids and Surfaces A: Physiochemical and Engineering Aspects*, 603, Stanley, S. K. and Bonnecaze, R. T., Fundamental Limits of Marangoni-driven Patterning, 125217, Copyright Elsevier (2020) and has been adapted to a two-column format.

To determine which applications MDP is best suited for, it is important to understand the fundamental limits of the aspect ratio (*AR*) and feature pitch (λ), shown in Fig. 1.1. Aspect ratio is defined as the peak-to-valley height divided by the feature half-periodicity, i.e. $AR = 2\Delta h/\lambda$. Generally, larger aspect ratios are desirable because they provide better etch contrast and improved optical properties, whereas smaller pattern pitches are often desirable as they allow for more densely packed features and shorter wavelength optical capabilities. To date, the maximum reported aspect ratio for MDP is roughly 0.05 and the minimum reported feature pitch is roughly 1.5 μm. Chapter 2 is dedicated to determining the limits of pattern aspect ratio and periodicity. Using modelling and simulation techniques, we perform a numerical analysis which shows the maximum aspect ratio for equal line-space patterning is roughly 0.5 and the fundamental limit of feature pitch is governed primarily by exposure capabilities and engineering constraints.

One issue in MDP is the leftover residual layer that blocks access to the substrate and necessitates a breakthrough etch for subsequent patterning. To avoid this extra processing step, we investigate the possibility of inducing a dewetting event during MDP, which could expose the underlying substrate during the annealing step. Accessing this dewetting regime through MDP could additionally improve the aspect ratio of the resulting pattern beyond the limits mentioned previously. In Chapter 3, we explore the conditions necessary to induce this dewetting event by simulating MDP across a broad parameter space. Knowing these conditions *a priori* could help design future polymer systems for Marangoni-facilitated dewetting.

Another primary issue in MDP is pattern control. When generating two-dimensional shapes like squares, simulations show that the corners and edges of the shape are significantly rounded, as shown in Fig. 1.2. In this example, the pattern target is a 50x50 μm^2 square and the photomask is a square of the same dimensions. Note in the feature and extracted contour that the corners are rounded, the edges are bowed inwards, and the extracted contour is too small relative to the target. To mitigate these issues, we implement an algorithm to optimize the initial exposure in a pixel-by-pixel fashion to generate more favorable flow patterns and sharper topography, which is presented in Chapter 4. Later, in Chapter 5, we experimentally validate this work using a polystyrene polymer system and show that improved patterning can indeed be achieved using this technique.

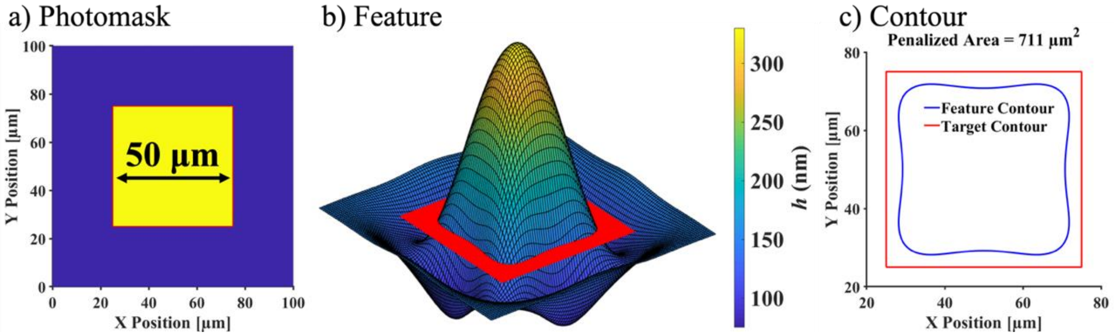

Figure 1.2 Photomask, simulated feature, and pattern contour compared to 50x50 μm^2 target. Yellow regions of the photomask are exposed with higher surface tension, whereas dark areas are opaque. The polymer flows towards the center of the exposed, higher surface tension region. Feature profile and contours were taken at an annealing time of 5,000 seconds. The red outline in a) shows the target dimensions. Feature contours are extracted at $h = h_0 = 150$ nm, denoted by the red cut in b). This red cut is for demonstration only and do not represent the dimensions of the target. Note that the features are not drawn to scale, where the pattern pitch is 100 μm and the feature height is in nanometers.

Finally, in Chapter 6, we describe a previously demonstrated polymer-coating and heating process capable of quickly planarizing and even reversing the bias of an initially conformal polymer film [17]. Bias is defined as the difference between open and trench region film heights (see Fig. 1.3). The polymer is a low-molecular-weight random copolymer composed of polystyrene (PS) and poly(4-*tert*-butoxycarbonyloxystyrene) (PTBSM). The copolymer is abbreviated as PS-co-PTBSM. Upon heating PS-co-PTBSM to temperatures above 190°C, the PTBSM subunits are deprotected to form poly(4-hydroxystyrene) (PHOST) subunits along with gaseous carbon dioxide and isobutylene that escape the film as shown in Fig. 1.3c. Spin coating the copolymer onto a substrate containing trenches initially produces a conformal film, but with sufficient annealing (~10 seconds at 240°C) the film quickly reverses in bias [17].

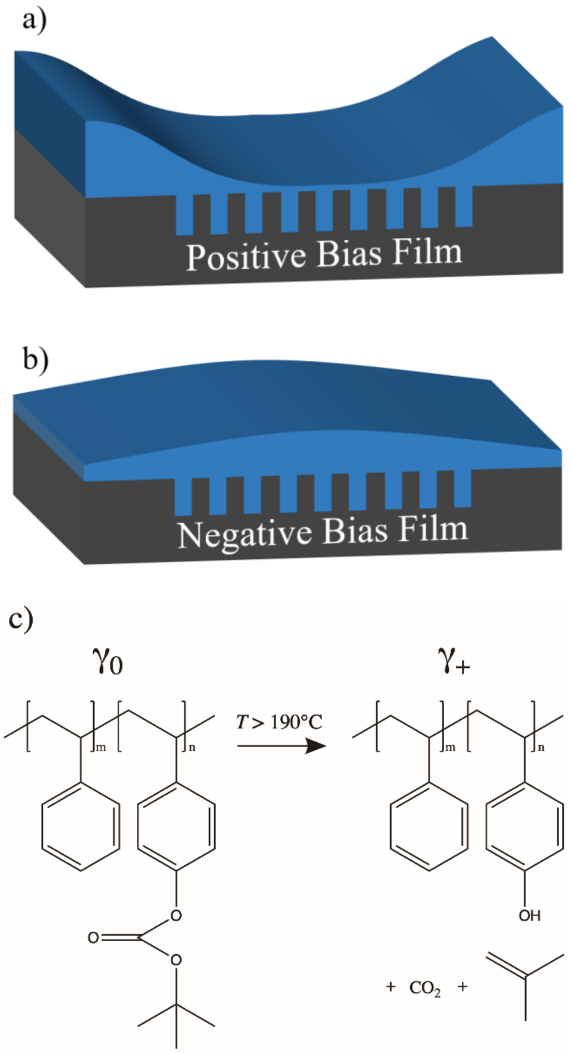

Figure 1.3 Depiction of thin films possessing (a) positive and (b) negative bias. Positive bias is characterized by a lower film height in trenched regions with respect to open regions, whereas negative bias is characterized by a higher film height in the trench regions with respect to the open regions. Bias is defined as the difference in film height between the open region and the trench region.

This reversal in bias is contrary to experience in leveling by traditional thermal reflow [18,19]. We present several theories for why this reversal in bias occurs, including thermocapillary-driven Marangoni flows and solvent-based solutal-driven Marangoni flows. We also propose a mechanism in which uneven rates of PTBSM deprotection across the film generate a gradient in surface tension and drive fluid into the trench regions. This is likely when considering that the protected PS-co-PTBSM is expected to possess a lower surface tension (γ_0) relative to the deprotected PS-co-PHOST (γ_+). Using modelling and simulation techniques, we show that an uneven deprotection reaction could drive a sufficient quantity of fluid into the trench regions and reverse the bias.

This work has answered questions essential to the advancement of MDP. Regarding the fundamental limits of this novel patterning process, we estimated the maximum aspect ratio and minimum feature pitch through an analytical and numerical analysis. We also performed an investigation on harnessing dewetting to go beyond the fundamental limits of MDP and avoid the breakthrough etch step. We also developed a strategy to address corner rounding and edge overlap issues related to two-dimensional patterning. This strategy hinged on iteratively simulating the flow process and optimizing the photoexposure field to improve pattern-target overlap. This strategy was implemented, and experimental results indeed showed improved shape control. Finally, we investigated a previously demonstrated bias-reversal process and developed a theory to explain this phenomenon.

Chapter 2: Fundamental Limits of Marangoni-driven Patterning[*]

2.1 INTRODUCTION

In the Marangoni effect fluid flows from regions of lower surface tension to regions of higher surface tension. The variations in surface tension can come about from variations in surface temperature (thermocapillary flow) or surface concentration (solutal Marangoni flow). The solutal Marangoni effect has been used to pattern thin polymer films by exposing them to UV light through a photomask [1–7]. A photochemical reaction takes place in the exposed regions that causes the surface energy of the film to increase. By heating the polymer film above its glass transition temperature, the polymer flows from the unexposed regions into the exposed regions of higher surface tension. This flow process forms features with hills and valleys possessing a peak-to-valley height, Δh, and a periodicity of λ. For equal line-space patterning, the aspect ratio, AR, of the feature is defined as the peak-to-valley height divided by the feature half-periodicity, such that $AR = 2\Delta h/\lambda$. A schematic of Marangoni-driven patterning (MDP) is shown in Fig. 2.1. Note that the films patterned to date have typically been 100-300 nm thick and the pattern pitches have ranged from roughly 1-200 μm.

MDP is similar in many respects to traditional photo and imprint lithography. In both photolithography and MDP, the photoexposure step triggers a photochemical reaction. But where photolithography relies on a solubility switch to drive feature formation, MDP instead harnesses surface tension gradients to drive fluid flow and generate features.

---

[*] This article has been published in *Colloids and Surfaces A: Physiochemical and Engineering Aspects,* 603, Stanley, S. K. and Bonnecaze, R. T., Fundamental Limits of Marangoni-driven Patterning, 125217, Copyright Elsevier (2020). Fig. 2.1 has been adapted to better fit the page. Other minor format changes have been made and additional commentary has been added. The author would also like to thank and acknowledge Dr. Chris Ellison and Gabriel Cossio for their help understanding feature aspect ratio.

Similar to imprint lithography, MDP results in a residual layer between the valleys and the substrate, which could be removed using selective, anisotropic etch techniques. Doing so would expose the underlying substrate for further patterning.

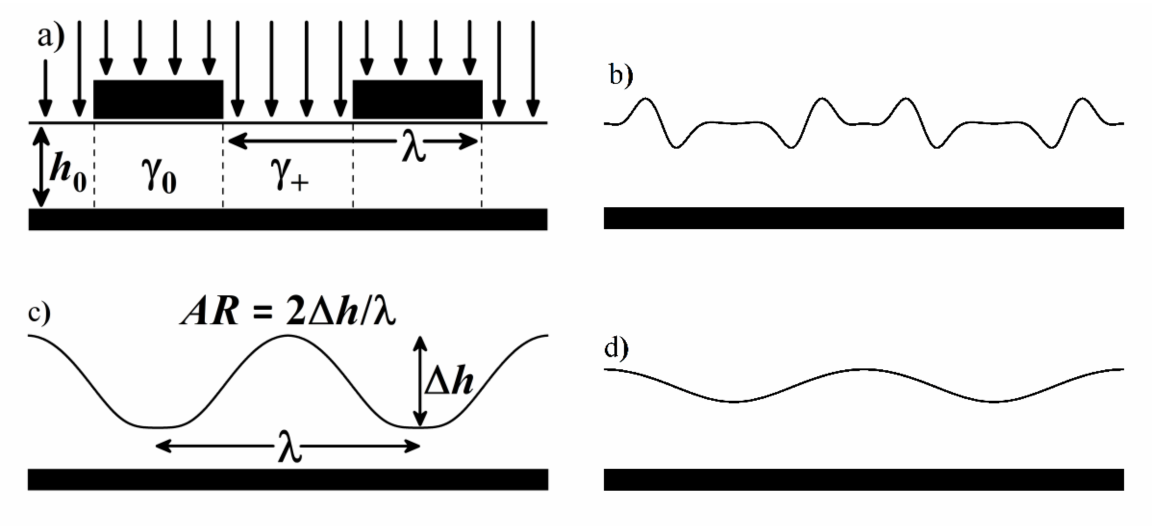

Figure 2.1 Schematic of Marangoni-driven patterning carried out using a contact exposure technique. a) Light exposure step in which an equal line-space photomask of periodicity λ is used to selectively expose to UV light the film of initial height, h_0. Exposed areas undergo a chemical reaction and possess a surface energy, or surface tension, of γ_+ while those unexposed areas remain unaffected and possess the nominal surface tension, γ_0. b) Annealing the film above its glass transition temperature causes the polymer film to flow into the exposed regions. The flow is initially strongest at the crossover between the exposed and unexposed regions, resulting double peaks. c) The double peaks eventually merge to form peaks and valleys with a peak to valley height of Δh and an aspect ratio, *AR*, where $AR = 2\Delta h/\lambda$. d) At long annealing times, the surface tension promoter dissipates due to diffusion effects and capillary forces eventually planarize the film. Note that the figures are not necessarily drawn to scale, as films patterned to date are typically several hundreds of nanometers thick and the pattern pitches have ranged from roughly 1-200 μm.

MDP possesses several processing characteristics that distinguish it from traditional patterning methods. Where in photolithography, toxic development solvents may be required, MDP relies solely on a heating step to drive feature formation. MDP also avoids the complications inherent to template fill and lift-off in imprint lithography. The distinguishing processing steps in MDP may be advantageous in roll-to-roll patterning. For instance, although a solvent develop step may be simple in wafer-scale photolithography, dragging a patterned web through a solvent development bath may not be ideal. Conversely, to develop the features with MDP, an annealing oven and perhaps a breakthrough etch chamber could be used to avoid the solvent develop step.

Technologies served by MDP could include functional coatings for improved surface adhesion [15], antifouling [16], improved light capture [14], and an etch mask for fabricating flexible electronics and flexible metamaterials. Flexible terahertz metamaterials [12,13] are a particularly promising application for MDP as the size requirements for terahertz metamaterials of 1-100 μm have been achieved in previous MDP experiments. The photoexposure step at these size scales could be performed in a roll-to-roll setting using optical maskless exposure techniques [11,20] or using photo-roll exposure techniques [21,22].

To gauge the full scope of applications for MDP, it is necessary to understand the physical limits of the patterning mechanism. The goal of this chapter is to determine an upper bound for the maximum possible feature aspect ratio, and a lower bound for the minimum printable feature half-pitch, λ for equal line-space MDP. High aspect ratio structures are desirable because they often provide improved etch protection for device fabrication or improved optical properties. Smaller feature pitches are beneficial for creating higher density structures and can interact favorably with shorter optical wavelengths. To date the largest reported aspect ratio (AR) is roughly 0.04 [6] and the smallest reported feature pitch is roughly 1.5 μm [3]. Using a previously developed model for MDP along with a linear analysis, we determine the maximum feature aspect ratio and the minimum feature pitch.

These limits are compared to previous experimental results to show that significant opportunities remain to improve feature quality.

The remainder of the chapter is as follows. First, a model for equal line-space MDP is presented and a framework for determining the maximum AR is outlined. A nonlinear and linear analyses are then performed to determine the steady-state feature height under various conditions. Using reasonable physical parameters and engineering constraints, the maximum feature aspect ratio and minimum printable half-pitch are determined and compared to previous literature results. Finally, we discuss barriers and strategies to realize these improvements and comment on potential research avenues for further improving the patterning process.

2.2 THEORY AND ANALYSIS

To understand the fundamental limits of the feature aspect ratio, we present a model for equal line-space MDP to determine the AR as a function of the polymer-substrate system. We then solve this model using both analytical and numerical methods and determine an upper bound for the feature aspect ratio and lower bound for the feature pitch.

2.2.1 Model for Marangoni-driven patterning

Several forces govern feature formation in MDP. Marangoni forces propel the fluid to regions of higher surface tension while capillary forces oppose the formation of surface features. Species diffusion also acts to dampen the features, causing the surface tension gradient to dissipate and weaken the Marangoni flow. Over time, capillary forces dominate and eventually replanarize the film. In extreme cases where very tall features are generated, the valleys come close to the substrate and can be influenced by polymer-substrate van der Waals interactions. Accounting for Marangoni, capillary, van der Waals, and diffusive forces, we present a model for MDP.

The fluid flow is modeled using the thin film equation, which is a reduced-order model derived from the Navier-Stokes equation under the lubrication approximation. This approximation takes advantages of the disparate thickness and pitch scales assuming $2h_0/\lambda = 2\varepsilon << 1$, which is typical of previous experiments. The thin film equation is expressed as [7,23]

$$\frac{\partial h}{\partial t}+\frac{\partial}{\partial x}\left(hu\right)=0. \tag{2.1}$$

Here, h is the film height, t is time, x is the lateral dimension, and u is the vertically averaged, lateral fluid velocity. The average fluid velocity can be expressed as [7,23]

$$u=\frac{1}{2\mu}h\frac{\partial\gamma}{\partial x}+\frac{1}{3\mu}h^2\frac{\partial}{\partial x}\left(\gamma\frac{\partial^2 h}{\partial x^2}\right)+\frac{A}{6\pi\mu}\frac{1}{h^2}\frac{\partial h}{\partial x}, \tag{2.2}$$

where μ is the polymer viscosity, C is the mole fraction of the surface tension promoter, γ_0 is a nominal surface tension, and A is the Hamaker constant for a given polymer-substrate combination. The surface tension, γ, is assumed to follow a linear mixing rule according to

$$\gamma=\gamma_0+\Delta\Gamma C, \tag{2.3}$$

where $\Delta\Gamma$ is the difference in surface tension between the exposed and unexposed polymer species and C is the mole fraction of the higher surface tension component.

The first term in Eq. (2.2) accounts for the Marangoni forces while the second term accounts for capillary forces. In calculating the capillary pressure, the gradient of curvature is approximated as the second derivative in height. The third term in Eq. (2.2) accounts for the pressure caused by van der Waals forces, which begin to dominate in regions where the film nears the substrate (note the $1/h$ dependence). We note here that the third term in Eq. (2.2) assumes a single substrate material, where more complex expressions are required when the substrate is composed of multiple material layers [24]. Furthermore, the third term assumes the Hamaker constant is the same for both the high and low surface tension species.

Coupled to the thin film equation is the convection-diffusion equation, which tracks species concentration and is expressed as [25,26]

$$\frac{\partial(hC)}{\partial t}+\frac{\partial}{\partial x}\left(-Dh\frac{\partial C}{\partial x}+hCu\right)=0, \tag{2.4}$$

where D is the diffusivity of the surface tension promoter. D is assumed constant with respect to concentration. Note that the concentration here is not the surface concentration, but rather, it is a bulk concentration that is assumed vertically homogenous. This assumption is most valid in cases where the vertical diffusion time scale, t_{Dz}, is much shorter than the lateral advective time scale, t_{Adv} and has been shown to be valid for a past experimental system [7,8].

By scaling the variable quantities, we can express Eqs. (2.2) and (2.4) in dimensionless form. We employ the following scalings, with dimensionless variables denoted with an asterisk: $h^* = h/h_0$, $x^* = x/\lambda$, $C^* = C/C_0$, $t^* = t/t_M = t/(\mu\lambda^2/h_0\Delta\Gamma C_0)$ Here, h_0 is the initial film thickness, λ is the pattern periodicity, determined by the equal line-space photomask, C_0 is the maximum conversion of the photoproduct in the exposed regions, and t_M is the characteristic Marangoni flow time scale. Using these scalings, Eqs. (2.2) and (2.4) can be made dimensionless, with asterisks dropped for clarity, such that

$$\frac{\partial h}{\partial t}+\frac{\partial}{\partial x}\left\{\frac{1}{2}h^2\frac{\partial C}{\partial x}+\frac{\varepsilon^2}{3}h^3\frac{\partial}{\partial x}\left[\left(\frac{1}{\alpha}+C\right)\frac{\partial^2 h}{\partial x^2}\right]+\frac{V}{6\pi}\frac{1}{h}\frac{\partial h}{\partial x}\right\}=0, \tag{2.5}$$

and

$$\frac{\partial(Ch)}{\partial t}+\frac{\partial}{\partial x}\left\{-\frac{1}{Pe}h\frac{\partial C}{\partial x}+\frac{1}{2}h^2C\frac{\partial C}{\partial x}+\frac{\varepsilon^2}{3}h^3C\frac{\partial}{\partial x}\left[\left(\frac{1}{\alpha}+C\right)\frac{\partial^2 h}{\partial x^2}\right]+\frac{V}{6\pi}\frac{C}{h}\frac{\partial h}{\partial x}\right\}=0, \tag{2.6}$$

where, $\alpha = \Delta\Gamma C_0/\gamma_0$, $\varepsilon = h_0/\lambda$, $V = A/h_0^2\Delta\Gamma C_0$, and $Pe = h_0\Delta\Gamma C_0/\mu D$. α is a ratio of the Marangoni to capillary forces, ε is the ratio of the initial film thickness to the pattern pitch, V is a ratio of van der Walls forces to Marangoni forces, and Pe is the Péclet number and is a ratio of advective forces to diffusive forces.

To provide a sense for how these dimensionless numbers affect the aspect ratio, we note that larger values of α indicate stronger Marangoni forces and promote taller features, which is ideal for generating higher aspect ratio structures. Furthermore, note that larger values of Pe weaken the diffusive forces and promote taller features by preventing feature decay. ε can be thought of as a scaled film thickness, and smaller values of ε dampen capillary forces and promote taller features. Finally, larger values of V indicate stronger van der Waals forces. For positive V, van der Waals forces are attractive and promote taller features as the film nears the substrate, whereas negative V indicates repulsive forces, which dampen feature growth.

During the patterning process, diffusion of the surface tension promoter weakens the surface tension gradient. To maximize the peak-to-valley height and aspect ratio, we consider the case in which lateral diffusion is negligible, i.e. $D = 0$ and $Pe = \infty$, which allows for a steady-state to form. We note that this assumption of no diffusion is only applied in the lateral direction and the assumption of fast vertical diffusion is maintained. To determine a steady-state solution, we begin by performing a linear analysis of Eq. (2.5). This analytical solution will provide a framework for understanding how to maximize the feature aspect ratio. We will then perform a nonlinear, numerical analysis of Eqs. (2.5) and (2.6) (now coupled) to account for model features neglected in the linear analysis.

2.2.2 Linear Analysis

To derive a linearized, analytical expression for the steady-state height profile, $h_{\mathrm{Lin}}(x)$, we first assume that species transfer is negligible, which allows for a fixed concentration and permits us to ignore the convection diffusion equation altogether. For equal line-space patterning, we assume a sinusoidal initial concentration, which varies from 0 to 1 according to

$$C = \frac{1 - \cos\left(2\pi x\right)}{2}. \tag{2.7}$$

This assumed concentration gradient does not dissipate over time, and it provides an upper bound estimate of the AR within the linearized model. We also assume that the magnitude of the surface tension gradient is small relative to the absolute surface tension, i.e. $\alpha \ll 1$. This assumption allows us to neglect the concentration-dependence in the capillary flow term of Eq. (2.5) and facilitates an analytical result. We then perform a linearization by assuming that height variations are small relative to the initial film height. This results in

$h_{\mathrm{Lin}} = 1 - \eta(x)$, where $\eta(x) << 1$. By substituting h for h_{Lin} in Eq. (2.5) and by dropping terms that are $O(\eta^2)$ and smaller, the linearized form of Eq. (2.5) becomes

$$\frac{1}{2}\frac{\partial C}{\partial x} - \frac{\varepsilon^2}{3\alpha}\frac{\partial^3\eta}{\partial x^3} - \frac{V}{6\pi}\frac{\partial\eta}{\partial x} = 0. \tag{2.8}$$

Next, we determine the functional form of η. For positive α, the surface tension is greater in exposed regions of higher photoproduct concentration. This means that the film will be taller in regions of higher concentration. We therefore assume that η will possess a functional form similar to the concentration profile, such that $\eta = \tilde{\eta}\cos(2\pi x)$, where $\tilde{\eta}$ is the dimensionless feature amplitude. Inserting the expressions for η and C into Eq. (2.8), we find

$$\frac{\pi}{2}\sin(2\pi x) - \frac{\varepsilon^2}{\alpha}\frac{8\pi^3}{3}\tilde{\eta}\sin(2\pi x) + \tilde{\eta}\frac{V}{3}\sin\left(2\pi \mathrm{x}\right) = 0. \tag{2.9}$$

Solving for $\tilde{\eta}$, we find that the dimensionless feature amplitude is

$$\tilde{\eta} = \frac{3\pi}{2}\left(\frac{\alpha}{8\pi^3\varepsilon^2 - \alpha V}\right), \tag{2.10}$$

and the analytical expression for the dimensionless feature height is

$$h_{\mathrm{Lin}}\left(x\right) = 1 - \frac{3\pi}{2}\left(\frac{\alpha}{8\pi^3\varepsilon^2 - \alpha V}\right)\cos\left(2\pi x\right). \tag{2.11}$$

To help visualize the feature profile, Fig. 2.2 plots $h_{\mathrm{Lin}}(\mathrm{x})$ for varying ε, α, and V.

Note that the features get smaller for increasing ε in Fig. 2.2a and get taller for increasing α and V in Figs. 2.2b and 2.2c. These results are to be expected. Firstly, thicker films (increased ε) favor capillary forces over Marangoni forces, leading to shorter dimensionless feature heights. Next, increasing the surface tension difference relative to the capillary forces (increased α) increases the driving force and leads to taller films. Varying V, we must consider both repulsive and attractive van der Waals interactions. For negative V, the polymer-substrate interactions are repulsive, resulting in a negative pressure in the valleys that draws fluid into the valley regions and decreases the peak height. And for positive V, the polymer-substrate interactions are attractive, leading to a positive pressure in the valleys that forces fluid into the peak regions. This is why the film gets taller for increasing V.

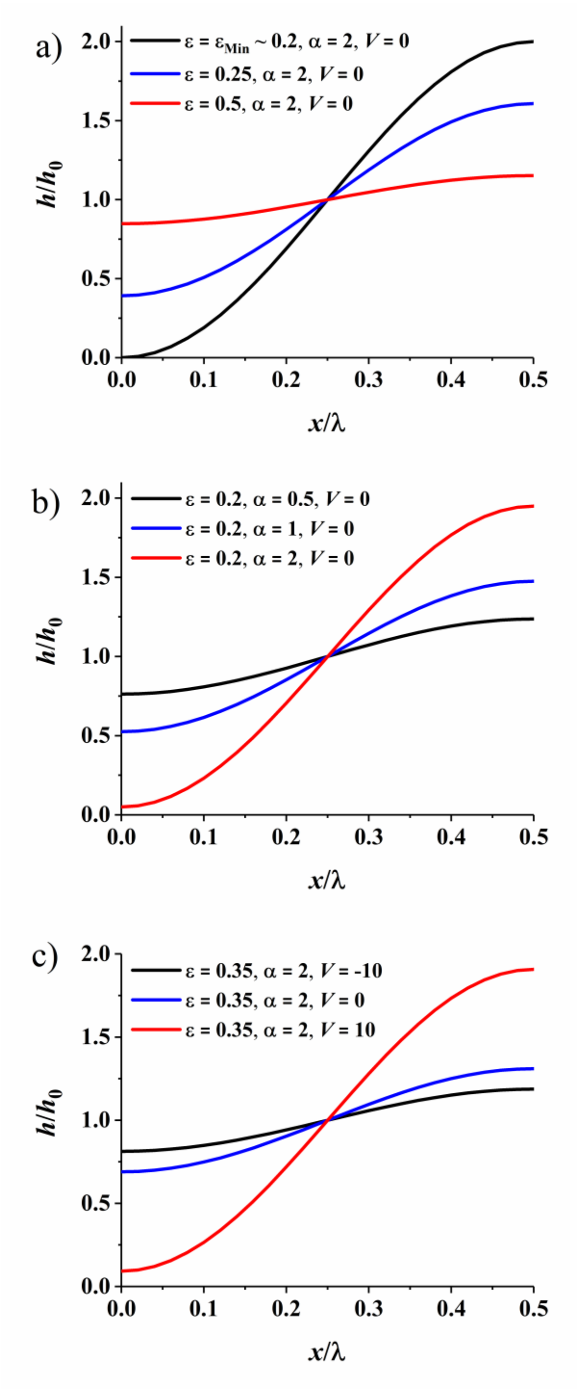

Figure 2.2 Feature profiles calculated using the linearized solution for varying a) ε, b) α , and c) *V*. Note that in Fig. 2.2a, there exists a critical value of ε at which the feature touches the substrate.

The dimensional peak-to-valley height derived from the linear solution, Δh_{Lin}, is related to the dimensionless feature amplitude $\tilde{\eta}$ by

$$\Delta h_{\mathrm{Lin}} = 2\tilde{\eta} h_0 = \frac{3\pi\alpha h_0}{8\pi^3\varepsilon^2 - \alpha V}. \qquad (2.12)$$

We can now use this expression to learn about the aspect ratio as a function of ε, α, and V. Substituting Δh_{Lin} for Δh in the equation for aspect ratio (see Fig. 2.1), we find that the expression for aspect ratio according to the linearized solution is

$$AR_{\mathrm{Lin}} = 2\frac{\Delta h_{\mathrm{Lin}}}{\lambda} = \frac{6\pi\alpha\varepsilon}{8\pi^3\varepsilon^2 - \alpha V}. \qquad (2.13)$$

Eq. (2.13) shows that to maximize the aspect ratio, we must maximize α and the quantity αV. We also must determine the lower bound on ε. We begin by considering the limiting case in which the feature amplitude is so large that it touches the substrate, as exhibited in Fig. 2.2a. In such a case, the dimensionless feature amplitude is equal to unity ($\tilde{\eta} = 1$). In this limit, $\varepsilon_{\mathrm{Min}}$ can be solved for by setting $\tilde{\eta} = 1$ in Eq. (2.10) and solving for ε, giving

$$\varepsilon_{\mathrm{Min}} = \left(\frac{\alpha V}{8\pi^3} + \frac{3\alpha}{16\pi^2}\right)^{1/2}. \qquad (2.14)$$

For $\varepsilon < \varepsilon_{\mathrm{Min}}$, the solution becomes non-physical because the film cannot pass below the substrate. This non-physical behavior is due to the linear nature of the current solution.

By inserting the expression for $\varepsilon_{\mathrm{Min}}$ into Eq. (2.13), we find that the aspect ratio as a function of $\varepsilon_{\mathrm{Min}}$ is

$$AR_{\mathrm{Lin}}\left(\varepsilon_{\mathrm{Min}}\right) = 4\left(\frac{\alpha V}{8\pi^3} + \frac{3\alpha}{16\pi^2}\right)^{1/2}. \qquad (2.15)$$

To complete the analysis, we must determine appropriate physical bounds for α and the quantity αV. To determine α_{Max}, we must maximize the surface tension gradient relative to the nominal low surface tension component. α_{Max} is therefore expressed as $\alpha_{\mathrm{Max}} = \Delta\Gamma_{\mathrm{Max}} C_{0\mathrm{Max}}/\gamma_{0\mathrm{Min}}$. We consider several reported surface tension values [27] for various polymers provided in Table S2.1 of the Supporting Information to determine reasonable values for $\Delta\Gamma_{\mathrm{Max}}$ and $\gamma_{0\mathrm{Min}}$. Although Table S2.1 is not an exhaustive list of polymers, it helps give a sense for surface tension limiting values. The quantity of interest, $\Delta\Gamma_{\mathrm{Max}}/\gamma_{0\mathrm{Min}}$, is roughly the same across the several temperatures in this table, where $\Delta\Gamma_{\mathrm{Max}}/\gamma_{0\mathrm{Min}} \approx 2$. Using this limiting value and noting that $C_{0\mathrm{Max}} = 1$ for complete photoconversion, we find that $\alpha_{\mathrm{Max}} = \Delta\Gamma_{\mathrm{Max}} C_{0\mathrm{Max}}/\gamma_{0\mathrm{Min}} \approx 2$. This estimated upper limit is much larger than α reported in previous experiments. Arshad et al. reported $\Delta\Gamma C_0 \approx 0.2$ mN/m, $\gamma_0 \approx 31$ mN/m and therefore $\alpha \approx 0.0064$ for their polystyrene-poly(phenyl acetylene) system [7]. From these estimates, there is up to ~300-fold improvement that could be made by engineering polymer systems that generate larger surface tension gradients.

To determine the limiting value of αV, we first expand the quantity into its component parts, where $\alpha V = A/h_0^2\gamma_0$. $(\alpha V)_{\mathrm{Max}}$ is therefore expressed as $(\alpha V)_{\mathrm{Max}} = A_{\mathrm{Max}}/h_{0\mathrm{Min}}^2\gamma_{0\mathrm{Min}}$. We take $A_{\mathrm{Max}} \approx 10^{-19}$ J to be an appropriate limiting value for the Hamaker constant because dielectric systems (ceramics and polymers included) possess Hamaker constants in the range of 10^{-20}-10^{-19} J [28]. Revisiting the surface tension values of Table S2.1 of the Supporting Information, we consider $\gamma_{0\mathrm{Min}} \approx 10$ mN/m to be an appropriate limiting value for polymer surface tension. We note that the nominal surface tension can be made arbitrarily small by simply increasing the temperature, however, we feel $\gamma_{0\mathrm{Min}} = 10$ mN/m is an appropriate estimate under reasonable conditions. We also consider $h_{0\mathrm{Min}} \approx 1$ nm to be an appropriate limiting value for the initial polymer film thickness. Using these limiting values, we find that $(\alpha V)_{\mathrm{Max}} = A_{\mathrm{Max}}/h_{0\mathrm{Min}}^2\gamma_{0\mathrm{Min}} \approx 10$. This value of αV is much larger compared to those seen in prior experiments. In calculating αV in experiments, we note that typical values of h_0 and γ_0 are $h_0 \approx 150$ nm and $\gamma_0 \approx 31$ mN/m [7]. We also assume a pure silicon oxide (dielectric) coating with a Hamaker constant of $A = 2.2\text{x}10^{-20}$ J [24], but we note that patterning has typically been done on silicon wafers with a native oxide which is characterized by mixed attractive (from the silicon oxide) and repulsive (from the pure Si) interactions. Combining these typical values, we estimate that αV in experiments is roughly $\alpha V \approx 3\text{x}10^{-5}$. This value is low compared to the estimated $(\alpha V)_{\mathrm{Max}} \approx 10$, which is primarily due to the thick coatings typically used in experiments. As the coating is made thinner down to $h_{0\mathrm{Min}} \approx 1$ nm, the value of αV increases as $1/h_0^2$.

Using $(\alpha V)_{\mathrm{Max}} = 10$ and $\alpha_{\mathrm{Max}} = 2$ in Eq. (2.15), we find that the upper limit for pattern aspect ratio (as determined by the linear analysis) is $AR_{\mathrm{MaxLin}} \sim 1.1$. From our analysis, we also learn that for $\alpha_{\mathrm{Max}} = 2$ and increasingly negative V, AR_{LinMax} tends to zero, as increasingly repulsive van der Waals forces serve to dampen the film height. Finally, for $\alpha_{\mathrm{Max}} = 2$ and $V = 0$, $AR_{\mathrm{LinMax}} \sim 0.78$.

We next perform a nonlinear analysis and see how accounting for the nonlinearities affects the predicted upper bound on pattern aspect ratio.

2.2.3 Nonlinear Analysis

For the nonlinear analysis, we now allow the concentration to vary in time subject to convection effects while still assuming no lateral diffusion ($D = 0$ and $Pe = \infty$). To determine the steady-state film height, Eqs. (2.5) and (2.6) are solved from $t = 0$ out to steady state. The dimensionless film height is initialized to $h(\mathrm{x}, t = 0) = 1$ and the dimensionless concentration is initialized to $C(x, t = 0) = [1-\cos(2\pi \mathrm{x})]/2$.

Eqs. (2.5) and (2.6) were solved numerically using the commercial solver, COMSOL Multiphysics for various values of ε, α, and αV. A simulation grid of 100 elements were used and a tolerance ranging between 10^{-8} to 10^{-7} was used.

Steady-state feature profiles as determined by the nonlinear solver are shown in Fig. 2.3 for the limiting values of α, and αV, where $\alpha = \alpha_{\mathrm{Max}} = 2$ and $\alpha V = (\alpha V)_{\mathrm{Max}} = 10$. Fig. 2.3 also provides a sample feature profile as determined by the linear model for comparison.

Note that by decreasing the value of ε by ~ 0.003% from ε = 0.31028 to ε = 0.31027, a solution bifurcation occurs. For ε = 0.31028, a steady-state develops, but for ε = 0.31027, rapidly increasing van der Waals forces cause the film to dewet. This analysis used to determine dewetting conditions is similar to what was done by Angela et al. [29] in their work on thermocapillary-driven dewetting and is also similar to the bifurcation analysis done by Stoop et al. regarding different regimes in elastic surface patterning [30]. The value of ε at which the solution changes from steady-state to dewetting defines $\varepsilon_{\mathrm{Min}}$ for this nonlinear analysis. Therefore, for $\alpha = \alpha_{\mathrm{Max}} = 2$ and $\alpha V = \alpha V_{\mathrm{Max}} = 10$, $\varepsilon_{\mathrm{Min}} \sim 0.31028$. Note that the value of ε = 0.31028 is larger than in past experiments, where thickness and pattern periodicities have typically been $h_0 \approx 150$, $\lambda \approx 25$ μm, and $\varepsilon = h_0/\lambda \approx 0.006$.

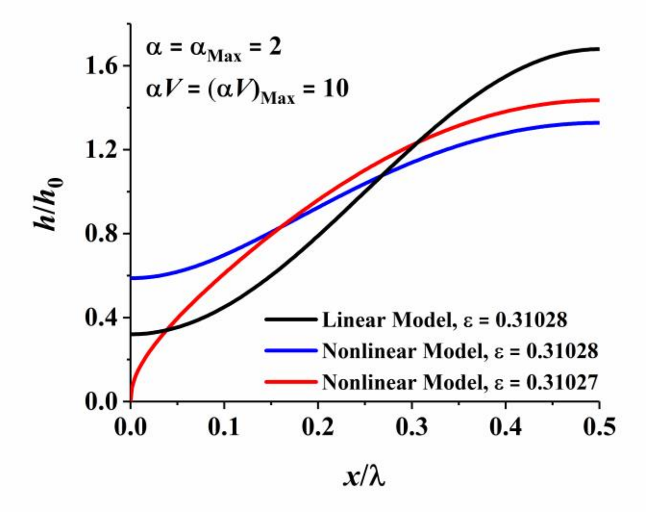

Figure 2.3 Steady-state and dewetting feature profiles as determined by the nonlinear and linear models for the limiting values of α, and αV, where $\alpha = \alpha_{\text{Max}} = 2$ and $\alpha V = \alpha V_{\text{Max}} = 10$. Note that by decreasing the value of ε by ~0.003% from ε = 0.31028 to ε = 0.31027, the film is forced to dewet due to the rapidly increasing van der Waals forces. This transition point defines the minimum value of ε for the nonlinear analysis. Also note that in comparing the linear and nonlinear models for ε = 0.31028, the linear model over predicts the feature height.

By comparing the linear and nonlinear models in Fig. 2.3 for ε = 0.31028, the linear model over predicts the feature height. Knowing this, we can expect the predicted maximum aspect ratio to be lower for the nonlinear model. We attribute this overprediction in the linear model to the fact that it neglects concentration dependence of capillary forces, as shown in Section S2.2 of the Supporting Information.

AR_{Nonlin} is calculated as

$$AR_{\text{Nonlin}} = 2\frac{\Delta h_{\text{Nonlin}}}{\lambda} = 2\Delta h^{*}_{\text{Nonlin}}\frac{h_0}{\lambda} = 2\Delta h^{*}_{\text{Nonlin}}\varepsilon \tag{2.16}$$

where $\Delta h^{*}_{\text{Nonlin}}$ is the dimensionless peak-to-valley height scaled by h_0. As seen in Fig. 2.3, $\varepsilon_{\text{Min}} \sim 0.31028$ and $\Delta h^{*}_{\text{Nonlin}} \sim 0.7397$ for the limiting values of $\alpha = \alpha_{\text{Max}} = 2$ and

$\alpha V = \alpha V_{\text{Max}} = 10$. Plugging these limiting values into Eq. (2.16), we find that $AR_{\text{Nonlin}} \sim 0.4591$, roughly half of the maximum aspect ratio predicted by the linear model.

We repeated this process of identifying the dewetting transition point, ε_{Min}, for different values of αV. In dimensional terms, this is synonymous with fixing the values of h_0, A, γ_0, and $\Delta\Gamma C_0$ and varying λ. Fig. 2.4a shows the dimensional peak-to-valley height as a function of λ for fixed values of h_0, A, γ_0, and α (remember $\alpha = \Delta\Gamma C_0/\gamma_0$). Note in Fig. 2.4 that the dewetting points integral to determining the maximum aspect ratio occur at $2h_0/\lambda = 2\varepsilon \approx 0.2$-$0.6$, which is arguably below the lubrication limit of $2\varepsilon << 1$. Going to smaller λ (larger ε) prior to the dewetting points in Fig. 2.4, the lubrication limit is eventually exceeded. Results from both the linear and nonlinear models are shown. Note that the peak-to-valley height increases with increasing pattern periodicity, i.e. decreasing ε. The peak-to-valley height also increases with initial film thickness as shown by comparing the several lines. At large enough λ, the valley region touches the substrate (linear) or dewets (nonlinear) and results cannot be taken to larger λ, as indicated by the end-point symbols. Results from past experimental studies are also shown.

Fig. 2.4b shows the aspect ratio as a function of λ for specified values of h_0, A, γ_0, and α. Again, note that aspect ratio improves with increasing λ and the endpoint symbols mark the point at which the valley region touches the substrate (linearized model) or dewets (nonlinear model). For the sake of completeness, we have reported the feature height and aspect ratio for pitches that extend down to 1 nm. Such small pitches may be printable by extremely precise printing tools like e-beam imaging systems, but are below practical printing limits for high-throughput tools. For reference, typical 193 nm immersion lithography tools are capable of printing pitches of roughly 80 nm [31].

Figs. 2.4a and 2.4b also showcase experimentally demonstrated peak-to-valley heights and aspect ratios from previous studies [1,2,4,6,7], which show the progress made over the last several years and emphasizes that more progress can still be made. Table 2.1 provides experimental conditions and results used to generate the literature values in Figs. 2.4a and 2.4b. We point out that the parameters in experiments were different from the limiting values probed in this study. This is why the experimental values fall far from the model curves. Note that the largest reported aspect ratio is roughly 0.045 and the largest possible aspect ratio as predicted from the nonlinear analysis is roughly 0.5. This means that there is roughly ten-fold improvement yet to be achieved.

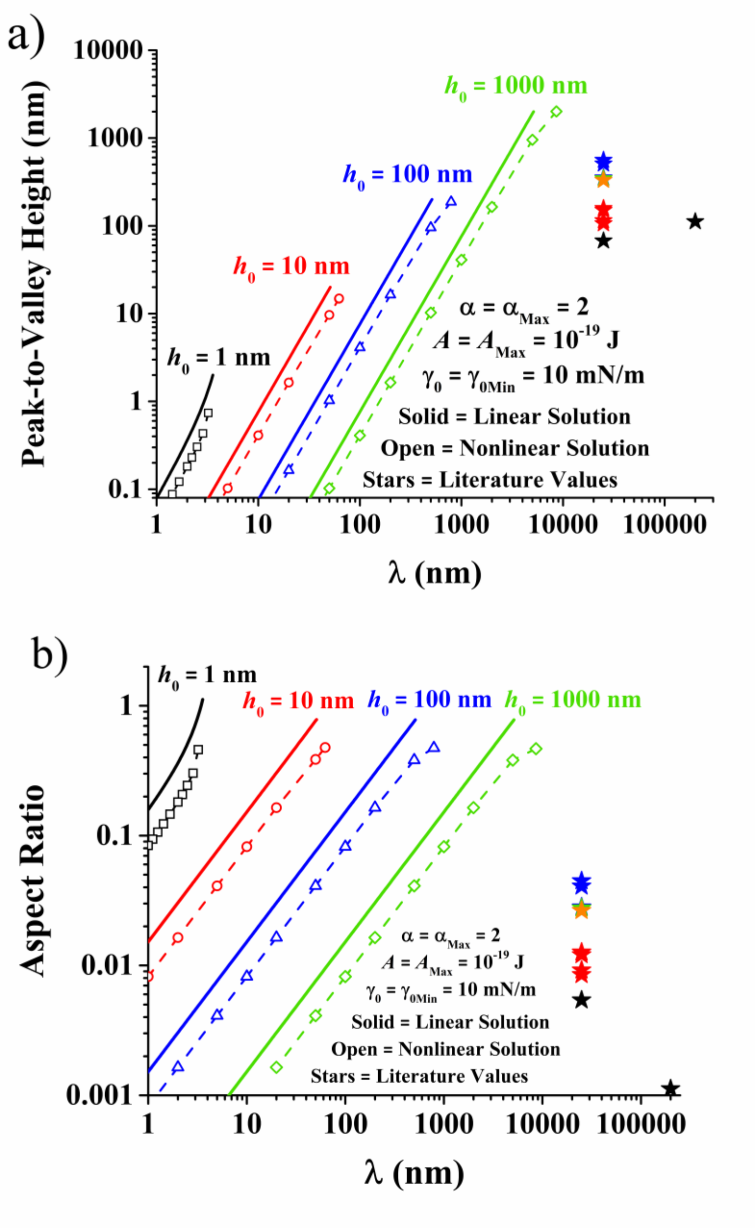

Figure 2.4 (a) Peak-to-valley height and (b) aspect ratio as a function of pattern periodicity, λ, for given values of h_0, A, γ_0, α, and V. The lines/symbols that terminate at the upper right of each series indicate when $\varepsilon_{\mathrm{Min}}$ is achieved where the film either touches the substrate (linearized model) or is barely stabilized against dewetting (nonlinear model). Experimental observations extracted from various references are also included. The symbol-reference pairs are as follows: ★ = [1], ★ = [7], ★ = [3], ★ = [4], ★ = [6]. Note that the values of h_0, α, A, and γ_0 reported in the figure apply only to the simulation results and not to the experiments. See Table 2.1 for the values used in experiments.

Table 2.1 Experimental conditions and reported feature heights/AR for the literature values reported in Figs. 2.4a and 2.4b. Data extracted from the indicated references. *Values extracted from feature profiles. †Values extracted from maximum recorded peak-to-valley height for given experiment.

Symbol	Ref./Year	P2V Height (nm)	AR	h_0 (nm)	λ (nm)
★	[1]/2012	67.6*	0.0054	150	$2.5\text{x}10^4$
★	[1]/2012	112*	0.0011	150	$2.0\text{x}10^5$
★	[7]/2014	106†	0.0085	145	$2.5\text{x}10^4$
★	[7]/2014	115†	0.0092	130	$2.5\text{x}10^4$
★	[7]/2014	151†	0.012	148	$2.5\text{x}10^4$
★	[7]/2014	158†	0.013	148	$2.5\text{x}10^4$
★	[3]/2014	331†	0.026	250	$2.5\text{x}10^4$
★	[4]/2014	346*	0.028	167	$2.5\text{x}10^4$
★	[6]/2017	352†	0.028	285	$2.5\text{x}10^4$
★	[6]/2017	509†	0.041	285	$2.5\text{x}10^4$
★	[6]/2017	560†	0.045	285	$2.5\text{x}10^4$

We now call attention to the fact that a sinusoid was used to initialize the concentration distribution because it facilitates an analytical solution. In practice, sharper distributions may form when using contact exposure techniques. To determine whether a sharper concentration profile would lead to further improved aspect ratios, we performed the nonlinear simulations using a step function to initialize the concentration distribution. The step was initialized such that the dimensionless size of the transition zone was 0.05 (5% of the full pattern periodicity) and the simulations were performed at conditions similar to those used for the sinusoidal concentration distribution. Due to the highly convective nature of the problem, small oscillations appeared in the concentration profile that negatively affected the simulation. To dampen the ringing effects, we incorporated artificial diffusion into the model by setting Pe in Eq. (2.6) to $5\text{x}10^9$, which allowed for diffusion of the sharp, unwanted gradients. This allowed the extraction of the plateau in peak-to-valley height. Note this plateau decays at times much larger than patterning times in practice due to the artificial diffusion and does not significantly affect the plateau value. Section S2.3 of the

Supporting Information provides further details regarding the simulation setup and a visual comparison of the sinusoid and step function concentration distributions. Fig. 2.5 shows the calculated aspect ratio for both the step and sine function initial concentration profiles and it can be seen that the aspect ratio does not change significantly when using a step concentration distribution. We did not obtain the dewetting points for h_0 = 100 nm, and h_0 = 1000 nm. However, given that the best possible aspect ratio as seen in Fig. 2.5 by the sinusoidal concentration profile is relatively constant for varying h_0, we have no reason to believe that the aspect ratio would be markedly different in the case of a step function for h_0 > 10 nm.

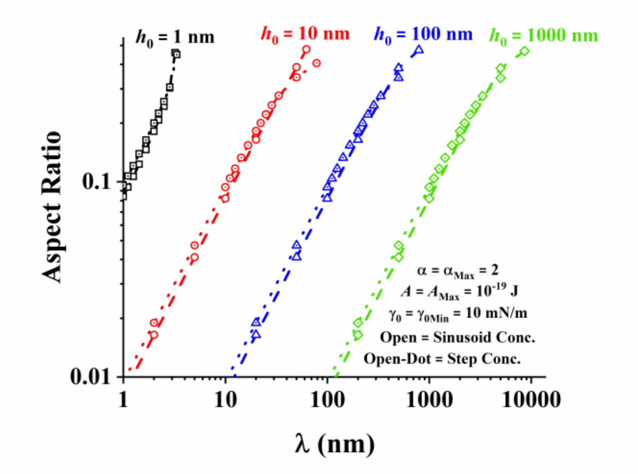

Figure 2.5 Aspect ratio as a function of pattern periodicity, λ, for given values of h_0, A, γ_0, α, and V. The symbols that terminate at the upper right of each series indicate when ε_{Min} is achieved, except for the step function profiles at h_0 = 100 nm and h_0 = 1000 nm.

For completeness, we report in Table 2.2 the values of ε_{Min} and corresponding values of Δh_{Nonlin} and AR_{Nonlin} used in creating Figs. 2.4a, 2.4b and Fig. 2.5 for the various values of h_0. We note that the maximum aspect ratio for the step function is slightly lower than that of the corresponding sine function at h_0 = 1 nm and h_0 = 10 nm. This may be due to the fact that ε_{Min} was determined to ~0.01% for the sine function and only ~0.1% for the step function. Increased ringing in the concentration field at higher accuracy values of $\varepsilon_{\mathrm{Min}}$ prompted the use of ~0.1% accuracy for the step function.

Note that the maximum value of AR_{Nonlin} ~ 0.4771 occurs for h_0 = 10 nm ($\alpha V = 10^{-1}$), showing a maximum in AR_{Nonlin} occurs at an intermediate value of h_0. This is contrary to the linearized model, which shows the maximum aspect ratio monotonically increasing for decreasing h_0 (or increasing αV). This discrepancy is likely a result of the nonlinearities now accounted for. It is apparent from Table 2.2 that the maximum aspect ratio as predicted by the nonlinear model is $AR_{\mathrm{NonlinMax}}$ ~ 0.5.

Table 2.2 Dewetting transition point values, $\varepsilon_{\mathrm{Min}}$ and associated accuracy for the step and sine function models for $\alpha = \alpha_{\mathrm{Max}} = 2$, $A = A_{\mathrm{Max}} = 10^{-19}$ J, and $\gamma_0 = \gamma_{0\mathrm{Min}} = 10$ mN/m (same as Figs. 2.4ab and 2.5). Corresponding $\Delta h^*_{\mathrm{Nonlin}}$ and $AR_{\mathrm{NonlinMax}}$ are also reported. The maximum aspect ratio observed was for the sine function case at h_0 = 10 nm, and is bolded.

C Distribution	h_0 (nm)	αV	$\varepsilon_{\mathrm{Min}}$ (% Acc.)	$\Delta h^*_{\mathrm{Nonlin}}$	AR_{Nonlin}
Sine	1	10	0.31028 (~0.01%)	0.7397	0.4591
Sine	10	10^{-1}	0.16020 (~0.01%)	1.489	**0.4771**
Sine	100	10^{-3}	0.12649 (~0.01%)	1.870	0.4730
Sine	1000	10^{-5}	0.11628 (~0.01%)	2.011	0.4676
Step	1	10	0.2991 (~0.1%)	0.7497	0.4485
Step	10	10^{-1}	0.1273 (~0.1%)	1.592	0.4052

2.2.4 Minimum Feature Pitch

We further extend our results to understand the lower bound on printable pitches for MDP. We note that the model does not obviate a lower limit. However, by imposing engineering constraints on h_0 and Δh, one can estimate a lower bound on feature pitch. One might assume that for an etch-barrier application, the minimum Δh that can be tolerated is roughly 10 nm and that the film thickness should not be less than 10 nm. For the proposed set of assumptions and constraints ($h_0 = \Delta h = 10$ nm) and $\alpha = \alpha_{\text{Max}}$, $A = A_{\text{Max}}$, and $\gamma_0 = \gamma_{0\text{Min}}$, and $Pe = \infty$, Fig. 2.4a shows that the minimum pitch would be roughly 50 nm. This minimum pitch is comparable with conventional high-throughput 193 nm immersion lithography tools that can print pitches of roughly 80 nm or larger [31].

2.3 DISCUSSION

The maximum achievable aspect ratio for MDP, as determined by the nonlinear analysis, is about 0.5. This is roughly ten-fold larger than the best aspect ratio achieved in experiments to date of roughly 0.045. To realize this improvement, new polymer systems must be engineered to minimize diffusion effects and achieve the largest possible surface tension driving force.

As feature decay is initiated by diffusion effects, it is essential to design a polymer system with minimal species diffusion. Examining the relative strength of convective forces to diffusive forces, characterized by the Péclet number ($Pe = h_0 \Delta\Gamma C_0 / \mu D$), we find it is similarly important to minimize the fluid viscosity. In practice, it is difficult to simultaneously lower polymer viscosity and diffusivity as the two quantities are inversely related according to the Stokes-Einstein relation [32]. For instance, lowering the fluid temperature reduces species diffusivity, but counterproductively increases the fluid viscosity. In an effort to decouple polymer diffusivity from viscosity, Jones et al. demonstrated MDP using a polymer blend [6]. They showed that by blending low molecular weight polystyrene homopolymer (low viscosity) with high molecular weight (low diffusivity) photoactive copolymer, the feature aspect ratio could be improved relative to a previous experimental system possessing comparable surface tension forces [7]. This strategy of using high molecular weight dopant polymers may be necessary in designing future polymer systems to ensure that *Pe* is sufficiently large to achieve a temporary steady state and the maximum feature height.

To maximize the feature aspect ratio, the relative strength of the Marangoni forces to capillary forces ($\alpha = \Delta\Gamma C_0/\gamma_0$) must be maximized. We estimated that $\alpha_{\mathrm{Max}} \approx 2$ and compare this to previously reported values of α. Arshad et al. reported $\Delta\Gamma C_0 \approx 0.2$ mN/m, $\gamma_0 \approx 31$ mN/m and therefore $\alpha \approx 0.0064$ for their polystyrene-poly(phenyl acetylene) system. Jones et al. reported a homopolymer-copolymer blend with $\Delta\Gamma C_0 \approx 0.2$ mN/m and we further assume that their bulk polystyrene system had $\gamma_0 \approx 30$ mN/m (see Table S2.1 in the Supporting Information). Therefore, the system of Jones et al. possessed $\alpha \approx 0.0067$. Considering these two reported values of α, we find that there is up to ~300-fold improvement available in raising α. One might ask why only a ten-fold improvement is available in aspect ratio while a 300-fold improvement is available in α. This is because the aspect ratio is sublinear in α, where $AR_{\mathrm{Lin}}(\varepsilon_{\mathrm{Min}}) \propto \alpha^{1/2}$ in the linearized model (see Eq. (2.15)).

To achieve such a large surface tension driving force, one could design a photoswitchable polymer system in which the exposed region undergoes a radical change in surface tension. Foreseeable challenges exist in achieving this large surface tension difference. Jones et al. noted that when using a polymer blend to reduce diffusion effects, large surface tension differences could lead to immiscibility between blended polymers and further noted that this could lead to phase segregation [33] and potentially directed film dewetting [6]. To maintain miscibility, Jones et al. used a copolymer containing the photoactive monomer for increasing the surface tension along with a monomer unit dedicated to promoting polymer miscibility. This copolymer strategy was effective at preserving miscibility, but we note that doing so may in fact decrease the achievable surface-tension difference between exposed and unexposed regions.

We note that our analysis was performed for *strict* MDP in which dewetting was not allowed. It is possible (and perhaps encouraging) that triggering dewetting during the patterning process could enable higher aspect ratio features, as the dewetting event would cause the feature to bead up and become taller. This is an extremely promising avenue of exploration for future experimental and simulation work.

In designing a polymer-substrate system, one must be conscious of the resulting Hamaker constant. We note that the maximum aspect ratio as determined by the more accurate nonlinear model is practically insensitive to αV at the size scales considered (see Fig. 2.4). This means one need not be overly concerned with the resulting Hamaker constant as it may be sufficient to design a polymer-substrate system with a positive or even slightly negative Hamaker constant in the low surface-tension region.

2.4 CONCLUSION AND FUTURE WORK

To understand the full scope of potential applications for MDP, it is important to understand the maximum feature aspect ratio and minimum pattern pitch. To determine these previously unknown values for equal line-space MDP, we have presented a model for MDP and derived a linearized solution that compared well with numerically generated results. Using reasonable bounds on physical parameters, it was found that the maximum aspect ratio for MDP is roughly 0.5 according to the full nonlinear model. Comparing this upper bound to previous experimental results, it was shown that roughly ten-fold improvement in aspect ratio is available. It was also shown that for a set of reasonable engineering constrains ($h_0 = \Delta h = 10$ nm), the minimum printable pitch is roughly 50 nm, which is comparable to conventional high-volume printing capabilities.

To realize improved aspect ratios, the newly designed polymer system should simultaneously exhibit relatively low diffusivity and low viscosity so as to maximize Pe. Furthermore, the relative strength of the surface tension gradient to the absolute surface tension could be improved by up to 300-fold. In practice, it may be difficult to achieve large surface tension gradients due to the miscibility issues outlined by Jones et al. Finally, Marangoni-facilitated dewetting is a promising avenue of future exploration that may allow for aspect ratios beyond the predicted 0.5 limit.

Future work could potentially refine the estimate by more accurately accounting for various forces. A key assumption in modelling the flow was that the pattern periodicity was large relative to the film thickness, also known as the lubrication approximation. Although the lubrication-based model provided good model-experiment agreement in past work [7], it may worsen as the film is made thicker relative to the pattern pitch. More complete multiphase modelling could be implemented to account for the inertial forces neglected while in the lubrication regime. We also note that as part of the lubrication approximation, one may also approximate the gradient in film curvature as the second derivative in the film height. This allowed for the analytical solution presented earlier and greatly simplifies the calculation. Similar to the lubrication approximation, this approximation worsens when aspect ratio becomes large. To more fully capture the effect of capillary forces, one could numerically simulate the system using the full nonlinear expression for the gradient of curvature. Finally, the assumption of a vertically equilibrated concentration could be relaxed by implementing a moving boundary model that accounts for the complete two-dimensional concentration field. This would better capture rotational flow effects and help understand their impact on pattern aspect ratios.

SUPPORTING INFORMATION

S2.1 Table of Polymer Surface Tensions

Table S2.1 is provided as a survey of surface energies/tensions of various polymers. This table is by no means exhaustive, but help provide a sense for possible upper bounds on $\Delta\Gamma$ and lower bounds on γ_0. $\Delta\Gamma_{Max}$ is calculated by taking the difference between the smallest and largest values of γ at a given temperature. Note that the ratio $\Delta\Gamma_{Max}/\gamma_{0Min}$ is relatively constant with temperature, staying around $\Delta\Gamma_{Max}/\gamma_{0Min} \approx 2$.

Table S2.1 Surface tension values for various polymers at 20, 140, and 180°C. Table adapted from Bicerano [27]. Mn is number-average molecular weight, Mw is weight-average molecular weight, Mv is viscosity-average molecular weight, and M is for cases where the type of molecular weight was not provided.

Polymer	Molecular Weight	γ (20°C) [mN/m]	γ (140°C) [mN/m]	γ (180°C) [mN/m]
Poly(dimethyl siloxane)	Mn = 162	15.7	-	-
Poly(dimethyl siloxane)	Mn = 1,274	19.9	-	-
Poly(dimethyl siloxane)	Mn = 75,000	20.9	14.3	12.3
Polytetrafluoroethylene	M = 1,088	21.5	13.7	11.1
Polytetrafluoroethylene	M = inf	23.9	16.9	14.6
Atactic Polypropylene	Mn = 3,000	28.3	23.5	21.9
Linear Polyethylene	Mw = 67,000	35.7	28.8	26.5
Poly(vinyl acetate)	Mw = 11,000	36.5	28.6	25.9
Polystyrene	Mn = 1,680	39.3	30	26.9
Poly(methyl methacrylate)	Mv = 3,000	41.1	32	28.9
Poly(ethylene oxide)	M = 6,000	42.9	33.8	30.7
Poly(ethylene terephthalate)	Mn = 25,000	44.6	36.7	34.2
Poly(propylene isophthalate)	Unspecified	49.3	39.3	36
	$\Delta\Gamma_{Max}$	33.6	25.6	24.9
	γ_{0Min}	15.7	13.7	11.1
	$\Delta\Gamma_{Max}/\gamma_{0Min}$	2.14	1.87	2.24

S2.2 Determining the Origin of Difference Between Linear and Nonlinear Solutions

As was seen in Fig. 2.3, the linearized solution overpredicted the peak-to-valley height and aspect ratio relative to the sinusoidal nonlinear model. To determine whether the nonlinearities themselves were responsible for the difference, we solved the nonlinear model using key simplifications used to generate the linearized solution. Those simplifications were namely to neglect convective species flow and to neglect the concentration dependence of capillary forces. The simulation results in this section were generated using 50 elements, a tolerance of 10^{-7} and by setting $\varepsilon = 0.3$, $\alpha = 2$, and $V = 5\text{x}10^{-6}$

and $Pe = \infty$. Comparing lines one and two of Table S2.2, one can see that the nonlinearities account for little difference between the two solutions.

The next hypothesis for the difference was that because the linearized model did not account for convective transport of the surface-tension promoter, it might over-predict the feature height. Comparing lines one and three in Table S2.2, one can see that adding convection effects to the nonlinear solution results in a very minor decrease in peak-to-valley height.

The final hypothesis was that that because the linearized model neglected the concentration dependence of capillary flow, it was underrepresenting the dampening effect of capillary forces and therefore overpredicting the feature height. We tested this hypothesis by neglecting convection while accounting for the concentration dependence of capillary forces and found that this made the largest difference. Doing so halved the peak-to-valley height compared to the linearized solution (compare lines one and four of Table S2.2). These results strongly suggest that the inclusion of concentration-dependent capillary forces in the nonlinear model is primarily responsible for dampening the feature height in the nonlinear model and gives rise to shorter feature heights relative to the linearized solution.

Table S2.2 Table shows the dimensionless peak-to-valley height ($\Delta h/h_0$) resulting from solving the linear and nonlinear models under different assumptions. The model assumptions were to include/neglect convection effects and the concentration dependence of capillary forces. In solving the model, the parameters were set to $\varepsilon = 0.3$, $\alpha = 2$, and $V = 5\text{x}10^{-6}$, and $Pe = \infty$.

Solution Type	Model Assumptions	$\Delta h/h_0$
Linearized	Neglect Convection / Neglect Conc. Dep.	0.844
Nonlinear	Neglect Convection / Neglect Conc. Dep.	0.887
Nonlinear	Include Convection / Neglect Conc. Dep.	0.797
Nonlinear	Neglect Convection / Include Conc. Dep.	0.467

S2.3 Simulation Setup for the Case of Step Concentration Profiles

Fig. S2.1 compares the initial concentration distributions generated by a sinusoid and smoothed step function, which were used in numerically solving the full nonlinear model. The sinusoid is expressed as $C/C_0 = [1-\cos(2\pi x)]/2$. The step function was generated using a built in COMSOL Multiphysics step function with a transition zone with a dimensionless size of 0.05 (5% of the full pattern periodicity). In solving the model, the tolerance was typically set between 10^{-7} and 10^{-5}.

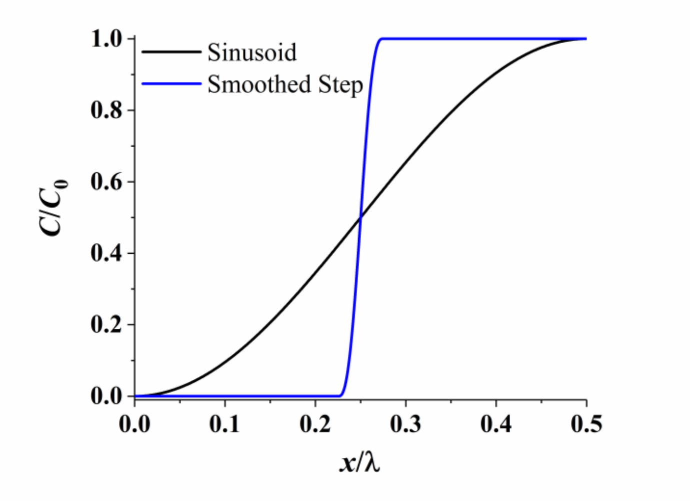

Figure S2.1 Comparison of concentration distributions initialized using a sinusoid (black) and smoothed step function (blue). The transition zone is of dimensionless size 0.05 (5% of the full domain length).

Due to the highly convective nature of the problem and sharp gradients generated by the step function, oscillations appeared in the concentration profile that negatively affected the simulation. To dampen these ringing effects, we incorporated artificial diffusion into the model by setting the Péclet number (Pe in Eq. (2.6)) to be $Pe = 5\text{x}10^9$, which allowed for diffusion of the sharp, unwanted oscillations. This allowed the extraction of the plateau in peak-to-valley height. Note this plateau decays at times much larger than patterning times in practice due to the artificial diffusion, and does not significantly affect the plateau value. To further reduce the oscillations, it was necessary to run the simulations using 500 – 2,000 elements, which were more than the 50 – 100 elements using in the sinusoidal case. Although these measures for the most part reduced the oscillations in the concentration field, significant oscillations still existed in several derivative terms. We performed mesh and tolerance refinement studies for some cases as well as an increased diffusion study, which showed the peak-to-valley height remained practically unchanged as the oscillations were dampened. This gave us confidence in the resulting solutions where oscillations in the derivative terms still existed. Note that although a temporary steady-state appeared to form, the peak-to-valley height continued to gradually increase/decrease. It is suspected that these very gradual changes were due to the added diffusion effects or perhaps the concentration ringing effects. The peak-to-valley height was extracted at a time of 10 or 100 dimensionless time units where the systems appeared to be at steady-state.

Chapter 3: Harnessing Marangoni-driven Patterning to Facilitate Dewetting in Thin Polymer Films[†]

3.1 INTRODUCTION

Patterned, thin polymer films have many applications ranging from microfluidics and photonics to the fabrication of integrated circuits. Focused laser-spike annealing (FLaSk) has been harnessed to pattern thin polymer films [34–37] and has been promoted as an alternative patterning technique to traditional photolithography. FLaSk uses a direct-write laser to locally heat a thin polymer film, which leads to a gradient in temperature and a consequent gradient in surface tension. This surface tension gradient induces a shear flow away from the laser spot and generates valleys along the path traversed by the laser. If the Marangoni flow is strong enough, a dewetting event can be induced, exposing the underlying substrate for subsequent pattern transfer. A primary advantage offered by FLaSk is its simplicity; it can harness simple polymers such as polystyrene, it involves a single write/anneal step and it does not require the use of developing solvents as in photolithography.

A similar patterning method called Marangoni-driven patterning (MDP) has also been explored as an alternative patterning technique [1–6]. harnesses photochemically-imposed surface tension gradients to direct the flow of melt-state, thin polymer films and generate topography. Relative to direct-write FLaSk, MDP could be performed with higher throughput using large-area exposure techniques. MDP is performed using a light exposure step to alter the chemical composition of the light-exposed regions which increases the surface tension there. The polymer is then heated above its glass transition temperature to promote flow into the programmed regions of higher surface tension. For contact exposure systems where a sharp transition in photoexposure occurs, a strong surface tension gradient forms and annealing the film produces doubled peaks. These peaks eventually merge and the pattern grows until the surface tension gradient diffuses and capillary forces dominate and replanarize the film. A schematic of this process is illustrated in Fig. 3.1. The resulting patterns could be directly used as functional coatings for improved light capture [14], improved adhesion [15], and antifouling [16,38]. The pattern could also be used as an etch barrier for pattern transfer into the underlying substrate. As in imprint lithography, a breakthrough etch would be required to remove the residual layer underlying the valley regions [39].

[†] The author would like to acknowledge and thank Dr. Chris Ellison and Dr. Amanda Jones for helpful discussions regarding polymer dewetting.

MDP possesses several distinguishing characteristics relative to more common patterning techniques. For instance, photolithography requires a solvent development step to generate the patterns, whereas MDP requires only a heating step. Additionally, MDP could be performed using contact-free exposure methods, providing an advantage over imprint lithography which can suffer from defects arising from polymer-template contact. These advantages are magnified at the roll-to-roll (R2R) production scale. R2R photolithography would require the web to pass through a solvent bath, which may not be ideal. On the other hand, MDP would require an annealing step to develop the pattern potentially followed by a breakthrough etch to expose the underlying substrate.

A major drawback to Maranogni-driven patterning is the need for the breakthrough etch, adding steps to the patterning process. To eliminate the need for a breakthrough etch, it has been speculated that a dewetting event could be initiated by MDP to expose the underlying substrate. Such a dewetting event would be triggered ss the valleys approach the substrate and magnify van der Waals forces until the film eventually touches the substrate. Fig. 3.1 illustrates the dewetting event and how it might come about. Another major benefit of this dewetting event is that the feature aspect ratio could be greatly improved because dewetted films bead up and become taller. As mentioned in the previous chapter, experiments have recorded a maximum aspect ratio of roughly 0.05 and analyses showed that MDP is limited to an aspect ratio of roughly 0.5 for equal line-space patterning. These seemingly small aspect ratios could be greatly improved if a dewetting event were made possible.

Dewetting has not yet been reported for MDP, but it is hypothesized that by judiciously selecting the polymer-substrate system, dewetting can be induced. For example, a polymer system must be capable of generating sufficiently strong surface tension gradients during the photoexposure step. This is because strong gradients in surface tension generate large topography and allow the valley regions to approach the substrate.

To investigate the conditions required for dewetting and provide guidance for designing experiments, a theoretical model for equal line-space MDP is developed and used to construct a wetting-dewetting stability diagram. Physical parameter estimates are then used to determine where the polymer system previously demonstrated by Arshad et al. [7] would lie on the stability diagram. Finally, future experiments are suggested to further validate the accuracy of the predictions and demonstrate dewetting facilitated by MDP.

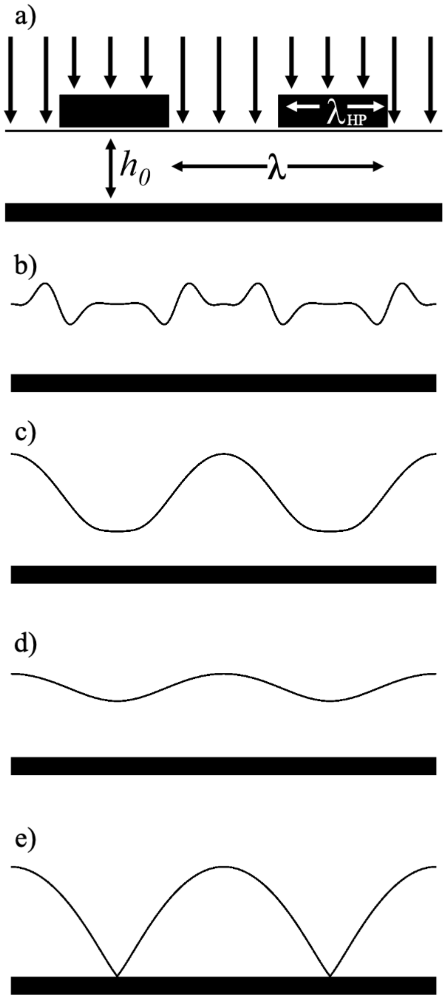

Figure 3.1 Schematic and possible outcomes of MDP performed using a line-and-space photomask. a) UV light interacts with polymer film in regions unobstructed by the photomask, raising the surface tension in exposed regions. λ is the full-pitch of the equal line-space photomask and λ_{HP} the resulting half-pitch of the surface tension gradient and resulting pattern. h_0 is the initial film thickness. b) Heating the film above its glass transition temperature allows the film to flow into the exposed regions of higher surface tension, resulting in the film being deflected. Initially double peaks form where the gradient is strongest. c) The double peaks eventually merge, and the film height continues to grow. d) If the Marangoni forces are not strong enough, the film will eventually relax back to flat as diffusion erases the surface tension gradient and capillary forces replanarize the film. e) If the film is deflected far enough, van der Waals forces become strong and dewetting occurs. Portions of this figure have been published in *Colloids and Surfaces A: Physiochemical and Engineering Aspects*, 603, Stanley, S. K. and Bonnecaze, R. T., Fundamental Limits of Marangoni-driven Patterning, 125217, Copyright Elsevier (2020).

3.2 METHODOLOGY

3.2.1 Model for Marangoni-driven patterning

To gain insight into the conditions necessary to cause the transition from replanarization behaviour to dewetting behaviour, the interplay of Marangoni, capillary, and van der Waals forces were modelled using the thin film equation in conjunction with the convection diffusion equation. The thin film equation [7,23],

$$\frac{\partial h}{\partial t}+\frac{\partial}{\partial x}\left(h\left\langle u\right\rangle\right)=0, \tag{3.1}$$

tracks the surface height of the film over time, where h is the height the film, t is time, x is the lateral dimension, and $\langle u \rangle$ is the vertically averaged, lateral fluid velocity. Eq. (3.1) is derived from the Navier-Stokes equation by invoking the lubrication approximation, which harnesses the disparate vertical and lateral length scales to neglect inertial terms [23]. In the case of MDP the characteristic height of the film is h_0 and is much smaller than the feature half-pitch, λ_{HP}, i.e. $h_0/\lambda_{HP} = \varepsilon << 1$. The expression for $\langle u \rangle$ is as follows:

$$\left\langle u\right\rangle=\frac{\Delta\Gamma C_0}{2\mu}\left(h\frac{\partial C}{\partial x}\right)+\frac{\gamma_0}{3\mu}\left(h^2\frac{\partial^3 h}{\partial x^3}\right)+\frac{A}{6\pi\mu}\left(\frac{1}{h^2}\frac{\partial h}{\partial x}\right), \tag{3.2}$$

where $\Delta\Gamma$ is the difference in surface tension between the reacted and non-reacted states of the polymer, C_0 is the initial mole fraction of the photoproduct species, C is the concentration of the photoproduct species normalized by C_0, γ_0 is the surface tension of the unreacted species, μ is the polymer viscosity, and A is the Hamaker constant associated with the air-polymer-substrate system. The thin film equation is coupled to a convection-diffusion equation [40]

$$\frac{\partial\left(hC\right)}{\partial t}+\frac{\partial}{\partial x}\left(-Dh\frac{\partial C}{\partial x}+\left\langle u\right\rangle hC\right)=0, \tag{3.3}$$

which is used here to track the concentration of reacted species. Here, D is the diffusion coefficient of the reacted species and hC is the product of the film height and the concentration. It is assumed that the diffusion coefficient is constant. The model assumes a uniform distribution of the surface tension promoter in the vertical direction, which is valid in cases of fast vertical diffusion relative to the lateral species flux.

Eq. (3.2) accounts for Marangoni-driven flow (first term), capillary pressure-driven flow (second term) and disjoining pressure-driven flow (third term). The surface tension and its resulting gradient are calculated by assuming a linear relation between photoconversion and surface tension such that $\gamma = \gamma_0 + \Delta\Gamma C$ where C varies from zero to one.

The second term in Eq. (3.2) accounts for the capillary flow assumes that the difference in surface tension is small relative to the absolute surface tension, i.e. $\Delta\Gamma C_0/\gamma_0 << 1$. This allows us to neglect the influence of concentration on the capillary flow and allows for one fewer parameter in the analysis. Note that in the previous chapter that the additional influence of concentration on capillary forces was included to more fully capture the effects of using a large surface tension gradient. The third term in Eq. (3.2) accounts for the disjoining pressure-driven flow caused by van der Waals forces and assumes a simple air-polymer-substrate system wherein the substrate is composed of a single material. Were the model to account for multiple substrate layers, additional terms would be required [24]. However, modelling a single-layer substrate material greatly simplifies the analysis of the conditions required for dewetting.

Due to the symmetry of an equal line-space photomask, no-flux (or symmetry) boundary conditions were used. These boundary conditions can be expressed as

$$\left(h\langle u\rangle\right)\Big|_{x=0,\lambda_{\mathrm{HP}}}=0, \tag{3.4}$$

$$\left(-Dh\frac{\partial C}{\partial x}+\langle u\rangle hC\right)\Bigg|_{x=0,\lambda_{\mathrm{HP}}}=0. \tag{3.5}$$

To cast the governing equations in a more general form, Eqs. (3.1) and (3.3) were nondimensionalized, with $h=\bar{h}h_0$, $x=\bar{x}\lambda_{\mathrm{HP}}$, and $t=(3\mu\lambda_{\mathrm{HP}}^4/h_0{}^3\gamma_0)\bar{t}$. The nondimensional equations are as follows, with bar superscripts dropped for clarity:

$$\frac{\partial h}{\partial t}+\frac{\partial}{\partial x}\left[W\left(h^2\frac{\partial C}{\partial x}\right)+\left(h^3\frac{\partial^3 h}{\partial x^3}\right)+V\left(\frac{1}{h}\frac{\partial h}{\partial x}\right)\right]=0, \tag{3.6}$$

$$\frac{\partial(hC)}{\partial t}+\frac{\partial}{\partial x}\left[-M\left(h\frac{\partial C}{\partial x}\right)+W\left(h^2C\frac{\partial C}{\partial x}\right)+\left(h^3C\frac{\partial^3 h}{\partial x^3}\right)+V\left(\frac{C}{h}\frac{\partial h}{\partial x}\right)\right]=0, \tag{3.7}$$

Here, *M*, *V*, and *W* are nondimensional numbers which represent collections of constants. *W*, *V*, and *M* are expressed as,

$$W=\frac{3\Delta\Gamma C_0\lambda_{\mathrm{HP}}^2}{2\gamma_0 h_0^2}, \tag{3.8}$$

$$V=\frac{A\lambda_{\mathrm{HP}}^2}{2\pi h_0{}^4\gamma_0}, \tag{3.9}$$

$$M=\frac{3\mu D\lambda_{\mathrm{HP}}^2}{\gamma_0 h_0{}^3}. \tag{3.10}$$

These three characteristic quantities can be understood as a ratio of forces. *W* is the ratio of Marangoni forces to capillary forces, *V* is the ratio of van der Waals forces to capillary forces and *M* is the ratio of diffusion to capillary forces. The magnitude of these three quantities determines whether the film will reach a dewetting state or replanarization state.

The parameter spaces of W, V, and M were probed to identify contours defining the transition between replanarization and dewetting and thereby understand the conditions necessary to induce dewetting in MDP. We restrict our analysis to positive values of V, which implies a positive Hamaker constant. A negative Hamaker constant would result in repulsive interactions and inhibit dewetting.

To understand the limitations of the model, the assumption of fast vertical diffusion is called into question. The validity of this assumption can be determined by examining the ratio of characteristic time scales for vertical diffusion and lateral convection. The time scale for vertical diffusion, t_{Diff}, can be taken as

$$t_{\mathrm{Diff}} = \frac{h_0^{\;2}}{D}. \tag{3.11}$$

The initial lateral flux time scale is predominantly governed by Marangoni-driven convection. The initial convective time scale can therefore be taken as the Marangoni flow timescale, t_{Mar}, which is expressed as

$$t_{\mathrm{Mar}} = \frac{2\mu\lambda_{\mathrm{HP}}^2}{\Delta\Gamma C_0 h_0}. \tag{3.12}$$

For the assumption of fast vertical equilibration to hold, the vertical diffusion time scale must be much smaller (i.e. faster) than the Marangoni-driven convection time scale. In other words, $t_{\mathrm{Diff}} / t_{\mathrm{Mar}} = \Delta\Gamma C_0 h_0^{\;3} / 2\mu D\lambda_{\mathrm{HP}}^2 << 1$. Note that this ratio can be rewritten as

$$\frac{t_{\mathrm{Diff}}}{t_{\mathrm{Mar}}} = \frac{\Delta\Gamma C_0 h_0^3}{2\mu D\lambda_{\mathrm{HP}}^2} = \frac{W}{M}\varepsilon^2. \tag{3.13}$$

Therefore, for the assumption of fast vertical diffusion to hold, $W\varepsilon^2/M$ must be much less than unity. By requiring that $W\varepsilon^2/M \leq 0.1$ and assuming $\varepsilon = 0.1$, the validity of the fast vertical diffusion assumption is tested. As previous experiments have been performed using $\varepsilon \approx 0.01$, we will also use $\varepsilon = 0.01$ to test the assumption of fast vertical diffusion.

3.2.2 Simulation Methodology

The model was solved using the finite element method with the general form PDE interface in COMSOL Multiphysics. The concentration was initialized using a step function that transitioned from zero to one at the midpoint of the domain, which is representative of an equal line-and-space photomask. Because contact printing is not limited by the blurring effects of diffraction, a step function is appropriate. The step function was smoothed using a transition region of size 0.05 (5% of the full pitch). This smoothing helped avoid drastically negative concentrations and other computational issues associated with using a very sharp step function. To explore a more general exposure pattern, a sinusoid was also used to smoothly vary the concentration profile from zero to one.

Default shape functions and quartic element orders were used. Symmetry boundary conditions, also known as no flux boundary conditions, were used for both variables h and hC. To simulate pattern formation for the case of a sine function concentration distribution, 100 elements were used and the relative tolerance was set to 10^{-8}. In the case of the step function concentration distribution, 200 elements were used and the relative tolerance was set to 10^{-7}.

The dewetting event was indicated by a stopping criterion, where the simulation was stopped when the film height dropped to or below zero.

3.2.3 Feature Evolution and Calculation of Dewetting Contours

The evolution of the feature profile and concentration profile for initially stepped and sinusoidal concentration profiles possessing M, $V = 1$ and $W = 10$ are shown in Fig. 3.2. Note that the main difference between the step and sine function is the film height, with the step function resulting in marginally taller features at equivalent times, likely due to the fact that the stepped concentration requires slightly more time to diffuse and blur the surface tension relative to the sine concentration.

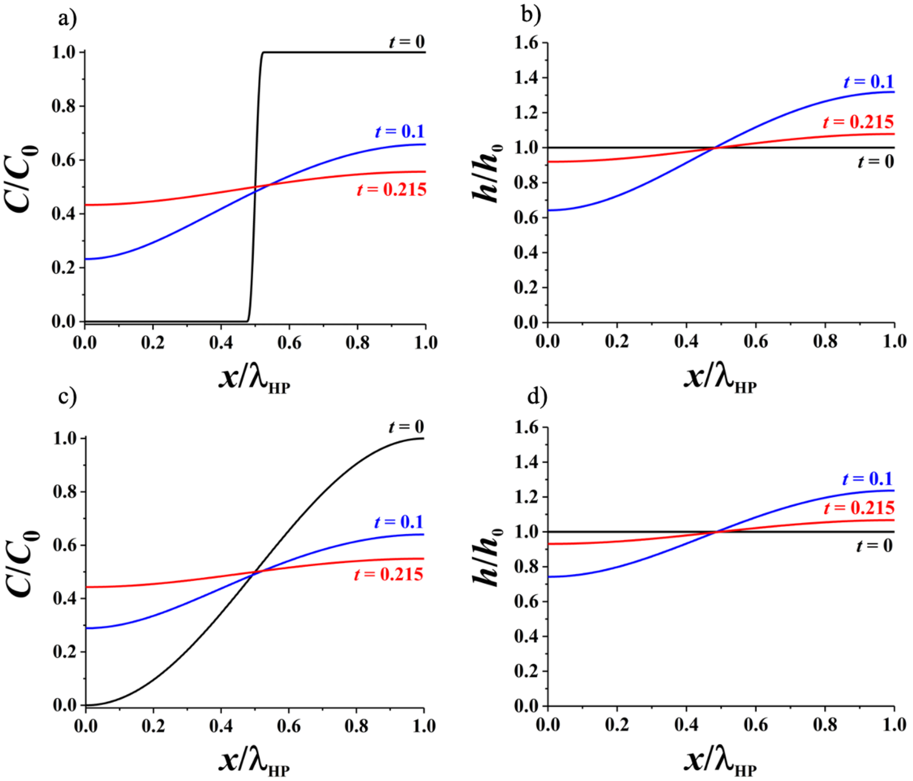

Figure 3.2 a) Normalized concentration profiles and b) normalized film height profiles for a simulation in which the initial concentration was a step function. c) Normalized concentration profiles and d) normalized film height profiles for a simulation in which the initial concentration was a sinusoid. Simulation conditions for all component figures were M, V, = 1, and $W = 10$.

By increasing the strength of the Marangoni forces (increasing *W*) relative to the capillary forces, the film can be made to deflect further towards the substrate to sufficiently amplify the van der Waals forces and cause dewetting. There must therefore exist a critical value of *W* at which dewetting will occur. To demonstrate this principle, Fig. 3.3a shows the feature evolution for a stepped concentration film possessing *W* = 10.7 and *V*, *M*, = 1. Fig. 3.3b shows the feature evolution under the same conditions, but for *W* = 10.8. Note that the film replanarizes for *W* = 10.7, but *W* = 10.8 leads to dewetting. *W* = 10.8 is therefore the critical value for dewetting to occur.

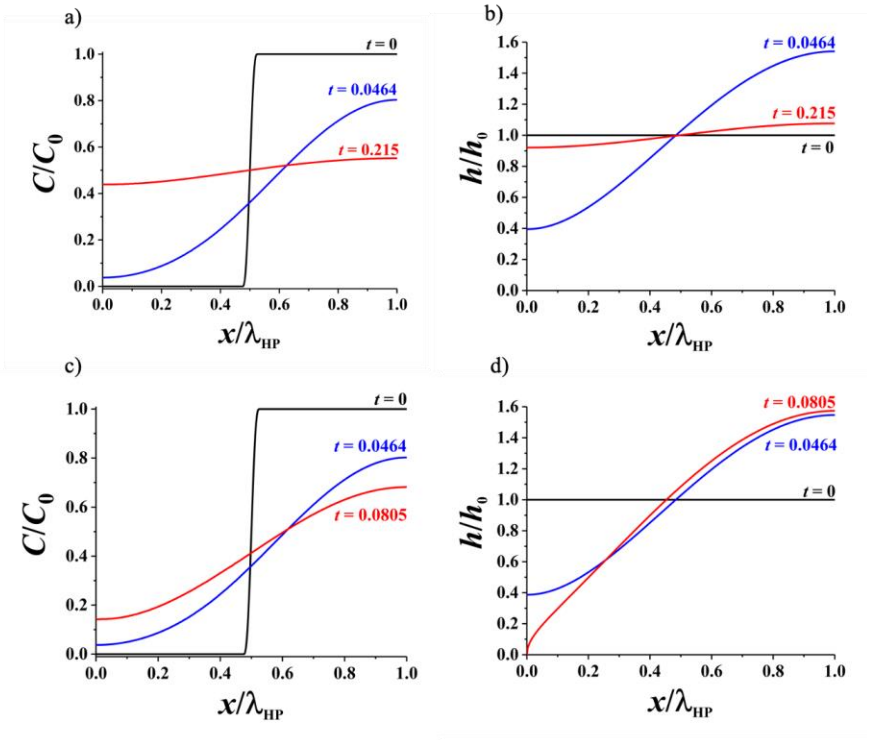

Figure 3.3 a) Normalized concentration profiles and b) normalized film height profiles for a simulation in which the initial concentration was a step function. Simulation conditions for a) and b) were *M*, *V*, = 1, and *W* = 10.7. c) Normalized concentration profiles and d) normalized film height profiles for a simulation in which the initial concentration was a step function. Simulation conditions for c) and d) were *M*, *V*, = 1, and *W* = 10.8. Note that the ~1% increase in the value of *W* leads to dewetting, which can be seen by comparing b) and d).

Note that the nondimensional time reported for dewetting in this case is 0.0805. The uncertainty associated with this time is quite large, as the time required for dewetting is highly dependent on the exact value of *W*. By improving the accuracy of *W* from 10.8 to 10.75, the nondimensional time required for dewetting changed from 0.0805 to 0.0949, which is roughly an 18% change in nondimensional annealing time. Therefore, the exact time at which dewetting occurs is not known to good precision, but the critical value of dewetting is correct to within ~1%.

The critical value of *W* over a large parameter space was determined by fixing *M* and *V* while iteratively changing *W* for both stepped and sinusoidal initial concentration profiles. The critical value of *W* was determined over several decades of *M* and *V* and this value is reported to within ~1%.

3.3 RESULTS AND DISCUSSION

3.3.1 Contour Map Defining Dewetting and Replanarization

Fig. 3.4 presents a contour map showing where the onset of dewetting occurs for a given value of *V*. For a polymer-film system possessing values of *W* and *M* that fall below the respective curve, replanarization would occur. On the other hand, a polymer-film system possessing values of *W* and *M* that lie on or above the curves, dewetting would occur.

It is interesting to note that the dewetting curves are very similar for the stepped and sine function concentration profiles. The sine function concentration contours lie slightly above their stepped concentration counterparts and therefore require marginally stronger Marangoni forces to trigger a dewetting event.

Note the dashed lines associated with Fig. 3.4. These lines delineate where the assumption of fast vertical diffusion is applicable. As an example, a polymer-film system possessing values of *W* and *M* that lie below the appropriate dashed line can be assumed to exhibit fast vertical diffusion. On the other hand, a polymer-film system possessing values of *W* and *M* that lie above the appropriate dashed line, the assumption of fast vertical diffusion is poor and the resulting dewetting contours may not correctly predict the transition from replanarization to dewetting.

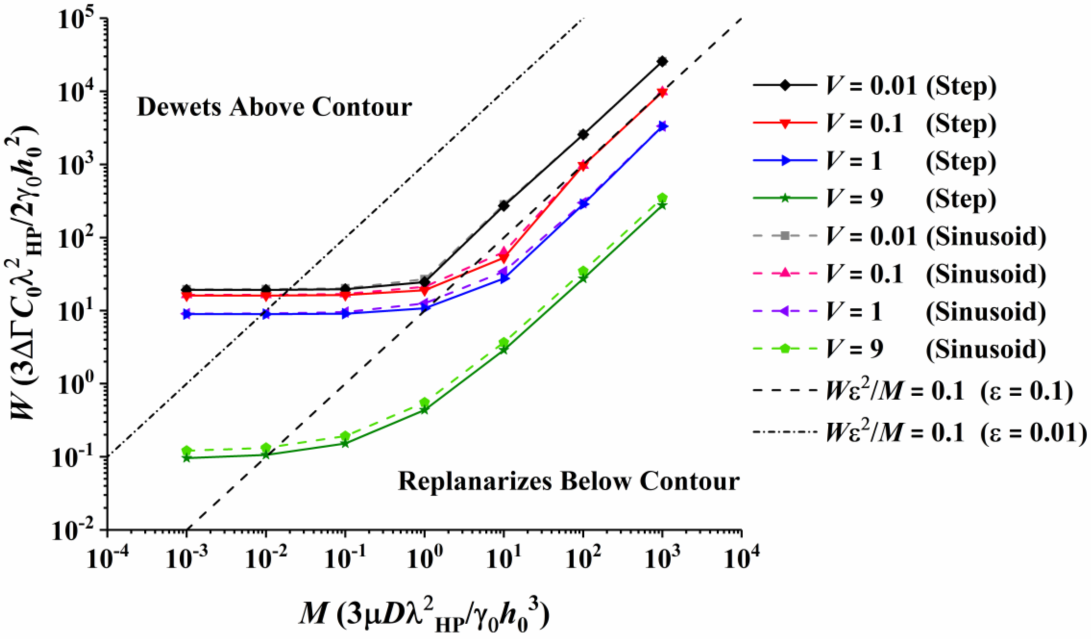

Figure 3.4 Constant *V* contours defining the transition from planarization to dewetting. For a given value of *V*, regions below the contour replanarize while regions above the contour dewet. The validity of the simulation results depends on whether fast vertical diffusion can be assumed, i.e. $W\varepsilon^2/M \leq 0.1$. This borderline is provided for $\varepsilon = 0.01$ (typical of past experiments) and for $\varepsilon = 0.1$ (more general value). Note that for a value of $\varepsilon = 0.1$, the domain is fairly restricted, but for typical experimental conditions in which $\varepsilon = 0.01$, the domain is much less restricted.

These results are valuable as they give guidance for experimental design. For a given polymer system, knowing the experimental parameters such as the polymer viscosity, diffusivity, surface tension, etc. one can predict whether replanarization or dewetting will occur.

3.3.2 Comparison to Prior Experiments

The modelling results will now be compared to past patterning experiments performed by Arshad et al. [7]. The polymer system used by Arshad *et al.* relied on low MW polystyrene photochemistry to induce Marangoni flow and did not exhibit dewetting. The physical parameters for this polymer system at various temperatures are reproduced here in Table 1. The photomask consisted of an even line-space pattern possessing a 25 µm full pitch (lines were 12.5 µm wide) and the film height was between 130 nm and 150 nm. Other physical parameter values and estimates provided in ref. [7] are reproduced here in Table 1.

It is critical to note that the substrate used by Arshad *et al.* was a silicon wafer with a thin native oxide coating, which is not conducive to dewetting. Although the native oxide can promote dewetting (as indicated by a positive Hamaker constant of 2.2(4)x10^{-20} J [24] for an air-polystyrene-silicon oxide system), the bulk silicon largely works against dewetting because the interactions between polystyrene and pure silicon is repulsive (as indicated by a negative Hamaker constant of -1.3(6)x10^{-19} [24] for an air-polystyrene-silicon system). To evaluate a substrate more conducive to dewetting, the substrate under consideration will be pure silicon oxide, opposed to the silicon and native oxide substrate employed by Arshad et al. The Hamaker constant and the calculated parameters *W*, *V*, and *M* are provided here in Table 1.

Table 3.1 Physical parameters for system taken from ref. [7]. Air-polystyrene-SiOx Hamaker constant, *A*, taken from ref. [24].

T (°C)	λ_{HP} [μm]	h_0 [nm]	$\Delta\Gamma$ [mN/m]	C_0	γ_0 [mN/m]	μ [Pa-s]	D [10^{-14} m^2/s]	A [10^{-20} J]	M	V	W
120	12.5	145	2	0.064	32.2	2550	0.363	2.2	44	0.038	44
126	12.5	148	3	0.064	31.7	1000	2.15	2.2	98	0.036	65
136	12.5	130	3.1	0.064	31.1	250	4.49	2.2	77	0.062	88
140	12.5	148	3.1	0.064	30.8	150	5.91	2.2	42	0.037	69

Fig. 3.5 overlays the physical parameters *M* and *W* exhibited by the experiments of Arshad et al. with the wetting-dewetting transition contours for $V = 0.01$. All points fall below the wetting-dewetting contours shown. To force the film into a dewetting regime, several changes to the polymer system could be made. Firstly, the value of *W* could be independently increased by prolonging the exposure to increase the photoconversion, C_0 and thereby strengthen the surface tension gradient. However, taken to an extreme, this increased photoconversion could significantly alter the film viscosity, diffusivity, and surface tension and thereby inadvertently change the value of *M* and *V*.

The value of *M* could also be independently lowered to bring the polymer system into the dewetting regime. This could be accomplished by independently lowering the polymer viscosity or diffusivity. Doing so is difficult, however, because a *decrease* in viscosity often results in a comparable *increase* in diffusivity. For instance, raising the temperature of the film will reduce the viscosity but also increase diffusivity. Jones et al. recently investigated the effects of doping low molecular weight polystyrene films similar to those employed by Arshad et al. with a high molecular weight polystyrene-poly(tert-butyloxystyrene) copolymer (the copolymer was primarily responsible for increasing the surface tension). The low molecular weight polystyrene provided the film with a low viscosity, while the high molecular weight copolymer simultaneously reduced the diffusivity of the surface tension gradient. Large feature aspect ratios were reported and the feature valleys came within ~14 nm of the substrate. However, dewetting was not observed. As the feature approached the substrate so closely, this polymer system would be a good candidate for observing dewetting in the future. As necessary polymer properties for this copolymer blend system are not known, the exact reason for why it did not dewet is not clear. Although the native oxide in their experiments could have enable dewetting, it is possible that the bulk silicon prevented it.

In addition to changing the polymer properties, the film geometry can also be changed. For instance, the initial film height can be easily changed by spin coating the polymer to a different initial thickness and the pattern periodicity can be changed by specifying a different half pitch in the photomask. In manipulating the initial film thickness, h_0, and photomask half pitch, all three values, M, V, and W are allowed to vary, adding some complexity to the polymer-film-mask design process.

The dewetting contours provide a powerful tool for predicting whether dewetting will occur for a given polymer system. Validating these curves with experiments using polymer-substrate systems that allow for dewetting is the next critical point of research in furthering MDP. Furthermore, the experiments are needed to determine the effects of dewetting on the feature aspect ratio.

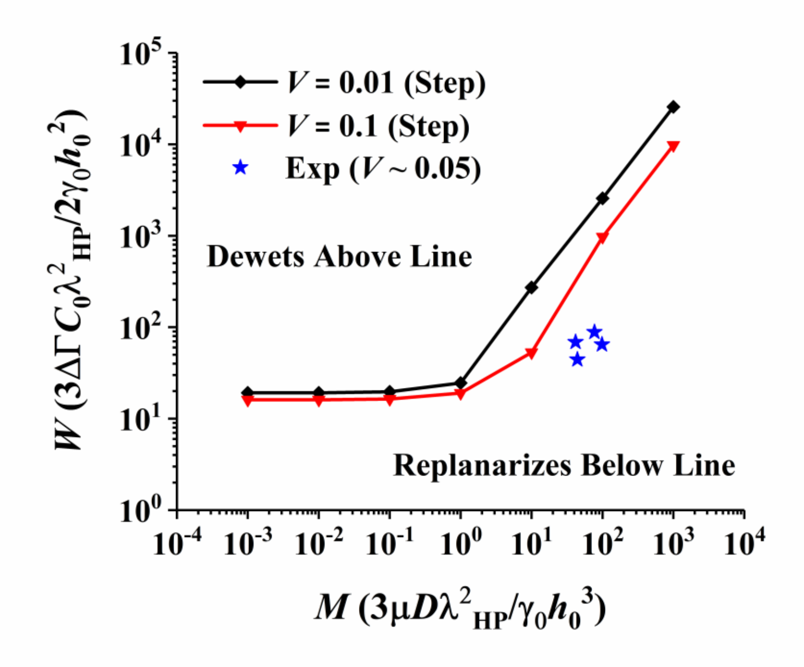

Figure 3.5 Constant V contours defining the transition from planarization to dewetting. For a given value of V, regions below the contour replanarize while regions above the contour dewet. Assuming silicon oxide as the substrate, experimental values were overlaid with the model predictions, showing that the conditions tested by Arshad et al. would not lead to dewetting.

Our model for MDP was not capable of simulating the flow dynamics beyond the dewetting point. This is due to the no-slip condition imposed at the substrate. More intricate models like those used by Schwartz et al. [41] and Park et al. [42] simulate dewetting dynamics by imposing a precursor film thickness which is programmed to persists after the dewetting event and allows the bulk of the film to continue flowing on top of the precursor film. Using a model like this, the dynamics of dewetting in MDP could be explored more fully and potentially offer some predictive control over the amount of substrate uncovered during the dewetting event. Such a model could also reveal how the aspect ratio improves after the dewetting event relative to the non-dewetting case.

3.4 CONCLUSIONS

A polymer flow model for Marangoni-driven patterning was presented and generalized by nondimensionalizing the governing equations. Several dimensionless parameters, *M*, *V*, and *W* became apparent, each of which is a ratio of the relevant forces. The *M*, *V*, and *W* parameter space was explored to understand where the critical points (or contours) at which the transition from wetting to dewetting occurs. The contours were then compared to previous patterning experiments using polystyrene performed by Arshad et al. Using this framework of wetting-dewetting regimes provides guidance in designing polymer systems that would promote or prevent dewetting. Future work must focus on experimentally validating our simulation results and determining the impact of dewetting on the feature aspect ratio.

Additional future work could include predicting dewetting conditions for systems exhibiting very strong Marangoni forces, whereas here it was only explored for the case in which $\Delta\Gamma C_0/\gamma_0 << 1$. Additionally, numerical predictions could be made for systems possessing two or more substrate layers which require more complex expressions to account for van der Waals forces. Finally, the model presented here only predicts the critical values of *M*, *V*, and *W* necessary for dewetting, but does not elucidate the dynamics after dewetting, as the model could not account for the movement of contact lines. By employing reduced order modelling techniques similar to those used by Schwartz et al. [41] and Park et al. [42], post-dewetting dynamics and resulting aspect ratio in could be better understood.

Chapter 4: Control of Marangoni-driven patterning by an optimized distribution of surface energy‡

4.1 INTRODUCTION

The Marangoni effect can be used to pattern thin polymer films by applying photochemically induced surface energy or tension variations on a film created by UV light through a photomask [1–6] or a digital light projection (DLP) system. On heating the film above its glass transition temperature, the polymer flows from regions of lower to higher surface tension, creating features that resemble the initial pattern of photoexposure. A schematic of Marangoni-driven patterning (MDP) is shown in Fig. 4.1 using a photomask. First, UV light that passes through the photomask initiates a photochemical reaction that increases the surface energy of the polymer. Once the temperature of the polymer is above the glass transition temperature, double peaks first form at the interface between exposed and unexposed regions where the surface tension gradient is largest. The double peaks then merge to form a single peak with a central height of h_c. At longer times the surface tension promoter diffuses and the surface tension gradient wanes. Eventually, capillary forces replanarize the film. When the film is quenched before replanarization, the variations in film height can be locked into place for use as an etch mask (with a breakthrough etch as is done in imprint lithography [39]) or for controlled surface topography. The aim of this paper is to show how topography can be controlled by manipulating the distribution of Marangoni forces.

---

‡ Note that most of the research and material in this chapter has been reproduced from S.K. Stanley, C.J. Ellison, R.T. Bonnecaze, Control of Marangoni-driven patterning by an optimized distribution of surface energy, *J. Appl. Phys.* **127** (2020) with the permission of AIP Publishing. Additional commentaries have been included. The author would like to acknowledge and thank Dr. Baldea for a helpful conversaion regarding genetic algorithsms, Dr. Chris Mack for a helpful converstaions regarding photolithography, and Dr. Kamy Sepehrnoori for helpful conversations regarding numerical simulation.

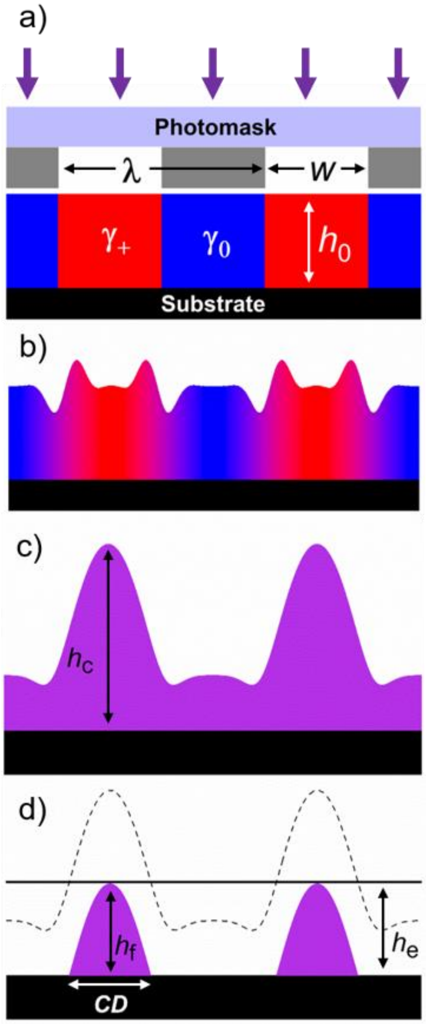

Figure 4.1 Schematic of Marangoni-driven patterning and breakthrough etch. a) Example line-space photomask of periodicity λ and space-width *w* is used to selectively expose the polymer film of initial height h_0 to UV light. The surface energy or tension in the exposed areas (red) increases due to the photochemical reaction, as indicated by the γ_+ symbol. The surface tension in unexposed areas (blue) remains unchanged as indicated by the γ_0 symbol. b) Annealing the film causes the polymer to flow from the unexposed, lower surface tension regions, into the higher surface tension regions. Note the double peaks that form at short times where the gradient in surface tension is greatest. c) Double peaks merge and the surface tension gradient diffuses as indicated by the solid color. Central feature height is indicated by h_c. d) Anisotropic breakthrough etch of height h_e exposes the underlying substrate, leaving features of height h_f and width *CD*. Note that the figures are not drawn to scale as the film height is typically hundreds of nanometers while the feature periodicity is typically tens of microns.

MDP possesses several distinguishing characteristics relative to traditional patterning techniques. For one, it does not require developing solvents as in photolithography. Furthermore, MDP avoids the challenges associated with template fill and lift-off associated with imprint lithography. MDP can be adapted to roll-to-roll (R2R) pattern production using a photo-roll mask system similar to that demonstrated by Ok et al. [21] and developed by sending the web through a conventional R2R annealing oven. In general the photoexposed patterns can be created with contact photomasks or DLP projector, similar to what is done for maskless lithography [11] and continuous liquid interface printing [43]. DLP projection printing can add flexibility and customizability to the R2R patterning process not available to template-based patterning technologies.

At the R2R scale, Marangoni-driven patterning could be used in fabricating features on flexible substrates for applications with size requirements in the 1-100 µm range. Potential applications include patterned coatings for improved surface adhesion [15], optical coatings for improved light capture [14], and an etch mask. As an etch mask, Marangoni-driven patterning could be used in the fabrication of terahertz metamaterials on flexible substrates [13,44] for use in security screening applications [45], high-speed data transfer [46], terahertz cloaking [47], and wireless strain detection [12].

To improve feature aspect ratios and expand the functionality of Marangoni-driven patterning, several polymer chemistries have been explored. Initial work focused on the UV-triggered dehydrogenation of polystyrene to poly(phenyl acetylene), which increases the surface tension in light-exposed regions [1,7]. The maximum aspect ratio shown in these studies was around 0.013. Later studies explored the use of small molecule, photosensitizer dopants [3] as the surface tension promoter and the inclusion of photoactivated crosslinking agents [4] to prevent feature dissipation at elevated temperatures.

In addition to advances made in the chemistry of Marangoni patterning, work has been done to understand how the transport mechanisms affect pattern evolution. Arshad et al. employed the thin film equation coupled with the convection diffusion equation to model the formation of features made using an equal line-and-space photomask [7]. The model showed good agreement with experiment and provided a predictive tool for further exploring and improving Marangoni-driven patterning.

Their theoretical treatment showed that faster processing times could be achieved by operating at higher annealing temperatures since the lower polymer viscosities allow features to form more rapidly. Their treatment also showed that to increase feature aspect ratios, one must increase the surface tension difference between the exposed and unexposed regions. It was also shown that improved feature aspect ratios could be obtained by lowering the viscosity of the bulk polymer while simultaneously lowering the diffusivity of surface tension promoter. In practice this is difficult, as lowering polymer viscosity is often associated with increased diffusivity. Recently, Jones et al. demonstrated a decoupling of viscosity from diffusivity in Marangoni-driven patterning by doping a high molecular weight (MW) poly(tert-butoxystyrene-rans-styrene) (P(tBOS-ran-S)) copolymer (the primary surface tension promoter) into low MW polystyrene. In their study, the bulk, low MW polystyrene kept the viscosity relatively low while the use of the higher MW P(tBOS-ran-S) lowered the diffusivity of the surface tension promoter and allowed

the surface tension gradient to persist for longer. The effect was to produce aspect ratios around 0.04, more than twice the aspect ratios seen using polystyrene alone [6].
Although advances have been made in improving the chemistry for Marangoni-driven patterning, there have been no studies on how to improve shape control. Although features formed using Marangoni-driven patterning resemble the initial photoexposure pattern, they do not replicate the target pattern with great fidelity due to flow and diffusion effects. These effects result in features with severely rounded corners. In short, what you see on the photomask is not what you get in practice.

Similar issues are present in optical lithography, where diffraction and other process effects can distort the final pattern and prohibit the use of an intuitive photomask, i.e. using a photomask identical to the target pattern. To compensate for these effects, model-based optical proximity correction (OPC) is performed to generate a better performing photomask pattern. OPC involves simulating the lithographic exposure and resist development steps to determine what the final pattern will look like. Using optimization techniques, the edges of the photomask pattern are repeatedly adjusted until the simulated resist pattern contour sufficiently matches the target pattern contour [48]. The optimized photomasks are often non-intuitive, obtainable only through simulation and optimization, given that experimental trial and error procedures would be prohibitively expensive.

Inspired by model-based OPC, here we present a method for simulating and optimizing photomasks for two-dimensional Marangoni-driven patterning. This method first simulates Marangoni-driven patterning for a fixed annealing time and then extracts the feature contour that would result after an anisotropic etch of a specified etch height (h_e as shown in Fig. 4.1) for comparison to the target. The photomask then is adjusted iteratively so that the Marangoni-driven pattern is as close as possible to the target feature. The photomask optimization methods outlined here could be easily adapted to suit the needs of other photoexposure methods for MDP.

The outline of the remainder of the chapter is as follows. First, a model for Marangoni-driven patterning is presented. Then an objective function is developed to quantify the overlap of the resulting feature with that of a square target. Next, two approaches for improving the feature-target overlap are presented. The first relies on resizing the photomask relative to the intuitive photomask. The second approach is a pixel-based optimization method which uses a genetic algorithm to manipulate the photomask and improve the feature-target overlap beyond what is capable by simple photomask resizing. The results of these two approaches at several annealing temperatures and times are presented and discussed.

4.2 METHODOLOGY

4.2.1 Model for Marangoni-driven patterning

A predictive model for Marangoni patterning was first developed by Arshad et al. for line-and-space Marangoni-driven patterning [7]. The model showed good agreement with experiments. The model uses the thin-film equation [7,23,25,26,40,49]

$$\frac{\partial h}{\partial t} + \nabla \cdot \left(h \langle \mathbf{u} \rangle \right) = 0, \tag{4.1}$$

to track the evolution of the height of the film over time. Here h is the height the film, t is time, ∇ is the two-dimensional (x,y) gradient operator, and $\langle \mathbf{u} \rangle$ is the vertically averaged, lateral fluid velocity.

The average velocity $\langle \mathbf{u} \rangle$ is given by

$$\langle \mathbf{u} \rangle = \frac{\Delta\Gamma}{2\mu} h\nabla C + \frac{\gamma_0}{3\mu} h^2 \nabla\left(\nabla^2 h\right), \tag{4.2}$$

where $\Delta\Gamma$ is the difference in surface tension between the reacted and non-reacted states of the polymer, γ_0 is a constant, nominal surface tension, μ is the polymer viscosity, and C is the mole fraction of reacted polymer. The first term in Eq. (4.2) accounts for the Marangoni flow and assumes surface tension is linearly related to concentration. The second term in Eq. (4.2) accounts for the capillary flow using only γ_0, which is assumed to be the surface tension of the dominant polymer component. Eqs. (4.1) and (4.2) are the reduced order form of the Navier-Stokes equations made possible by the lubrication approximation, when vertical length scales are much smaller than the lateral length scale λ, i.e. $h_0/\lambda = \varepsilon << 1$. This holds true for Marangoni-driven patterning where $h_0/\lambda \sim 0.001\text{-}0.01$ is typical.

The thin film equation is coupled to a convection-diffusion equation [25,26,50]

$$\frac{\partial\left(hC\right)}{\partial t} + \nabla \cdot \left(-Dh\nabla C + \langle \mathbf{u} \rangle hC \right) = 0, \tag{4.3}$$

which describes the evolution of the concentration of the photoproduct. Here, D is the diffusion coefficient of the photoproduct, and it is assumed constant. Note that the concentration expressed in Eq. (4.3) is not the surface concentration, but rather the bulk concentration, which is assumed to be vertically homogeneous. This assumption is possible when the vertical diffusion time scale (t_{Dz}) is short with respect to the lateral advective time scale (t_{Adv}), i.e. $t_{\mathrm{Dz}}/t_{\mathrm{Adv}} << 1$ [26]. This condition is satisfied for a typical Marangoni-driven patterning system, which will be shown later.

4.2.1.1 Geometric and Physical Parameters

To demonstrate the proposed photomask optimization methods, we have chosen a repeating 35x35 μm^2 square as the target pattern, with a characteristic length L = 35 μm and periodicity λ = 100 μm. The optimization methods presented here can be generally applied to any polymer system. Owing to the availability of data for the polystyrene-poly(phenyl acetylene) system studied by Arshad et al. [7], this chemistry was chosen for the photomask optimization study here. When polystyrene (PS) is exposed to UV light, its backbone undergoes a dehydrogenation reaction to produce poly(phenyl acetylene) (PPA), which imparts a higher surface tension to the polymer film in the exposed areas.

The T_g of the PS-PPA system studied by Arshad et al. was approximately 61°C [7] and the physical parameters for the PS-PPA system at 120°C and 140°C are used for this photomask optimization study. The initial film height, photomask periodicity, and physical parameters of the polymer system at annealing temperatures of 120°C and 140°C are presented in Table 4.1. Note that in the model $\gamma_0 = \gamma_{PS}$ and $\Delta\Gamma = \gamma_{PPA} - \gamma_{PS}$.

4.2.1.2 Nondimensionalization

Eqs. (4.1)-(4.3) were non-dimensionalized as follows. The height and concentration variables were nondimensionalized by the initial film height and concentration, respectively, such that $h^* = h/h_0$ and $C^* = C/C_0$. The lateral length is scaled by the target square length and so $\nabla^* = L\nabla$. Because the Marangoni flow dominates at early times, the fluid velocity is scaled with the Marangoni velocity, $\langle u \rangle_M$ (first term of Eq. 4.2), such that $\langle \mathbf{u} \rangle^* = \langle \mathbf{u} \rangle / \langle u \rangle_M = \langle u \rangle / (\Delta\Gamma C_0 h_0 / L\mu)$. For completeness, we note that the capillary velocity scale is $\langle u \rangle_C = \gamma_0 h_0^3 / L^3 \mu$. The time is scaled using the Marangoni flow time scale such that $t^* = t/t_M = t/(L/\langle u \rangle_M) = t/(\mu L^2 / h_0 \Delta\Gamma C_0)$. Note here that the lateral diffusion time scale is $t_{Dxy} = L^2/D$, and will be used later. Dropping asterisks for clarity, the non-dimensionalized equations become:

$$\frac{\partial h}{\partial t} + \nabla \cdot \left(h \langle \mathbf{u} \rangle \right) = 0, \tag{4.4}$$

$$\langle \mathbf{u} \rangle = \frac{h}{2} \nabla C + \frac{\kappa}{3} h^2 \nabla \left(\nabla^2 h \right), \tag{4.5}$$

$$\frac{\partial (hC)}{\partial t} + \nabla \cdot \left(\langle \mathbf{u} \rangle hC - \frac{1}{Pe} h \nabla C \right) = 0, \tag{4.6}$$

where $\kappa = \langle u \rangle_C / \langle u \rangle_M = (\gamma_0 / \Delta\Gamma C_0)(h_0/L)^2$ is the ratio of capillary to Marangoni velocity scales and $Pe = t_{Dxy}/t_M = h_0 \Delta\Gamma C_0 / \mu D$ is the Péclet number, a ratio of Marangoni-driven transport to lateral diffusive transport. The numerical solution to Eqs. (4.4)-(4.6) is necessary to determine the feature shape and quality. Details regarding the simulation of Eqs. (4.4)-(4.6) can be found in Secs. S4.1, S4.2, and S4.3 of the Supporting Information.

A summary of the scaling parameters and non-dimensional parameters is provided in Table 4.1. In addition typical values of the parameters for the polymer system considered here are reported. Significant physical insight and expectations on the patterning of the polymer films may be drawn from the table. The assumption of vertically homogenized concentration is reasonable since $t_{Dz}/ t_M << 1$ is satisfied for the cases considered. Note also that the Marangoni velocity is much higher than the capillary velocity. For smaller values of κ, Marangoni forces are relatively strong, and it can be anticipated that taller features will result relative to systems exhibiting larger values of κ. Likewise, for larger values of Pe, one would expect taller features due to the smaller influence of diffusion, which acts to weaken Marangoni forces. We may determine what annealing times are best based on the time scales for Marangoni flow t_M and diffusion of the photoproduct t_{Dxy}. Annealing times ~ $O(t_M)$ can be expected to show patterns with the larger heights. For annealing times beyond the diffusion time, lower heights are expected as diffusion will have diminished the strength of the Marangoni force. Ideally, one would like $t_M << t_{Dxy}$ for the largest heights and t_M to be small for the fastest processing. Note for the polymer system here, higher temperature reduces the relative importance of diffusion to Marangoni flow while also accelerating the patterning process.

Table 4.1 Physical and geometric parameters used in simulations. Physical parameters taken from Arshad et al. [7]

	Annealing Temperature	
Parameter	120°C	140°C
h_0 [nm]	150	150
λ [µm]	100	100
L [µm]	35	35
γ PS [mN m^{-1}]	32.2	30.8
γ PPA [mN m^{-1}]	34.2	33.9
$\Delta\Gamma$ [mN m^{-1}]	2.0	3.1
μ [Pa s]	2550	150
D [10^{-14} m^2 s^{-1}]	0.363	5.91
C_0 [mole frac.]	0.064	0.064
$\langle \mathbf{u} \rangle_M$ [nm/s]	0.22	5.7
$\langle \mathbf{u} \rangle_C$ [nm/s]	0.00099	0.016
t_M [10^3 s]	160	6.2
t_{Dxy} [10^3 s]	340	21
t_{Dz} [10^3 s]	0.0062	0.00038
κ	0.0046	0.0029
Pe	2.08	3.33

4.2.2 Pattern Quality

As mentioned earlier, a repeating 35x35 μm^2 square was chosen as the target pattern for this study. The intuitive choice of photomask for this case would be a repeating 35x35 μm^2 square photomask, which is shown in Fig. 4.2. The yellow regions in the figure represent transparent parts of the photomask, which allow light to pass and expose the underlying polymer film. The blue regions represent opaque parts of the photomask that block light and leave the film unexposed. As the exposed regions are of higher surface tension, it can be expected that fluid will initially flow from the blue regions towards the yellow regions.

An example feature formed using this square photomask is shown in Figs. 4.3a and 4.3b, which was achieved after annealing at T = 120°C for t/t_M = 0.049 and t/t_M = 0.16. The after-etch contour for these shapes is shown as the intersection of the red square and feature. The red squares in Figs. 4.3a and 4.3b is level with the initial film height and helps visualize the contour that would result from an anisotropic etch of height h_0. The contour of the after-etch feature is overlaid with the target square contour in Figs. 4.3c and 4.3d. The feature contours exhibit significant corner rounding and are far from the desired square pattern. Figs. 4.3e and 4.3f show the normalized concentration contours at the two annealing times. As time progresses, the initially square exposure pattern is blurred by diffusion, which prevents the feature from forming into the desired square pattern.

We note here that several minor contours and features can exist at h_0 due to the formation of small ripples and the presence of the double peaks at early times. When detected, these minor ripples and contours were ignored in this analysis.

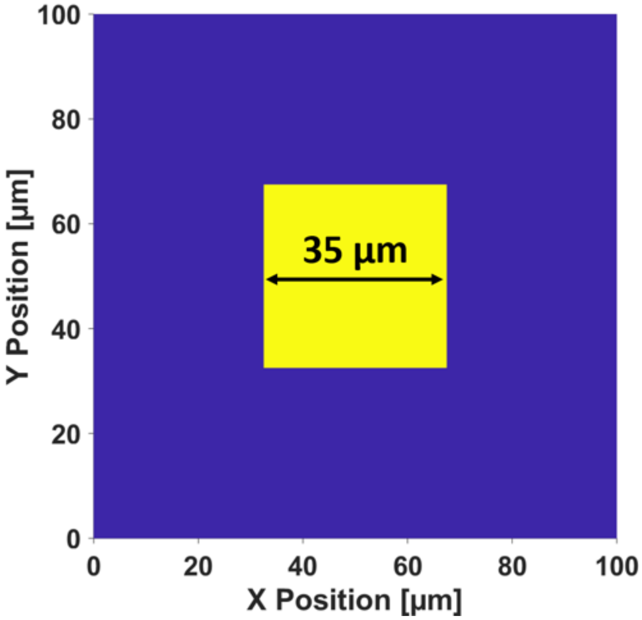

Figure 4.2 Repeating 35x35 µm^2 square photomask pattern. Yellow areas represent exposed regions and blue areas represent unexposed regions. The exposed regions of the polymer film possess a higher surface tension relative to the unexposed regions, meaning that fluid will flow into the yellow region.

A quantity called the penalized area is used to quantify the difference between the feature contour and the target contour. The penalized area is the sum of two areas, the first being the area enclosed by the feature contour but not the target contour and the second area is that enclosed by the target contour but not the feature contour. The penalized area can be expressed mathematically as the symmetric difference of two areas as given by

$$A_{\mathrm{FT}} = \left(A_{\mathrm{F}} \setminus A_{\mathrm{T}} \right), \tag{4.7}$$

$$A_{\mathrm{TF}} = \left(A_{\mathrm{T}} \setminus A_{\mathrm{F}} \right), \tag{4.8}$$

$$A_{\mathrm{P}} = A_{\mathrm{FT}} \cup A_{\mathrm{TF}} = A_{\mathrm{F}} \,\Delta\, A_{\mathrm{T}}, \tag{4.9}$$

where A_F is the area enclosed by the feature contour, A_T is the area enclosed by the target contour, A_{FT} is the area enclosed by the feature, but not the target, and A_{TF} is the area enclosed by the target but not the feature. The penalized area, A_P, is expressed as the union of these two areas or the symmetric difference of A_F and A_T. A penalized area of zero represents perfect feature-target overlap. Note that we report the penalized area in this paper as normalized by the area of the target square. The penalized area for the features shown in Fig. 4.3 is reported in in Figs. 4.3c and 4.3d. Information on how the penalized area was calculated can be found in Sec. S4.4 of the Supporting Information. We will also examine how the post-etch feature height (h_f in Fig. 4.1) is affected as we manipulate the photomask.

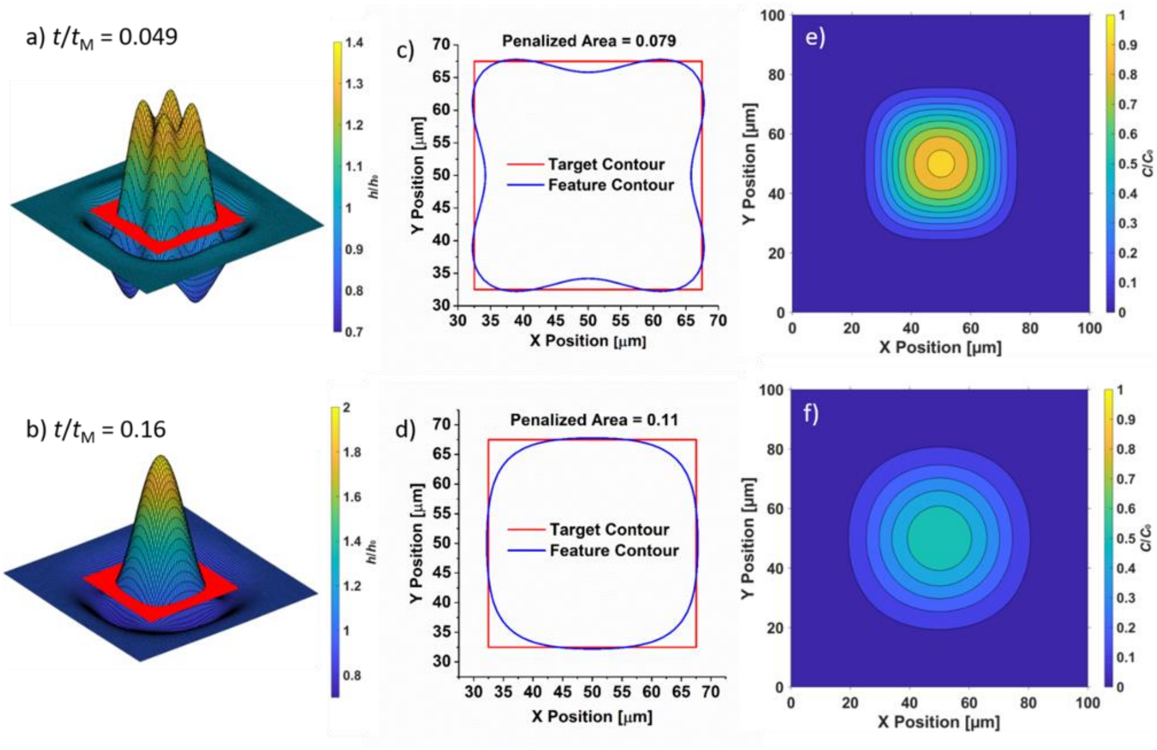

Figure 4.3 a,b) Features formed using a 35x35 μm^2 square photomask annealed at 120°C. The pre-etch film height, h/h$_0$, is indicated by the associated color bars. The red squares in a) and b) help visualize the contour that would result from an anisotropic etch of height h$_0$. c,d) Feature contours overlaid with the target 35x35 μm^2 square. Notice that the feature corners are significantly rounded. The penalized area, a dimensionless metric for determining feature-target overlap, is also reported with each contour. e,f) Contours of the concentration, C/C$_0$. Contours levels range from 0 to 1 in intervals of 0.1. The dimensionless annealing times for a,c,e) and b,d,f) were 0.049 and 0.16, respectively.

4.2.3 Penalized Area and Feature Height Evolution for the Intuitive Photomask

We calculate the penalized area and post-etch feature height over time for the intuitive 35x35 μm^2 photomask, where the etch height was set equal to the initial film height, i.e. $h_e = h_0$. Fig. 4.4a shows the evolution of the penalized area and its component parts over time at T = 120°C. The penalized area fluctuates, but generally increases over time. Note that at early times for $T = 120°C$, the component A_{FT} is zero. This is because the feature contour at these times is completely enclosed by the square target. However, as time goes on and the feature begins to relax, the feature contour begins to expand beyond the confines of the target square. This suggests that at early times, the intuitive photomask is too small and could be enlarged to reduce the penalized area when targeting short annealing times. At later annealing times, the intuitive photomask is too large and could be made smaller to reduce the penalized area when targeting later annealing times.

Fig. 4.4b shows the post-etch feature height for the intuitive 35x35 μm^2 square photomask annealed at 120°C and 140°C. The feature height eventually reaches a maximum as capillary forces begin to dominate. Similar to what was found by Arshad et al [7], the 140°C case exhibits taller feature heights relative to the 120°C case. This is primarily because the surface tension gradient is larger at 140°C. By scaling the normalized feature height by κ, the height curves at 120°C and 140°C mostly collapse on top of one another, as shown in the inset of Fig. 4.4b. As will be seen in later results, the post-etch feature height is typically taller at the 140°C annealing temperature. Taller feature heights are generally more desirable, so we would ideally target later times for patterning. But the penalized area also increases with time, so there is a conflict which will become more apparent later.

In the next section, we present the effects of resizing the square photomask on the feature-target overlap and the feature height. In the subsequent section, we present the pixel-based photomask optimization method and its effects on the feature-target overlap and feature height.

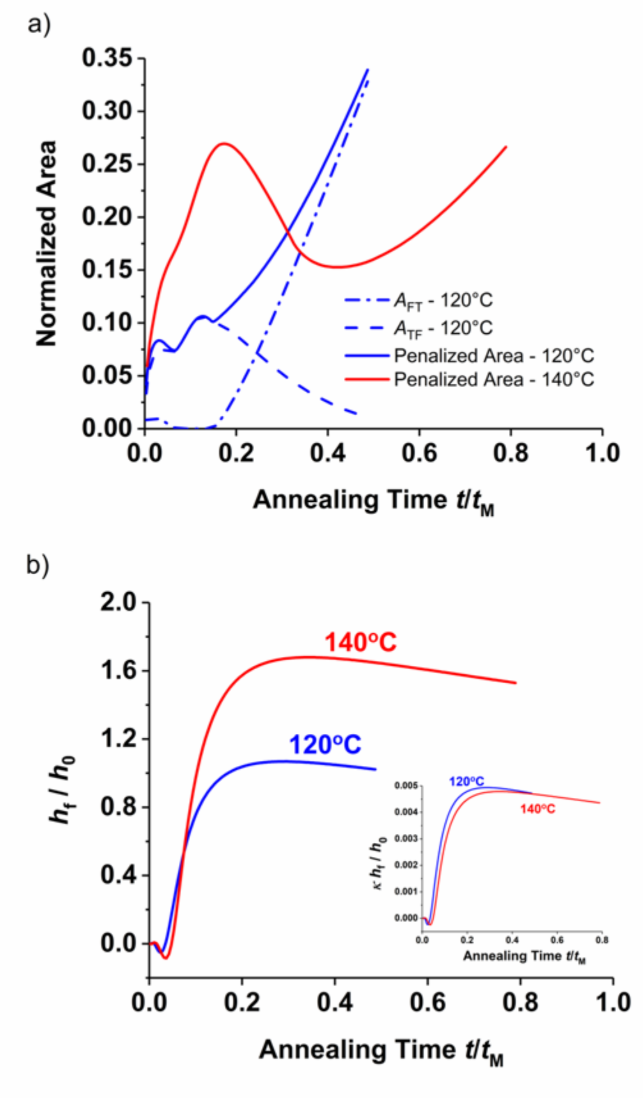

Figure 4.4 a) Penalized area and its component parts vs. scaled annealing time at 120°C and 140°C. b) Normalized feature height vs. scaled annealing time at T = 120°C and T = 140°C. Inset shows that the curves mostly collapse when scaling the feature height by κ.

4.3 PHOTOMASK RESIZING

By resizing the photomask, significant improvements to the penalized area can be achieved. Fig. 4.5 demonstrates this by comparing the features that result from the intuitive photomask (Fig. 4.5a) and a resized photomask (Fig. 4.5b), both annealed at 140°C for t/t_M = 0.16. Figs. 4.5c and 4.5d show the features that form and Figs. 4.5e and 4.5f show the resulting feature-target overlap. As can be seen, the resized photomask clearly improves the feature-target overlap and reduces the penalized area by five-fold. The feature corners, however, are still severely rounded and simple photomask resizing cannot compensate for this. The pixel-based optimization method shown later will prove to produce much sharper corners.

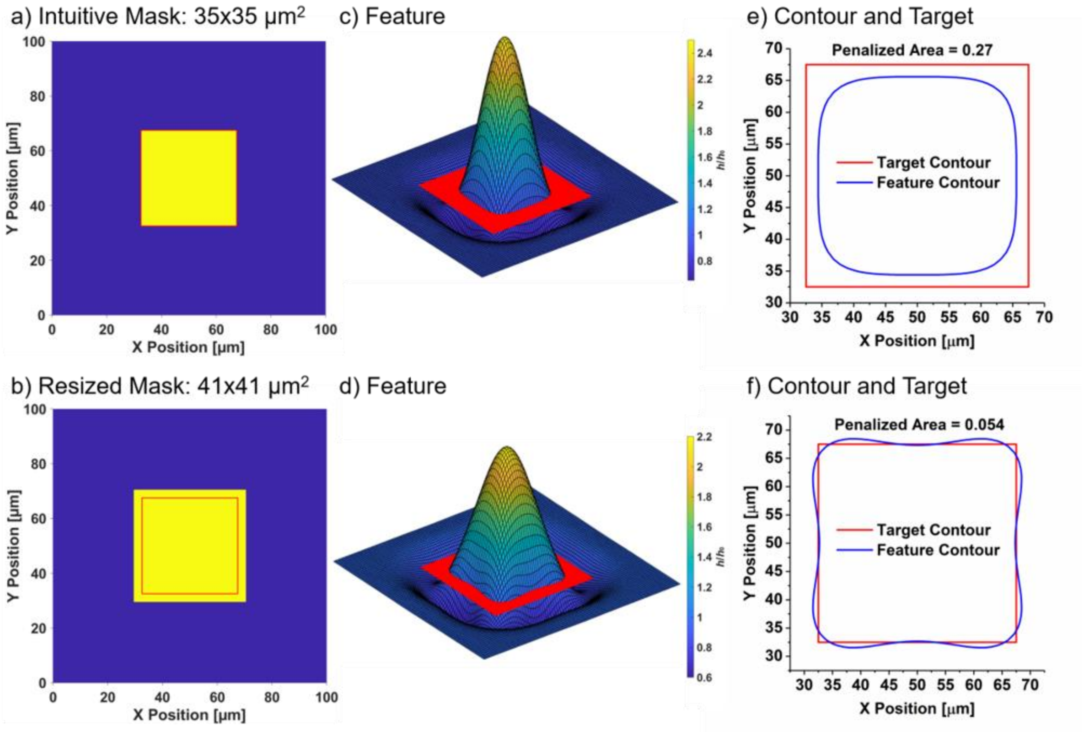

Figure 4.5 a) Intuitive and b) resized photomasks. Red outline overlays the target with the photomask. c,d) Features resulting from annealing at 140°C for t/t_M = 0.16. Red cross-section defines the relevant after-etch contour taken at h_0. e,f) After-etch contour overlaid with the target 35x35 µm^2 square contour.

To more fully understand the effects of resizing the photomask, a parameter sweep was performed in which the penalized area was calculated for various photomask sizes and temperatures. The annealing times for the 120°C case were t/t_M = 0.049, 0.097, 0.16, 0.23, and for the 140°C case the times were t/t_M = 0.079, 0.16, 0.26, 0.37, 0.47.

The penalized areas for these conditions are shown in **Table 4.2**. The photomasks which performed best for a given annealing temperature and time are underlined. Significant improvements were seen for several annealing times and temperatures, which shows that a significant "first-order" correction can be achieved by simply resizing the photomask. Also note the trend in Table 4.2 where larger square photomasks are required at early times, but smaller ones are required at later times.

Table 4.2 Penalized area for several square photomask sizes (left-most column) at select dimensionless annealing times and temperatures (Left: T = 120°C, **Right: T = 140°C**). The objective used to calculate the penalized area is a 35x35 μm^2 square. Underlined values indicate the best square photomask among those tested for a given dimensionless annealing time. Note that the 35x35 μm^2 square photomask is the intuitive choice of photomask. Annealing temperature is 120°C for the regular font and 140°C for the bold font.

	Dimensionless Annealing Time [t/t_{M}] (Left: *T* = 120°C, **Right: *T* = 140°C**)				
Size [μm]	0.049, **0.079**	0.097, **0.16**	0.16, **0.26**	0.23, **0.37**	0.29, **0.47**
27	0.44, **0.53**	0.41, **0.48**	0.30, **0.36**	0.19, **0.25**	0.162, **0.18**
29	0.35, **0.46**	0.36, **0.44**	0.26, **0.34**	0.17, **0.23**	0.159, **0.17**
31	0.26, **0.37**	0.28, **0.39**	0.22, **0.30**	0.15, **0.20**	0.159, **0.16**
33	0.17, **0.28**	0.20, **0.34**	0.16, **0.27**	0.14, **0.18**	0.163, **0.158**
35	0.079, **0.18**	0.095, **0.27**	0.11, **0.23**	0.13, **0.16**	0.17, **0.156**
37	0.083, **0.087**	0.047, **0.18**	0.087, **0.18**	0.14, **0.14**	0.19, **0.157**
39	0.15, **0.082**	0.13, **0.075**	0.12, **0.12**	0.16, **0.134**	0.22, **0.16**
41	0.26, **0.14**	0.24, **0.054**	0.20, **0.087**	0.21, **0.133**	0.26, **0.17**
43	0.38, **0.24**	0.36, **0.15**	0.32, **0.093**	0.30, **0.14**	0.33, **0.19**

Fig. 4.6a compares the penalized area resulting from the intuitive photomask to that of the best-performing resized photomasks (underlined values in Table 4.2). Fig. 4.6b shows the fold-improvement resulting from resizing the photomasks, with a maximum of 5-fold improvement made possible.

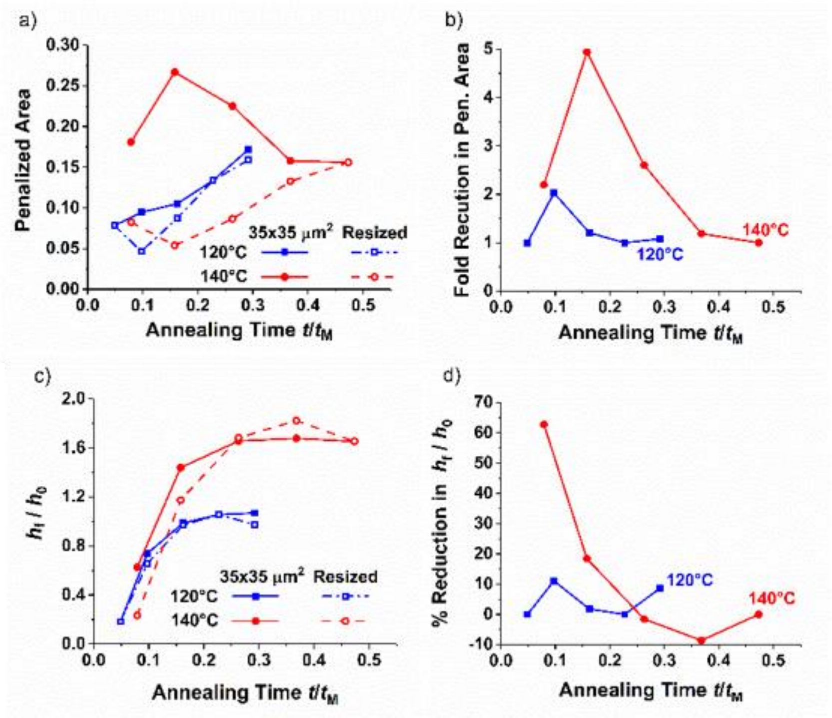

Figure 4.6 a) Penalized area at various annealing times for the intuitive 35x35 μm^2 photomask and the best-performing resized photomasks. b) Fold reduction in penalized area when comparing the penalized areas generated by the intuitive 35x35 μm^2 photomask to the best-performing resized photomasks at each annealing time and temperature. c) Normalized feature height at various annealing times for the intuitive 35x35 μm^2 photomask and the best-performing resized photomasks. d) % reduction in feature height when comparing the feature heights generated by the intuitive 35x35 μm^2 photomask to the best-performing resized photomasks at each annealing time and temperature.

Biasing the photomask can significantly improve the penalized area; however, this often comes at the expense of feature height. This fact is shown in Fig. 4.6c, which compares the post-etch feature height achieved when using the intuitive photomask to that achieved from using the optimally resized photomask. Fig. 4.6d shows the percent reduction in feature height, with the maximum reduction being roughly 60%. In some cases, small to modest improvements in feature height were observed.

To understand why resizing the photomask leads to worsened feature heights in some cases, we examine the feature height evolution for three different sized photomasks. Fig. 4.7 shows the normalized feature height over time for 25x25 μm^2, 35x35 μm^2, and 45x45 μm^2 square photomasks at 120°C. Note that at early times, smaller photomask sizes result in taller feature heights. This is because the fluid must travel a shorter distance to reach the feature center. However, at moderate annealing times, capillary forces begin to dominate sooner for these finer features, making them decay sooner relative to broader features with lower capillary pressures. Therefore, smaller photomask sizes tend to produce taller features at early annealing times but produce smaller features at later annealing times. This presents a conflict between feature height and penalized area. As the photomask is enlarged at early times to reduce the penalized area, the feature height can suffer. The same is true at later times, where the feature height can also suffer as the photomask is shrunken to reduce the penalized area.

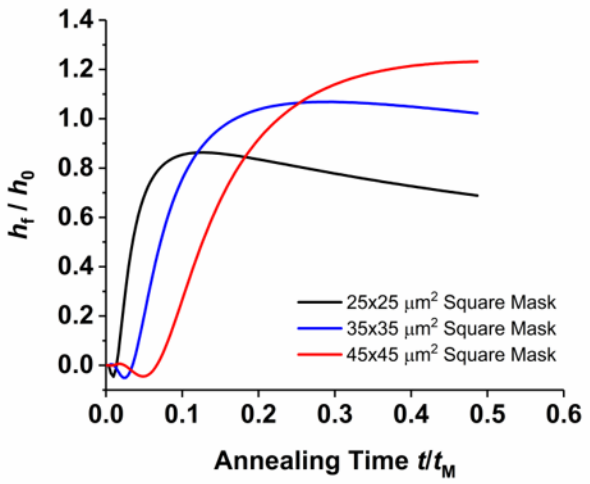

Figure 4.7 Normalized feature height over time for various square photomask sizes annealed at 120°C. Note that the smaller square photomask exhibits taller feature heights at early annealing times. The earlier onset of feature decay for the smaller photomask results in shorter features at later times relative to those achieved by larger photomasks.

4.4 PIXEL-BASED EXPOSURE OPTIMIZATION

4.4.1 Photomask and Optimization Setup

To obtain improvement beyond simple photomask resizing, the photomask was optimized using a pixel-based optimization method. The photomask can be thought of as being made up of pixels that are either on (exposed area) or off (unexposed area). The state of each pixel can be thought of as a variable to be optimized for the photomask. Fig. 4.8 shows this photomask representation in which each pixel is a binary variable (1 = exposed, 0 = unexposed). Due to symmetry, only one-eighth of the photomask needs to be manipulated and then copied into the other regions (region shown in Fig. 4.8 as the lightly outlined region). To reduce the number of isolated pixels in the resulting photomask, the variable pixels are restricted to a subset of the photomask. This can be seen in Fig. 4.8 in the bold outlined region, where variables exist in only a trapezoidal subsection of the photomask. To the left of the bold trapezoid, pixels are always off, while to the right, pixels are always on.

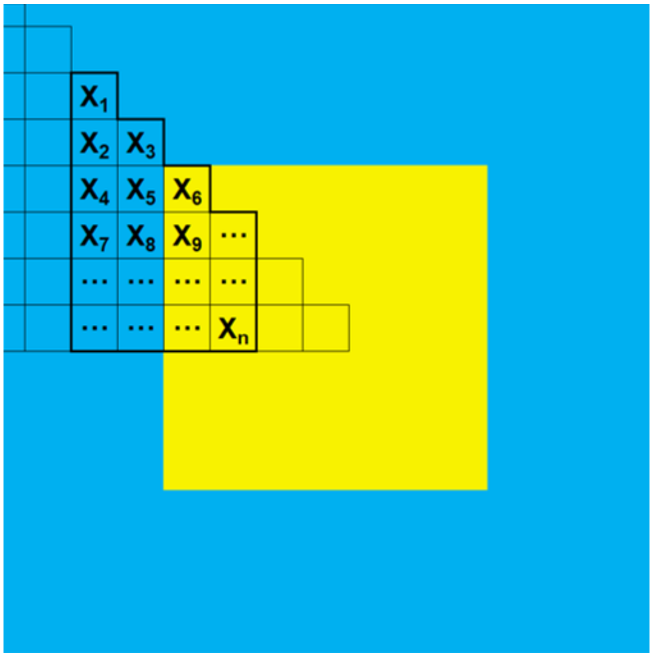

Figure 4.8 Photomask representation. Yellow pixels represent transparent, exposed photomask regions, while the blue areas represent closed photomask region. Note that only one-eighth of the photomask needs to be manipulated due to symmetry (light outline). Also note that the variable domain has been restricted to a subset of the whole domain (bold outline).

The photomask grid was arranged such that the center of each pixel was a point on the simulation domain. As explained in Sec. S4.1 of the Supporting Information, the simulation grid was composed of 1x1 μm^2 pixels. We therefore chose to construct the photomask using the same 1x1 μm^2 pixels. It is worth noting that this pixel size of 1x1 μm is well within manufacturability limits for contact photomasks.

The annealing time for each photomask optimization was fixed, such that time was not a variable handle. Consistent with the photomask resizing study, the optimization was performed for fixed annealing times of t/t_M = 0.049, 0.097, 0.16, 0.23 for the 120°C case and t/t_M = 0.079, 0.16, 0.26, 0.37, 0.47 for the 140°C case. MATLAB's built-in genetic algorithm toolbox was used to carry out the optimization. Details regarding the genetic algorithm optimization can be found in Sec. S4.5 of the Supporting Information. To ensure that the chosen simulation grid size was sufficient for convergence of the resulting pixelated photomasks, mesh and time-step refinements were performed for the final, optimized photomasks, the results of which can be found in Sec. S4.6 of the Supporting Information.

4.4.2 Optimization Results

Fig. 4.9 shows the convergence of the genetic algorithm optimization, presenting the minimum penalized area for several generations. The initial point at generation zero for each fixed annealing time reflects the "first-order" correction to the intuitive 35x35 μm^2 square photomask, which are also found as the underlined values in Table 4.2.

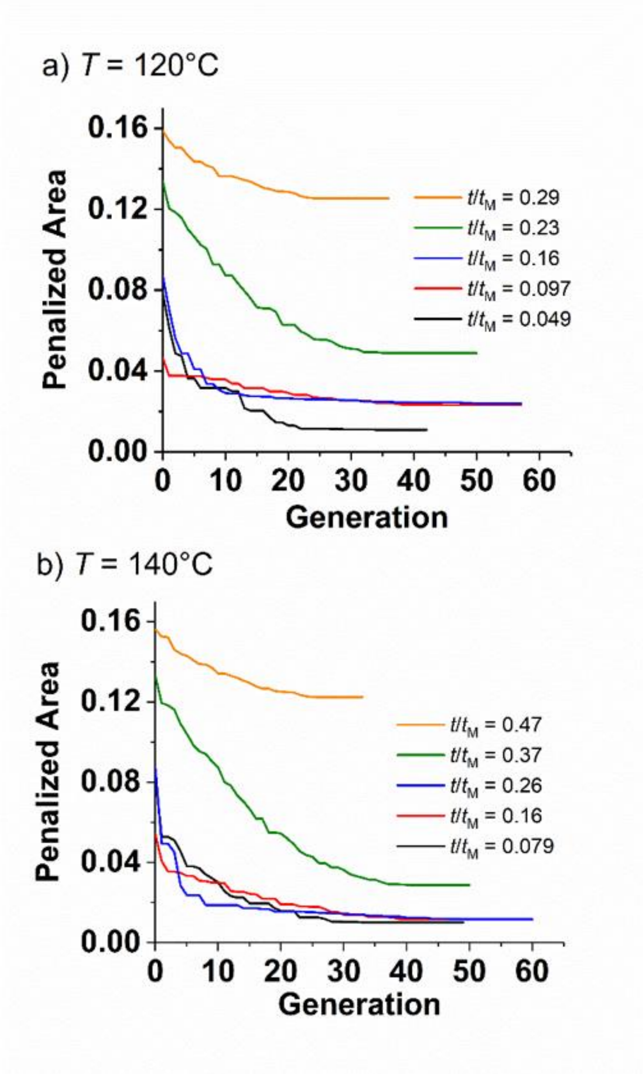

Figure 4.9 Genetic algorithm convergence plot for optimizations at a) 120°C with fixed annealing times of t/t_M = 0.049, 0.097, 0.16, 0.23, 0.29 and b) 140°C with fixed simulation times of t/t_M = 0.079, 0.16, 0.26, 0.37, and 0.47. The initial point at generation zero for each fixed annealing time reflects the “first order” correction to the intuitive 35x35 μm^2 square photomask (underlined values in Table 4.2). The progression terminates when the photomask population becomes homogeneous.

The smallest penalized area was achieved for t/t_M = 0.079 at 140°C while longer fixed annealing times often resulted in larger penalized areas. The greatest reduction in penalized area was also observed for $t/t_M = 0.079$ at 140°C, resulting in an eight-fold reduction in penalized area when compared to the resizing correction. The smallest improvements were observed for $t/t_M = 0.29$ at 120°C and for $t/t_M = 0.47$ at 140°C, where the penalized area was reduced by roughly 1.25-fold when compared to the resizing correction.

An auxiliary experiment was performed (not shown here) in which mask optimizations were done with different genetic algorithm parameters, which produced unique final photomasks with very comparable penalized areas. While the masks were different from one another, their qualitative features were quite similar. Small differences in the penalized area appears to lead to small differences in the pixel pattern.

To determine the effect of simulation grid size on the optimized photomasks, simulations were repeated for each optimized photomask using twice the number of grid points (see Sec. S4.6 of the Supporting Information). The resulting penalized areas for the two simulation grid sizes showed very good agreement in some cases, while modest differences were seen in other cases. For the case possessing the worst agreement in penalized area, visual inspection revealed that the resulting contours sufficiently matched one another to maintain confidence in the results and effectiveness of the method.

Fig. 4.10 shows the optimized photomask shape, resulting feature and penalized area for the 120°C optimization at $t/t_M = 0.049$. The other optimized photomasks at the tested temperatures and times can be found in Sec. S4.7 of the Supporting Information. The red square outline in Fig. 4.10a shows the size of the intuitive 35x35 μm^2 square photomask. Figs. 4.10b and 4.10c can be directly compared to Figs. 4.3a and 4.3c, respectively, which show the feature and contour resulting from the intuitive 35x35 μm^2 photomask. The reduction in penalized area is significant and the improved overlap with the target is clearly visible. The feature corners for the optimized photomasks are also very sharp. It is interesting to note the shape of the optimized photomask. The effect of the optimization was to extend the corners and central edges. Similar effects were seen for almost all of the optimized photomasks.

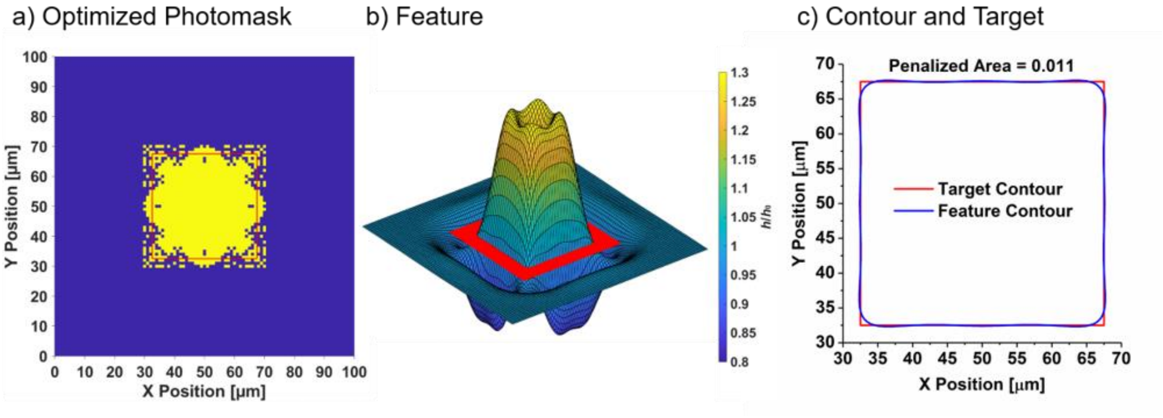

Figure 4.10 a) Optimized photomask for the 120°C optimization at $t/t_M = 0.049$. The red square depicts the size of the intuitive 35x35 μm^2 square photomask. b) Resulting feature. Note that the feature height is not to scale so as to clearly visualize the feature shape. Red cross-section defines the relevant after-etch contour. c) After-etch contour overlaid with the target 35x35 μm^2 square contour.

Due to the pixelated photomask representation, the optimized photomasks possess several isolated pixels. Pixelation at this scale is manufacturable. If necessary, pixelation could be reduced through the use of a weighted objective function that penalizes isolated pixels. Note that one test revealed that by disproportionately seeding the initial population of guesses in the GA optimization, a less pixelated photomask could be produced. This method, however, did not reduce the objective function as much compared to using a balanced population seed (see Sec. S4.8 of the Supporting Information).

Fig. 4.11a compares the penalized area resulting from the intuitive 35x35 μm^2 square photomask to that achieved by the optimized photomasks. The reduction in penalized area is significant, especially at early annealing times. Fig. 4.11b shows the fold-reduction in penalized area for the optimized photomasks relative to the intuitive photomask. The maximum reduction in penalized area observed was roughly 23-fold, which is roughly 4-fold better than the maximum reduction seen from simple photomask resizing. At longer annealing times, it generally became more difficult to influence the final pattern. This is due to the degeneration of the concentration gradient over time. As time goes on, diffusion degrades the concentration gradient imparted by each pixel, leading to less control over the final pattern at later times.

It is interesting to note that the higher annealing temperature of 140°C always resulted in a lower penalized area at comparable annealing times. This is likely due to a combination of effects, mainly the stronger Marangoni forces (lower value of κ) and/or weaker diffusion forces (higher value of Pe) at this temperature. As Marangoni forces become stronger, each concentration pixel can more greatly influence the flow, resulting in more control over the final pattern. Similarly, weaker diffusive forces allow the concentration gradient to be maintained for longer periods, again resulting in more control over the final pattern at a specified annealing time.

The reduction in penalized area always came at the cost of feature height. This can be seen in Fig. 4.11c, which compares the feature height resulting from the intuitive 35x35 μm^2 square photomask to that achieved by the optimized photomasks. Feature height reductions ranged from 2.9% (T = 120°C, t/t_M = 0.049) to 55% (T = 140°C, t/t_M = 0.047). This can be seen in Fig. 4.11d, which shows the percent reduction in feature height for the optimized photomasks relative to the intuitive photomask. As mentioned earlier, the reduction in feature height is due to the resizing of the photomask. The serifs added to the corners of some masks may also reduce the feature height as they can direct flow away from the center of the photomask.

This study generally suggests that stronger Marangoni forces and weaker diffusion forces offer greater shape control in Marangoni-driven patterning.

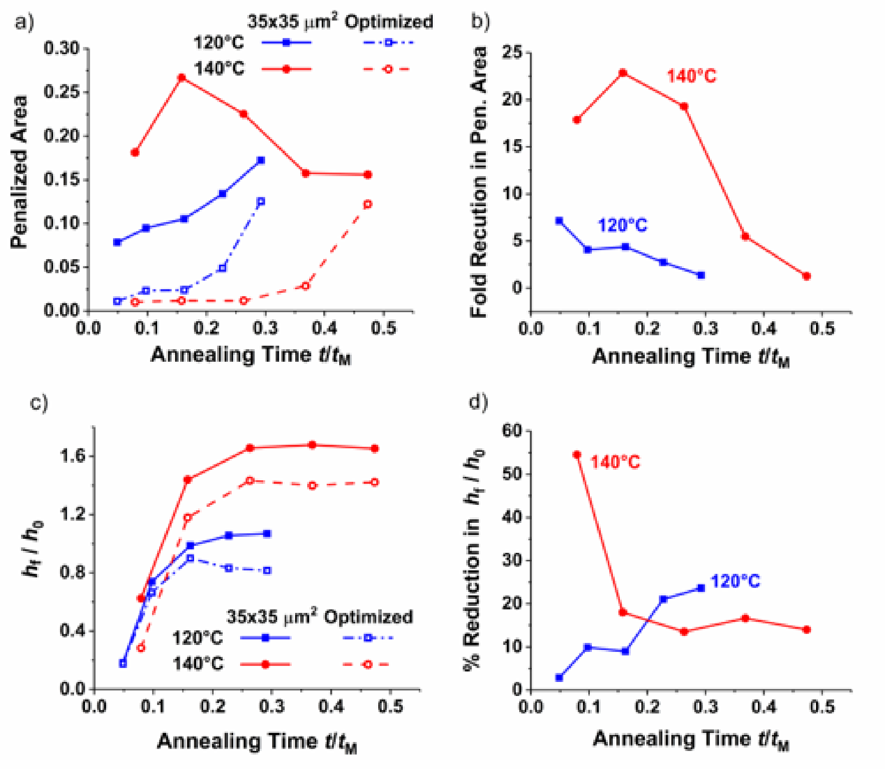

Figure 4.11 a) Penalized area at various annealing times for the intuitive 35x35 μm^2 photomask and the photomasks optimized using the genetic algorithm. b) Fold reduction in penalized area when comparing the penalized areas generated by the intuitive 35x35 μm^2 photomask to the optimized photomasks at each annealing time and temperature. c) Normalized feature height at various annealing times for the intuitive 35x35 μm^2 photomask and the photomasks optimized using the genetic algorithm. d) % reduction in feature height when comparing the feature heights generated by the intuitive 35x35 μm^2 photomask to the optimized photomasks at each annealing time and temperature.

4.5 CONCLUSIONS

A predictive model and simulation tool for two-dimensional Marangoni-driven patterning were presented. It was shown that for a square target pattern a good final shape can be obtained by simply resizing the intuitive square photomask. Superior control of the pattern was shown to be possible by pixel-level control of the surface tension in the Marangoni-driven patterning. Using a genetic algorithm as the means to optimize the photoexposure, excellent feature quality can be achieved. At early to mid-annealing times significant reductions in the penalized area were achieved, while modest reductions were observed at later annealing times. This was attributed to diffusion weakening the influence of the concentration pixels. The optimization results also suggest that stronger Marangoni forces and weaker diffusion forces provide more shape control. Although the optimization consistently improved the feature-target overlap, it also led to a decrease in feature height. The reduction in feature height is attributed to resizing the photomask and the addition of serifs that redirect flow away from the center of the feature.

The photomask optimization method presented here could be applied to control the pattern of any polymer film that undergoes Marangoni-driven patterning. Furthermore, the concepts presented here apply to contact photomask optimization and other exposure methods such as maskless lithography.

SUPPORTING INFORMATION

S4.1 Simulation Setup

Eqs. (4.4)-(4.6) were solved using an explicit finite difference method. Spatial derivatives were computed using fourth-order accurate, central differencing and temporal derivatives were computed using two-point, forward time differencing. The symmetry boundary conditions were implemented by repeating the domain at cells beyond the boundary and then calculating derivatives using these repeated cells. Note that the entire square domain was solved. Unless otherwise stated, an adaptive time stepping method similar to that outlined by Valli et al. [51] was used. The maximum relative change in film height between successive time steps was restricted to 0.00025 and the time step typically ranged between

10^{-7} and 10^{-5} dimensionless time units. Adaptive time stepping allowed for a significant reduction in simulation time for photomask optimization. For the purpose of checking convergence, appropriate constant time steps were also used (see Sec. S4.2 of the Supporting Information). Other results demonstrating good convergence, mass conservation, and verification are provided in Secs. S4.2 and S4.3 of the Supporting Information.

The simulation grid was comprised of 101 grid points in the *x*- direction and 101 points in the *y*- direction, resulting in a total of 10,201 evenly spaced grid points. The spacing between grid points was therefore 1 µm. The normalized film height (h/h_0) was initialized to unity for all x and y and the normalized mole fraction field variable (C/C_0), initialized to unity in exposed grid pixels and was initialized to zero in unexposed grid pixels.

S4.2 Convergence and Conservation Study

The adaptive time stepping method introduced oscillations in the higher order derivative terms that were not observed when using a constant time step. These oscillations, however, were shown to be inconsequential given that the adaptive time stepping solutions were in good agreement with constant time stepping solutions, as will be shown here. Furthermore, the chosen grid size of 1x1 µm^2 will also be shown here to be sufficient for convergence for simple square patterns.

To check that the adaptive time stepping method and chosen simulation grid size of 1x1 µm^2 was sufficient for convergence, a study was performed in which a constant time step was used for a grid of size 0.5x0.5 µm^2. The constant time steps used were checked for temporal convergence. Fig. S4.1 shows the after-etch feature height (h_f in Fig. 4.1) as a function of time for square photomasks of size 25x25 μm^2 and 51x51 μm^2 at annealing temperatures of 120°C and 140°C. The adaptive time stepping method is compared to the constant time stepping methods at various grid sizes. Note that the adaptive time stepping solutions closely follow the constant time stepping solutions. Prior to accounting for the anisotropic etch, the maximum relative absolute difference between the pairs of curves shown in Fig. S4.1 was 0.29%, which is acceptable for the sake of convergence.

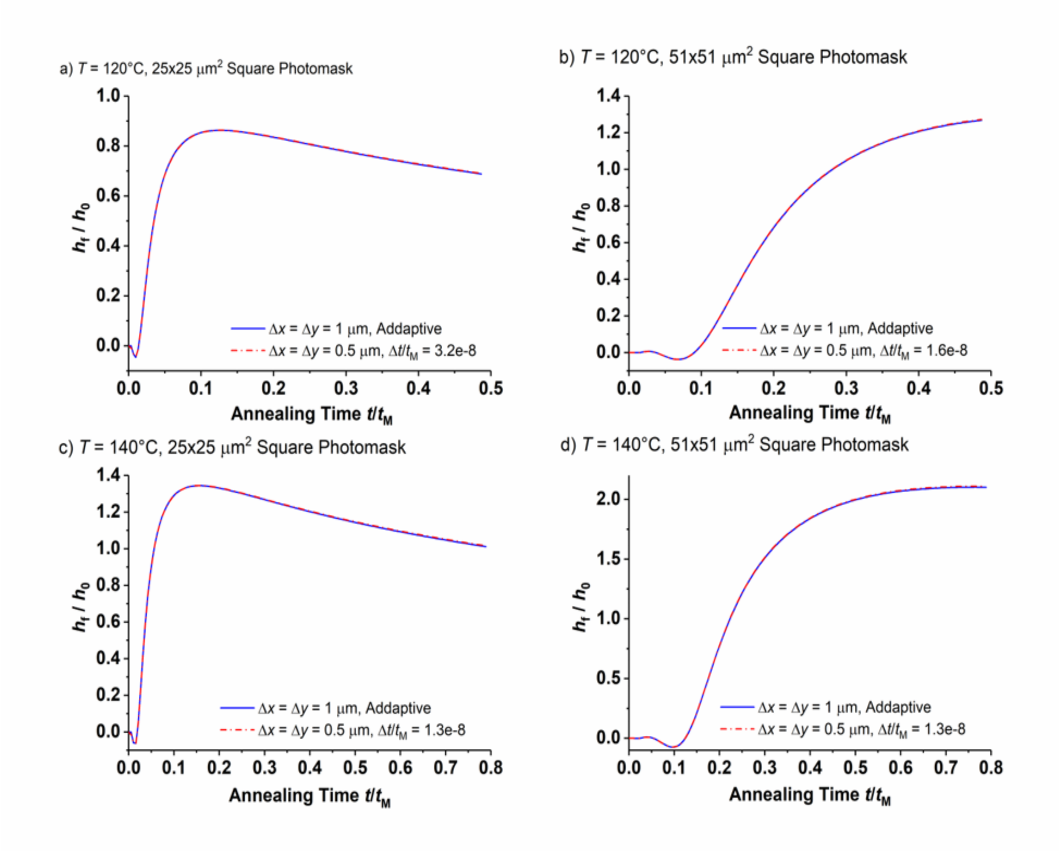

Figure S4.1 Normalized feature height over time calculated using adaptive and constant time stepping methods on simulation grid sizes of 1x1 μm^2 and 0.5x0.5μm^2, respectively. Simulations were performed using square photomasks of size 25x25 μm^2 and 51x51 μm^2 at annealing temperatures of 120°C and 140°C.

Fig. S4.2 shows the penalized area, normalized to the target square area, (see Sec. 4.2.2) as a function of time for square photomasks of size 25x25 μm^2 and 51x51 μm^2 at annealing temperatures of 120°C and 140°C. Again, the adaptive time stepping method is compared to the constant time stepping method at a finer grid size. The maximum absolute, relative difference between the pairs of curves shown in Fig. S4.2 was 0.97%. It is suspected that this error does not arise from convergence issues alone, but also from the increased precision in feature contouring offered by the finer simulation grid, which leads to greater accuracy in calculating the penalized area. Although the 0.97% error may seem large, it is viewed as acceptable when considering the high computational cost associated with using the 0.5x0.5 μm^2 simulation grid size.

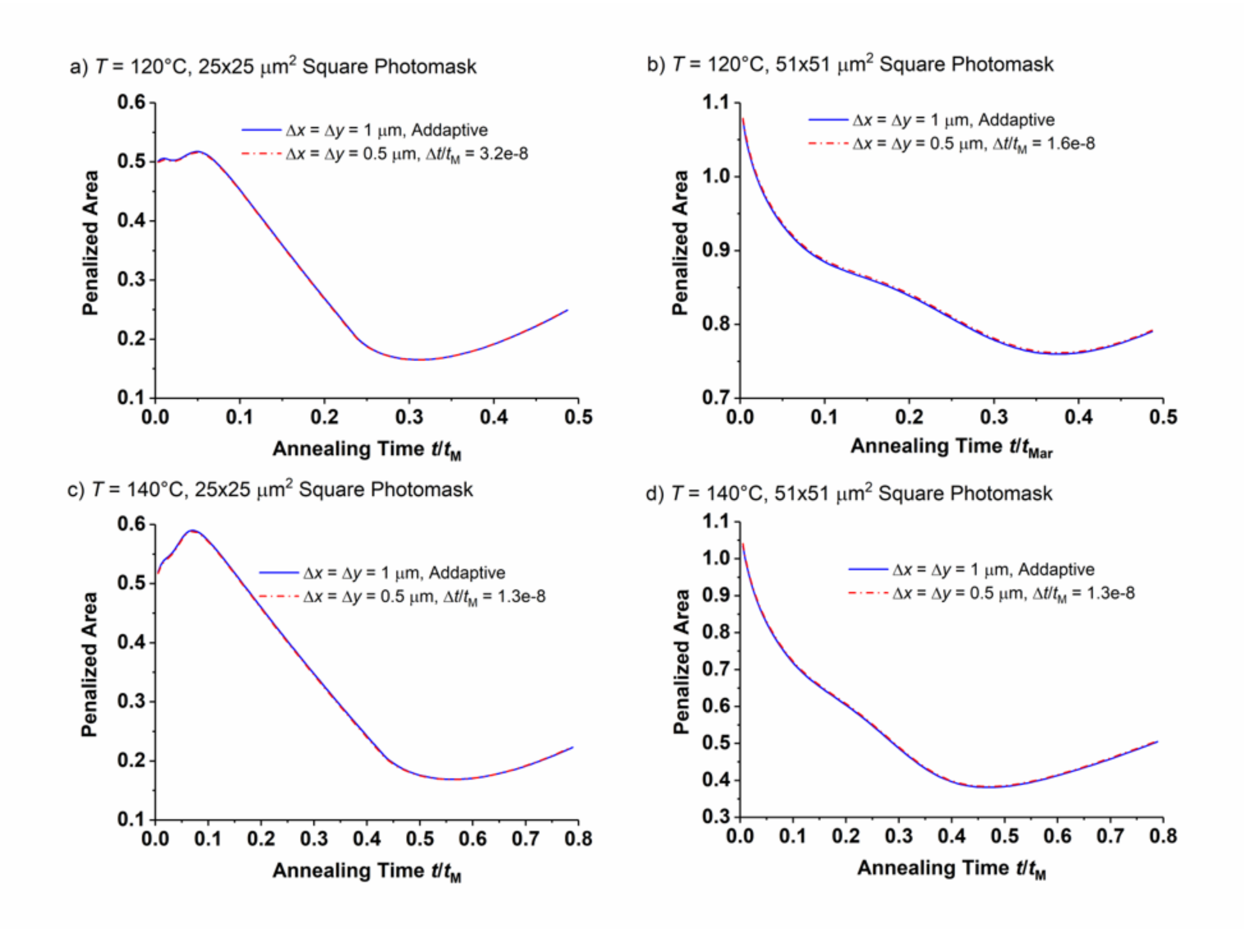

Figure S4.2 Penalized area over time calculated using adaptive and constant time stepping methods on simulation grid sizes of 1x1 µm^2 and 0.5x0.5µm^2, respectively. Simulations were performed using square photomasks of size 25x25 µm^2 and 51x51 µm^2 at annealing temperatures of 120°C and 140°C.

To determine whether the model conserved volume and species, the volume and species amount were calculated for square photomasks of size 25x25 µm^2 and 51x51 µm^2 at annealing temperatures of 120°C and 140°C. Fig. S4.3 shows the progression of the volume and species, which have been normalized to their respective initial volume and species quantities to reveal the relative amount of volume and species loss over time. At the latest annealing time, the largest relative losses are less than 0.3%, which shows that the model is sufficiently conservative **for the tested square photomasks of size 25x25 μm^2 and 51x51 μm^2.**

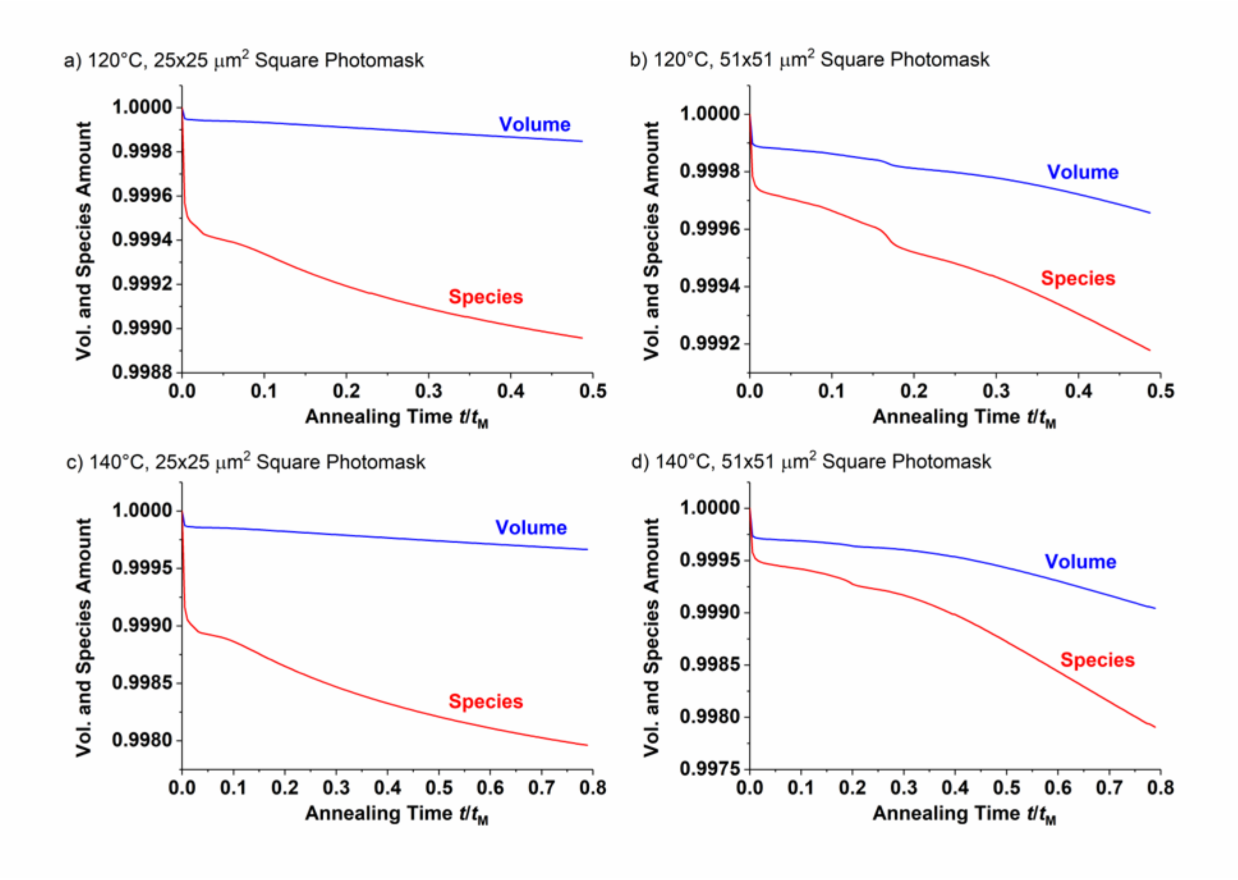

Figure S4.3 Plots showing the progression of relative volume and species loss for square photomasks of size 25x25 μm^2 and 51x51 μm^2 at annealing temperatures of 120°C and 140°C.

S4.3 Model Verification

The flow model was verified using the commercial finite element solver, COMSOL Multiphysics. Eqs. (4.1)-(4.3) were solved using the general form PDE interface with no-flux, symmetry boundary conditions implemented for both variables *h* and *hC*. For the purpose of calculating third and fourth order derivatives in h, two other variables, h_{xx} and h_{yy} were declared. The initial concentration was implemented using COMSOL's built-in step function with a smoothing transition zone of size 1 µm. A mapped mesh was used and the element size was set to 1 µm. Quartic element orders were used for all equations. Taking advantage of the symmetry, only a quarter of the square was simulated. The relative tolerance used by the solver was set to 1e-4.

The finite difference simulation was performed using the adaptive time stepping method with a grid size of 101x101 points (1x1 µm^2 grid size). The finite element and finite difference flow simulations were carried out at 120°C using a square photomask of size 35x35 µm^2 for 15 non-dimensional time units. Fig. S4.4 shows the post-etch height for the finite element and finite difference models. The two results practically overlap. Prior to accounting for the anisotropic etch, the maximum relative difference between the two curves is 0.16%, which is sufficient to verify the two model implementations.

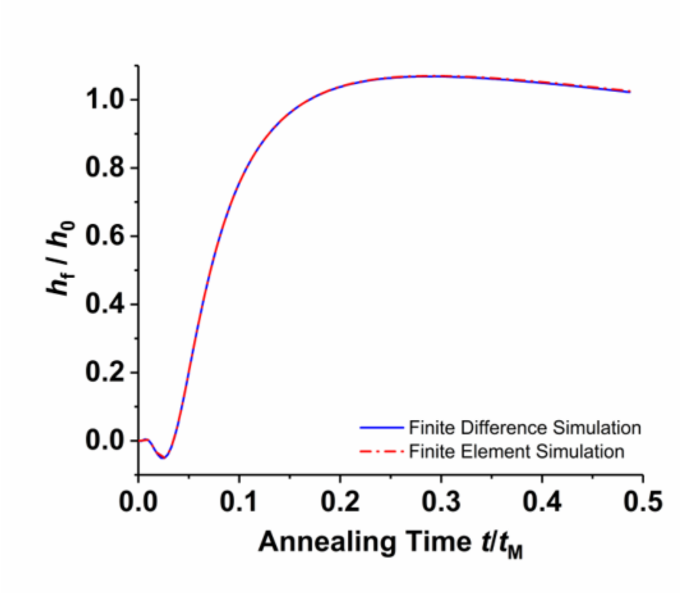

Figure S4.4 Normalized feature height for the C++ and COMSOL model implementations which were calculated using a 35x35 µm^2 square photomask at an annealing temperature of 120°C.

S4.4 Calculating the Penalized Area

To calculate the penalized area, a grid size of 0.025x0.025 µm^2 was used to count the number of points that fell within the penalized area. Note that this grid size used to calculate the penalized area was finer than the 1x1 µm^2 simulation grid. The penalized area was calculated by gridding the feature domain and determining which grid points fell within and on the target and feature contours. Using these points, the symmetric difference was evaluated and the sum of points contained by the symmetric difference were multiplied by the square grid size. To check that the grid size used in summing the penalized area was sufficiently fine, the penalized area was calculated using grid sizes of 0.1x0.1 µm^2, 0.05x0.05 µm^2, 0.025x0.025 µm^2, and 0.01x0.01 µm^2 for a 35x35 µm^2 photomask at

120°C. Fig. S4.5 shows the penalized area over time for a 35x35 μm^2 square photomask pattern annealed at 120°C. Although the curves appear to converge, it is expected that at certain annealing times, roughly 2% absolute, relative error still exists between the calculated and actual penalized areas for the 0.01x0.01 μm^2 grid size and 5% absolute, relative error for the 0.025x0.025 μm^2 grid size. This error is expected to arise, in part, from the points that fell on the target square contour (which could either artificially increase or decrease the penalized area). The error is also expected to arise from the error inherent to approximating the area of curved shapes using squares. As a finer grid is used, the error decreases.

The residual error of roughly 2-5% is arguably small and is not expected to significantly affect the photomask optimization. Due to the high computational cost associated with calculating the objective function at a grid size of 0.01x0.01 μm^2, the 0.025x0.025 μm^2 grid was used for calculating the penalized area.

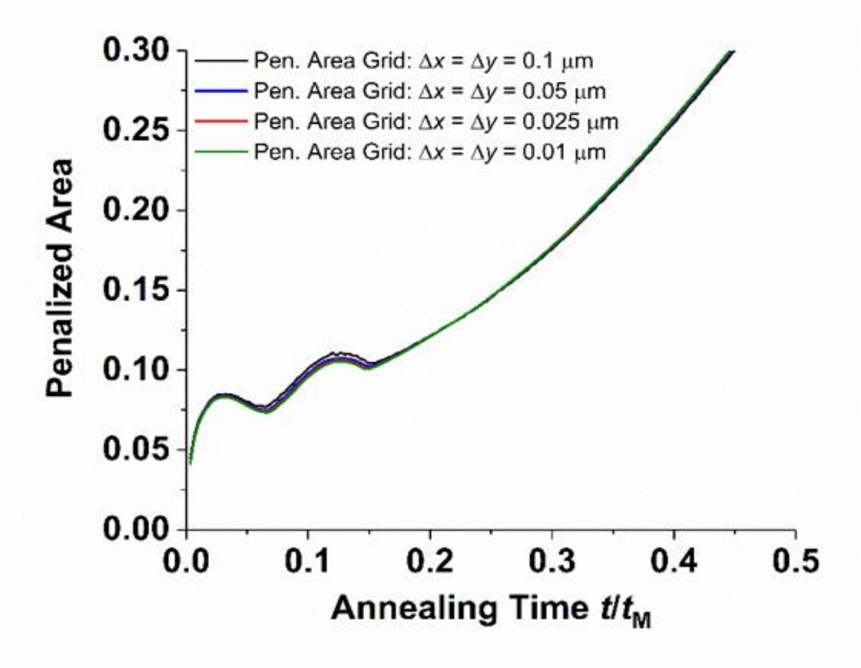

Figure S4.5 Penalized area over time calculated using various grid sizes. Simulations were performed using a square 35x35 μm^2 photomask at an annealing temperature of 120°C.

S4.5 Genetic Algorithm Implementation

To obtain improvement beyond simple photomask resizing, a genetic algorithm was used to further optimize the photomask. A genetic algorithm (GA) is a heuristically based optimization method capable of searching large solution spaces. Instead of navigating the solution space through a form of gradient descent, a GA evaluates the fitness (or objective function) at several sample points in the solution space. This group of sample points makes up a population. To update and ideally improve the population of sample points, a GA mimics evolution and natural selection that occurs within living populations [52]. Points that possess superior objectives are termed "elite children", and are chosen to persist without alteration into the next generation. These elite children, among others in the population, are then chosen to “breed”, or crossover their genetic material by randomly exchanging variable values in an effort to produce an improved population with better fitness. “Mutation” seen in living populations can also be simulated by randomly changing variable values of individuals in the population. In the context of photomask optimization, the value taken on by a single photomask pixel (for example, X_1 as shown in Fig. 4.8) can be considered a gene, while a collection of genes (X_1 , X_2 , … , X_n) comprises an individual photomask. By generating several different photomasks, a large initial population is formed. The fitness of each individual photomask in the population is evaluated by simulating the resulting fluid flow for a fixed annealing time and calculating the penalized area objective. A handful of the best photomasks, or elite children, are then chosen to persist into the next generation. The remaining non-elite children are then updated through a form of variable recombination to generate a new population (note that the population size does not change from generation to generation).

MATLAB’s built-in GA toolbox was used to carry out the optimization. Because the photomask representation is binary, the variables were constrained to take on values of one or zero. A binary tournament selection function was used along with a crossover function designed to maintain integer variables [53]. The population consisted of 56 individuals and was initialized using square photomasks of sizes ranging from 25x25 μm^2 up to 51x51 μm^2 in 2 μm intervals. The variable domain was restricted to be of size 25x25 μm^2 or greater and was also restricted to be of size 51x51 μm^2 or smaller. This restriction on the variable domain can be seen in Fig. 4.8 and ensured that pixel islands did not form far from the main photomask and also prevented pixel holes from being inserted near the interior of the photomask. Each photomask consisted of 260 variables.

The number of elite children was set to four, meaning that the best four photomasks from the current population were carried over to the subsequent generation without alteration. The crossover fraction was set to unity, which meant that all non-elite children were chosen for crossover and none were chosen for random mutation. The algorithm ran until all individuals in the population were identical. This indicated that genetic crossover had homogenized the population.

S4.6 Convergence Study for Optimized Photomasks

The simulation grid size permitted one grid point per photomask pixel, which allowed for rapid testing of each photomask iteration. This choice of pixel size was sufficient for convergence when using a simple square photomask (as seen in Sec. S4.1 of the Supporting Information) but it may not always be sufficient for convergence when using highly pixelated photomasks.

To understand whether the simulation of pixelated, optimized photomasks had converged, the 1x1 μm^2 simulation grid was refined to produce a 0.5x0.5 μm^2 simulation grid. The concentration profile was modified to account for the finer grid size using simple linear interpolation. Simulations were run at an appropriate constant time step for temporal convergence. Table S4.1 shows the penalized area and pre-etch feature height at the two simulation grid sizes for the optimized photomasks. The absolute, relative percent difference is also given to provide understanding of the convergence quality.

Table S4.1 Comparison of penalized area and pre-etch feature heights using the coarse (1x1 μm^2) and fine (0.5x0.5 μm^2) simulation grid size. The absolute, relative percent difference between the results are provided.

Simulation Conditions	Penalized Area			Pre-Etch Feature Height h_c/h_0		
	1x1 μm^2 grid	0.5x0.5 μm^2 grid	% Diff.	1x1 μm^2 grid	0.5x0.5 μm^2 grid	% Diff.
120°C, $t/t_M = 0.049$	0.0110	0.0118	6.9	1.177	1.178	0.041
120°C, $t/t_M = 0.097$	0.0233	0.0235	0.52	1.665	1.666	0.060
120°C, $t/t_M = 0.16$	0.0240	0.0240	0.13	1.899	1.900	0.043
120°C, $t/t_M = 0.23$	0.0489	0.0500	2.1	1.833	1.835	0.10
120°C, $t/t_M = 0.29$	0.125	0.126	0.33	1.816	1.818	0.10
140°C, $t/t_M = 0.079$	0.0101	0.0106	4.9	1.284	1.286	0.15
140°C, $t/t_M = 0.16$	0.0117	0.0131	11	2.180	2.183	0.16
140°C, $t/t_M = 0.26$	0.0117	0.0154	24	2.433	2.440	0.29
140°C, $t/t_M = 0.37$	0.0288	0.0308	6.7	2.399	2.404	0.24
140°C, $t/t_M = 0.47$	0.122	0.123	0.70	2.422	2.428	0.25

Note that the largest percent differences are observed for the penalized area and not the pre-etch feature height. The penalized area is therefore much more sensitive to the initial concentration profile.

The best case ($t/t_M = 0.16$, $T = 120$°C) displayed a 0.13% absolute, relative difference in penalized area when comparing the coarse and fine grid simulations, which is acceptable; however the worst case ($t/t_M = 0.26$, $T = 140$°C) displayed a 24% absolute, relative difference in penalized area, showing that the 1x1 μm^2 simulation grid was insufficient for convergence in this particular case. To visually inspect what this 24% difference looks like, Fig. S4.6 shows the contours resulting from the coarse and fine grid masks for the conditions $t/t_M = 0.26$ and $T = 140$°C. As can be seen, the contours closely match one another with small differences existing near the corners of the contour. Although the measure of penalized area can be sensitive to the initial grid size, the actual contours sufficiently match one another to maintain confidence in the results and effectiveness of the method.

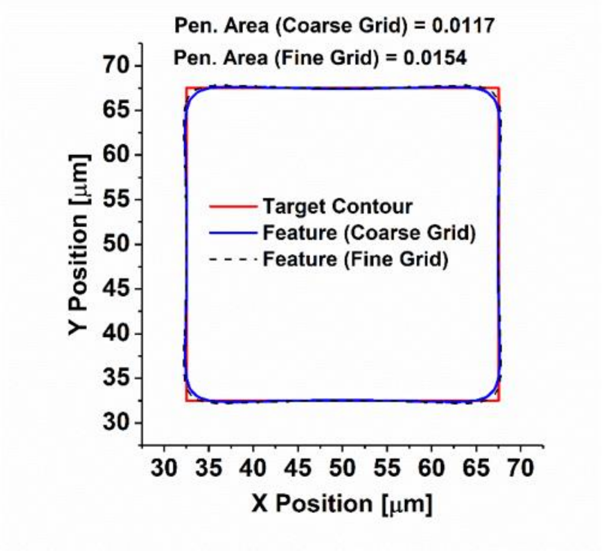

Figure S4.6 Target contour (red) overlaid with feature contours (blue and black) formed using the optimized photomask for conditions t/t_M = 0.26 and T = 140°C. The blue contour is that formed using a coarse, 1x1 μm^2 simulation grid, whereas the black, dashed contour is that formed using a fine 0.5x0.5 μm^2 simulation grid.

S4.7 Optimized photomasks with corresponding feature profiles and contours

The optimization was performed at various fixed annealing times and temperatures. Fig. S4.7 shows the optimized masks obtained using the annealing temperature of 120°C. The resulting feature profiles and after-etch feature contours are also provided. Fig. S4.8 shows the optimized masks obtained using the annealing temperature of 140°C. Again, the resulting feature profiles and after-etch feature contours are also provided.

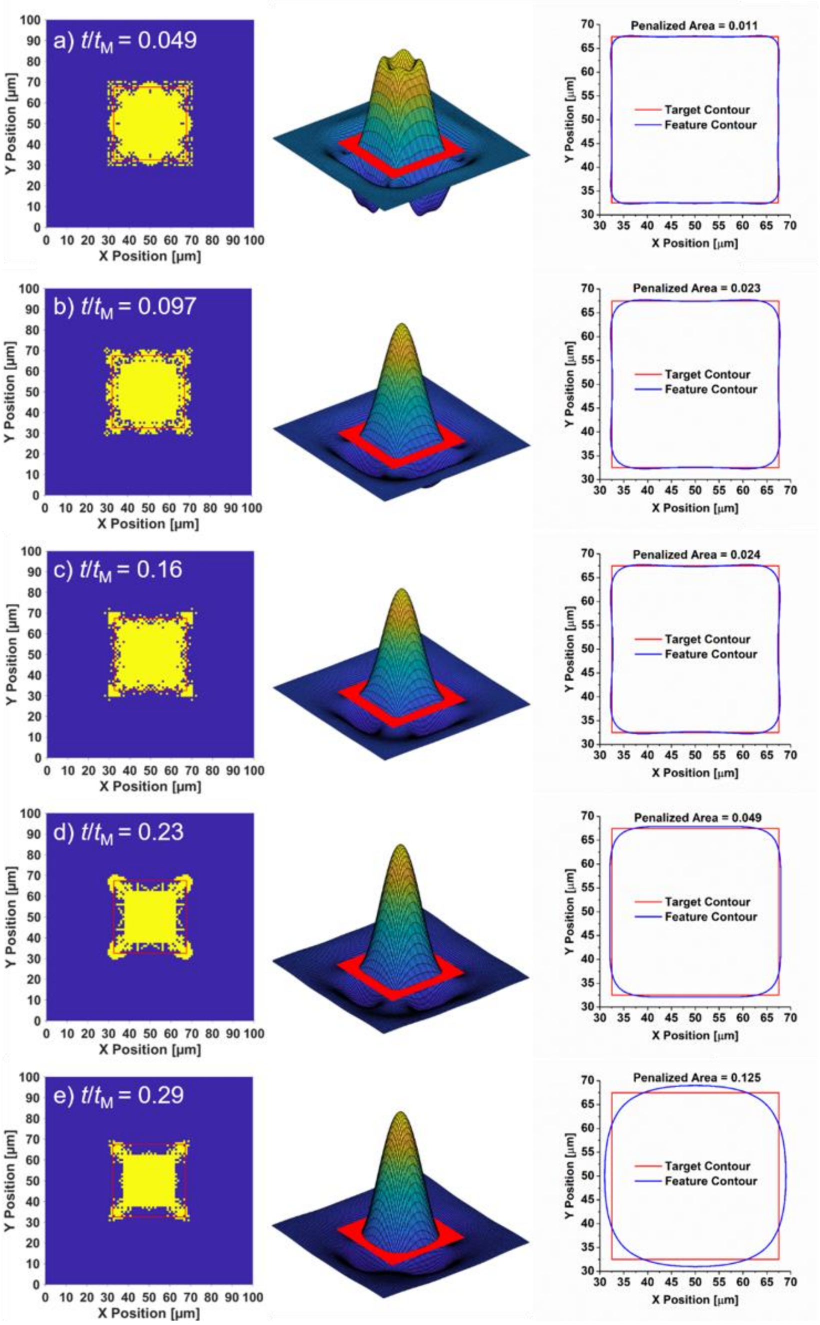

Figure S4.7 Optimized photomasks (left column), resulting feature (middle column), and feature contours (right column) with associated penalized area. Optimizations performed at 120°C for a) $t/t_M = 0.049$, b) $t/t_M = 0.097$, c) $t/t_M = 0.16$, d) $t/t_M = 0.23$, and e) $t/t_M = 0.29$. Note that the feature heights are not to scale not to scale so as to clearly visualize the feature shape.

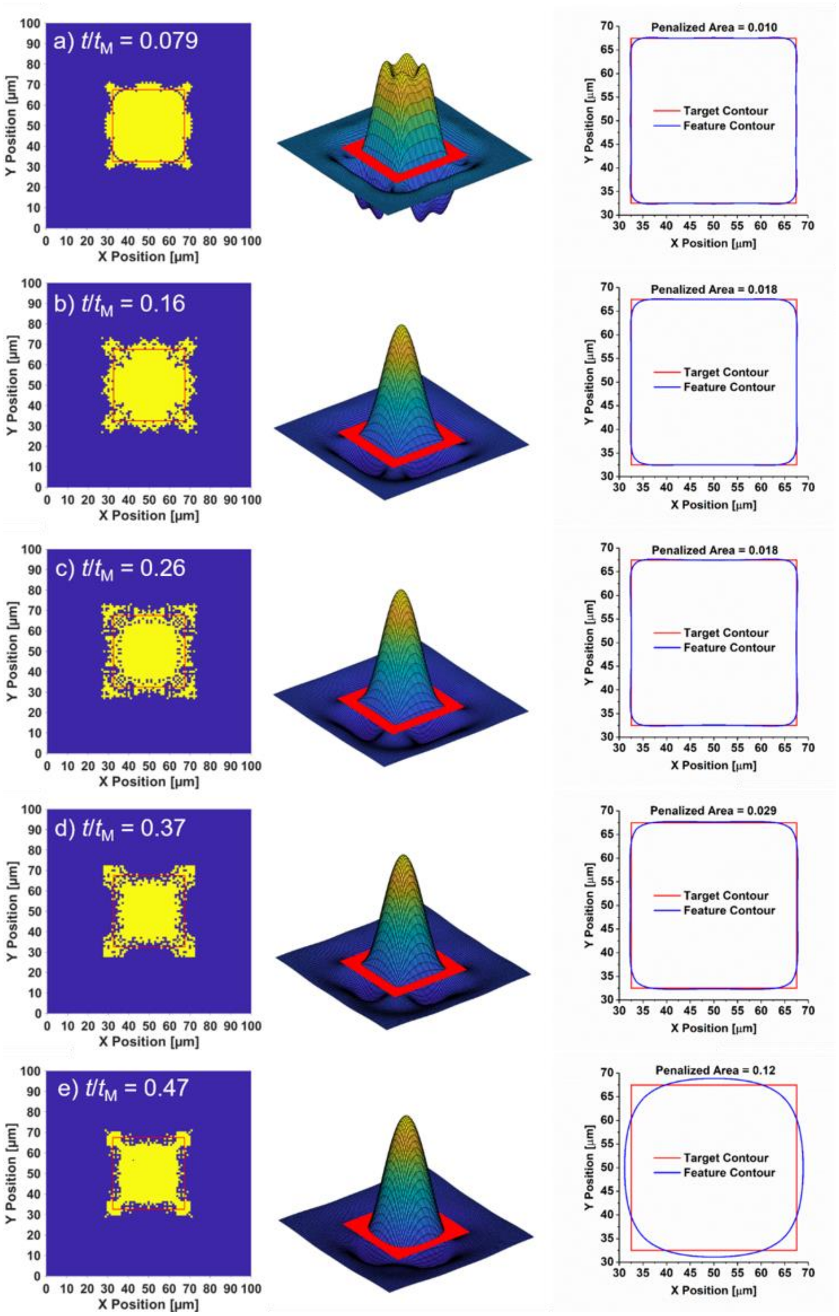

Figure S4.8 Optimized photomasks with overlaid target contour (left column), resulting feature (middle column), and feature contours (right column) with associated penalized area. Optimizations performed at 140°C for a) t/t_M = 0.079, b) t/t_M = 0.16, c) t/t_M = 0.26, d) t/t_M = 0.37, and e) t/t_M = 0.47. Note that the feature heights are not to scale not to scale so as to clearly visualize the feature shape.

S4.8 Effects of Using a Weighted Population Seed

Fig. S4.9 shows the results of an optimization performed at 120°C for $t/t_{\mathrm{M}} = 0.049$ in which the initial population seed was filled with 32 square masks of sizes ranging from 33x33 μm^2 to 47x47 μm^2 in two-micron intervals and 24 additional masks, all of size 35x35 μm. Using this initial population, small changes to the photomask are made by the algorithm and the improvement to the penalized area is not as good compared to that seen in Fig. 4.5. Admittedly, only modest changes are made using the biased initial population and the results are less than ideal; however, the outcome gives direction to future work on how to mitigate the problem of highly pixelated photomasks.

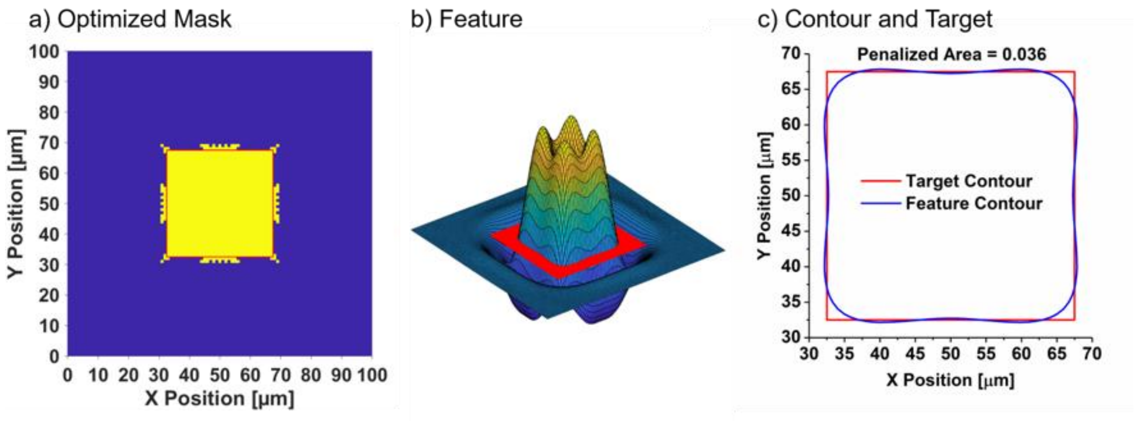

Figure S4.9 a) Optimized photomask and overlaid target contour. b) Resulting feature. c) Feature contour and target. Optimization performed at 120°C for using an initial population seed containing a disproportionate amount of 35x35 μm^2 square photomasks. Note that the feature height is not to scale so as to clearly visualize the feature shape.

Chapter 5: Parameter Estimation and Photoexposure Optimization for a Real Marangoni-driven Pattern System[§]

5.1 INTRODUCTION

Applying topography to polymer thin films has several applications in the electronics, optics, adhesive, and antifouling industries. Several methods and techniques exist for patterning thin films, including optical lithography and imprint lithography. One alternative patterning method that has been explored in recent years is Marangoni-driven patterning (MDP), which harnesses photo-imposed surface tension gradients to generate topography in thin polymer films [1–8,54]. This relatively new patterning technique has potential applications in functional coatings for improving light capture [14], adhesion [15] and antibiofouling properties [16]. Patterns could also be used as an etch barrier for electronics fabrication. On account of its processing advantages, MDP is particularly promising for patterning at the roll-to-roll scale and could be applied in generating flexible functional coatings, electronics and metamaterials. Considering the size scales previously demonstrated by MDP, one particularly promising application is in patterning flexible terahertz spectrum metamaterials [13,44,47].

MDP begins by selectively exposing a photosensitive polymer film of initial thickness, h_0, to UV light using a photomask. Contact photomasks have been used historically for the exposure step, but other maskless exposure techniques could also be used [11]. In the UV exposed regions of the film, a chemical reaction occurs and increases the surface energy. This surface energy profile is dormant and activates upon heating the polymer above its glass transition temperature, which allows the polymer to flow into the regions of higher surface tension. Initially, where the surface tension gradient is sharp, double peaks form but eventually merge into a more sinusoidal topography with central height, h_c. If the polymer is annealed for long enough, diffusion of the surface tension promoter weakens Marangoni forces, allowing capillary forces to replanarize the film. If the polymer is cooled below its glass transition temperature, the topography can be preserved. This topography can then be used as a functional coating or could be used as an etch barrier for pattern transfer.

[§] The author would like to acknowledge and thank Saurabh Usgaonkar and Dr. Chris Ellison from the University of Minnesota for synthesizing the polystyrene sample used in this investigation. The author would also like to acknowledge Dr. Andrei Dolocan for his suggestions regarding optical profilometry.

For etch barrier applications, a breakthrough etch would be required to expose the underlying substrate, which is typical for imprint lithography techniques [39]. Ideally, an anisotropic breakthrough etch would be performed so as to preserve the shape of the pattern. This etch would remove a thickness of film, h_e, and generate features with a final central height of h_f and critical dimension, CD. A process flow for MDP is provided in Fig. 5.1.

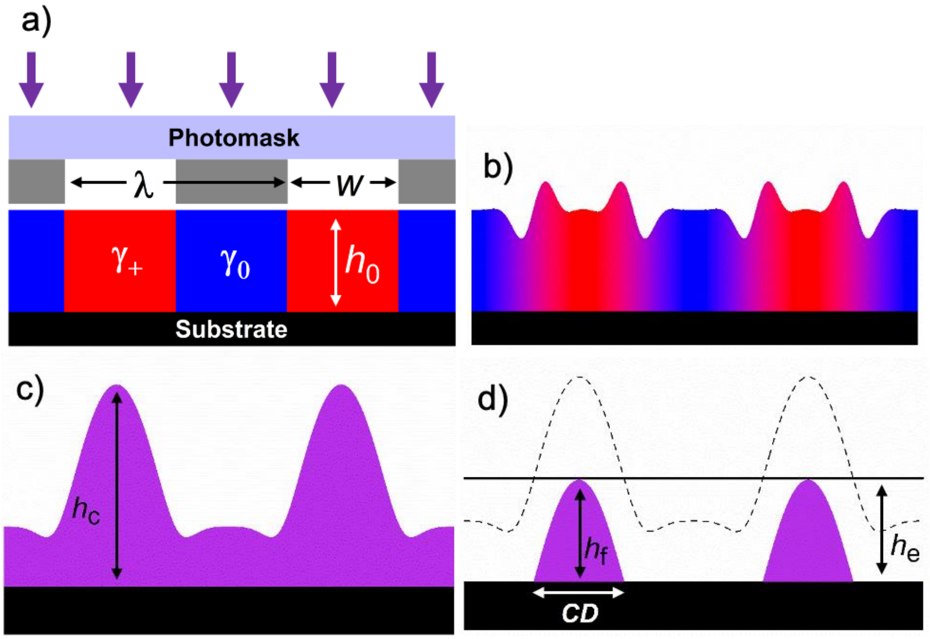

Figure 5.1 Schematic of Marangoni-driven patterning and breakthrough etch. a) Example line-space photomask of periodicity λ and space-width w is used to selectively expose the polymer film of initial height h_0 to UV light. The surface energy or tension in the exposed areas (red) increases due to the photochemical reaction, as indicated by the γ_+ symbol. The surface tension in unexposed areas (blue) remains unchanged as indicated by the γ_0 symbol. b) Annealing the film causes the polymer to flow from the unexposed, lower surface tension regions, into the higher surface tension regions. Note the double peaks that form at short times where the gradient in surface tension is greatest. c) Double peaks merge and the surface tension gradient diffuses as indicated by the solid color. Central feature height is indicated by h_c. d) Anisotropic breakthrough etch of height h_e exposes the underlying substrate, leaving features of height h_f and width CD. Note that the figures are not drawn to scale as the film height is typically hundreds of nanometers while the feature periodicity is typically tens of microns. Figure and caption adapted from S.K. Stanley, C.J. Ellison, R.T. Bonnecaze, Control of Marangoni-driven patterning by an optimized distribution of surface energy, J. Appl. Phys. 127 (2020), with the permission of AIP Publishing.

Controlling the feature shape and critical dimensions is essential in patterning applications, and it has been shown in simulations that MDP suffers from poor shape control [8]. Simulations show that two-dimensional patterns generated using an intuitive square-shaped photomask results in rounded corners, curved edges, and contours that are too small or too large, as shown in Fig. 5.2. Although difficult to disentangle the dominant cause for this poor pattern overlap, it likely results from a combination of detrimental diffusion and capillary forces. Diffusion causes the initially square surface tension profile to blur into a more circular shape and causes the flow to assume a similar, circular shape. Additionally, capillary forces drive the surface to assume a minimal energy conformation, thereby rounding the corners. To compensate for these forces, it is possible to manipulate the exposure and initial surface tension field to generate more favorable flow patterns and better feature-target overlap. In recent simulation-based work, we demonstrated an algorithm for optimizing the film exposure and resulting surface tension gradient for improved pattern formation [8]. This work showed that by judiciously placing exposure "pixels" in the photomask, the fluid flow could be altered to form sharper features more in line with the target contour. Building on that work, here we experimentally determine the effectiveness of the photomask optimization method.

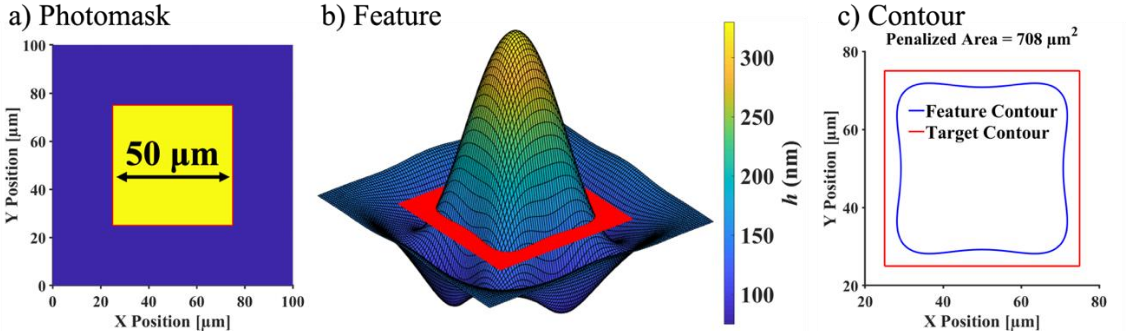

Figure 5.2 Photomask, simulated features, and pattern contours compared to 50x50 µm^2 target. Yellow regions of the photomask are exposed with higher surface tension, whereas dark areas are opaque. The polymer flows towards the center of the exposed, higher surface tension region. Feature profile and contours were taken at an annealing time of 5,000 seconds. The red outline in a) shows the target dimensions. Feature contours are extracted at $h = h_0 = 150$ nm, denoted by the red cut in b). This red cut is for demonstration only and do not represent the dimensions of the target. Note that the features are not drawn to scale, where the pattern pitch is 100 µm and the feature height is in nanometers. Details regarding the simulation will be provided later.

The remainder of the chapter is as follows. For a new polystyrene (PS) system, we determine the polymer properties such as the surface tension difference, viscosity, and diffusivity using a least-squares parameter estimation approach. Using these estimated parameters, optimized photomask patterns are generated using the photomask simulation and optimization algorithm. We then design and purchase an actual photomask that mirrors the simulated/optimized photomask and use it for patterning. These patterns are then characterized and compared to those made using the intuitive photomask geometry and the improvement is quantified.

5.2 EXPERIMENTAL

5.2.1 Materials

Polystyrene was synthesized and the molecular weight was characterized by Saurabh Usgaonkar and Dr. Chris Ellison from the University of Minnesota in a manner similar to that performed by Katzenstein et al. [1]. It was found that M_n ~ 2,100 gm/mol, M_w ~ 2,300 gm/mol and PDI ~ 1.1.

99.9% purity Toluene from Sigma-Aldrich was used as the spin coating solvent. <100> silicon wafers with roughly 2 nm native oxide layers from University Wafer were cleaved into ~1.5 cm square coupons and used as the spin coating substrate.

5.2.2 Methods

PS was dissolved in toluene at roughly 4 wt% PS and spin coated on a ~1.5 cm square coupon of silicon using a Headway Research Inc. PWM spin coater. Spin speeds were adjusted to achieve a target thickness of 150 nm. A post apply bake was performed around 100°C to drive off residual solvent. This and other annealing steps were performed on an IKA© RCT Basic hotplate. The thickness of a given film after baking was measured at several points across the coupon using a J. A. Woolam ellipsometer and the height was then averaged. These average film thicknesses are reported in Table 5.1 as $h_{0\mathrm{Avg}}$ with corresponding standard deviations.

The samples used for parameter estimation of physical properties for the model were patterned using a 5”x5”x0.09” chrome-on-quartz, line-space photomask from Photronics with a pitch of λ = 10 μm or λ = 20 μm. Masks with square and L-shape patterns were designed in the CAD editor, KLayout, and manufactured on a 5”x5”x0.09” chrome-on-quartz blank. The mas was ordered from Photomask Portal. The periodicity of the optimized features was $\lambda = 100$ μm. Masks with square and L-shape patterns were fabricated with a specified CD tolerance of 0.1 μm and a wet etch was prescribed, resulting in slightly rounded pixels with estimated radius of curvature $r_c \approx 0.3$ μm.

The exposure process was performed by contacting the spin-coated substrate to the photomask using a custom vacuum stand and placing a 265 nm Thorlabs LED lamp roughly 3.8 cm above the photomask. The LED current was set to 300 mA and voltage to 5.7 V and the exposure was carried out for 15 minutes at a separation distance of 3.8 cm. In the time between determining the polymer parameters and using the optimized photomask, the polymer appeared to weaken in potency, delivering shorter features for the same 15 minute exposure time. To recover the feature height, it was found that 30 minutes of exposure produced similar peak-to-valley heights to those previously achieved. We therefore used this exposure time of 30 minutes when patterning with the optimized photomask.

It has been shown that upon exposure, the UV light reacts with the polystyrene, dehydrogenating the backbone to form a double bond [1]. This results in the production of a copolymer of polystyrene and poly(phenyl acetylene) (see Fig. 5.3), where the polymer regions containing poly(phenyl acetylene) possess a relatively higher surface tension. It is expected that the photoconversion is small enough to prevent significant crosslinking [1], and owing to the suspected low conversion, the viscosity and diffusivity of the exposed and unexposed polymer are assumed to be practically the same.

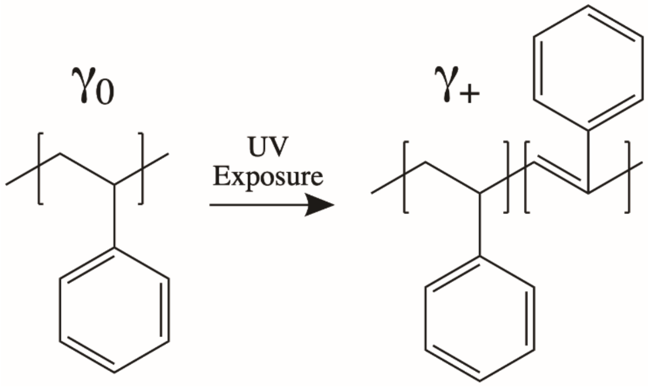

Figure 5.3 Reaction diagram for conversion of polystyrene to poly(phenyl acetylene). UV exposure causes a reaction leading to dehydrogenation of the polymer backbone. The pure polystyrene species imparts a surface tension, γ_0, whereas the exposed polymer, now containing some poly(phenyl acetylene), imparts a higher surface tension, γ_+.

After exposing the samples, they were annealed at the center of the hotplate where the temperature was around 120-121°C. Although the hotplate setpoint was 115°C, we noted a ~5-6°C offset at the center which is why we report an annealing temperature of 120-121°C. We also note that it was important to restart the hotplate when it reached its set point to reset the controller and avoid large temperature fluctuations. The samples were annealed for a given amount of time and then removed onto a room-temperature metal pad for rapid cooling. The resulting line-space topography and some square shapes were characterized using an Asylum Research MFP-3D Origin atomic force microscope (AFM) with the height data taken from the height retrace channel. A roughly -6% height offset was later observed when measuring a calibration grating with 200 nm steps, but we do not suspect this offset greatly affected our results.

Some samples were annealed multiple times to extract the topography at several points in time. The two-dimensional square and L-shaped features were characterized using a Keyence VK-X1100 optical profilometer. Due to the reflective nature of the underlying silicon, Newton’s rings formed which disrupted the measurement capabilities of the profilometer. To overcome this issue, the patterned samples were first coated in roughly 50 nm of aluminum using a Kurt J. Lesker PVD75 e-beam deposition tool. This made the pattern surface reflective and allowed for better imaging.

5.3 CHARACTERIZATION OF POLYMER PROPERTIES

5.3.1 Line-Space Experiments

Before performing the photomask optimization, it was necessary to understand the polymer properties, including the surface tension difference, viscosity, and diffusivity, for the purpose of accurately simulating feature development. The parameters were obtained by performing line-space simulations and experiments and tuning the parameters until good overlap between simulations and experiments was achieved.

The experimentally determined features were obtained by patterning with a 10 μm and 20 μm pitch line-space photomask. Two pitches were used to check that the estimated parameters were consistent. The coupons with 10 μm features were annealed for roughly 1, 2, 4, 6, and 8 minutes, while the 20 μm features were annealed for roughly 3, 6, 15, 30, and 60 minutes. Note that taking the wafer off the hot plate occasionally required a couple of seconds to lift and maneuver to a cooling block. These extra seconds were recorded for accurate modeling, but we report in text the approximate times. Several replicates were run to test sample-to-sample variability. Four separate wafer coupons were patterned using the 10 μm full-pitch patterns and seven separate coupons were patterned for the 20 μm full-pitch patterns, with eleven total samples tested. In one instance, data at t = 8 minutes was not collected and in another instance, data collected at t = 30 minutes was not used for modeling.

For a given coupon, AFM scans were obtained at several points across the wafer at each time point. This process was performed such that each coupon was annealed to the first time point, characterized, and then annealed and characterized again at the next time point. Note that the 10 μm features were annealed for a shorter time because the diffusion time scale and subsequent feature evolution time scale is shorter for more densely packed features. AFM traces of the features were often biased with linear and/or low-frequency noise, which was reduced using a splining technique in postprocessing steps. The film height was then adjusted such that the calculated volume of fluid across the trace was made equal to the starting volume calculated using the average initial film height, $h_{0\mathrm{Avg}}$. This correction was made because the AFM scans measured only the relative film height and not the absolute height from the substrate surface.

The feature profiles were then averaged for each coupon at each time point. Fig. 5.4a shows an example AFM scan of 10 μm pitch patterns and a trace extracted from the scan. Fig. 5.4b shows for a similar 10 μm pitch pattern (Sample 1 in Table 5.1) the average feature profile and standard deviation obtained at t = 70 seconds. This profile was obtained by averaging several traces across the coupon. An optimization algorithm will later be used to tune the physical parameters until the model sufficiently matches the averaged feature profiles.

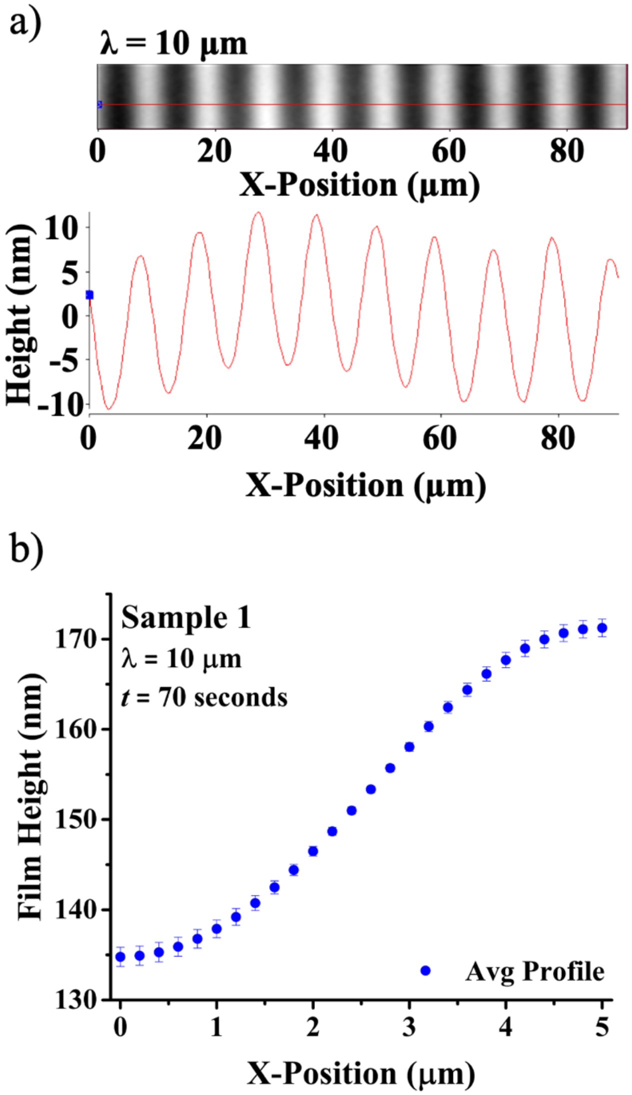

Figure 5.4 a) Example AFM scan and trace of 10 μm pitch line-space pattern. Low-frequency or linear noise that exists in the trace was reduced using a splining technique. Note that the reported height is only relative and had to be adjusted to an absolute scale by ensuring the volume under the curves was consistent with the initial volume calculated from the initial film thickness, $h_{0\mathrm{Avg}}$. b) Averaged traces and ±1 standard deviation for a similar 10 μm pitch line-space pattern (Sample 1 in Table 5.1) taken at t = 70 seconds.

We acknowledge the existence of significant sample-to-sample variability as seen in the peak-to-valley heights shown Fig. 5.5. Note in Fig. 5.5b that the maximum peak-to-valley height varies between roughly 75 nm and 120 nm. Measures were taken to carefully replicate each sample, however, the variability persisted. We speculate that the variation in peak-to-valley height is due to vial-to-vial differences in the dissolved polymer, differences in the lamp power or perhaps poor vacuum contact between mask and substrate, which could lead to variations in exposure dose and alter the strength of the surface tension gradient. To mitigate the effect of sample-to-sample variability in the photomask optimization step, we chose to optimize the photomask using the estimated physical parameters for Sample 8 because it exhibited moderate peak-to-valley heights between extremes. A sensitivity analysis using parameters from other samples that exhibited relatively smaller/larger peak-to-valley heights is provided in Section S5.1 of the Supporting Information. Although the variability did disrupt the square pattern to some degree under certain conditions, the analysis showed that the optimized mask patterns could be resistant to the sample-to-sample variation.

For the 10 μm pitch samples, the decay time scale is very short, with the maximum peak-to-valley height already achieved before/by the first time point. Having no earlier time points causes the parameter estimation problem to be underspecified, resulting in multiple quality solutions for the 10 μm geometry. Fortunately, data for the 20 μm samples was typically sufficient to distinguish between solutions to the parameter estimation problem.

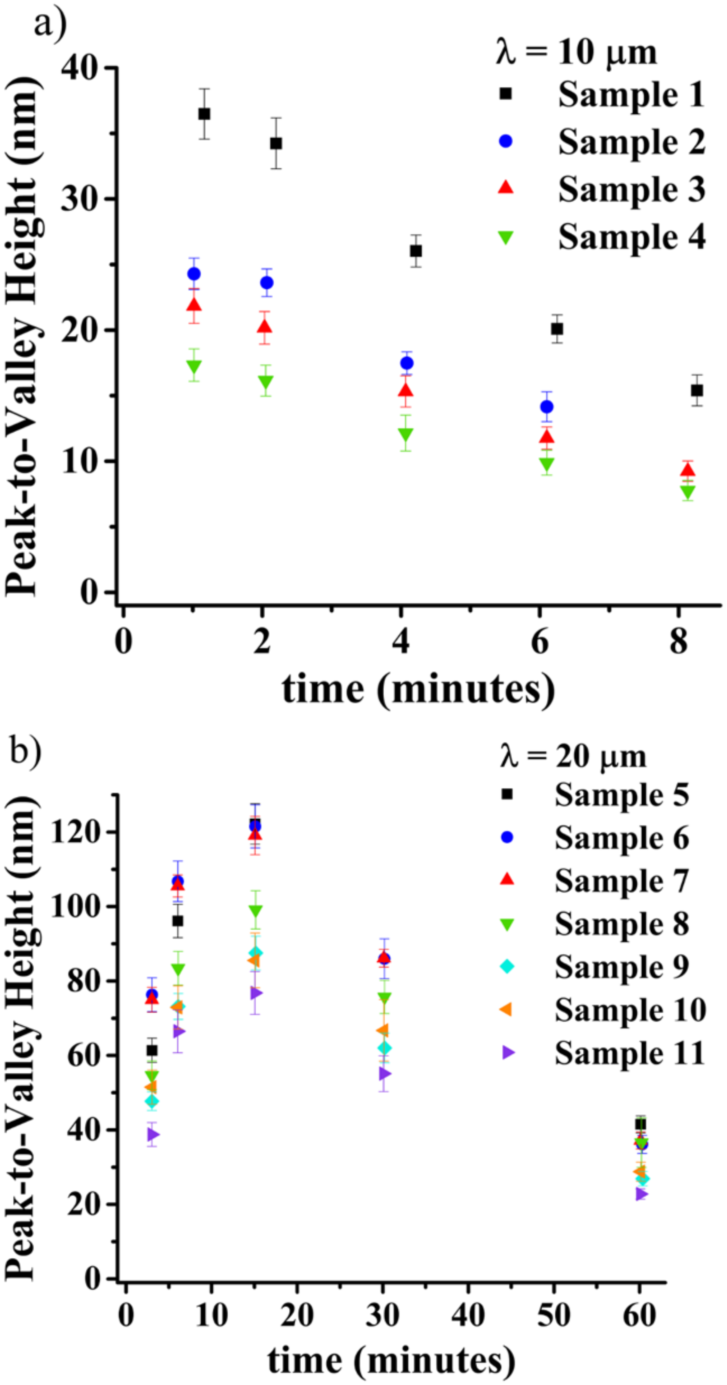

Figure 5.5 Peak-to-valley heights taken from experimental data with ±1 standard deviation. a) Data from 10 μm pitch samples. b) Data from 20 μm pitch samples.

5.3.2 Model for MDP

MDP was simulated as demonstrated previously using the thin film equation [7,8]

$$\frac{\partial h}{\partial t} + \nabla \cdot \left(h \langle \mathbf{u} \rangle \right) = 0, \tag{5.1}$$

which tracks the height, h, of the fluid over time, t. ∇ is the lateral (x, y) gradient operator and $\langle \mathbf{u} \rangle$ is the vertically averaged fluid velocity. $\langle \mathbf{u} \rangle$ is expressed as

$$\langle \mathbf{u} \rangle = \frac{\Delta\Gamma C_0}{2\mu} h \nabla C + \frac{\gamma_0}{3\mu} h^2 \nabla \left(\nabla^2 h \right), \tag{5.2}$$

where the first term accounts for Marangoni-driven flow and the second accounts for capillary pressure-driven flow. Here, C is the mole fraction of converted polystyrene, normalized by the initial conversion, C_0. $\Delta\Gamma$ is the difference in surface tension between pure polystyrene and the poly(phenyl acetylene) species and is modulated by the initial conversion, C_0. γ_0 is the surface tension of the polystyrene component and μ is the polymer viscosity, which is assumed constant. Note that Eq. (5.2) assumes a linear relation between surface tension and concentration, such that $\gamma = \gamma_0 + \Delta\Gamma C_0 C$. It also neglects concentration dependence in the capillary flow term, which is acceptable when the modulated surface tension difference, $\Delta\Gamma C_0$, is small relative to the polymer surface tension, i.e. $\Delta\Gamma C_0/\gamma_0 << 1$. This condition has been shown to be satisfied for previous experiments with polystyrene [7,54].

The convection-diffusion equation is used to track the polymer mole fraction. This equation is expressed as

$$\frac{\partial \left(hC \right)}{\partial t} + \nabla \cdot \left(-Dh \nabla C + \langle \mathbf{u} \rangle hC \right) = 0, \tag{5.3}$$

where hC is the product of the film thickness, h, and normalized mole fraction, C, and D is the polymer diffusivity, which is assumed constant. The first term after the operator accounts for convective transport while the second term accounts for diffusive transport.

The transport equations are nondimensionalized using scalings similar to those in reference [8]: $\bar{h} = h / h_{0\mathrm{Avg}}$, $\bar{\nabla} = \nabla\lambda$, $\overline{\langle\mathbf{u}\rangle} = \langle\mathbf{u}\rangle / \langle\mathbf{u}\rangle_{\mathrm{Mar}} = \langle\mathbf{u}\rangle / \left(h_{0\mathrm{Avg}}\Delta\Gamma C_0 / \mu\lambda\right)$, and $\bar{t} = t / t_{\mathrm{Mar}} = t / \left(\lambda / \langle\mathbf{u}\rangle_{\mathrm{Mar}}\right)$. The nondimensional versions of Eqs. (5.1)-(5.3) are expressed as follows, with bar superscripts dropped for clarity:

$$\frac{\partial h}{\partial t} + \nabla \cdot \left(h\langle\mathbf{u}\rangle\right) = 0, \tag{5.4}$$

$$\langle\mathbf{u}\rangle = \frac{1}{2} h\nabla C + \frac{\kappa}{3} h^2 \nabla\left(\nabla^2 h\right), \tag{5.5}$$

$$\frac{\partial\left(hC\right)}{\partial t} + \nabla \cdot \left(-\frac{1}{Pe} h\nabla C + \langle\mathbf{u}\rangle hC\right) = 0. \tag{5.6}$$

Here, $\kappa = (\gamma_0/\Delta\Gamma C_0)(h_{0\mathrm{Avg}}/\lambda)^2$, which is a ratio of capillary and Marangoni velocity scales, and $Pe = h_{0\mathrm{Avg}}\Delta\Gamma C_0/\mu D$ is the Peclet number, a ratio of Marangoni-driven convective transport to diffusive transport.

For the line-space simulations, the film thickness, h, was initialized to a uniform thickness, $h_{0\mathrm{Avg}}$. $h_{0\mathrm{Avg}} \approx 150$ nm was typical for the several samples shown in Table 5.1. For the two-dimensional photomask optimizations, the initial thickness was set to 150 nm to match the thicknesses targeted in line-space experiments. The actual average thickness in two-dimensional patterning experiments ranged between roughly 146 nm and 157 nm.

For the one-dimensional line-space geometries, the concentration field was initialized using a sharp transition, where the unexposed region possessed a normalized concentration of zero and immediately transitioned to unity in the exposed regions. Two-dimensional concentration fields were initialized in a similar way, where the unexposed regions were assigned a normalized concentration of zero, and exposed “pixels” were assigned a normalized concentration of unity. Because the patterns were periodic, symmetry boundary conditions were implemented. The model was solved using an explicit finite difference method with fourth order derivatives and adaptive time stepping.

For the one-dimensional, line-space simulations, the half-period grid consisted of 26 points. For two-dimensional square and L-shaped simulations, the full-period grid consisted of 100x100 (10,000) points and a grid spacing of 1 μm. After optimizing the photomasks, several simulations were performed again on a finer grid of 200x200 (40,000) points and acceptable conservation and convergence was observed. Values obtained from simulations are reported for the finer, 200x200 grid.

5.3.3 Parameter Estimation Method

The polymer parameters were tuned using a least-square parameter estimation method, which compared the line-space simulation pattern profiles to experimental pattern profiles and modified the unknown physical parameters until sufficient experimental-simulation overlap was achieved. The least-squares objective, *J*, is expressed as

$$J = \frac{1}{mn}\sum_{i=1}^{m}\sum_{j=1}^{n}\left[\frac{h_{\text{Exp}}\left(t_i, x_j\right) - h_{\text{Sim}}\left(t_i, x_j\right)}{2\sigma_{\text{Exp}}\left(t_i, x_j\right)}\right]^2. \tag{5.7}$$

Here, $h_{\mathrm{Exp}}(t_i,x_j)$ and $h_{\mathrm{Sim}}(t_i,x_j)$ are the experimental (average) and simulated film heights, respectively and $\sigma_{\mathrm{Exp}}(t_i,x_j)$ is the standard deviation observed in experiments. Each are evaluated at time i and position j. The difference between experimental and simulated profiles are normalized by the standard deviation. This normalization aids in comparing J in the 10 and 20 μm line-space patterns, which generate different sized features.

With the objective in mind, we now consider the three variable handles used in minimizing the objective. Were none of the parameters known, the variable handles would naturally be t_{Mar}, Pe, and κ. However, embedded in these parameters are $h_{0\mathrm{Avg}}$ and λ, which are both known *a priori*. The average thickness, $h_{0\mathrm{Avg}}$, is determined from ellipsometry, and the pattern pitch, λ, is determined by the photomask. Removing $h_{0\mathrm{Avg}}$ and λ from t_{Mar}, Pe, and κ, the variable handles become

$$t^*_{\mathrm{Mar}} = \frac{\mu}{\Delta\Gamma C_0}, \tag{5.8}$$

$$Pe^* = \frac{\Delta\Gamma C_0}{\mu D}, \tag{5.9}$$

$$\kappa^* = \frac{\gamma_0}{\Delta\Gamma C_0}. \tag{5.10}$$

The optimizer was allowed to manipulate t^*_{Mar}, Pe^*, and κ^* while holding $h_{0\mathrm{Avg}}$ and λ constant. Because experimental data was collected at t = [1,2,4,6,8] minutes or t = [3,6,15,30,60] minutes for the 10 μm and 20 μm pitch line-space patterns, respectively, the simulations collected pattern profiles at those same time points in order to evaluate the objective function, J. In a few instances, experimental data was not available at a particular time point, in which case the simulation did not collect that time point. The objective was minimized using a bounded implementation of the Nelder-Mead method in MATLAB [55], a derivative-free optimization algorithm. Forward simulations that took an extremely long time seemed to be indicative of parameters that poorly fit the data. To avoid excessive computational time, a time cap of typically two minutes on the forward simulation was implemented. (Forward simulations for the optimal parameters took roughly 2-10 seconds to solve.) Furthermore, the optimization was performed from several starting points to provide some assurance that the global optimum and correct parameters had been found.

For each sample, the optimized parameters and objective function are provided in Table 5.1, along with the pattern periodicity, average initial thickness, and maximum measured peak-to-valley height. Table 5.1 also provides values of $\Delta\Gamma C_0$, μ, and D which are calculated assuming γ_0 = 32.2 mN/m, the polystyrene surface tension calculated by Arshad et al. at 120°C [7]. One set of parameters (**bolded** in Table 5.1) stood out as producing generally the smallest objective. We call this the primary parameter set. However, a second, distinct set of parameters (non-bolded in Table 5.1) also showed decent agreement with experiments, which, in several cases, was within the bounds set by the standard deviation. We call this the secondary parameter set. The main question to answer is which parameter set, primary vs. secondary, is correct and should be used as part of the photomask optimization.

For the primary parameter set at λ = 20 μm, J is generally an order of magnitude smaller than the secondary parameter set, suggesting that the primary parameters are correct. However, the objective functions at λ = 10 μm are very similar for both sets of parameters, which is perhaps due to insufficient data at early times for λ = 10 μm. Additional data points could have more fully specified the problem and allowed for more distinct optima at λ = 10 μm.

Fig. 5.6 compares the experimental vs. simulation pattern profiles for Sample 7 and Sample 11 (λ = 20 μm). These two samples are exhibited because they displayed the largest and smallest secondary objectives, respectively for λ = 20 μm. For Sample 7, the secondary objective is large, meaning there is poor overlap in feature profiles when using this parameter set. This can be seen in Fib. 6a at 3 minutes. But at 30 minutes (Fig. 5.6b), both the primary and secondary parameters generate features that overlap well with experiments. For Sample 11 at 3 minutes and 30 minutes (Fig. 5.6c and 5.6d), good overlap is seen for both primary and secondary parameter sets, which makes it difficult to conclude on the correct parameter set.

Table 5.1 also provides the average and standard deviation of each parameter, which is calculated as the average/standard deviation of all the samples. The standard deviation helps characterize the sample-to-sample variability seen in experiments. Note the standard deviation is not a confidence interval. One indicator that the secondary parameters may be incorrect is the large difference between parameters at 10 μm and 20 μm pitch as well as the large standard deviation in the parameters.

We also compare the parameters determined in this work to those parameters determined by Arshad et al. for a similar polystyrene system at 120°C. This comparison is shown in Table 5.1. Note that for the primary parameter set, the diffusivity is very comparable, but the viscosity is roughly and order of magnitude different. The opposite is true for the secondary parameter set, where the viscosity is of a similar magnitude but the diffusivity is an order of magnitude different. Perhaps this is due, in part, to the interchangeability of viscosity and diffusivity in the Peclet number, where $Pe = h_{0\mathrm{Avg}}\Delta\Gamma C_0/\mu D$. Any increase in the viscosity can be compensated for by a commensurate change in D. Also, note that the value of $\Delta\Gamma C_0$ reported by Arshad et al. is larger than the primary parameter set by roughly 3-6 fold. It is possible there was a lower conversion in this study that led to this difference. Despite some evidence that the primary parameters are correct, we have chosen to optimize photomask patterns using both the primary and secondary parameter sets using the estimated physical parameters for Sample 8. This sample was chosen because it exhibited moderate peak-to-valley heights. A type of sensitivity analysis was performed to determine how robust the photomask is when patterning under slightly different conditions. This sensitivity study is provided in section S5.1 of the supporting information.

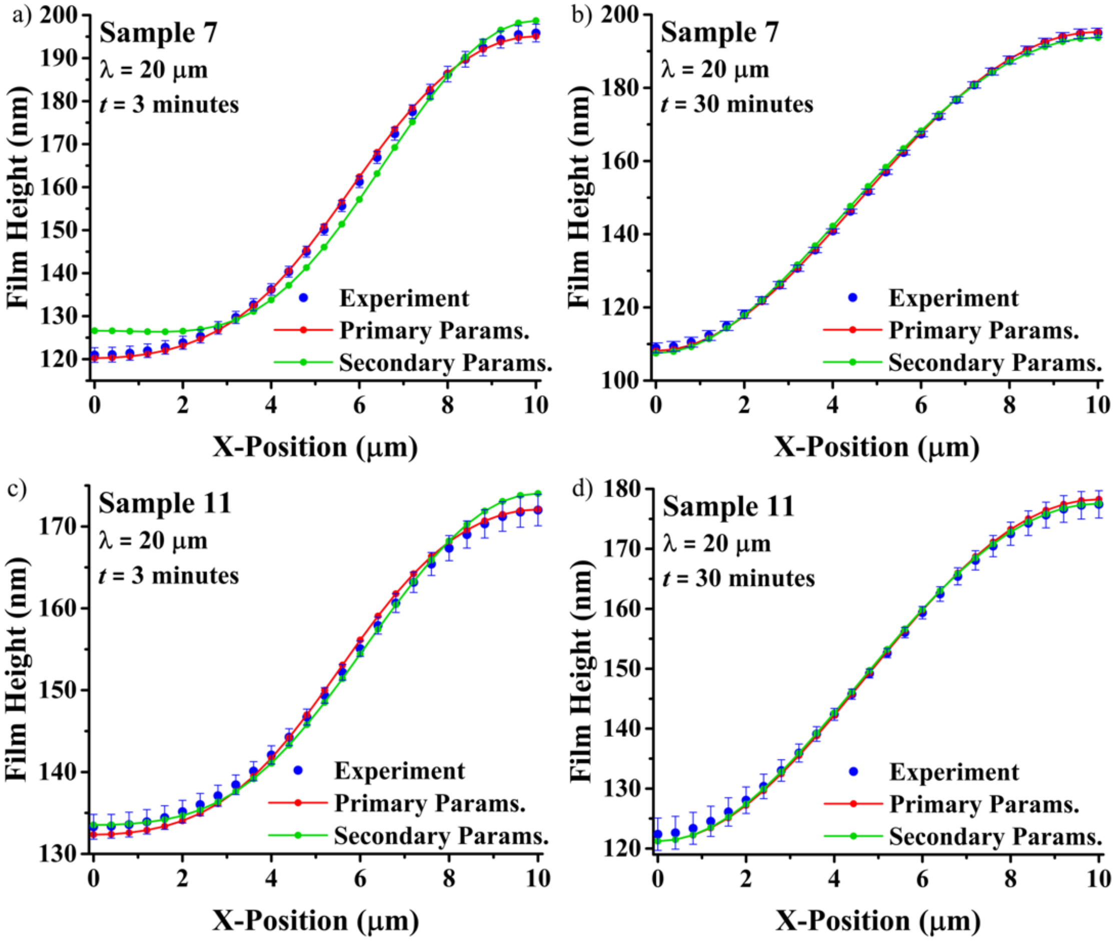

Figure 5.6 Averaged trace and standard deviation for 20 μm pitch line-space patterns with overlaid simulation profiles. Sample 7 experiment and simulation profiles provided at annealing times a) t = 3 minutes and b) t = 30 minutes. Sample 11 experiment and simulation profiles provided at annealing times c) t = 3 minutes and d) t = 30 minutes. In all cases, blue points represent experimental values with ±1 standard deviation, where red and green points represent simulation data obtained using the primary and secondary parameters in Table 5.1, respectively. Note that good overlap is achieved for the primary parameter set in a) where poor overlap is seen for the secondary parameters. In some cases, though, the secondary parameter set performs well, which makes difficult the task of determining which parameter set is correct.

Table 5.1 Optimized parameter summary. Sample numbers and associated feature pitch (λ), average initial height ($h_{0\mathrm{Avg}}$) with sample standard deviation, and maximum recorded average peak-to-valley height (Δh_{Max}) are reported. Optimal objective function, J, is reported along with optimized variable handles t^*_{Mar}, Pe^*, and κ^*, all reported to three digits. The optimal, primary parameters are provided first in **bold** while the generally sub-optimal, secondary parameters are provided in non-bolded text. *Note that Sample 4 possessed a more optimal solution that was inconsistent with the rest of the 5 μm and 10 μm pitch optimal parameters. For this reason, a different local optimum is reported so as not to skew the parameter averages. Values of $\Delta\Gamma C_0$, μ, and D are calculated assuming $\gamma_0 = 32.2$ mN/m as reported in ref. [7]. Average parameter values and corresponding standard deviation of all calculated values are also provided, which helps characterize the sample-to-sample variability seen in experiments. Note that the standard deviation is not a confidence interval. Furthermore, values of $\Delta\Gamma C_0$, μ, and D for a similar polystyrene system as determined in ref. [7] at 120°C are also provided along with the resulting values of t^*_{Mar}, Pe^*, and κ^*.

Sample #	λ (μm)	$h_{0\mathrm{Avg}}$ (Std) (nm)	Δh_{Max} (nm)	J (10^{-2})	t^*_{Mar} (10^6 s/m)	Pe^* (10^7 m^{-1})	κ^* (10^2)	$\Delta\Gamma C_0$ (10^{-2} mN/m)	μ (Pa-s)	D (10^{-15} m^2/s)
1	10	153(2)	36.5	**1.34**	**3.11**	**5.78**	**7.28**	**4.43**	**138**	**5.57**
				3.02	3.29	0.296	0.397	8.12	2670	92.6
2	10	150(.7)	24.3	**3.57**	**4.79**	**3.60**	**10.8**	**2.98**	**143**	**5.80**
				3.88	4.87	0.208	0.634	50.8	2480	42.1
3	10	151(.4)	21.8	**2.45**	**4.39**	**4.11**	**12.7**	**2.54**	**112**	**5.53**
				2.68	4.57	0.176	0.563	57.2	2620	47.9
4*	10	150(.4)	17.3	**2.75**	**4.98**	**3.92**	**16.2**	**1.98**	**98.7**	**5.13**
				2.89	5.29	0.139	0.613	52.5	2780	35.8
5	20	147(.6)	122	**1.3**	**2.88**	**7.08**	**6.52**	**4.94**	**142**	**4.91**
				25.1	3.12	1.66	1.76	1.83	569	103
6	20	158(.4)	122	**1.39**	**2.39**	**9.03**	**6.95**	**4.64**	**111**	**4.64**
				43.1	2.71	1.22	1.14	2.82	765	136
7	20	153(.6)	119	**3.56**	**2.22**	**10.1**	**7.41**	**4.35**	**96.5**	**4.46**
				48.6	2.56	1.28	1.14	2.82	720	153
8	20	148(.2)	99.1	**1.82**	**3.07**	**7.46**	**9.09**	**3.54**	**109**	**4.37**
				13.7	3.39	1.18	1.73	1.86	631	86.9
9	20	153(.2)	87.5	**3.07**	**3.84**	**5.46**	**9.98**	**3.23**	**124**	**4.77**
				13.6	4.03	0.910	1.81	1.78	719	61.5
10	20	149(.9)	85.5	**1.84**	**3.49**	**6.44**	**10.4**	**3.11**	**109**	**4.44**
				14.5	3.62	0.922	1.61	2.00	724	76.2
11	20	150(.5)	76.8	**5.85**	**4.61**	**4.23**	**11.0**	**2.92**	**135**	**5.13**
				8.52	4.70	0.841	2.28	1.41	664	45.2
Avg. (%StDev)	-	-	-	-	**3.61(27)**	**6.11(35)**	**9.85(29)**	**3.51(27)**	**120(14)**	**4.98(10)**
					3.83(24)	0.803(65)	1.24(51)	35.2(62)	1390(71)	80.0(49)
Ref. [7] at 120°C	25	145	106	-	19.9	1.38	2.52	12.8	2550	3.63

5.3.4 Characterizing Patterns Resulting from an Intuitive Photomask

We next present simulation results showing the effects of using an intuitive 50x50 μm^2 square photomask and a 50x25 μm^2 L-shape photomask in patterning features with those same dimensions. The annealing time was set to 5,000 seconds, which was around the time that the quadruple peaks (which form in the case of a square) began to merge for various sized square masks in simulations. The initial film thickness was set to $h_0 = 150$ nm, which is comparable to $h_{0\text{Avg}}$ from the line-space experiments. For the purpose of comparing the feature to the target square or L-shape, a contour of the feature is extracted at $h = h_0$. Doing so simulates the effect of an anisotropic breakthrough etch for pattern transfer applications.

Fig. 5.7a shows the intuitive 50x50 μm^2 square mask and resulting feature and contour. Using the intuitive photomask causes the feature profile to undershoot the target square and resulted in rounded corners and curved edges. To quantify the improvement in pattern-target overlap, the penalized area is calculated, which is a sum of areas that fall within and outside the feature and target contours [8]. More precisely, the penalized area is calculated by summing the area that falls within the target (A_T) but outside the feature and also summing the area that falls within the feature (A_F) but outside the target. These areas can be expressed as

$$A_\text{FT} = \left(A_\text{F} \setminus A_\text{T}\right) \tag{5.11}$$

$$A_\text{TF} = \left(A_\text{T} \setminus A_\text{F}\right) \tag{5.12}$$

$$A_\text{P} = A_\text{FT} \cup A_\text{TF} = A_\text{F} \,\Delta\, A_\text{T} \tag{5.13}$$

Here, A_{FT} is the area within the feature but outside of the target, where A_{TF} is the area within the target but outside of the feature. A_P is the penalized area and is the symmetric difference of A_{FT} and A_{TF}. Smaller penalized areas indicate more square-like feature contours. The penalized area is therefore the objective function we will minimize in the photomask optimization to drive the pattern contour towards the target. Fig. 5.7b shows the results from using an intuitive 50x25 μm L-shape mask. Note that the resulting L-shape is obtuse and conforms poorly to the target. We will attempt to improve this shape contour as well.

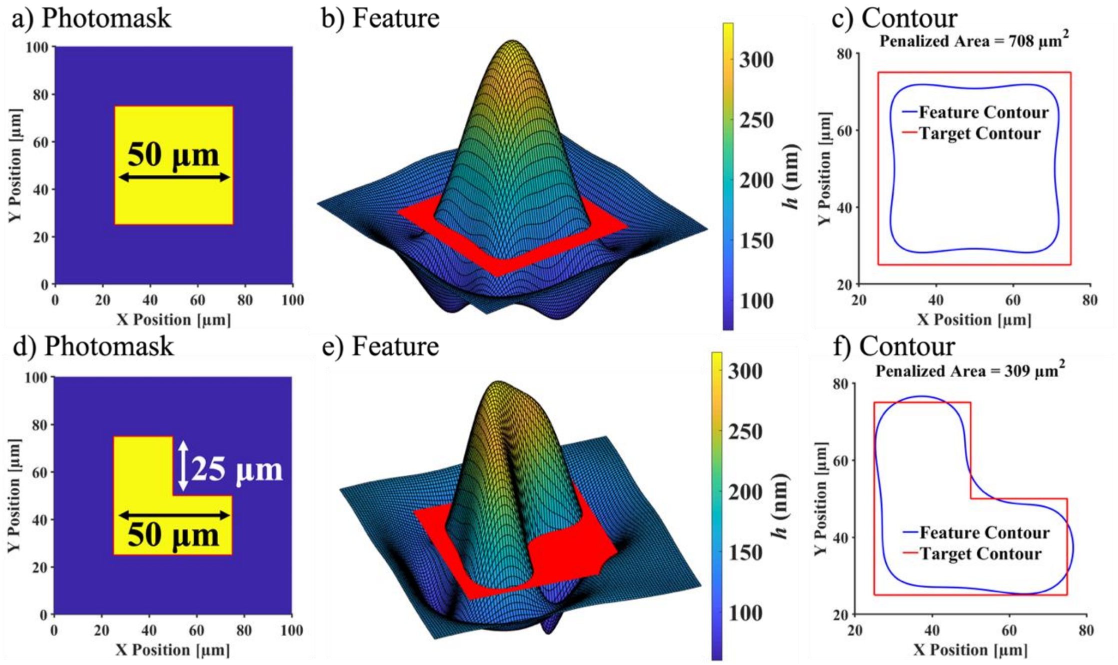

Figure 5.7 Intuitive square and L-shaped photomasks, simulated features, and pattern contours compared to target. a) and d) Photomasks, where yellow regions of the photomask are exposed with higher surface tension and dark areas are opaque. The polymer flows towards the exposed, higher surface tension regions. The red outline shows the target dimensions. b) and e) Feature profile and contours taken at an annealing time of 5,000 seconds. Feature contours are extracted at $h = h_0 = 150$ nm, denoted by the red cut. This red cut is for demonstration only and does not represent the dimensions of the target. Note that the features are not drawn to scale, where the pattern pitch is 100 μm and the feature height is in nanometers. c) and f) Contours extracted at $h = h_0 = 150$ nm compared to target shape.

5.4 OPTIMIZING THE PHOTOMASK

To correct the undershoot and sharpen the corners and edges of the resulting features, we optimized several photomasks in a pixel-by-pixel manner, similar to what was done in prior work [8]. Three different pixel sizes were tested: 1x1 μm^2, 2x2 μm^2, and 4x4 μm^2 pixels. This was done primarily for exposure considerations. As will be shown in simulations, smaller pixels typically offer better control over the simulated pattern shape, but pixels as small as 1x1 μm^2 may pose issues during the exposure step. In ideal contact printing, optical pattern transfer is nearly perfect. Under non-ideal conditions, however, sandwiched particles and other contacting issues can generate a gap between the substrate and mask and distort the exposure pattern, especially in cases where the pixel size is small. For this reason, several photomasks with progressively larger pixel sizes (1x1 μm^2, 2x2 μm^2, and 4x4 μm^2) were optimized.

For the square target patterns, the optimization procedure was carried out twelve times. Each optimized photomask corresponded to a different combination of pixel size, annealing time, and parameter set, where (3 pixel sizes) x (2 parameter sets) x (2 annealing times) = 12 total photomask. To summarize, the three pixel sizes were 1x1 μm^2, 2x2 μm^2, and 4x4 μm^2, the two parameter sets were the Sample 8 primary and secondary parameter sets, and the two annealing times were 5,000 seconds and 10,000 seconds for the primary parameter set, or 6,000 seconds and 12,000 seconds for the secondary parameter set. We also tested the effects of using a larger square photomask on the penalized area, as it was shown in previous work that upsized photomasks can improve the penalized area [8]. Simulations showed that among the different sized photomask seeds, the 58x58 μm^2 square dimensions performed the best and so this one was chosen to test the effect of upsizing.

The 50x25 μm^2 L-shape target patterns were optimized in a similar pixel-by-pixel fashion. Only six total photomasks were optimized for (3 pixel sizes) x (2 parameter sets) x (1 annealing time) = 6 total photomask. Only the short annealing time was used as optimization results for longer times were poor, which can be seen in Section S5.2 of Supporting Information. Note that to reduce the optimization time required for the 1x1 μm^2

pixel L-shape photomasks, a previously optimized 2x2 μm^2 mask was seeded into the genetic algorithm. This led the 1x1 μm^2 pixel masks to resemble the seeded mask and possess several 2x2 μm^2 pixels.

Fig. 5.8 shows the optimized photomasks with 1x1 μm^2 pixels for the square and L-shaped features at the short annealing time. Note that the square photomask is generally larger than the target so as to correct the previous undershoot. Furthermore, the corners have been elongated and the edges bowed outwards to compensate for the corner and edge rounding. These motifs are generally seen in all of the square-shaped photomasks. The L-shape mask, on the other hand, is larger in some areas and carved out in others. These pixel-level corrections had a generally positive effect on the outer regions of the resulting L-shape contour, but the concave, interior corner did not receive the same degree of correction. This highlights the limitation of the method in simultaneously optimizing different pattern structures.

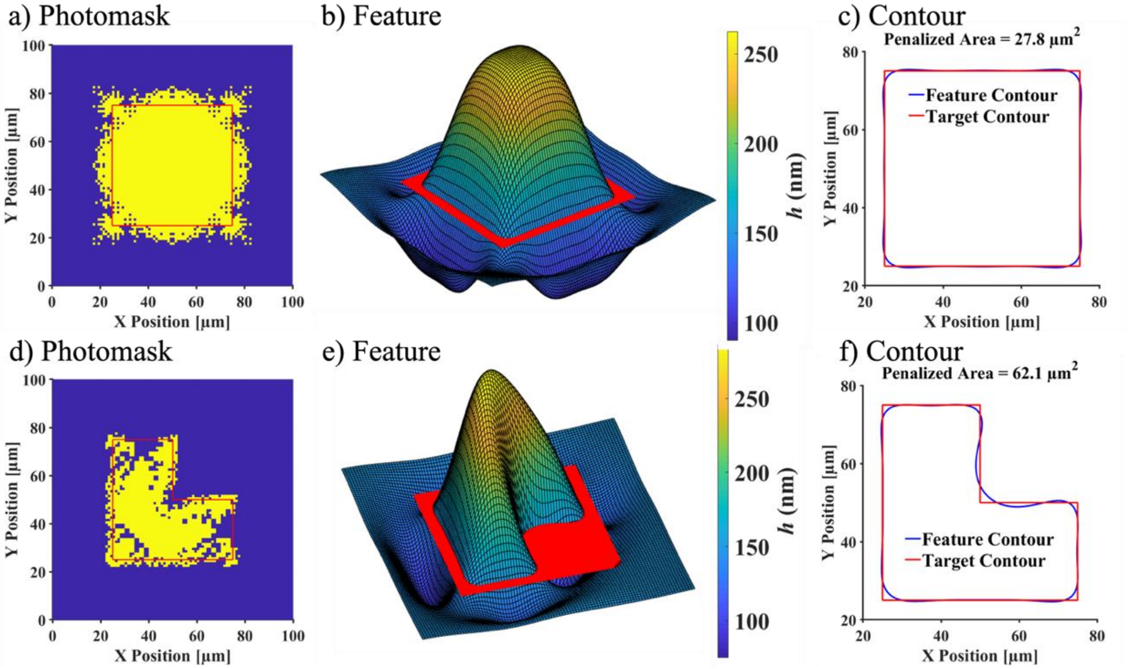

Figure 5.8 Optimized square and L-shaped photomasks with 1x1 μm^2 pixels, simulated features, and pattern contours compared to the corresponding targets. Feature profile and contours taken at an annealing time of 5,000 seconds. The optimized photomasks were obtained through the optimization method using the Sample 8 primary parameters. The red outline in a) and d) shows the target dimensions. The red cut in b) and e) is for demonstration only and does not represent the target dimensions. Feature contours are extracted at $h = h_0 = 150$ nm. Note that the features in b) and e) are not drawn to scale, where the pattern pitch is 100 μm and the feature height is in nanometers.

From simulations, the quality of the resulting patterns was satisfactory and comparable to our previous study. We next examine the effectiveness of the method in practice.

5.5 OPTIMIZED PHOTOMASK EXPERIMENTAL RESULTS

Each optimized pattern was repeated with a 100 μm pitch over a roughly 1x1 cm^2 square field. While several exposure fields were contained in two photomasks (one for square shapes and the other for the L-shapes) we will continue to refer to each exposure field as a photomask. Fig. 5.9 displays several optimized photomasks for the target square shape in their ideal and actual forms as imaged under an optical profilometer in reflection mode. Note that because the chrome is reflective, it appears brighter than the clear regions. Although all photomasks exhibit corner rounding at their pixel edges, it is most evident in the 1x1 μm^2 pixels. This corner rounding is likely due to the isotropic wet etch used in removing chrome regions.

a) 1 μm Pixels

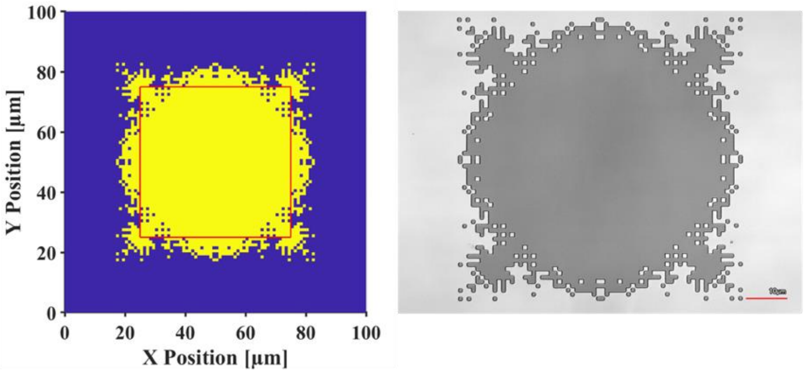

b) 2 μm Pixels

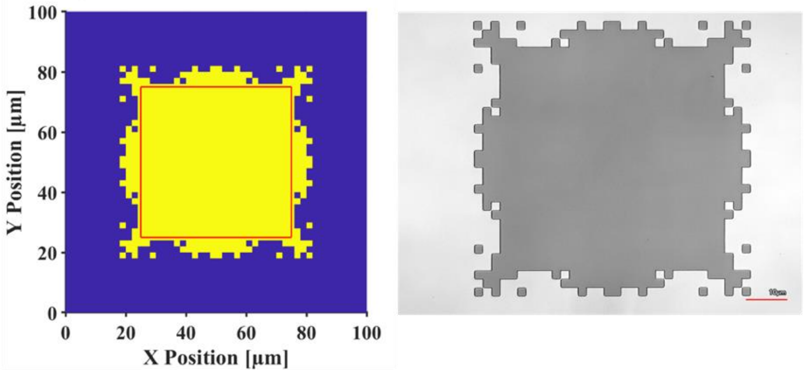

c) 4 μm Pixels

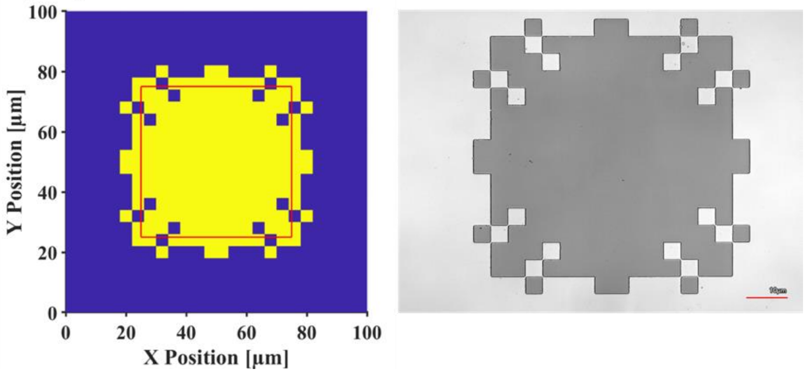

Figure 5.9 Optimized square target photomasks. Ideal (left) and actual photomasks (right) as imaged using an optical microscope. In the ideal images, the yellow regions represent clear, exposed areas, whereas the blue represents opaque areas covered by chrome. In the actual photomask images, the reflective chrome regions are lighter and the darker regions are transparent. The red scalebars in the microscope images correspond to 10 μm. a) Pixels are 1 μm wide. b) Pixels are 2 μm wide. c) Pixels are 4 μm wide.

a) 1 µm Pixels

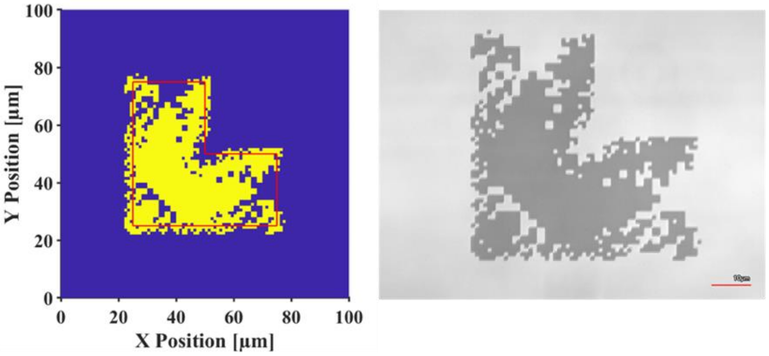

b) 2 µm Pixels

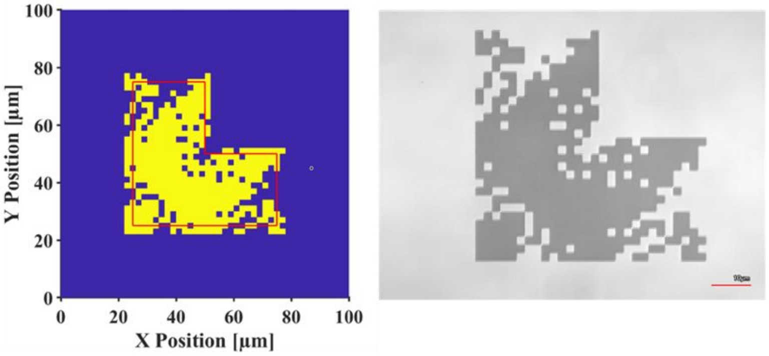

c) 4 µm Pixels

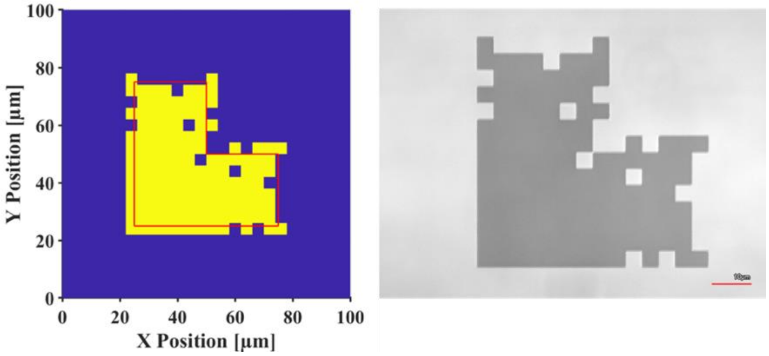

Figure 5.10 Optimized L-shaped target photomasks. Ideal (left) and actual photomasks (right) as imaged using an optical microscope. In the ideal images, the yellow regions represent clear, exposed areas, whereas the blue represents opaque areas covered by chrome. In the actual photomask images, the reflective chrome regions are lighter and the darker regions are transparent. The red scalebars in the microscope images correspond to 10 µm. a) Pixels are 1 µm wide. b) Pixels are 2 µm wide. c) Pixels are 4 µm wide. Note because a photomask with 2 µm wide pixels was seeded into the 1 µm pixel mask optimization, several 2 µm pixels persisted in the 1 µm wide pixel mask.

Samples were patterned using the new photomasks. Optical profilometry was performed using a 50x objective and the scan field of view was roughly 280x210 μm^2. This field of view allowed us to image four features at a time. As a check on the correctness of the optical profilometer, AFM was used to characterize two samples, one possessing short features and the other tall features. The peak-to-valley heights from the AFM measurements were comparable to those obtained from optical profilometry. Furthermore, AFM measurements of coated and uncoated sample halves showed that the metal coating did not significantly affect the peak-to-valley height.

The film topography as obtained from the optical profilometry was leveled using the associated Keyence analysis software. Although the software leveled the samples significantly, it appeared that a modest amount of bias remained in some of the samples. The leveled data was exported to MATLAB for further contour analysis. Ideally, the film contour would be taken at the initial film thickness, h_0. However, optical profilometry provides only relative film heights, and does not directly provide the absolute film thickness. Because of this, the film height used for contouring was estimated by first averaging the height near the connected square corners which were expected from simulations to change by less than roughly 15 nm in the flow process. This average height was then adjusted by the model-predicted height change at the corner and then this adjusted height was used to contour the feature. The target and simulated pattern contours were roughly centered over the extracted contours for comparison. The actual penalized area was calculated for the four features captured in the field of view. Using the Keyence software, several points along bisecting traces of the features were used to measure and average the peak-to-valley heights. In rare cases, features appeared to possess defects along the trace, in which case the peak-to-valley information was not collected at those points. The peak-to-valley height was also obtained in simulations from bisecting traces of the feature.

5.5.1 Square Shapes Results

Fig. 5.11 shows the pattern height for experiments performed with the 50x50 μm^2 square mask, the 58x58 μm^2 upsized square mask and the optimized mask with 1x1 μm^2 pixels. The annealing time for these samples was roughly 5,000 seconds. The associated target contours (dashed black), simulated contours (solid black), and actual pattern contours (solid red) are overlaid on top of the height plot. The simulated contours here were generated using the primary parameters. Fig. 5.11 shows that, for the most part, there is good agreement between the simulated and actual contours. The intuitive, 50x50 μm^2 squares produce significant rounding and it undershoots the target. By upsizing the photomask to 58x58 μm^2, the feature grows closer to the target, but is still severely rounded. The patterns resulting from the optimized photomask, however, conform much better to the target, with much flatter edges. This strongly suggests the optimization was successful. Figs. S5.4-S5.7 in the Supporting information show the full collection of results for the 50x50 μm^2 photomask and optimized photomasks. To quantify the effectiveness of the method, the penalized area for each sample was calculated and averaged and is reported in Table 5.2. Note that the bottom right feature contour in most of the images was typically smaller than the rest of contours and was therefore neglected in averaging the penalized area for each sample. This observed difference is likely due to the profilometer and not the samples themselves.

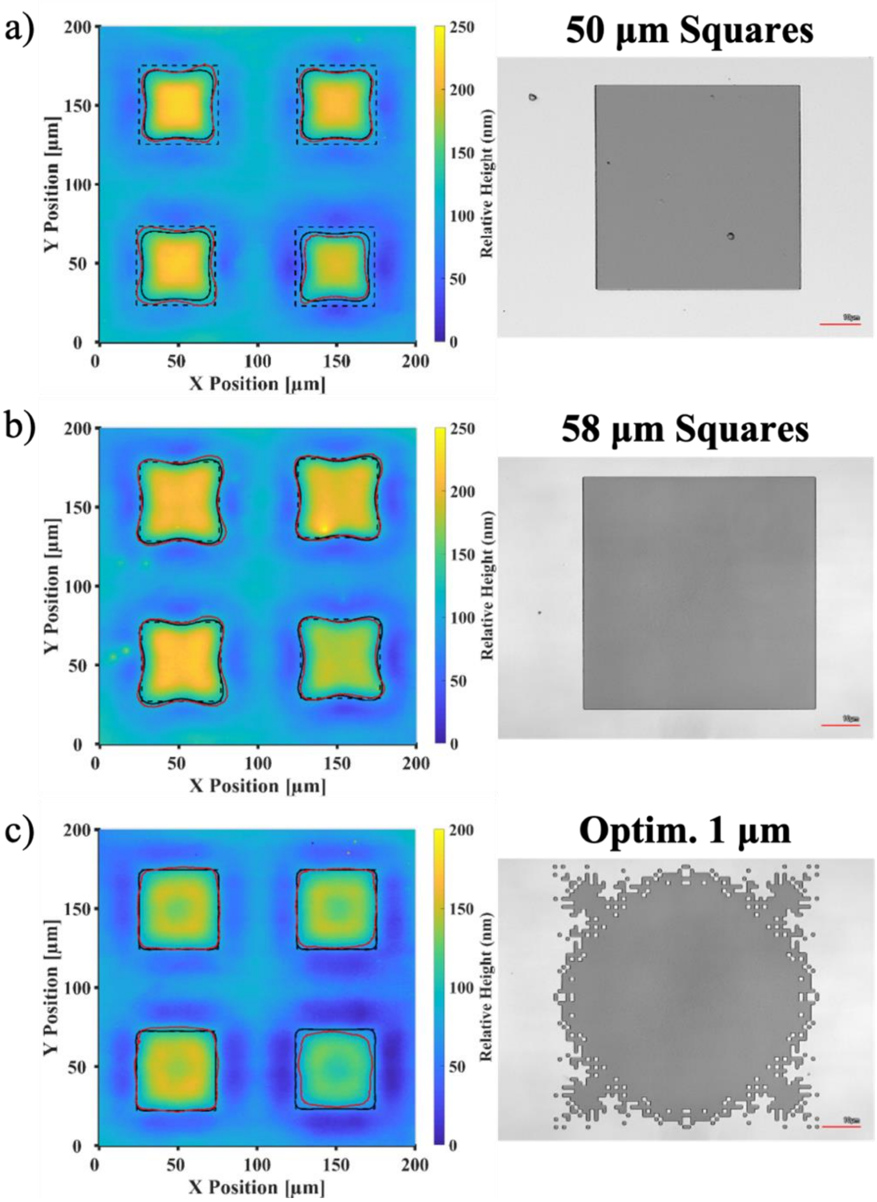

Figure 5.11 Feature height plots (left) and associated photomask pattern (right) used in generating the feature. Results shown are for the a) 50x50 μm^2 square mask, b) 58x58 μm^2 square mask, and the c) optimized mask with 1x1 μm^2 pixels. Samples were annealed for roughly 5,000 seconds. Actual feature contours are shown in red. Target (dashed black) and simulated (solid black) contours were roughly centered around the actual contours. The simulated contours here were obtained using the primary parameter set. The red scale bars in photomask images correspond to 10 μm. Note that point defects were occasionally present that may fall below or above the manually set color bar limits.

Table 5.2 Penalized area and peak-to-valley height data summary for the square target experiments. Standard deviations are provided in parenthesis. The penalized area was averaged for only three of the four squares, excluding the bottom right contour because it was typically smaller than the others. [*]The optimization for the primary, 10,000 second anneal, 1x1 μm^2 photomask was terminated early after sufficient improvement in the penalized area had been achieved. [†]Penalized area metrics obtained from only two shapes rather than the usual three so as to exclude a very misshaped pattern.

Parameter Set	Annealing Time (s)	Pixel Width (μm)	Predicted A_P (μm^2)	Average A_P Min. A_P (μm^2)	Predicted Δh (nm)	Average Δh (nm)
Primary	5,000	50 μm square	708	484(146) 317	235	158(8.6)
Primary	5,000	58 μm square	190	259(40) 213	175	148(9.5)
Primary	5,000	1	27.8	187(27) 152	161	109(8.0)
Primary	5,000	2	23.0	207(30) 175	160	134(6.7)
Primary	5,000	4	59.6	165(31) 135	167	129(9.6)
Primary	10,000	50 μm square	752	853(35) 822	325	298(6.3)
Primary	10,000	1	23.6[*]	160(30) 131	302	232(11)
Primary	10,000	2	23.6	440(102) 324	296	192(14)
Primary	10,000	4	43.4	164(52) 120	305	286(9.1)
Secondary	6,000	50 μm square	331	829(119) 747	140	241(14)
Secondary	6,000	1	27.7	619(37) 577	114	167(8.1)
Secondary	6,000	2	27.4	467(106) 378	113	213(8.5)
Secondary	6,000	4	54.6	372(33)[†] 349	114	203(12)
Secondary	12,000	50 μm square	367	895(79) 812	211	309(9.8)
Secondary	12,000	1	31.0	502(113) 392	186	272(11)
Secondary	12,000	2	65.6	550(32) 517	199	343(8.8)
Secondary	12,000	4	66.2	773(52) 716	199	344(10)

Fig. 5.12 compares the penalized area for the various photomasks and highlights the effect of changing the pixel size and parameter set. Overall, the optimization was clearly effective

at reducing the penalized area. However, the data generally show that pixel size does not impact the quality of the shape. Although the smaller pixel sizes performed slightly better in simulations, experimental and metrology limitations appear to negate the gains that come from controlling the mask at such fine pixel resolutions.

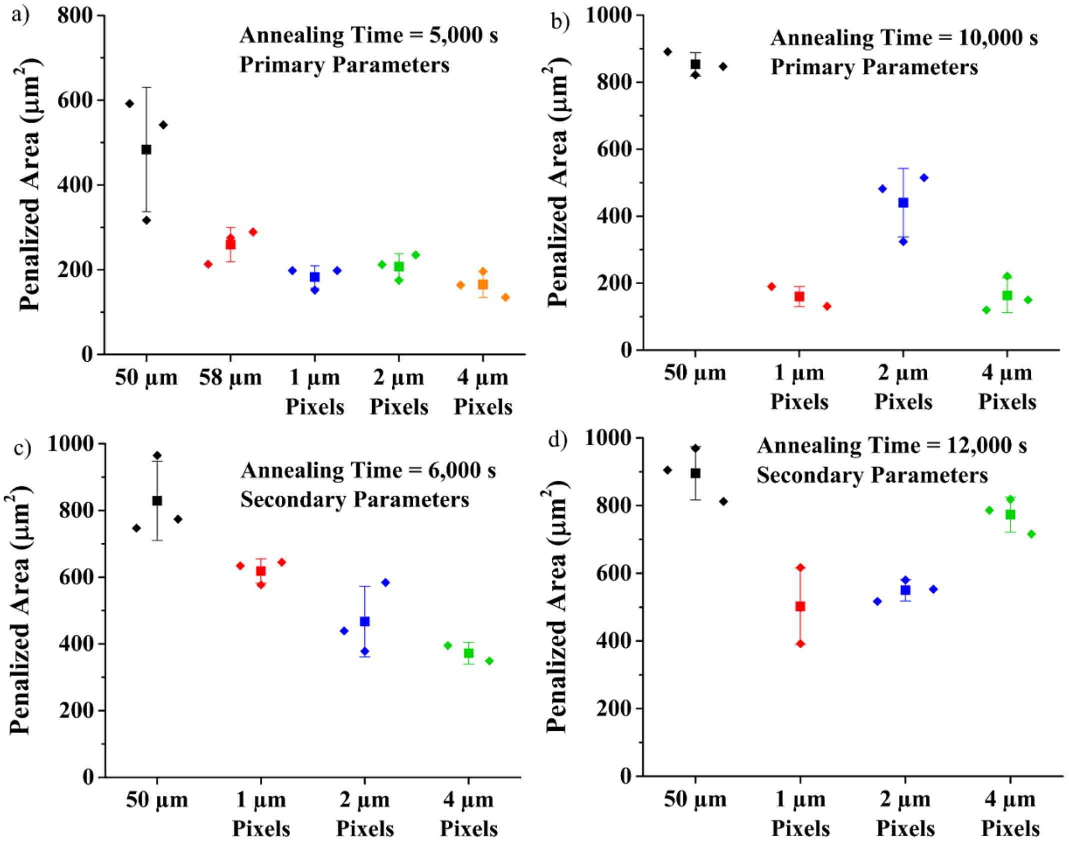

Figure 5.12 Comparison of penalized areas for the different square target photomasks. The square represents the average value bounded by ±1 standard deviation. In diamonds are the measured values for the corresponding photomasks.

The photomask optimization algorithm was clearly successful at lowering the penalized area, but from Table 5.2, it can be seen that the experimental penalized area values are still larger than the predicted values from simulation. This discrepancy is perhaps, in part, due to the sensitivity of the measurement. Fig. 5.11c shows that although the contours visibly conform closely to the simulated and target contours, small overlap errors result in a 7-fold difference in penalized area when compared to the simulated values. These overlap errors are likely due to minor leveling issues or defects that negatively impacted the flow. Fig. S5.1 in the Supporting Information also showed that visibly small changes in the feature contour can result in large changes in the penalized area. This sensitivity in the measurement shows that although the penalized area is a good single objective for optimizing the photomask, other metrics may be necessary when comparing features in experiments. Note that the 58x58 μm^2 mask resulted in a penalized area comparable to that of the optimized photomasks, but is clearly inferior due to the corner rounding and curved edges still present. To further distinguish the feature quality, one might use the metric of circularity [56], which is defined as

$$\text{Circularity} = \frac{P^2}{4\pi A} \tag{5.14}$$

where P is the perimeter of the contour and A is the area of the contour. For a perfect circle, the circularity is unity and different shapes take on other unique values. A perfect square, for instance, has a circularity of 1.273. To test whether the circularity could be used as a distinguishing metric, the mean circularity of the contours in Fig. 5.11 was calculated (excluding the lower right squares). The mean circularity produced by the photomasks is as follows: 50x50 μm^2 = 1.386, 58x58 μm^2 = 1.366, Optimized 1 μm = 1.265. The mean circularity of the pattern generated by the optimized mask comes much closer to the circularity of a perfect square of 1.273 and is clearly distinguished from the circularity of

1.366 generated by the 58x58 μm^2 mask. This shows that the circularity may serve as a second measure of pattern quality when faced with experimental and metrology limitations.

We lastly inspect the peak-to-valley height values listed in Table 5.2. From the table, it can be seen that the feature height typically worsened for the expanded and optimized masks relative to the 50x50 μm^2 mask patterns. This is in line with predictions made in our prior work [8]. Some of the patterns using the secondary parameter set at 12,000 seconds of annealing time were an exception to this trend, where the feature height increased by roughly 30 nm. This may be due to the variability in peak-to-valley height observed earlier or may be due to the possibility that the secondary parameter set is not correct. As a measure of which parameter set is correct, we plot in Fig. 5.13 the predicted and actual peak-to-valley height of the pattern generated by the 50x50 μm^2 square pattern. To account for the sample-to-sample variability seen earlier, we plot upper and lower bounds generated by simulating feature evolution using the Sample 5 and Sample 11 parameter sets, where sample 5 generated the largest Δh in experiments and sample 11 generated the smallest Δh in experiments. Sample 8 results are shown as a dashed line, and was included because its parameters were used in the optimization and provided a moderate Δh value. Note in Fig. 5.13 that the experimental Δh values fall mainly within the bounds set by the primary parameter set, suggesting that the primary parameters are correct.

We note that the penalized area for both the primary and secondary parameters was significantly reduced by the optimization. This suggests that the exact parameters may not need to be known with extreme precision, as extending the corners, and pulling out the edges of the mask may have been the most important factors in improving the feature-target overlap. This is not to say that the process cannot be improved with better parameter estimates. Under better clean room and exposure conditions and with improved metrology capabilities, the effect of more precise parameter estimates will be clearer.

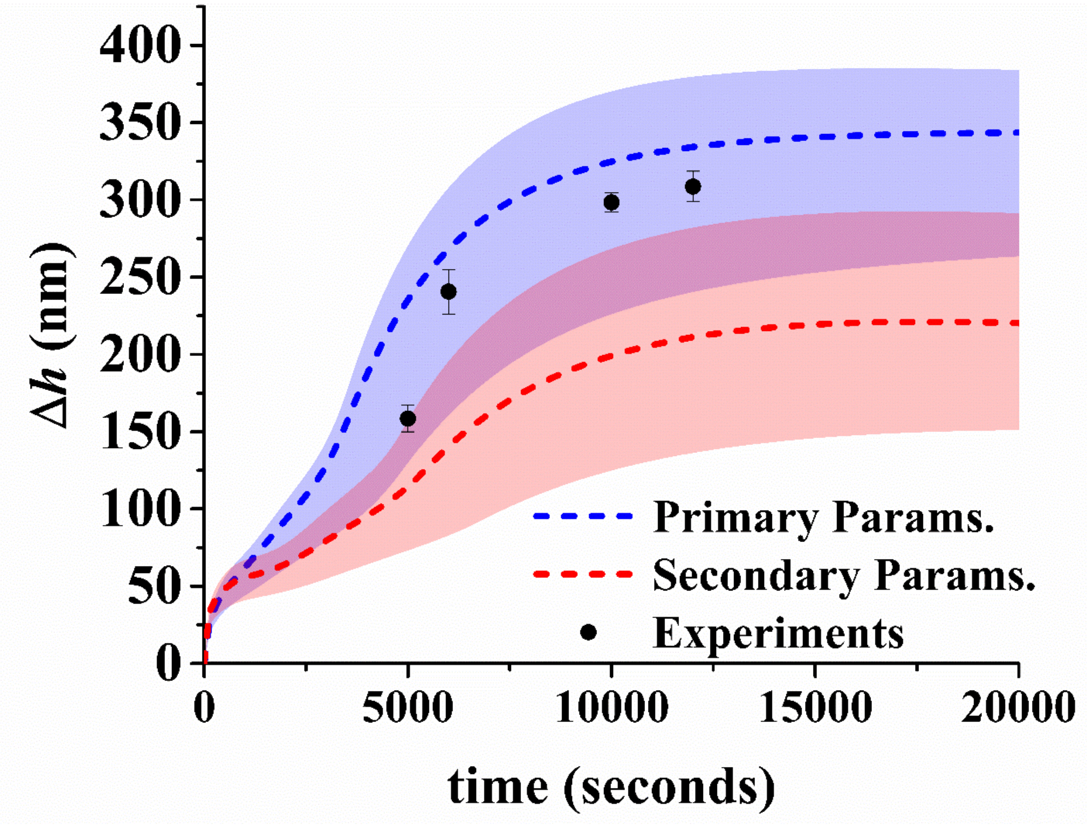

Figure 5.13 Peak-to-valley height over time (Δ*h*) for a 50x50 μm^2 square feature as predicted using the primary and secondary parameters. The dashed lines correspond to the Δ*h* predicted using the sample 8 parameters, whereas the upper and lower bounds correspond to the Δ*h* predicted using the sample 5 and sample 11 parameters, respectively. These upper and lower bounds help account for the sample-to-sample variability seen in Fig. 5.5. Experimental Δ*h* values for the 50x50 μm^2 square photomask are overlaid (see Table 5.2). These values fall mainly within the intervals set by the primary parameters, suggesting that the primary parameters are correct.

5.5.2 L-Shapes

As was done for the squares, Fig. 5.14 shows the pattern height for experiments performed with the 50x25 μm^2 L-shape mask and the optimized mask with 1 μm wide pixels. For the most part, good agreement is seen between the simulated and actual contours. The intuitive, 50x25 μm^2 L-shape performed as expected, producing obtuse L-shapes with rounded corners and edges. And the patterns resulting from the optimized photomask conform better to the target with flatter edges. Figs. S5.8 and S5.9 in the Supporting information show the full collection of results for the 50x25 μm^2 L-shape photomask and optimized photomasks. Again, to quantify the effectiveness of the method, the penalized area for each sample was calculated and averaged and is reported in Table 5.3. The bottom right feature contour in most of the images was again typically smaller than the rest of the contours and was therefore neglected in averaging the penalized area for each sample. The simulated penalized area is also reported. Table 3 also provides information regarding the simulated and measured peak-to-valley height (Δh). The peak-to-valley height here was typically measured using all four features except for one case in which only three were used due to what appeared to be a defect.

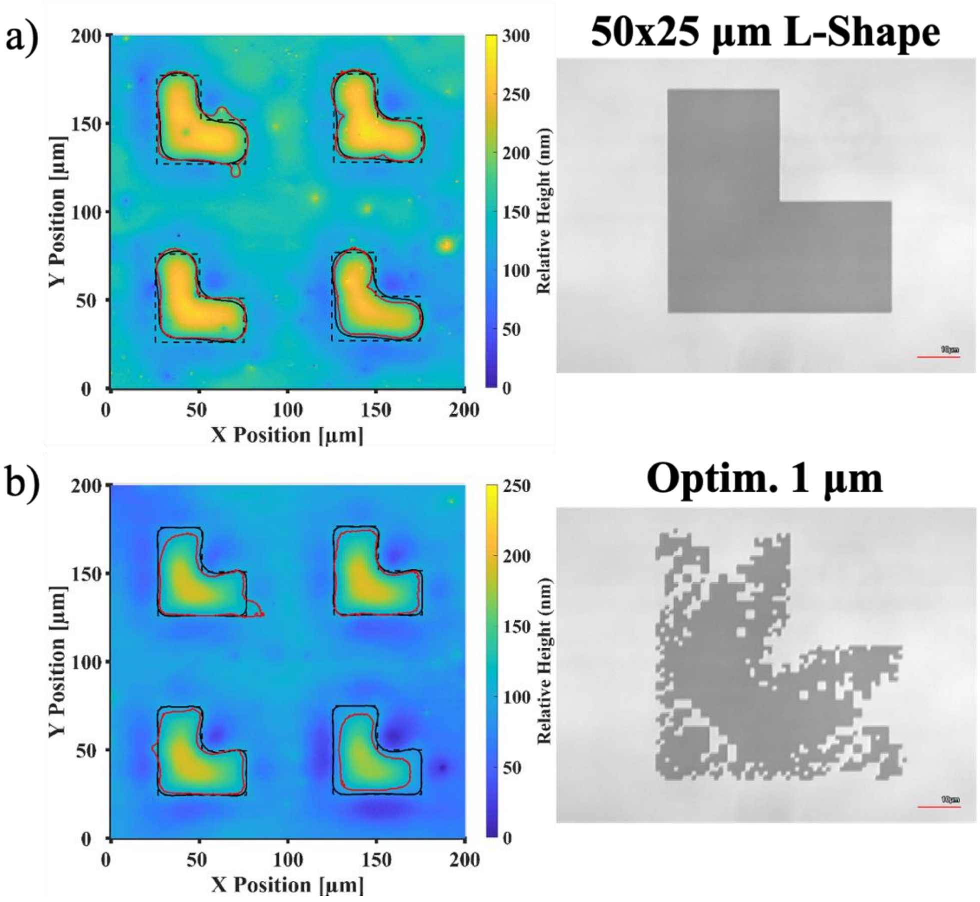

Figure 5.14 Feature height plots (left) and associated photomask pattern (right) used in generating the feature. Results shown are for the a) 50x25 µm^2 L-shape mask and b) optimized mask with 1x1 µm^2 pixels. Samples were annealed for roughly 5,000 seconds. Actual feature contours are shown in red. Target (dashed black) and simulated (solid black) contours were roughly centered around the actual contours. The simulated contours here were obtained using the primary parameter set. The red scale bars in photomask images correspond to 10 µm. Note that point defects were occasionally present that may fall below or above the color bar limits.

Table 5.3 Penalized area and peak-to-valley height data summary for the L-shape target experiments. Standard deviations are provided in parenthesis. The penalized area was averaged for only three of the four shapes, excluding the bottom right contour because it was typically smaller than the others. [*]Δh measured using only three of the four features. [†]Penalized area metrics obtained from only two shapes rather than the usual three so as to exclude a very misshaped pattern.

Parameter Set	Annealing Time (s)	Pixel Width (μm)	Predicted A_P (μm^2)	Avg. A_P Min. A_P (μm^2)	Predicted Δh (nm)	Measured Δh (nm)
Primary	5,000	50x25 μm L shape	310	350(16)[*] 331	244	200(6.1)
Primary	5,000	1	62.1	331(74) 278	205	151(15)
Primary	5,000	2	50.5	345(104) 244	205	162(8.4)
Primary	5,000	4	91.9	211(58) 170	225	161(7.3)
Secondary	6,000	50x25 μm L shape	198	347(75)[†] 294	164	221(13)
Secondary	6,000	1	61.0	578(250) 322	147	216(7.2)
Secondary	6,000	2	69.0	585(70) 504	147	160(9.6)
Secondary	6,000	4	87.9	409(147) 310	158	218(9.5)

For the L-shapes here, the penalized area was not significantly reduced in experiments despite the visible improvement seen in Fig. 5.14. It appears that small pattern defects resulted in large deviations in penalized area as before seen in the square shapes. Fig. 5.15 compares the penalized area for the various photomasks. Again, the data generally show that pixel size does not impact the quality of the shape. In this case, it appears that photomasks optimized using the primary parameter set perform much better than the secondary parameter set. This further suggests the primary parameter set is correct.

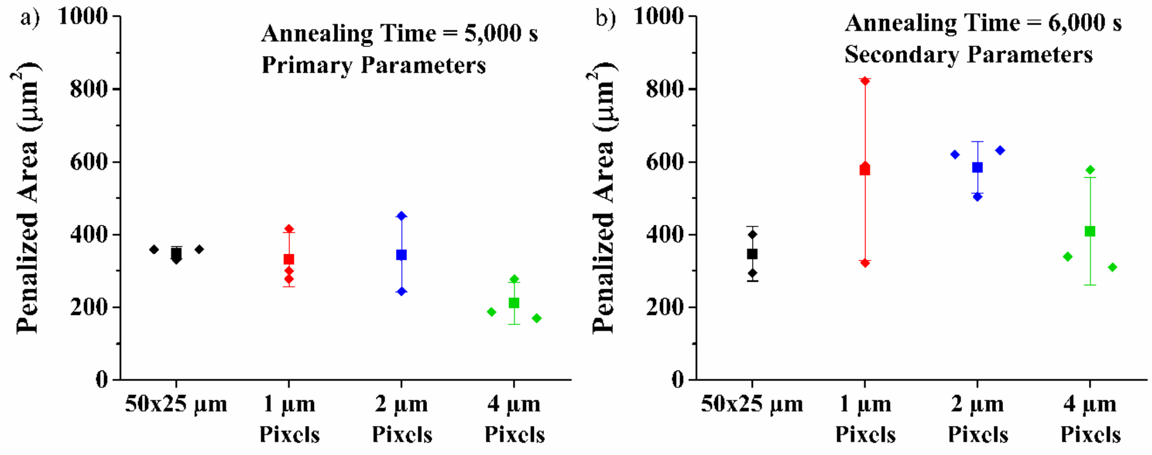

Figure 5.15 Comparison of penalized areas for the different L-shape target photomasks. The square represents the average value bounded by ±1 standard deviation. In diamonds are the measured values for the corresponding photomasks.

5.6 CONCLUSION

In this work, we experimentally evaluated the effectiveness of the photomask optimization algorithm developed previously [8]. We began by determining the polymer parameters using line-space experiments and a least-squares parameter estimation method. These parameters were input to the photomask optimization algorithm which generated photomask patterns that performed better in simulations relative to intuitive shapes. These optimized photomasks were manufactured and then used to perform MDP. The resulting patterns characterized using optical profilometry and the pattern contours and peak-to-valley heights were analyzed.

The photomask optimization was clearly effective at improving the pattern-target overlap. This was evidenced by the reduction in penalized area for the square case. In some cases, the penalized area did not reduce significantly, but upon visual inspection, it was clear the contours still overlapped well. This discrepancy in penalized area is likely to due to the sample-to-sample variability as well as defects and metrology issues mentioned earlier. Operating in a cleanroom with improved atmospheric conditions and using non-contact exposure methods could help reduce the sample-to-sample variability and reduce defect levels. Discrepancies may also be due to the choice of parameters, where several results suggested that the primary parameter set was correct. The secondary parameters, in some cases, significantly improved the penalized area, but this is perhaps due to the genetic algorithm consistently identifying favorable pattern motifs such as increasing the mask size and pulling outwards the mask corners and edges. With this in mind, alternative optimization methods that directly apply these motifs may prove faster and more practical than the current pixel-by-pixel optimization method.

For the L-shape target, the optimization did well at improving the outer, convex corners but performed poorly on the inner, concave corner. Difficulty optimizing for both the convex and concave corners may be a limitation of the patterning method or optimization algorithm. It is possible that this could be overcome by optimizing a variable intensity exposure field rather than a binary exposure field. This idea could extend beyond L-shapes and allow one to pattern very different sized features across the exposure field in the same step.

SUPPORTING INFORMATION

S5.1 Sensitivity Study

We performed a sensitivity analysis to determine the robustness of the photomask optimization method, which is especially important given the large variation in peak-to-valley height observed in the line-space experiments. The sensitivity analysis involved simulating feature formation for an optimized photomask with a different set of physical parameters. For example, the photomask in Fig. 10a was optimized using the Sample 8 primary parameters, but we now simulate feature formation using the Sample 5 and Sample 11 primary parameters shown in Fig. S5.1. The Sample 5 and Sample 11 parameters were chosen because these samples exhibited the tallest and smallest features, respectively, in the line-space experiments. This will give us an idea of how the sample-to-sample variation will affect the resulting feature and penalized area.

Fig. S5.1 shows that for the Sample 11 parameters, a relatively shorter, underdeveloped feature is generated that overshoots the target. The penalized area is also worsened, but it can be clearly seen that the corners and edges are still much improved compared to the intuitive case. Using the Sample 5 parameters, a taller feature is generated, and the feature contour conforms sufficiently well to the target. Note though that despite the good conformity seen in Fig. S5.1f, the penalized area has worsened by roughly four-fold from the original ~27 μm^2 to 104 μm^2. This suggests that the penalized area measurement can be fairly sensitive to small changes.

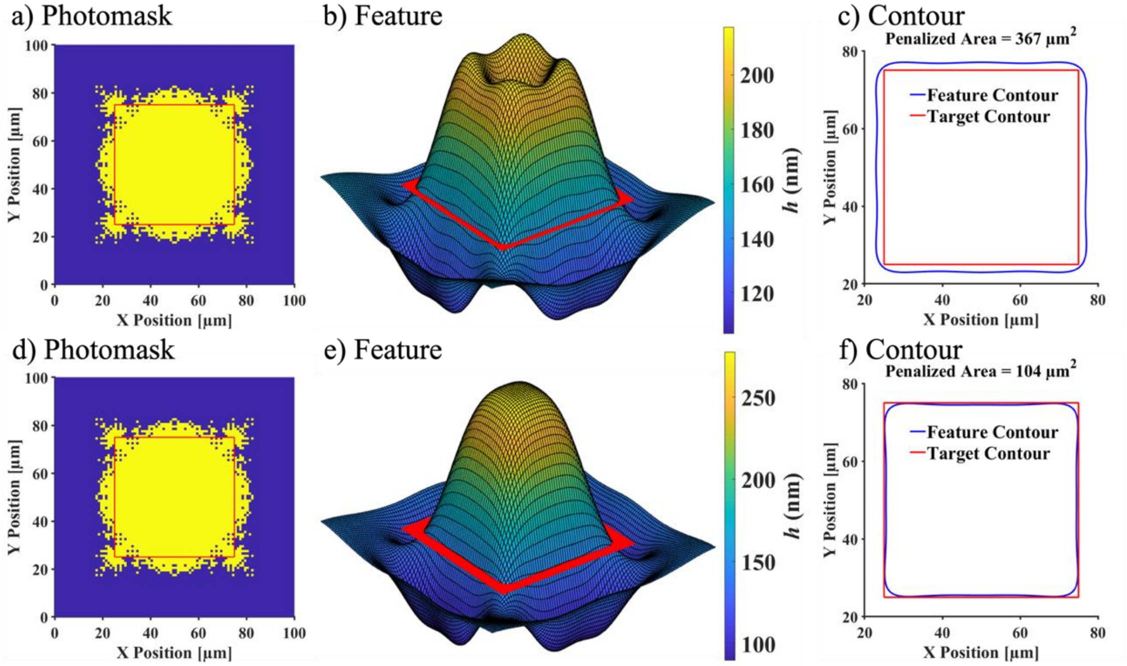

Figure S5.1 a) and d) are optimized square photomasks with 1x1 μm^2 pixels obtained using the sample 8 primary parameters and an annealing time of 5,000 seconds. Features and feature-target contours in b) and c) were obtained by simulating feature formation using the sample 11 primary parameters. Features and feature-target contours in e) and f) were obtained by simulating feature formation using the sample 5 primary parameters. The red outline in a) and d) shows the target dimensions. The red cut in b) and e) is for demonstration only and does not represent the dimensions of the target. Feature contours are extracted at $h = h_0 = 150$ nm. Note that the features in b) and e) are not drawn to scale, where the pattern pitch is 100 μm and the feature height is in nanometers.

We next examine the robustness of the method in the same way as before, but now for an optimized photomask made for a later annealing time (10,000 seconds). Fig. S5.2 shows the mask and the resulting feature height and contour. Note that the feature overlap using Sample 11 primary parameters is significantly worsened, but the Sample 5 parameters produce a relatively intact feature. These simulation results suggest that the optimized photomasks can be worsened by variations in the processing parameters. But the combined results of Fig. S5.1 and S5.2 suggest that the process can be resistant to process variations.

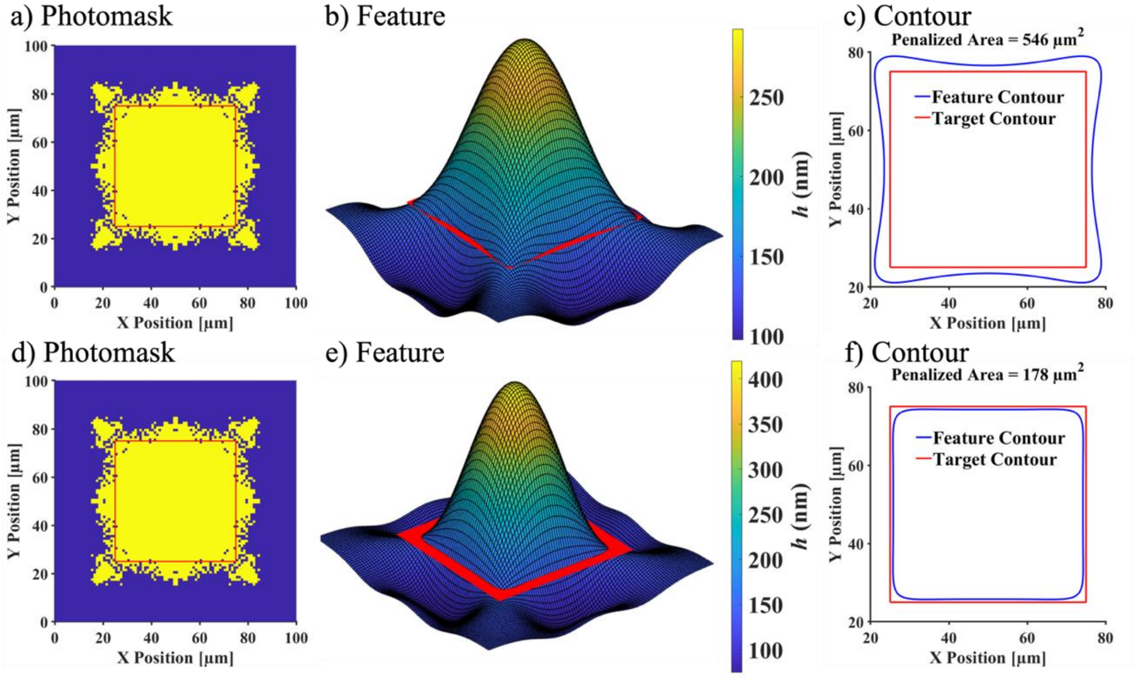

Figure S5.2 a) and d) are optimized square photomasks with 1x1 μm^2 pixels obtained using the Sample 8 primary parameters and an annealing time of 10,000 seconds. Features and feature-target contours in b) and c) were obtained by simulating feature formation using the Sample 11 primary parameters. Features and feature-target contours in e) and f) were obtained by simulating feature formation using the Sample 5 primary parameters. The red outline in a) and d) shows the target dimensions. The red cut in b) and e) is for demonstration only and does not represent the dimensions of the target. Feature contours are extracted at $h = h_0 = 150$ nm. Note that the features in b) and e) are not drawn to scale, where the pattern pitch is 100 μm and the feature height is in nanometers.

S5.2 Long-time Mask Optimization Results for L-Shaped Figures

As mentioned previously, the optimized L-shaped photomasks performed poorly when targeting longer annealing times (12,000 seconds for the secondary parameters). Fig. S5.3 shows the optimized photomask, feature and pattern contour for a photomask optimized using the secondary parameters and 1x1 μm^2 pixels. The outer edges and corners are now more rounded and the overlap at the interior, concave corner is very poor. This suggests that the concave corner is more difficult to improve, at the very least when co-optimizing for the convex corners. Due to the poor performance in this case, we chose not to generate an optimized photomask for this annealing time.

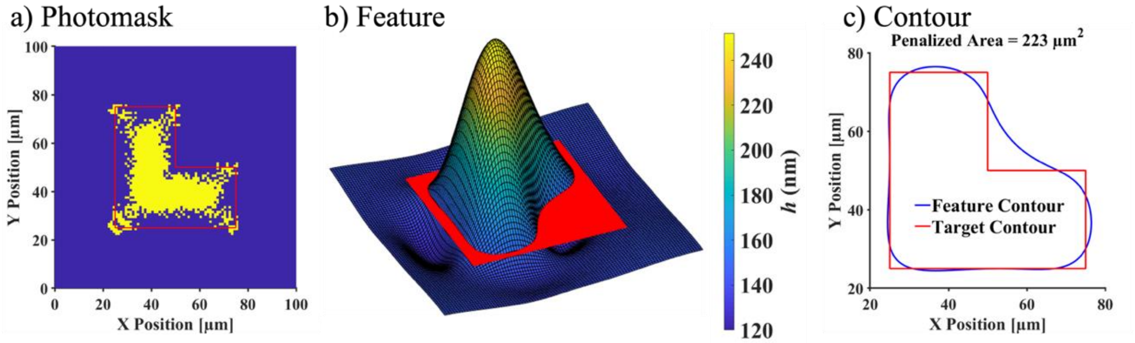

Figure S5.3 L-shaped photomask with 1x1 μm^2 pixels, simulated feature, and pattern contour compared to the target. Feature profile and contours taken at an annealing time of 12,000 seconds. The optimized photomasks were obtained through the optimization method using the Sample 8 secondary parameters. The red outline in a) shows the target dimensions. The red cut in b) is for demonstration only and does not represent the target dimensions. Feature contours are extracted at $h = h_0 = 150$ nm. Note that the feature in b) is not drawn to scale, where the pattern pitch is 100 μm and the feature height is in nanometers.

S5.3 All Experimental Feature Contours

Here we show the complete list of optimized photomasks along with the resulting features and contours compared to their corresponding targets. Figs. S5.4-S5.7 are for the square features and Figs. S5.8 and S5.9 are for the L-shapes. The annealing time and parameters used in obtaining the simulation results is listed in the figure captions.

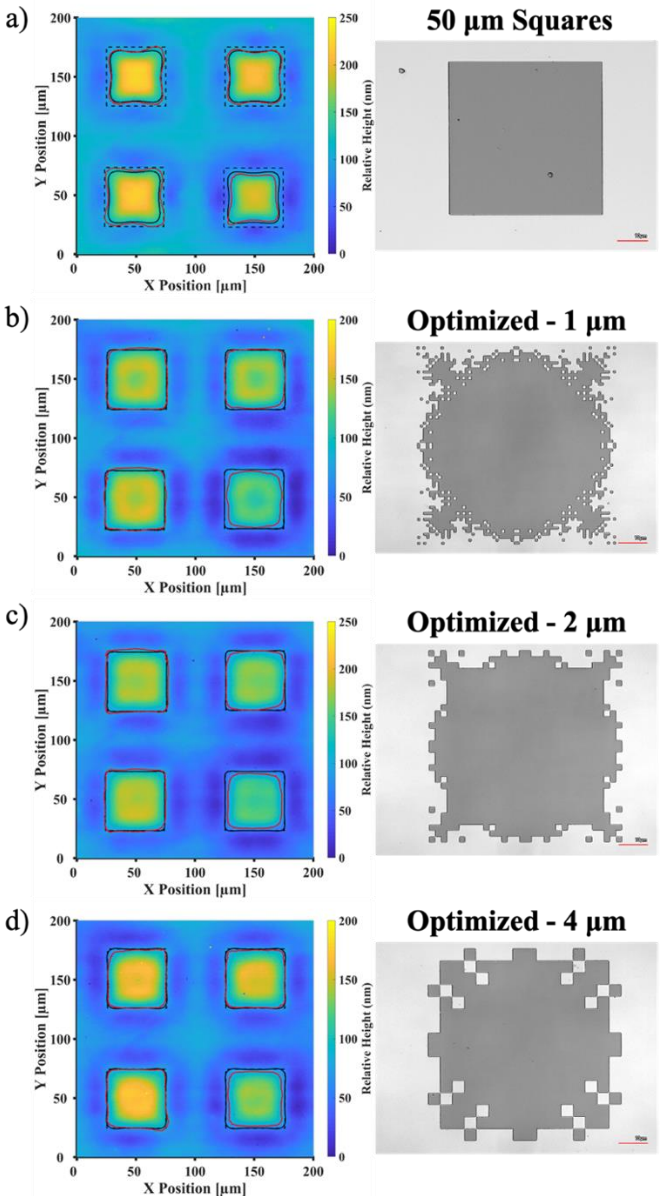

Figure S5.4 Feature height plots (left) and associated photomask pattern (right) used in generating the feature. Results shown are for the a) 50x50 µm^2 square mask and for the optimized masks with b) 1x1 µm^2 pixels, c) 2x2 µm^2 pixels, and d) 4x4 µm^2 pixels. Samples were annealed for roughly 5,000 seconds. Actual feature contours are shown in red. Target (dashed black) and simulated (solid black) contours were roughly centered around the actual contours. The simulated contours here were obtained using the primary parameter set. The red scale bars in photomask images correspond to 10 µm. Note that point defects were occasionally present that may fall below or above the color bar limits.

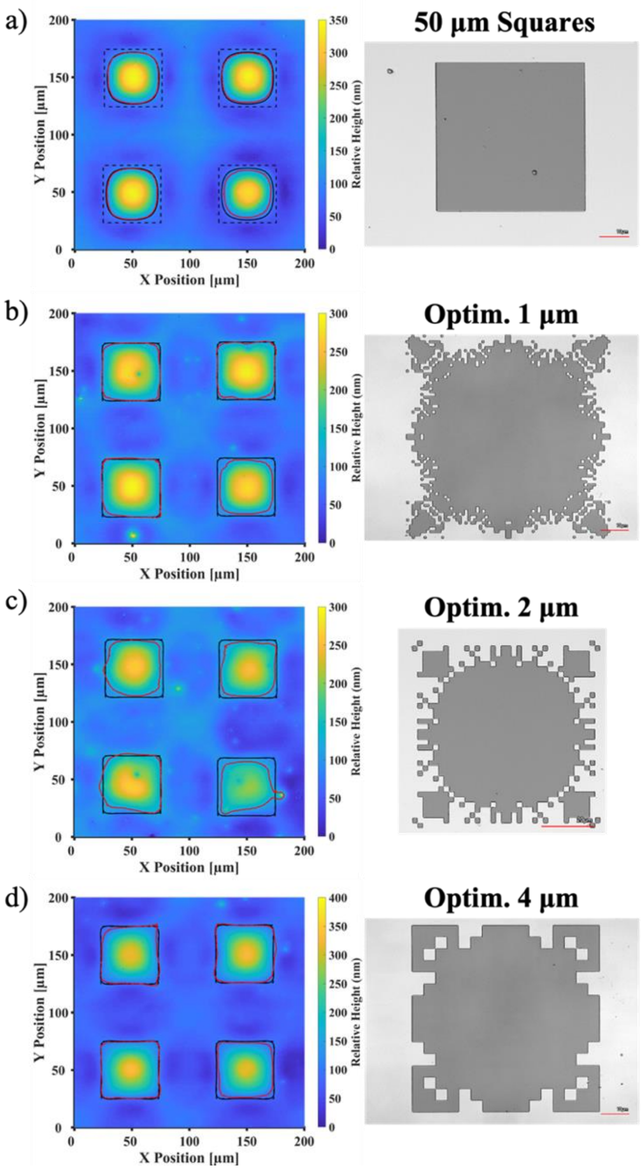

Figure S5.5 Feature height plots (left) and associated photomask pattern (right) used in generating the feature. Results shown are for the a) 50x50 µm^2 square mask and for the optimized masks with b) 1x1 µm^2 pixels, c) 2x2 µm^2 pixels, and d) 4x4 µm^2 pixels. Samples were annealed for roughly 10,000 seconds. Actual feature contours are shown in red. Target (dashed black) and simulated (solid black) contours were roughly centered around the actual contours. The simulated contours here were obtained using the primary parameter set. The red scale bars in photomask images correspond to 10 µm, except in c), where the scale bar is 20 µm. Note that point defects were occasionally present that may fall below or above the color bar limits.

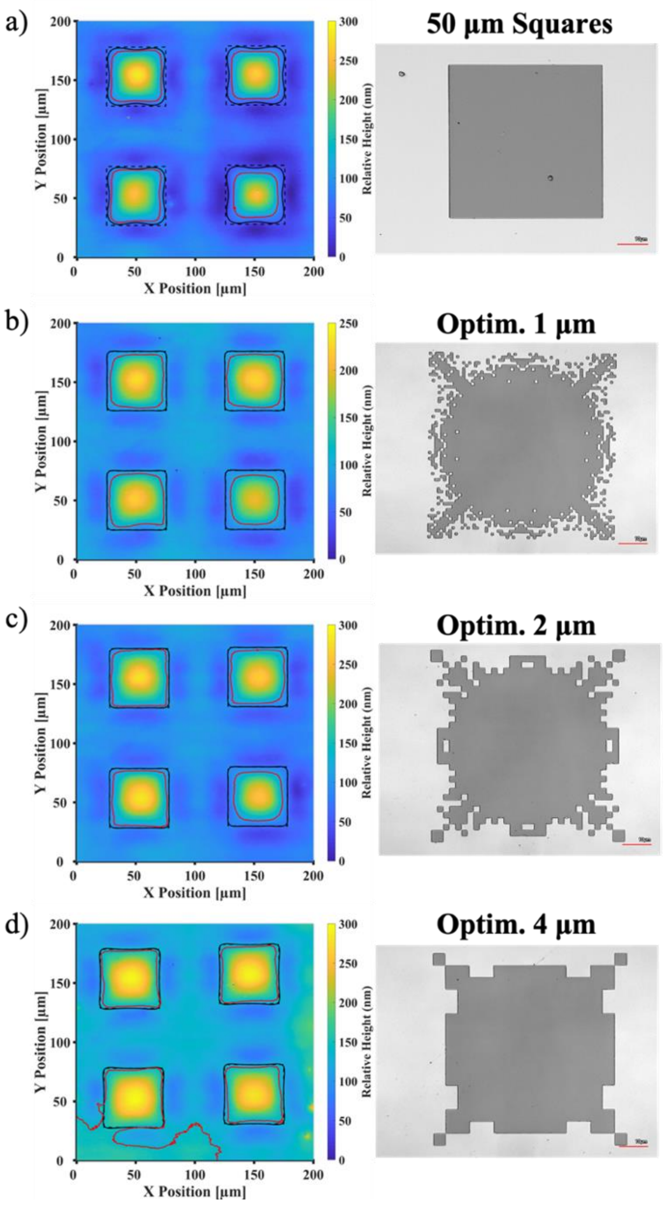

Figure S5.6 Feature height plots (left) and associated photomask pattern (right) used in generating the feature. Results shown are for the a) 50x50 µm^2 square mask and for the optimized masks with b) 1x1 µm^2 pixels, c) 2x2 µm^2 pixels, and d) 4x4 µm^2 pixels. Samples were annealed for roughly 6,000 seconds. Actual feature contours are shown in red. Target (dashed black) and simulated (solid black) contours were roughly centered around the actual contours. The simulated contours here were obtained using the secondary parameter set. The red scale bars in photomask images correspond to 10 µm. Note that point defects were occasionally present that may fall below or above the color bar limits.

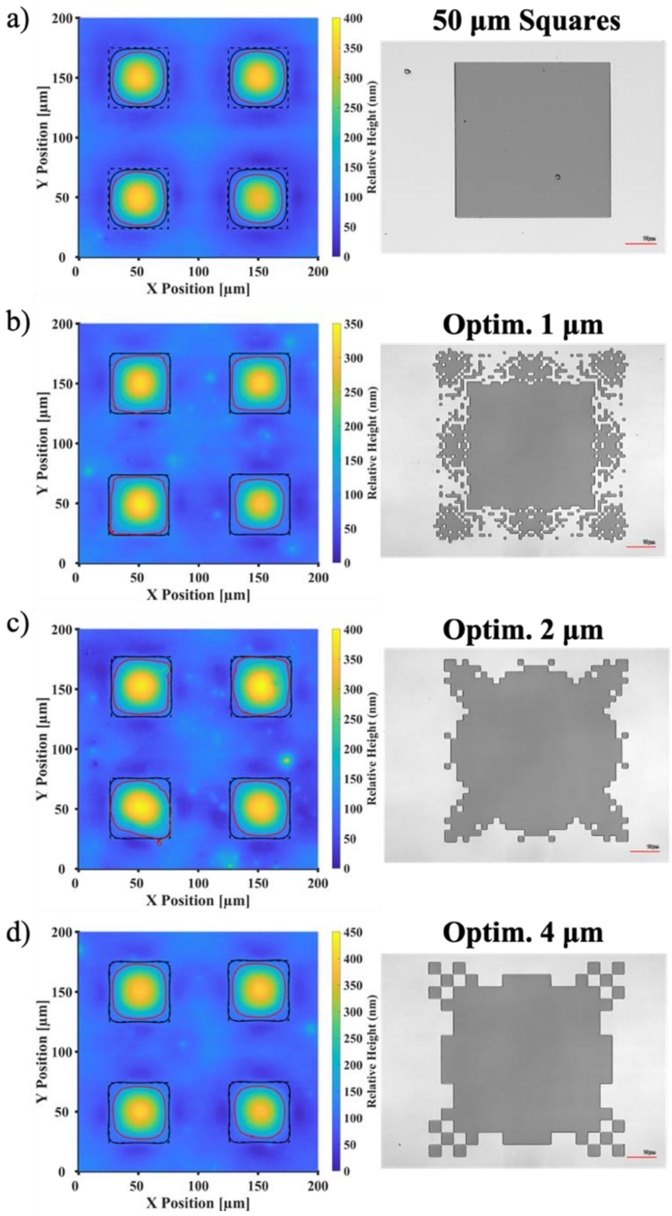

Figure S5.7 Feature height plots (left) and associated photomask pattern (right) used in generating the feature. Results shown are for the a) 50x50 μm^2 square mask and for the optimized masks with b) 1x1 μm^2 pixels, c) 2x2 μm^2 pixels, and d) 4x4 μm^2 pixels. Samples were annealed for roughly 12,000 seconds. Actual feature contours are shown in red. Target (dashed black) and simulated (solid black) contours were roughly centered around the actual contours. The simulated contours here were obtained using the secondary parameter set. The red scale bars in photomask images correspond to 10 μm. Note that point defects were occasionally present that may fall below or above the color bar limits.

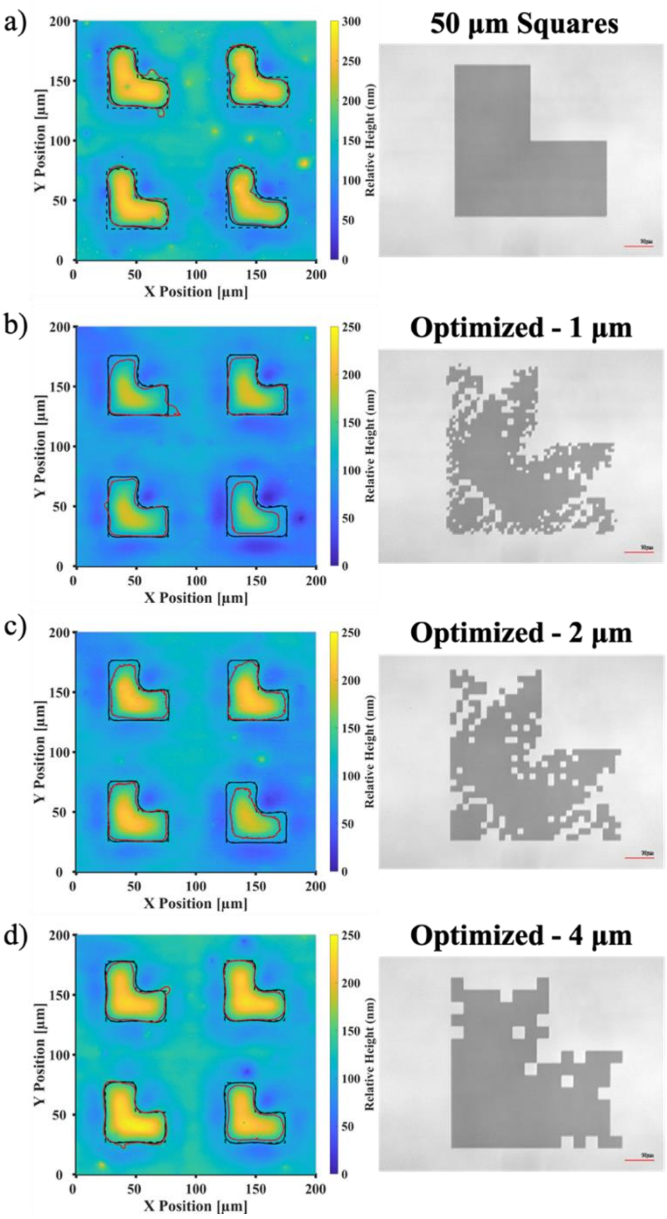

Figure S5.8 Feature height plots (left) and associated photomask pattern (right) used in generating the feature. Results shown are for the a) 50x25 µm^2 L-shape mask and for the optimized masks with b) 1x1 µm^2 pixels, c) 2x2 µm^2 pixels, and d) 4x4 µm^2 pixels. Samples were annealed for roughly 5,000 seconds. Actual feature contours are shown in red. Target (dashed black) and simulated (solid black) contours were roughly centered around the actual contours. The simulated contours here were obtained using the primary parameter set. The red scale bars in photomask images correspond to 10 µm. Note that point defects were occasionally present that may fall below or above the color bar limits.

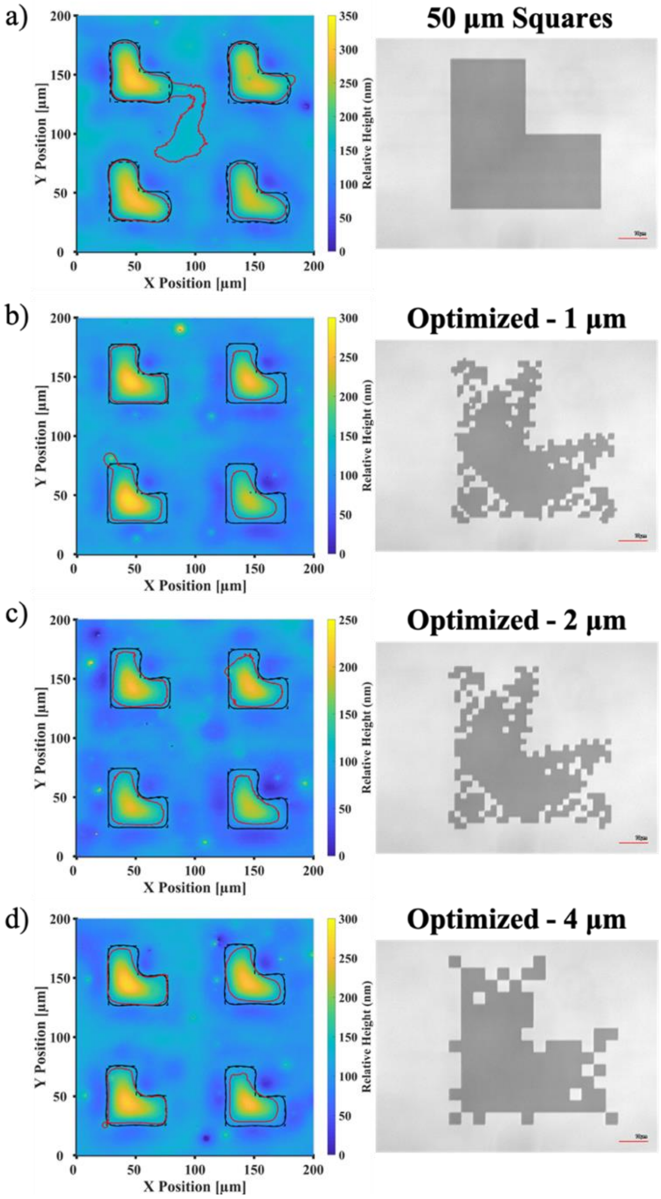

Figure S5.9 Feature height plots (left) and associated photomask pattern (right) used in generating the feature. Results shown are for the a) 50x25 µm^2 L-shape mask and for the optimized masks with b) 1x1 µm^2 pixels, c) 2x2 µm^2 pixels, and d) 4x4 µm^2 pixels. Samples were annealed for roughly 6,000 seconds. Actual feature contours are shown in red. Target (dashed black) and simulated (solid black) contours were roughly centered around the actual contours. The simulated contours here were obtained using the secondary parameter set. The red scale bars in photomask images correspond to 10 µm. Note that point defects were occasionally present that may fall below or above the color bar limits.

Chapter 6: Marangoni-driven Bias Reversal in Conformal Polymer Films**

6.1 INTRODUCTION

Spin-on polymer films are widely used in the microelectronics industry for patterning at micron and nanometer scales. Spin coating performed on initially flat substrates leads to uniform coating thicknesses [57–59]. However, when polymers are spin coated over existing topography such as trenches and vias, the polymer films conform to the topography during spinning and solidify with sufficient solvent evaporation [18]. Such conformal films can impose difficulties in the patterning process, such as causing poor depth of focus during imaging steps [19]. To planarize and reduce the impact of conformal films, thermal reflow can be used; however, this can require exceptionally long annealing times to level the film. For thermal reflow planarization, spun-on polymer films with an initially high bias are driven by capillary action into the unfilled trench regions. Due to the highly viscous nature of typical polymer films, the planarizing process is time-consuming, and the driving force slowly weakens as the film curvature decreases over time [19]. Alternative planarization methods could therefore be valuable to the semiconductor industry.

Here we describe a polymer-coating and heating process capable of quickly planarizing and even reversing the bias of an initially conformal polymer film. Bias is defined as the difference between open and trench region film heights (see Fig. 6.1). The polymer is a low-molecular-weight random copolymer composed of polystyrene (PS) and poly(4-*tert*-

---

** We would like to acknowledge and thank Dr. Xing-Fu Zhong of Brewer Science Inc. and his associates for performing the experimental work in this chapter and help creating several figures. We would also like to acknowledge Catherine Frank of Brewer Science Inc. for her help in editing.

butoxycarbonyloxystyrene) (PTBSM). The copolymer is abbreviated as PS-co-PTBSM. Upon heating PS-co-PTBSM to temperatures above 190°C, the PTBSM subunits are deprotected to form poly(4-hydroxystyrene) (PHOST) subunits along with gaseous carbon dioxide and isobutylene that escape the film. Spin coating the copolymer onto a substrate containing trenches initially produces a conformal film, but with sufficient annealing (~10 seconds at 240°C) the film quickly reverses in bias [17].

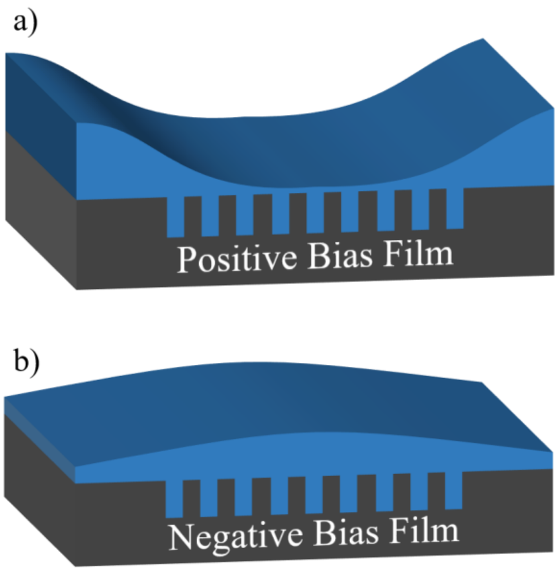

Figure 6.1 Depiction of thin films possessing (a) positive and (b) negative bias. Positive bias is characterized by a lower film height in trenched regions with respect to open regions, whereas negative bias is characterized by a higher film height in the trench regions with respect to the open regions. Bias is defined as the difference in film height between the open region and the trench region.

This reversal in bias is contrary to experience in leveling by thermal reflow alone [18,19]. The Stokes equation for viscous flow shows that the characteristic time, t_c, for thermal reflow by capillary forces is [19]

$$t_{\mathrm{c}} = \frac{w^4 \mu}{\gamma h_0^3}, \qquad (6.1)$$

where w is the width of the trench (or collection of trenches in the case presented here), μ is the film viscosity, γ is the surface tension of the film, and h_0 is the initial height of the film. As can be seen from Eq. (6.1), high-viscosity, thin films that conform to large trench widths yield unfavorable annealing times, which can be on the order of hours depending on the bias in the film thickness. Furthermore, bias reversal should not occur for capillary flow alone, meaning additional force(s) must be acting on the film. Van der Waals interactions between a silicon substrate and polystyrene film are repulsive [24] and could seek to level the film, but we will show later that these forces alone are insufficient to level the film. In this chapter we argue that Marangoni forces are primarily responsible for the rapid leveling and bias reversal.

The outline for the rest of this chapter is as follows: First we describe the experimental methods and observations of rapid planarization and bias reversal. We next analyze potential origins of the Marangoni driving force, namely, variations in temperature and solvent composition. We then present a theory that uneven rates of deprotection of PTBSM subunits is the cause of the bias reversal. To understand the impact of a spatially varying deprotection region, we implement a flow model and simulate the flow over a variety of conditions. The results show that a spatially varying deprotection reaction could indeed cause bias reversal.

6.2 EXPERIMENTAL METHODS AND RESULTS

6.2.1 Materials and Polymer Preparation

The polymer and solution were prepared in a manner similar to that outlined in reference [17]. The monomers used were styrene and 4-tert-butoxycarbonyloxystyrene (TBSM). The resulting copolymer, PS-co-PTBSM, was assumed to be composed of 1:1 Styrene:TBSM monomer. This assumption is appropriate because the monomer units are very similar and most all of the monomer was consumed in the synthesis. The polymer was typically dissolved using a mixture of propylene glycol methyl ether (PGMEA) and propylene glycol methyl ether acetate (PGMEA). The molecular weight of one particular sample possessed M_n = 3900 gm/mol and M_w = 6800 gm/mol. This molecular weight will later be used in estimating the polymer diffusivity. A different polymer sample with results shown in Figs. 6.4, 6.5, and 6.6 was prepared using a by-weight ratio of 60:40 PGME:PGMEA spin coating solvent. The solution was filtered using a 0.1-μm polytetrafluoroethylene membrane filter prior to spin coating. Potentially different polymer/solvent formulations were used for the reported auxiliary experiments.[††] We note that some formulations included a crosslinker, MY721, for delayed crosslinking. Results (not shown here) suggested that it had little effect on the planarization results.[‡‡]

Flat and pre-patterned silicon substrates with native oxide (Si-SiOx) were used. The patterned substrates contained trenches that were approximately 60 nm wide. The full pitch of the trenches was 120 nm and there were 100 trenches, meaning the trench region spanned approximately 12 μm. The patterned substrate possessed other sets of trenches of slightly varying geometries. These regions of trenches were separated by approximately 125 μm, meaning the full pitch of the patterns was approximately 137 μm. For some experiments, pattered substrates were coated with a few nanometers of TiN to determine the effects of using a different substrate material.

[††] Drawing on available experimental data, not all details were collected or given.

[‡‡] Dr. Xing-Fu Zhong reported this finding.

The trench depth varied somewhat. The depth of the trenches shown in Fig. 6.3 varied between roughly 210 nm and 222 nm and the depth of the TiN-coated trenches shown in Fig. 6.4 typically varied between roughly 195 nm and 221 nm with some extreme cases showing shallow depths around 150 nm.

6.2.2 Spin Coating and Annealing

The copolymer solution was spin-coated onto the trench-containing chips described earlier to achieve a prescribed mean thickness across the substrate. The films were annealed in one of two ways. The more conventional annealing method was to place the chip base in contact with the hot plate. The second method held the chip at a small distance from the hot plate in an inverted fashion, such that the polymer coating was closest to the hot plate. Heating times went up to 60 seconds at 240°C. After heating, the chips were removed to cool at room temperature.

6.2.3 Characterization of the Film and Polymer

The thicknesses of neat and annealed samples on flat substrates were measured using an ellipsometer. Samples coated on the trench-containing chips were cut crossways through the trenches and imaged using a scanning electron microscope (SEM) to directly measure the resulting bias. The film thickness was measured using an image analysis tool.

Water contact angle measurements were performed in prior work [17]. In that work, polymer films were spun onto flat Si-SiOx substrates and annealed for different times at 240°C, after which the contact angle was measured using a goniometer. We report here thickness vs. time measurements that were made in a similar fashion, where the thickness of the separate samples annealed under various conditions was measured using an ellipsometer.

The viscosity of a copolymer sample was determined using a rheometer with temperatures ranging between approximately 25°C and 280°C. The polymer sample was heated to 240°C for 60 seconds prior to measuring the polymer viscosity to deprotect the PTBSM subunits. The resulting viscosity versus temperature plot is shown in Sec. I of the Supporting Information section. Due to noisy data beyond 190°C, extrapolation was necessary to estimate the viscosity at 240°C, and it can be seen that the extrapolated viscosity lies around 10 Pa-s. The noisy data are likely the result of the incomplete deprotection reaction resuming past 190°C or due to low instrument sensitivity at lower viscosities.

6.2.4 Experimental Results

By heating the copolymer film to 240°C, the TBSM subunits are thermally deprotected according to the reaction shown in Fig. 6.2a. Water contact angle measurements on flat silicon-silicon substrates (no trenches) shown in Fig. 6.2b reveal that the deprotection reaction leads to a reduction in water contact angle, which is associated with increasing surface energy. Surface tension estimates presented later show that there is likely a strong increase in surface energy associated with deprotection.

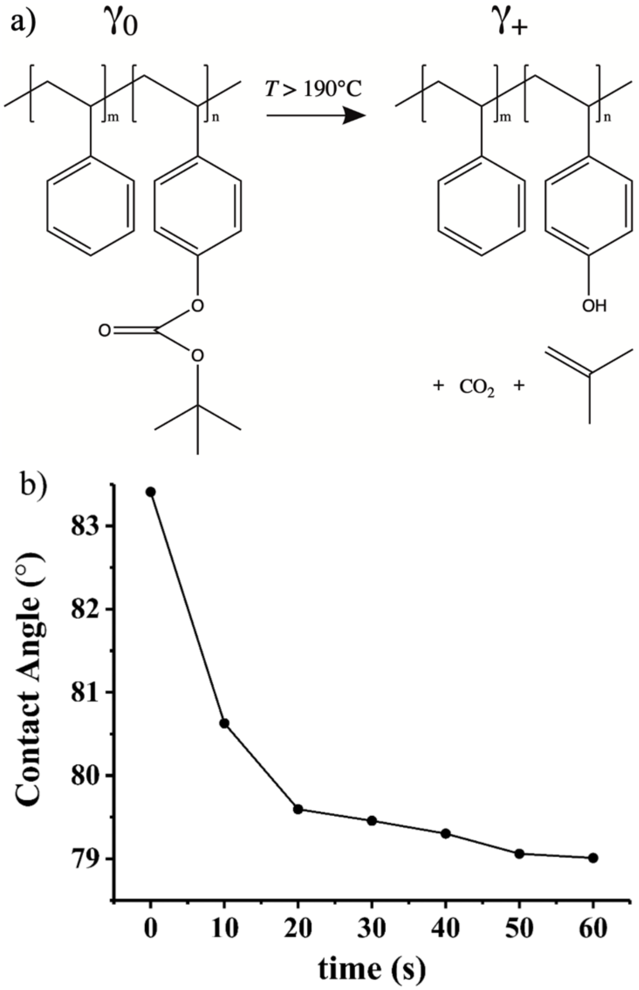

Figure 6.2 a) Thermal deprotection reaction in which PS-co-PTBSM forms PS-co-PHOST and gaseous carbon dioxide and isobutylene. Water contact angles show that PHOST subunits impart a higher surface tension compared to PTBSM subunits as indicated by the symbols γ_0 and γ_+. b) Water contact angle on separate polymer films measured at different annealing times. Note the decrease in water contact angle, suggesting an increase in film surface energy over time. Water contact angle data extracted from reference [17].

Annealing the films also led to thickness reduction as residual solvent is removed and the bulky protecting side group is expelled as gaseous CO_2 and isobutylene. Thickness reduction of 28%-32% were typical. To determine the thinning rate of the sample and the potential effects of using different spin-coating solvents, annealing experiments were performed on flat substrates. Fig. 6.3a shows the film thickness over time for various samples, coated using PGMEA as the only spin-coating solvent or a mixture of 40:60 PGME:PGMEA (by weight) as the spin-coating solvent. The effect of initial film thickness was also examined by spinning the samples either thin (~85 nm) or thick (~275 nm).

Fig. 6.3b shows the film thickness over time, now normalized by the initial film thickness. From 3b, it appears that using the different solvents had little effect on the thinning rate. However, it was noted in experiments not shown here that using only PGMEA as the spin coating solvent did not produce a reversal in bias, suggesting that solvent identity plays an important role in bias reversal.[§§] It is possible that initial film thickness had some impact on the thinning rate. This may be due to more residual solvent leftover in thicker films relative to the thinner films. Nonetheless, it appears that all samples thinned to completion by roughly 10 seconds. This fact will be used later in estimating the deprotection rate constant.

[§§] Dr. Xing-Fu Zhong reported this finding.

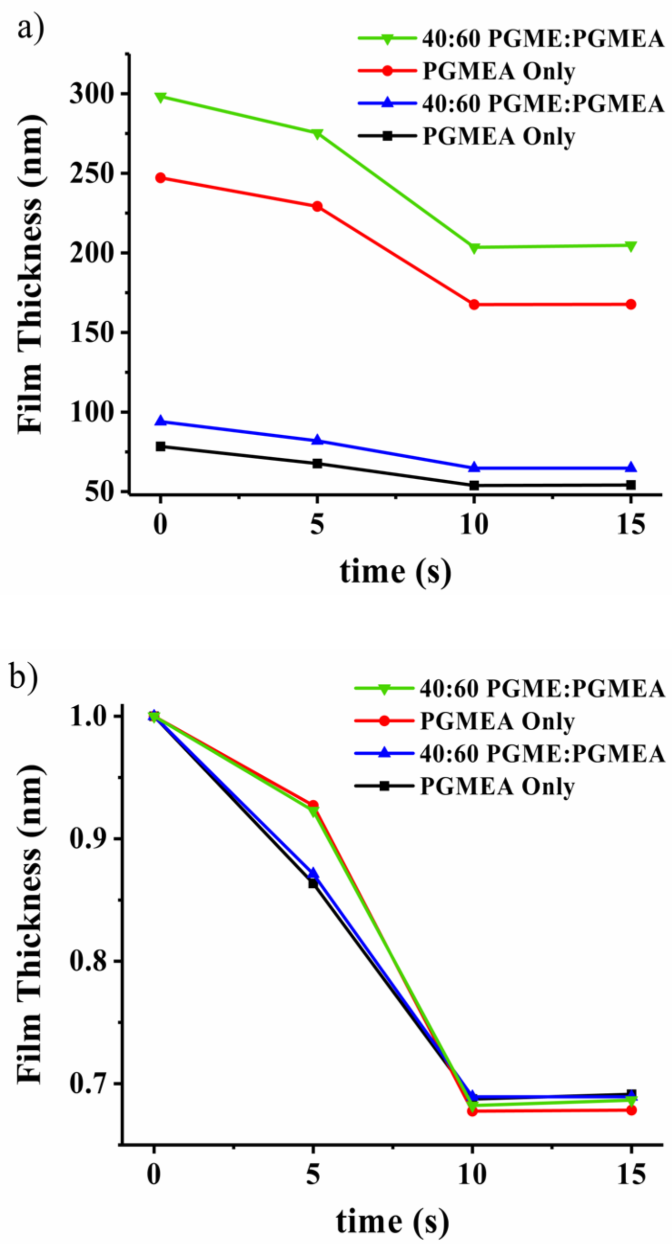

Figure 6.3 a) Film thickness over several annealing times for samples coated on flat Si-SiOx substrates. Samples were prepared using either PGMEA as the only spin-coating solvent or using a mixture of 40:60 PGME:PGMEA (by weight) as the spin-coating solvent. Thick and thin films were used to determine whether the reaction was thickness dependent. b) Film thickness normalized by the initial film thickness.

Annealing experiments were performed on the patterned substrates at various times. Cropped SEM images of the chip cross sections shown in Figs. 6.4 and 6.5 compare the film in the trench regions to the film in the surrounding open regions. Fig. 6.4 corresponds to the sample spun on Si-SiOx substrates, and Fig. 6.5 corresponds to the sample spun on TiN-coated substrates. Note that at t = 10 s, the film is notably thicker in the trench regions, as the bias has reversed. This behavior is very surprising. Fig. 6.6 shows the span of the trench regions at 0 s, 10 s, and 60 s for the sample spun on Si-SiOx substrates and emphasizes the magnitude of the bias reversal. At t = 10 s when the bias reversal is most obvious, there is a dome shape in the trench regions, which could not be achieved by simple spin coating and thermal reflow. And by the end of the annealing process at t = 60 s, the film possesses very little bias and almost appears flat.

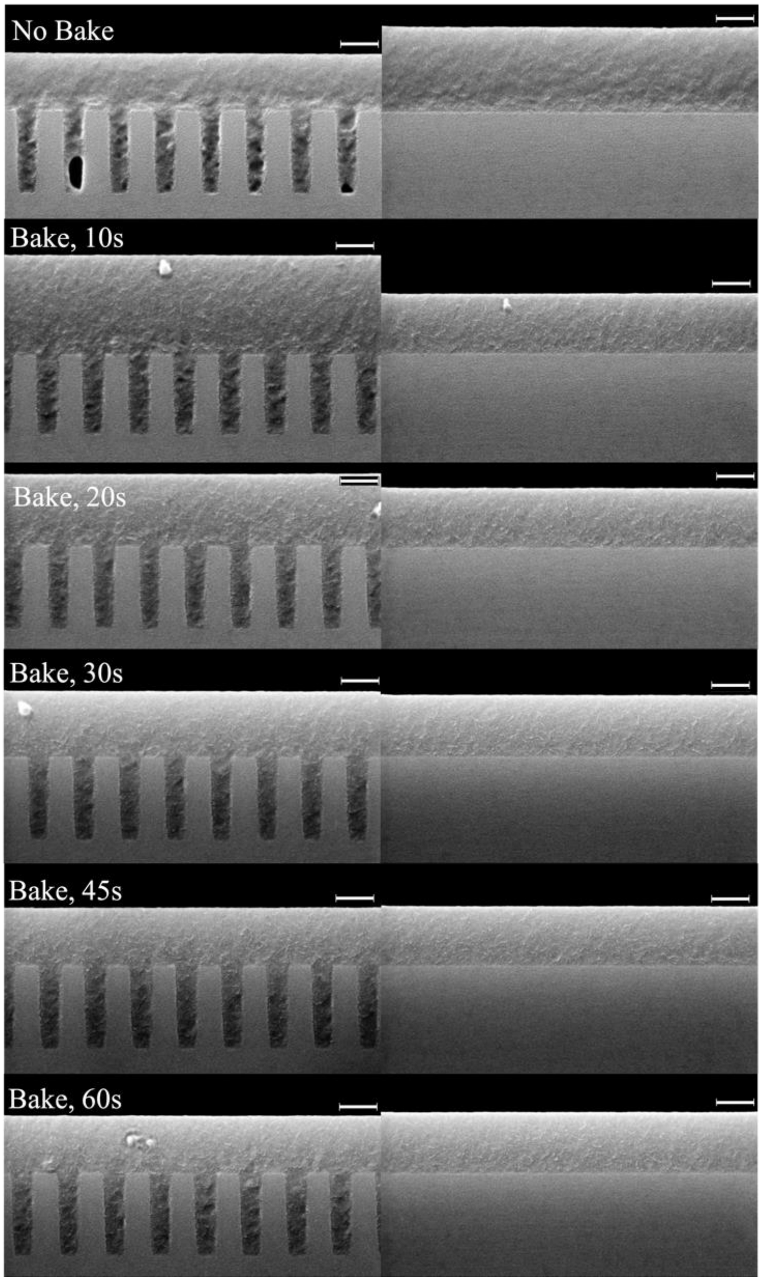
No Bake
Bake, 10s
Bake, 20s
Bake, 30s
Bake, 45s
Bake, 60s

Figure 6.4 SEM images of trench and open regions for the sample coated on Si-SiOx substrates annealed at 240°C for different times. Trench regions are on the left and open regions are on the right. Scale bars correspond to 100 nm. Note that at *t* = 10 s, the film is notably thicker in the trench regions, as the bias has reversed.

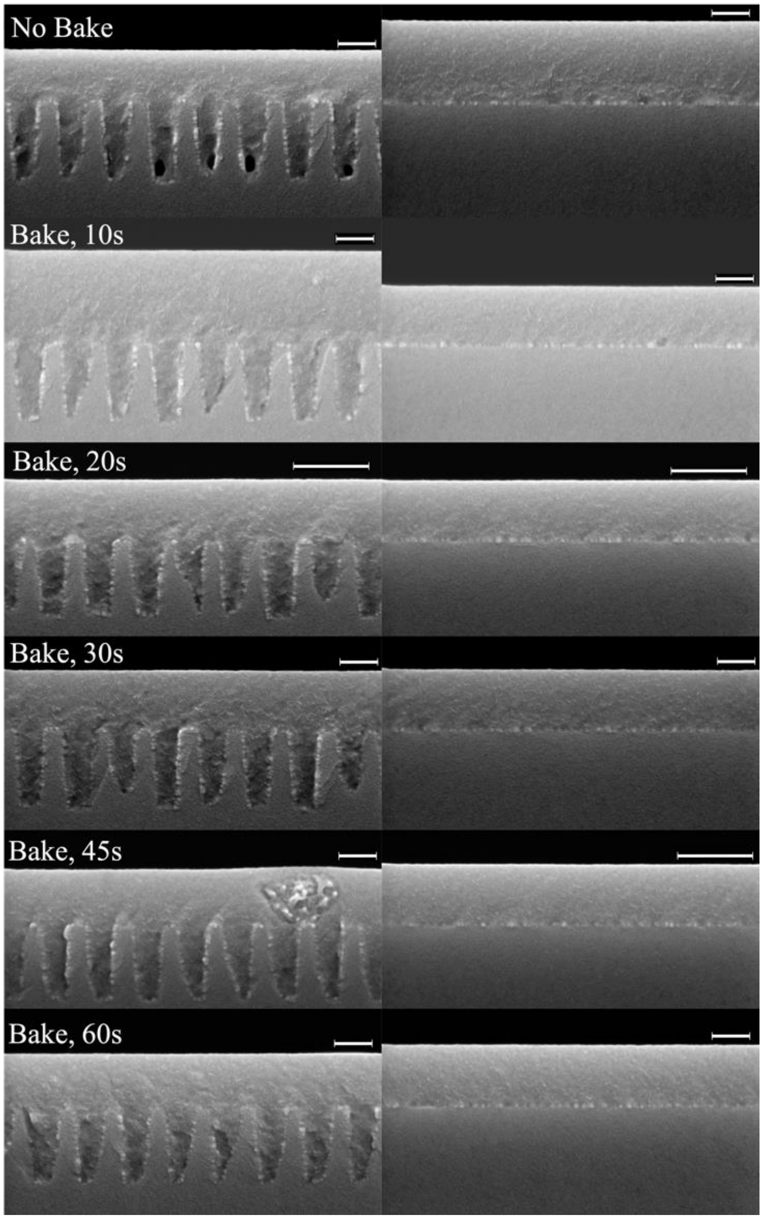

Figure 6.5 SEM images of trench and open regions for the sample coated on TiN substrates annealed at 240°C for different times. Trench regions are on the left and open regions are on the right. Smaller scale bars correspond to 100 nm and larger scale bars correspond to 200 nm. Note that at *t* = 10 s, the film is notably thicker in the trench regions, as the bias has reversed. Also note that the bright, thin TiN coating can be distinguished from the original substrate.

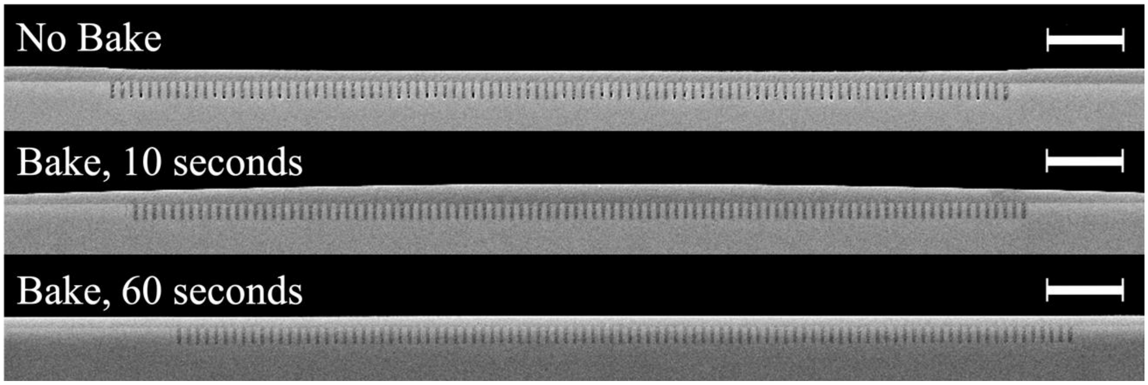

Figure 6.6 Wide-angle SEM images of trench and open regions for the sample coated on Si-SiOx substrates and annealed at 240°C for different times. At t = 0 s (no bake), a dip in height in the trench regions is visible. By t = 10 s, a dome is apparent, as significant polymer has flowed into the trench regions. By t = 60 s, the dome has relaxed, and the surface appears flatter relative to the 10 s bake.

Figs. 6.7a and 6.7b show the height of the film as measured from the base of the substrate (excluding trench depth) in the open and trench regions for both the Si-SiOx and TiN-coated substrates. Fig. 6.7c quantifies the bias as the difference between the open region thickness and trench region thickness, such that Bias = h_{Open} - h_{Trench}. By t = 10 s, the bias has gone from positive to negative with a minimum bias of -107 nm for the Si-SiOx substrate. At later times, the negative bias is dampened and even reverses back to positive, likely due to capillary forces leveling the now dome-like structure after the initial driving force subsides. It is surprising that the film thickness in the open regions increases at later times. This is perhaps due to sample-to-sample variability. The bias reversal appears to be slightly stronger for the Si-SiOx substrate, but the difference is not significant enough to conclude that the substrate identity is responsible for the bias reversal.

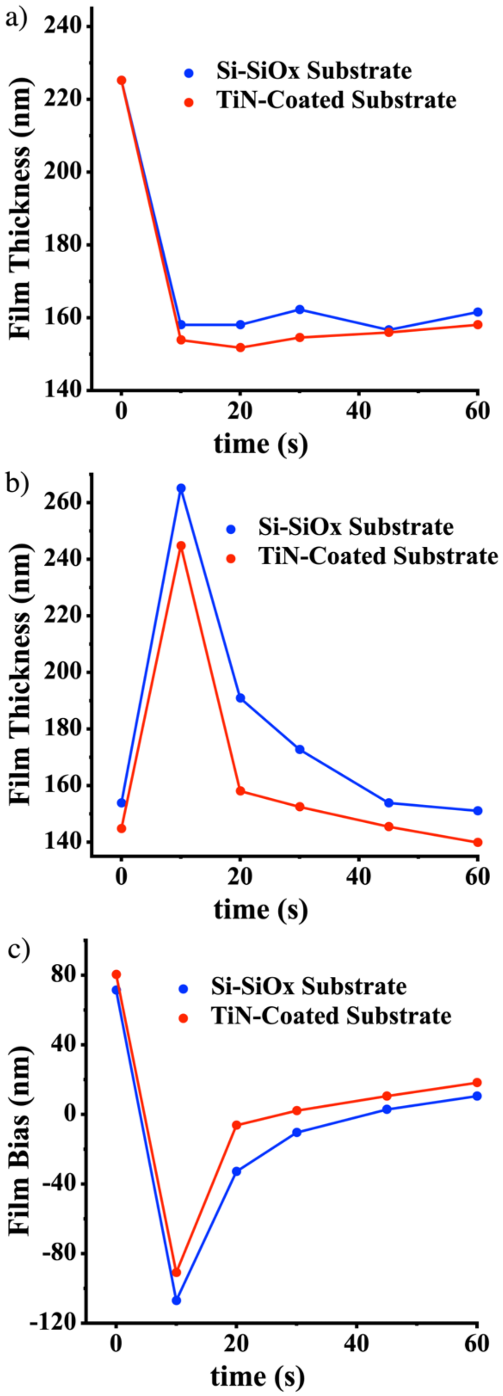

Figure 6.7 Film thickness measured from the substrate (excluding trench depth) in the a) open region and b) trench region over time. c) Film bias over time measured as Bias = h_{Open}-h_{Trench}.

To determine whether thermal gradients give rise to thermocapillary forces, annealing experiments not shown here were performed in which the substrate was held in an inverted fashion. This heating method produced planarization comparable to the conventional bake method, suggesting that thermal gradients are not responsible for the planarization process.[***] This is because thermal gradients would be reversed by heating the film upside-down. Further justification for disregarding thermal variations will be presented later.

The bias reversal is surprising. In the next section, we explore possible origins of the Marangoni driving force.

6.3 THEORY AND ANALYSIS

6.3.1 Examining Temperature Variations

Marangoni flows can arise from variations in temperature across a fluid. To examine temperature variations between thick and thin regions and determine whether they significantly affect planarization, we analyze the temperature distribution through the polymer film using the steady-state heat equation with a fixed temperature boundary condition at the polymer-silicon interface and a convective boundary condition at the polymer-air interface. Due to the small volume of material in question (roughly 10 µg/cm^2), we neglect any heat generated by the deprotection reaction and any heat lost due to residual solvent evaporation. We also neglect the geometry of the trenches, assuming that the film is positioned on a flat substrate. The temperature throughout the film can be expressed as

---

[***] Dr. Xing-Fu Zhong reported this finding.

$$T(z) = T_{\text{Base}} - z\frac{k_{\text{Conv}}\left(T_{\text{Base}} - T_{\text{Amb}}\right)}{k_{\text{Cond}} + k_{\text{Conv}}L}, \tag{6.2}$$

where T is the temperature throughout the film, T_{Base} and T_{Amb} are the base (240°C) and ambient temperature (25°C), respectively, z is position extending from the wafer surface to the thickness L (20 nm and 120 nm for thick and thin films, respectively), k_{Cond} is the thermal conductivity of the polymer, which was estimated at 240°C to be 0.16 W/m-K [60], L is the thickness of the film, and k_{Conv} is the convection coefficient at the polymer-air interface. k_{Conv} is liberally assumed to be 25 W/m^2-K, the maximum value in a range of reasonable natural convection coefficients (1-25 W/m^2-K [61]). Taking this into account, Eq. (6.2) shows that the temperature in a 154 nm thick film (representative of the initial trench region thickness and excluding the trench depth) would be 513.1448 K and the temperature in a 225 nm thick film (representative of the initial open region) would be 513.1424 K. This amounts to a ΔT of 0.0024 K and, where the temperature is hotter in the thinner regions. This shows that thermocapillary forces in fact work against replanarization (although minimally due to such a low ΔT) at early times because surface tension decreases with increasing temperature, and we can conclude that thermal variations are not responsible for the accelerated replanarization.

6.3.2 Examining Solvent Concentration Variations

Marangoni flows can also arise from compositional variations across a fluid surface. For the reacting polymer film under consideration, Marangoni flow could arise as a direct result of residual solvent compositional variations. Spun-on polymer films have been shown to carry up to tens of weight percent of residual solvent [62], which suggests the possibility of significant residual solvent in the copolymer. Dunbar has shown that solvents of different surface tensions and vapor pressures can evaporate at different rates in thin vs. thick regions during spin-coating, giving rise to Marangoni forces and striations during spin-coating [63]. Dunbar suggested that adding a less volatile cosolvent with higher surface tension could dampen the striations by creating favorable Marangoni forces in the trough region of the instability and promote leveling. It is possible that a similar phenomenon occurs in these annealing experiments. Table 6.1 provides the 25°C and 240°C surface tension and vapor pressure values of the solvents used in this experiment, PGME and PGMEA.

Table 6.1 Surface tension, liquid vapor pressure, and normal boiling points for PGME and PGMEA solvents at 25°C and 240°C. Data obtained from reference [64].

Parameter	PGME	PGMEA
γ(25°C) [mN/m]	27.9	26.7
P_{Vap}(25°C) [atm]	0.0159	0.00516
γ(240°C) [mN/m]	4.81	5.35
P_{Vap}(240°C) [atm]	15.6	8.41
Norm. Boiling Point [°C]	120.1	145.8

PGMEA possesses a lower vapor pressure and higher surface tension relative to PGME at 240°C, in line with Dunbar's suggestion for removing striations by promoting flow to the trough regions. Note, however, that Dunbar's analysis suggests stabilization and not a reversal in bias. It is possible that that the unique geometry of the trenches may render Dunbar's conclusions less applicable to our case.

We next note it is not likely that solvent exists in the film for sufficient time to cause Marangoni-accelerated leveling during the annealing step. Considering that the operating temperature (240°C) in experiments is much higher than the normal boiling points of the residual solvents, PGME (120.1°C) and/or PGMEA (145.8°C), it is reasonable to assume little resistance to evaporation at the surface of the film. Considering only the diffusional resistance in the thin film, a characteristic time scale for solvent removal can be taken as

$$t_{\mathrm{Diff}} = \frac{h^2}{D} \ , \tag{6.3}$$

where t_{Diff} is the characteristic diffusion time scale for solvent removal, h is the thickness of the film, and D is the solvent diffusivity. To be conservative, we approximate the solvent diffusivity as the self-diffusion coefficient of pure polystyrene at 240°C and of a similar M_n as a polymer used in this study (approximately 3900 gm/mol, which corresponds to 24 total monomer subunits). Using data from the literature [65] for PS melt diffusivity, the self-diffusion coefficient was estimated to be roughly $1.5\text{x}10^{-11}$ m^2/s (see Sec. II of the Supporting Information section). Note that the diffusivity of the smaller solvent molecules will be much higher than that of the polymer. Inserting this conservative estimate of diffusivity and the thickness in the deepest regions of the film including trench depth (~350 nm) into Eq. (6.3), we find that the time scale for solvent removal would be roughly 10 miliseconds, which is much less than the observed 10-second bias-reversal time scale. Thus, it is unlikely that solvent-induced surface tension gradients would have an effect on the planarization process.

It is still unclear why bias reversal was seen for the 40:60 PGME:PGMEA (by weight) spin-coating solvent mixture while no bias reversal was seen for pure PGMEA solvent. To completely rule out solvent effects one might perform a solvent prebake, where the film is heated above 150°C to drive off residual solvent, while keeping the temperature below 190°C to prevent the deprotection reaction from occurring. One could then observe whether bias reversal still occurs in these prebaked films.

6.3.3 Examining Polymer Concentration Variations

A final theory we present is that the bias reversal could arise from spatial variations in the deprotection reaction rate which would give rise to variations in surface tension. This increased reaction rate in the trench regions could arise from residual solvent stuck in the trench regions serving to quicken the reaction. A faster reaction could also be linked to the increased surface area in the trench region, where the substrate could act as a catalyst and provide more surface sites in the trench region. This catalytic surface theory is supported by the fact that the characteristic diffusion time for the polymer molecules to migrate from the substrate to the surface is roughly 10 miliseconds (approximated previously by $t_{\mathrm{Diff}} = h^2/D$). This short diffusion time shows that fast exchange between the catalytic substrate and the polymer surface is possible. For the substrate geometry in question, approximately four times more area is available in the trench regions compared to the open regions, which could proportionally increase the reaction rate in the trenched areas.

To investigate the effect of an accelerated reaction, we implemented a flow model to understand how much greater the reaction rate would have to be in the trench regions to achieve a reversal in bias. A model is laid out for calculating the film height over time, which is then used to calculate the film bias and compare to experiments. To model the fluid flow, we solved the thin film equation [7,18,19,23,26]

$$\frac{\partial h}{\partial t} = -\frac{\partial}{\partial x}\left(h\langle u\rangle\right) - k\frac{\Delta h_{\%}}{\Delta C}h, \tag{6.4}$$

$$\langle u\rangle = \frac{h}{2\mu}\frac{\partial\gamma}{\partial x} + \frac{h^2}{3\mu}\frac{\partial}{\partial x}\left(\gamma\frac{\partial^2\Phi}{\partial x^2}\right) + \frac{h^2}{3\mu}\frac{\partial}{\partial x}\left(\frac{A}{6\pi h^3}\right), \tag{6.5}$$

with the convection-diffusion-reaction equation [7,26]

$$\frac{\partial\left(hC_{\mathrm{PTBMS}}\right)}{\partial t} = \frac{\partial}{\partial x}\left(Dh\frac{\partial C_{\mathrm{PTBMS}}}{\partial x}\right) - \frac{\partial}{\partial x}\left(hC_{\mathrm{PTBMS}}\langle u\rangle\right) - kh, \tag{6.6}$$

where h is the film thickness, Φ is the fluid height as calculated from the base of the trenches, C_{PTBSM} is the PTBSM subunit mole fraction and hC_{PTBSM} is the product of the film height and the PTBSM subunit mole fraction. $\langle u\rangle$ is the average fluid velocity in the x direction, D is the diffusivity of the copolymer molecules, and k is the position-dependent rate constant for the assumed zeroth-order deprotection reaction (with a faster reaction and larger k existing in the trench region). Fig. 6.8 provides a diagram of the initial film height, thickness, and substrate geometry.

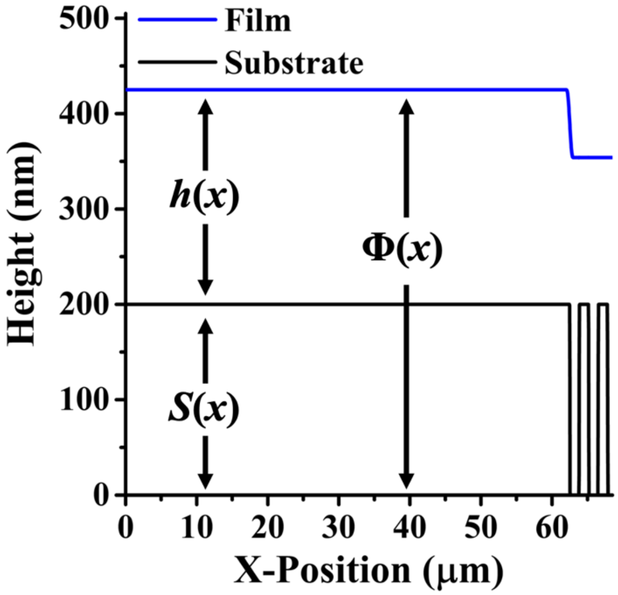

Figure 6.8 Diagram of the adjusted film height, Φ(x), film thickness, *h*(x), and substrate geometry, S(x). The adjust film height is calculated as Φ(x) = *h*(x) + S(x).

The substrate geometry, $S(x)$, and film thickness, $h(x)$ are used to calculate the film height, such that $\Phi(x) = S(x) + h(x)$. The use of Φ is necessary for calculating the film curvature and capillary pressure because the film thickness alone does not capture the curvature. For more information regarding the use of a film height variable, see references [18,19]

Eq. (6.4) tracks the film thickness over time by accounting for convective terms and film thinning. Together, $k\Delta h_{\%}/\Delta C$ is the percentage rate of change in film height, which is then multiplied into h to determine the thinning rate. Eq. (6.5) calculates the vertically averaged fluid velocity by accounting for Marangoni flow in the first term, capillary pressure-driven flow in the second term, and van der Waals pressure driven flow in the third term. Eq. (6.6) tracks the PTBSM subunit mole fraction by accounting for diffusion effects in the first term, convective effects in the third term, and losses by an assumed zeroth-order reaction in the third term. Assuming a linear relation between concentration and film thickness, the reaction is assumed to be of order zero because the film thinning plots in Fig. 6.3 were fairly linear up until the reaction stopped. We also assume $\Delta h_{\%}/\Delta C = 0.3/0.5 = 0.6$ because experiments showed the film height reduced by ~30% for the 0.5 mole fraction reduction in PTBMS. We note that the zeroth order assumption and chosen value of $\Delta h_{\%}/\Delta C$ neglect any thinning related to solvent escape, which was not quantified here.

The copolymer surface tension is assumed to be linearly related to composition and is calculated by weighting homopolymer surface tension values by their respective subunit mole fractions such that $\gamma = C_{\mathrm{PS}}\gamma_{\mathrm{PS}} + C_{\mathrm{PTBMS}}\gamma_{\mathrm{PTBMS}} + C_{\mathrm{PHOST}}\gamma_{\mathrm{PHOST}}$. Because there is 1:1 conversion from PTBMS to PHOST, the mole fraction of PHOST can be easily calculated as $C_{\mathrm{PHOST}} = C_{0\mathrm{PTBMS}} - C_{\mathrm{PTBMS}}$, where $C_{0\mathrm{PTBMS}}$ is the initial subunit mole fraction of PTBSM. Therefore, $\gamma = C_{\mathrm{PS}}\gamma_{\mathrm{PS}} + C_{\mathrm{PTBMS}}\gamma_{\mathrm{PTBMS}} + (\mathrm{C}_{0\mathrm{PTBMS}} - C_{\mathrm{PTBMS}})\gamma_{\mathrm{PHOST}}$. Given that the initial concentration of PTBSM is constant and the concentration of the nonreacting PS subunits is constant, the gradient in surface tension is calculated as

$$\frac{\partial\gamma}{\partial x} = \left(\gamma_{\mathrm{PTBMS}} - \gamma_{\mathrm{PHOST}}\right)\frac{\partial C_{\mathrm{PTBSM}}}{\partial x} = -\Delta\Gamma\,\frac{\partial C_{\mathrm{PTBSM}}}{\partial x}, \tag{6.7}$$

where $\Delta\Gamma = (\gamma_{\mathrm{PHOST}} - \gamma_{\mathrm{PTBMS}})$. In this form, $\Delta\Gamma$ will be positive because the surface tension of PHOST is expected to be greater than that of PTBSM.

The domain geometry and physical parameters were chosen to mirror the experimental conditions for the Si-SiOx patterned substrate experiment (see Fig. 6.4). Due to symmetry, only half of the domain was simulated. The half-domain width was 68.5 μm, the half-domain trench region width was 6 μm, and the trench depth was set to 200 nm. Due to the impracticality of implementing 100, 60 nanometer-wide trenches over the ~12 μm trench region, we simplified the setup by using five total trenches (2.5 trenches in the half-domain). To understand the effect of adding more trenches, a setup using 10 total trenches (five trenches in the half-domain) was also used. For the five and ten-trench setup, the trench widths were ~1.3 μm and ~0.63 μm, respectively. These trenches were implemented using a square pulse train with 100 nm smoothing. We initialize the film height using a step function smoothed over a 1 μm region, with the film height (Φ) as measured from the base of the trenches set to 425 nm in the open region (h = 225 nm) and 354 nm in the trench regions (or 154 nm thick when neglecting trench depth). This is a simplification of the actual film height seen in experiments, which transitions sharply at the crossover from the trench to open regions and tapers slowly as it approaches the center of the trench and open regions. Fig. 6.8 shown previously shows the initial setup for the five-trench case. The TBSM subunit mole fraction was initialized to 0.5 across the domain, reflecting the 1:1 ratio of styrene and TBSM in the copolymer.

The Hamaker constant for an air-polystyrene-silicon system is approximately $-1.3\text{x}10^{-19}$ J [24] and is the value for A that we used in the model. Because the native oxide layer is thin with respect to the polymer film and substrate thickness, it is acceptable to neglect the van der Waals contribution from the oxide layer.

The surface tension of low-molecular-weight polystyrene at 240°C was estimated to be roughly 25 mN/m by extrapolating high-temperature surface tension data for polystyrene (M_n = 9,300) from reference [27]. Obtaining the surface tension of PTBSM and PHOST was less straightforward. Several estimates were obtained by considering a collection of correlations provided in the literature [27] (see Sec. III of the Supporting Information for procedure). Estimates for γ_{PHOST} averaged to be ~34 mN/m. Estimates for γ_{PTBSM} varied, with one estimate around 21 mN/m and the other around 29 mN/m. We found that this variation does not greatly impact the effects of capillary forces, however it significantly impacts the Marangoni flow. Because of this, we set $\gamma_{\text{PTBSM}} = 21$ mN/m for the purpose of calculating the capillary pressure but varied the value of $\Delta\Gamma$ for calculating the Marangoni flow. From the correlations considered, the value of $\Delta\Gamma$ was found to be roughly 2 mN/m or 14 mN/m. Augsburg *et al.* determined the room temperature solid surface energy of PHOST and poly(4-*tert*-butylestyrene) to be 44.1 and 22.0 mN/m, respectively [66]. This combination is similar to the copolymer system reported here and shows a room temperature $\Delta\Gamma$ of roughly 22 mN/m, adding weight to our higher prediction of 14 mN/m. Nonetheless, we perform a parameter sweep in which the value of $\Delta\Gamma$ is varied between 0 mN/m and 20 mN/m and calculate the resulting bias.

The reaction rate in the open regions was chosen empirically to mirror the thinning rates seen in Figs. 6.3 and 6.7. $k_{\text{Open}} = 0.06$ was found to cause film thinning by ~30% at $t = 10$ s seconds like was seen in experiments.

Integral to our theory that a faster deprotection reaction occurs in the trench regions, we made the rate constant in the trench region, k_{Trench}, larger by using a multiplier, so $k_{\text{Trench}} = \alpha k_{\text{Open}}$, where $\alpha \geq 1$. This increase was implemented using a step function that transitioned at the onset of the trench regions and was smoothed over a 1-μm region. To prevent the concentration from going negative due to the zeroth-order reaction, a second step function was used to stop the reaction (drive k to zero) when C_{PTBSM} dropped below 0.2% of the initial concentration, $C_{0\mathrm{PTBSM}}$. The full expression for k as used in the model is

$$k = k_{\mathrm{Open}} + (k_{\mathrm{Trench}} - k_{\mathrm{Open}}) Step_{\mathrm{Pos}}\left(x\right) Step_{\mathrm{Conc}}\left(C_{\mathrm{PTBSM}}\right) \tag{6.8}$$

$Step_{\mathrm{Pos}}(x) = 0$ in the open region and smoothly transitions to unity in the trench regions. $Step_{\mathrm{Conc}}(C_{\mathrm{PTBMS}}) = 1$ for C_{PTBMS} greater than roughly 0.001 and smoothly transitions to zero as C_{PTBMS} drops below 0.001, thereby turning off the zeroth-order reaction. As part of our investigation to understand how much faster the reaction would have to proceed in the trench region and cause bias reversal, we varied the multiplier, α, between 1 and 10, where α = 1 represents no increase in reaction rate. Table 6.2 provides the physical parameters used in the simulation and provides the various references from which they were extracted.

The model was implemented in COMSOL Multiphysics, a commercial solver. All partial differential equations (PDEs) were solved using the general form PDE interface with default shape functions and quartic element orders. Due to the symmetry involved, no-flux boundary conditions were implemented. 2000 elements were used in the mesh and the relative error tolerance was set to either 1×10^{-6} or 1×10^{-5}.

Fig. 6.9a and 6.9b provide sample film height profiles at several times for $\Delta\Gamma = 14$ mN/m and $\alpha = 1$ as well as $\Delta\Gamma = 14$ mN/m and $\alpha = 4$ for the five-trench setup. Fig. 6.9c provides the corresponding simulated bias curves and compares these to the experimental bias curve. Bias was calculated as the height difference between the edge of the open and trench regions of the domain. Notice that for $\alpha = 1$ (no difference in reaction rate), there is practically no leveling. This shows that capillary-driven and van der Waals-driven leveling are very weak and cannot be responsible for bias reversal. However, for $\Delta\Gamma = 14$ mN/m and $\alpha = 4$ and, Marangoni forces are strong enough to drive flow towards the trench regions and reverse the bias to levels comparable to experiment. After the reaction has terminated after ~10 s, capillary leveling dampens the bias reversal. Note, however, that capillary leveling does not occur as quickly in the simulations as was reported in experiments, perhaps due to an overestimation of the viscosity. As a possible explanation for this, we note that the molecular weight between batches varied and it is expected the viscosity likewise varied. Reducing the polymer viscosity in simulations could improve this overlap; however, we have chosen to continue our analysis using the experimentally derived viscosity value of 10 Pa-s.

Fig. 6.9c shows that for the case in which $\Delta\Gamma = 14$ mN/m and $\alpha = 4$, bias reversal comparable to experiments can be achieved. To determine more generally what values of α and $\Delta\Gamma$ are required to generate *any* bias reversal, i.e. Bias < 0, a parameter sweep was performed, where α varied between 1 and 10 in intervals of 1 and $\Delta\Gamma$ varied between 0 mN/m and 20 mN/m in intervals of 2 mN/m. Fig. 6.10a is a level plot showing the calculated/interpolated minimum bias achieved during annealing for the $\Delta\Gamma$ and α combinations. A red contour at the Bias = 0 level shows conditions required for bias reversal according to the model. To the left of the red contour, the bias is positive, showing no reversal, whereas to the right of the red contour, bias reversal is achieved. For $\Delta\Gamma \geq \sim 5$ and $\alpha \geq \sim 2$, bias reversal is possible. These values of $\Delta\Gamma$ and α are not unreasonable. As mentioned earlier, it is possible the viscosity was actually lower than estimated. Were the viscosity indeed lower, the requirements of $\Delta\Gamma \geq \sim 5$ and $\alpha \geq \sim 2$ would be relaxed, such that even smaller values of $\Delta\Gamma$ and α would lead to bias reversal.

Fig. 6.10b shows the Bias = 0 contour for both the 5-trench and 10-trench cases. Note that there is little difference between the two cases, suggesting that adding more trenches to the simulation would not greatly affect the results.

Table 6.2 Physical parameters used in the simulations and their associated references, where SI stands for the Supporting Information section. Note that α and $\Delta\Gamma$ were varied as part of a parameter sweep between the reported ranges.

Parameter	μ (Pa-s)	D (10^{-11} m^{2}s^{-1})	A (10^{-19} J)	γ_{PS} (mN/m)	γ_{PTBMS} (mN/m)	γ_{PHOST} (mN/m)	$\Delta\Gamma$ (mN/m)	k_{Open} (1/s)	α (1)
Value(s)	10	1.5	-1.3	25	21	34	0-20	0.06	1-10
Ref.	SI	[65],SI	[24]	[27]	[27], SI	[27], SI	[27,66], SI		

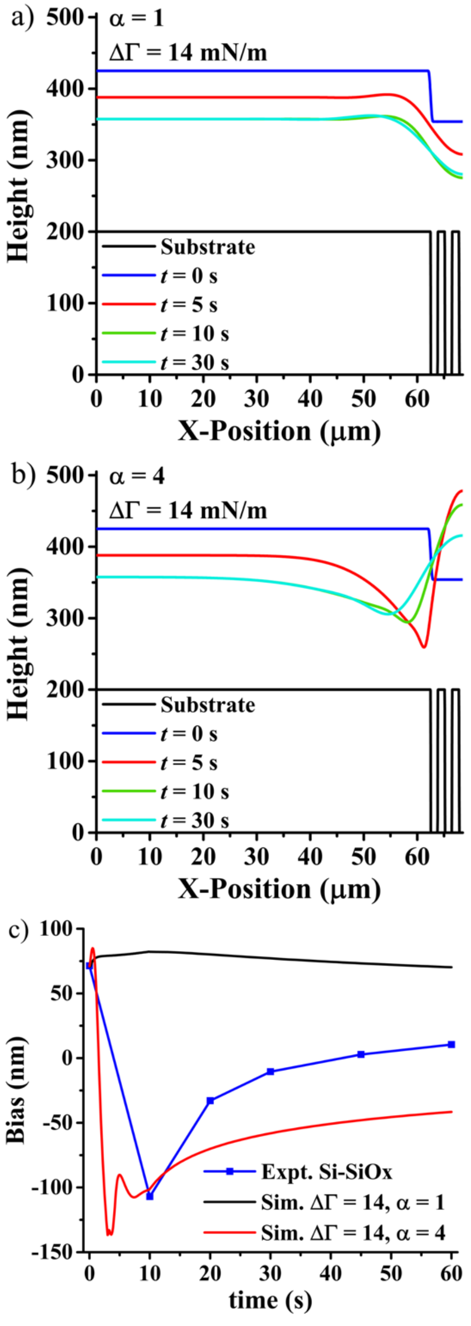

Figure 6.9 Adjusted film height, Φ(x), obtained at several times using a five-trench substrate for a) ΔΓ = 14 mN/m and α = 1, and for b) ΔΓ = 14 mN/m and α = 4. c) Bias over time for simulated results compared to experimental results featured previously.

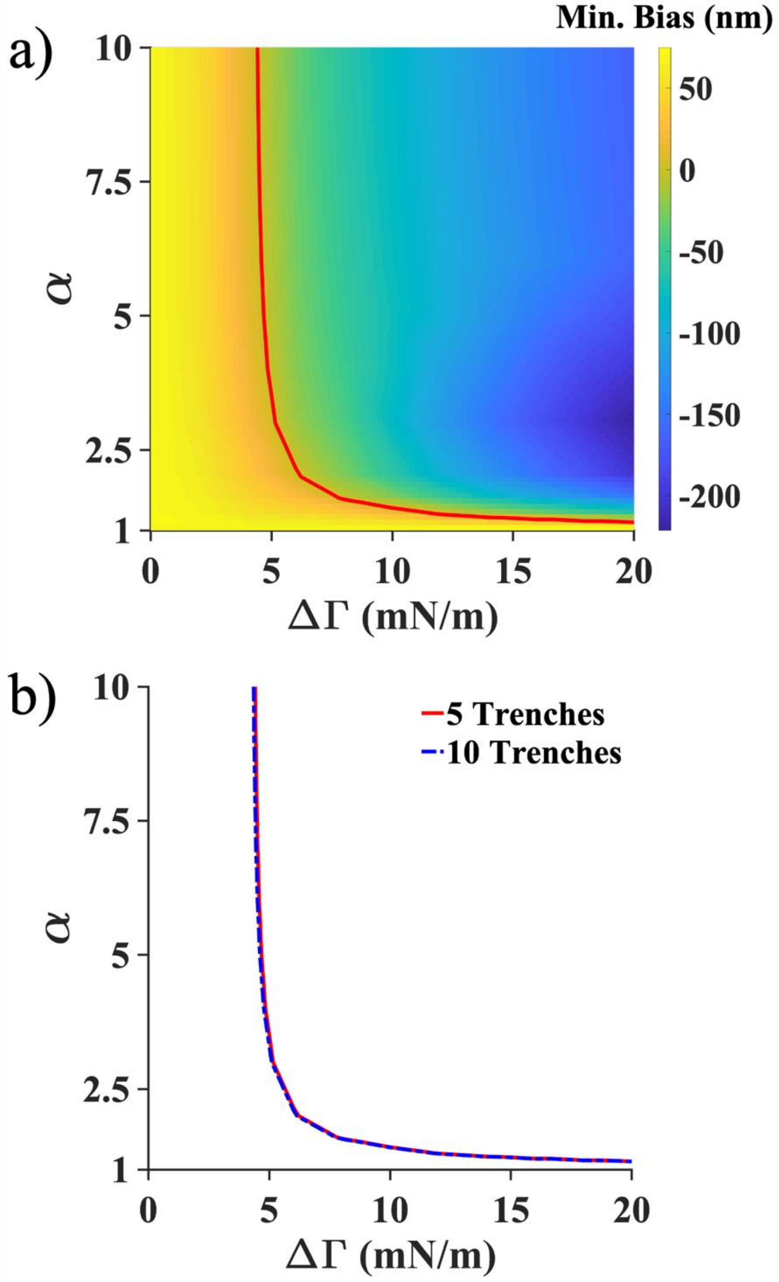

Figure 6.10 a) Minimum bias calculated/interpolated across a range of ΔΓ and α. Red line denotes the contour at which the minimum bias is zero. Regions to the left of the contour did not reverse in bias, whereas regions to the right did. b) Contours denoting zero bias for the 5-trench and 10-trench geometries. The similarity in contours suggests that adding more trenches to the simulation domain would not greatly affect the results.

To determine the values of ΔΓ and α that would achieve bias reversal *comparable to experiments*, we developed an objective, *J*, expressed as

$$J = 100\%\text{x}\left.\frac{\left|\text{Bias}_{\text{Sim}} - \text{Bias}_{\text{Exp}}\right|}{\text{Bias}_{\text{Exp}}}\right|_{t=10\,\text{s}} \tag{6.9}$$

Here, Bias_{Sim} is the bias calculated from the simulation and Bias_{Exp} is the bias calculated from the experiment, both determined at t = 10 s. As can be seen, the objective represents the percentage deviation from the experiment at t = 10 s. Due to the poor overlap in capillary-driven bias dampening shown in Fig. 6.9c (likely due to the viscosity estimate), we chose not to add the later time points into the objective.

Fig. 6.11a shows the objective calculated/interpolated across a range of ΔΓ and α for the 5-trench version of the simulation. The red line encloses the regions where $J \leq 10\%$. In other words, the red line encloses the parameter space that achieves a bias within 10% of the experimental bias at t = 10 s. As can be seen, for values of ΔΓ around 15 mN/m and reaction rates roughly three times that in the open region (α ~ 3) can lead to bias reversal comparable to experiment. For more extreme values of ΔΓ, even smaller increases in the trench region reaction rate can lead to comparable bias reversal. Again, Fig. 6.11b shows the J = 10% contour for both the 5-trench and 10-trench geometries, which shows good overlap and suggests that adding more trenches would not greatly affect the results.

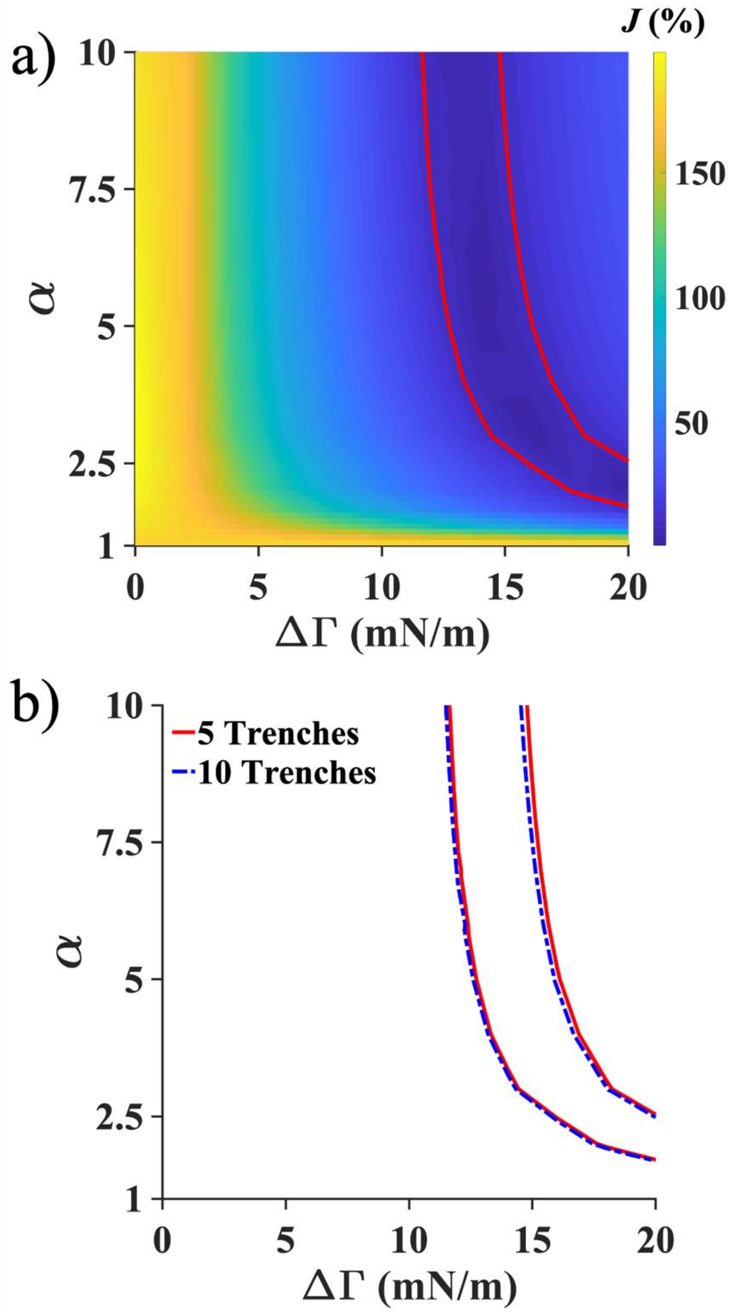

Figure 6.11 a) Objective, J, calculated/interpolated across a range of ΔΓ and α for the 5-trench geometry. Red contours enclose regions where the simulated bias reversal at *t* = 10 s is within 10% of that achieved in experiments. b) Comparison of the contours for the 5-trench and 10-trench setups. Note that only a small difference is observed, suggesting that adding more trenches would not greatly affect the results.

The fact that comparable leveling can occur for as little as three-fold increases in the reaction rate in the trench regions adds significant weight to our theory that polymer concentration variations give rise to a Marangoni force strong enough to cause bias reversal. The ~200 nm trench depth in experiments provides a roughly four-fold increase in the surface area compared to the open regions and could proportionally increase the reaction rate in the trench regions. This four-fold increase in surface area is above the minimum two-fold reaction rate increase predicted from simulations. It is also possible that residual solvent leftover in the trench regions at early times could, in some way, promote faster deprotection. A solvent pre-bake could help confirm or rule out this possibility. Furthermore, attempting bias reversal for different sized trench geometries would help determine the effects of substrate surface area.

The role of polystyrene subunits in the planarization process is still unclear. Theory suggests that increasing the ratio of TBSM subunits should prolong the experienced surface tension gradient and lead to stronger leveling. On the contrary, experiments using pure PTBSM (not shown here), no bias reversal was seen.[†††] It has been shown that pure PTBSM deprotects more quickly with respect to PS-co-PTBSM (see Sec. IV of the Supporting Information). It is possible that by increasing the base reaction rate (k_{Open}), the time scale of deprotection would be much shorter than the flow time scale and prevent the process of accelerated leveling.

[†††] Dr. Xing-Fu Zhong reported this finding

6.4 CONCLUSION

In summary, we presented the results of a planarization experiment involving a random copolymer composed of polystyrene and PTSBM spun on to a patterned silicon substrate with trenches. The initially conformal film surprisingly leveled after only a few seconds of heating at 240°C. The film even showed a reversal in bias, which, to the authors' knowledge, is unprecedented (see pending patent by Zhong et al. [17]), and is expected to be driven by Marangoni flow. Control experiments demonstrated that the bias reversal was not due to temperature variations, and calculations supported this conclusion.

It was noted in experiments not shown here that varying the ratio of PGME:PGMEA resulted in different levels of bias reversal. A theory in line with this observation was presented, suggesting that residual solvent mixture could be responsible for forming a favorable surface tension gradient. However, it was also noted that at such high temperatures, residual solvents should not persist long enough in the polymer to impart meaningful concentration differences across the film required for Marangoni flow. A simple solvent pre-bake experiment was then suggested to fully rule out solvent effects. This is left for future work.

A final theory was presented in which a faster deprotection reaction in the trench region gives rise to a polymer concentration gradient and subsequent Marangoni force. A flow model for this process was presented and reasonable physical parameters were used in the simulation. Simulations showed that $\Delta\Gamma \sim 14$ and $\alpha \sim 4$ gave bias reversals comparable to experiments. This is not unreasonable, considering the fact that the surface area in the trench regions is roughly four times that in the open regions, which could cause a proportional increase in reaction rate if the reaction is indeed surface-catalyzed. Future work could include using different sized trenches to determine the effects of substrate surface area. The possibility of slightly higher solvent content in the trenches was also considered as a potential driver for increasing the reaction in the trench regions. A solvent pre-bake experiment should help in confirming or ruling out this possibility, again left for future work.

SUPPORTING INFORMATION

S6.1 Viscosity Data and Extrapolation

The polymer viscosity was determined using a TA Instruments AR2000 EX rheometer with temperatures ranging between approximately 25°C and 280°C. The polymer sample was heated to 240°C for 60 seconds prior to measuring the polymer viscosity to deprotect the PTBSM subunits. The resulting log-viscosity vs. inverse temperature plot is shown below in Fig. S6.1 Due to the noisy data around and beyond 190°C, extrapolation was necessary to obtain the viscosity at 240°C. The noisy data are likely the result of the incomplete deprotection reaction resuming past 190°C or are due to low instrument sensitivity at lower viscosities. The viscosity is assumed to follow an Arrhenius-like relationship, which was used to fit to the non-noisy liquid region data. This fit line is also shown in Fig. S6.2. The viscosity fit equation is as follows:

$$\log\left(\mu / Pa \cdot s\right) = 0.00031 \exp\left(4190\mathrm{K} / T\right). \tag{6.10}$$

Here, μ is viscosity and T is temperature in Kelvin. Extrapolating to 240°C, the estimated viscosity is about 10 Pa-s.

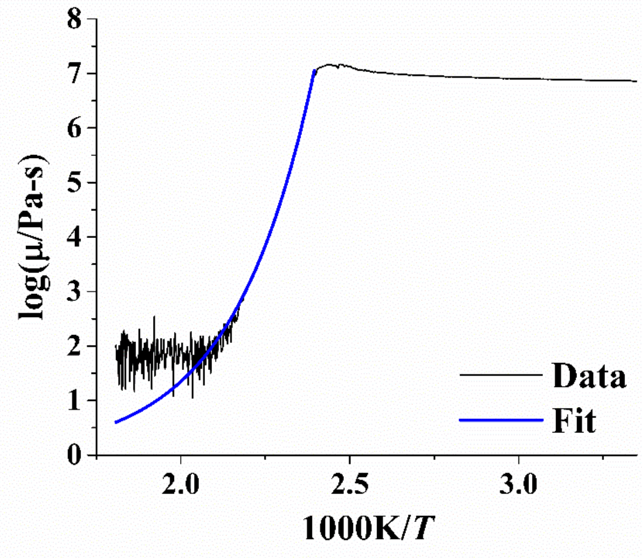

Figure S6.1 Log-viscosity vs. inverse temperature plot for deprotected PS-co-PTBSM sample, which has presumably converted into PS-co-PHOST. Data and Arhenius-like fit are provided.

S6.2 Estimating Polymer Self Diffusivity

To estimate the diffusivity of the PS-co-PTBSM copolymer, we assume the copolymer behaves similarly to pure polystyrene. The number average molecular weight (M_n) of one sample of PS-co-PTBSM was about 3900 gm/mol, which corresponds to a number of monomer units (N) of about 24. We extracted from reference [65] high-temperature diffusivity data for narrow M_n polystyrene fractions. The molecular weight fractions of interest were M_n = 2100 gm/mol and M_n = 4000 gm/mol, corresponding to N = 20 and N = 38, respectively. The temperature-dependent diffusivity for the N = 20 and N = 38 fractions with corresponding quadratic fits are shown below in Fig. S6.2. The fit equations used for N = 20 and N = 38 are, respectively, as follows:

$$\log\left(D/m^2s^{-1}\right) = -2.71\left(1000\mathrm{K}/T\right)^2 + 8.23\left(1000\mathrm{K}/T\right) - 16.45, \tag{6.11}$$

$$\log\left(D/m^2s^{-1}\right) = -1.47\left(1000\mathrm{K}/T\right)^2 + 1.86\left(1000\mathrm{K}/T\right) - 9.25. \tag{6.12}$$

Here, *D* is polymer diffusivity and *T* is temperature in Kelvin. Using these fit equations, the diffusivity of each fraction was extrapolated out to 240°C, giving D = $1.98\text{x}10^{-11}$ and D = 6.46 x 10^{-12} m^2/s for the N = 20 and N = 38 fractions, respectively. By further assuming a relationship of D $\propto$ $N^{-\alpha'}$, we calculated α' to be 1.74 for the N = 20 and N = 38 samples at 240°C. This value of α' is slightly different from the more general correlation suggested in reference [65], which determined α’ to be 2. Using α’ = 1.74, the diffusivity was determined for polystyrene of N = 24 (approximate number of monomer units in PS-co-PTBSM samples) to be approximately 1.44 x 10^{-11} m^2/s. Reference [65] also provides a broadly applicable correlation that estimates the diffusivity as 1.66 x 10^{-11} m^2/s, which is in close agreement with our more specific estimate from the data. We therefore view 1.5 x 10^{-11} m^2/s as an appropriate estimate for the self-diffusion coefficient of PS-co-PTBSM.

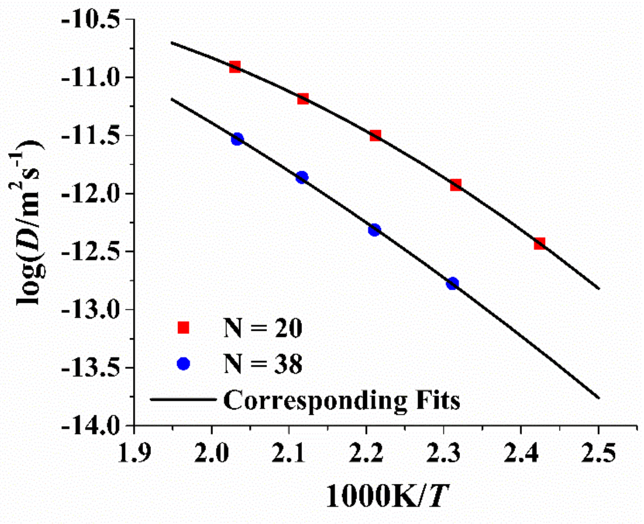

Figure S6.2 Log-diffusivity vs. inverse temperature data extracted from reference [65]. Black lines correspond to quadratic fits used to extrapolate out to 240°C.

S6.3 Surface Tension Estimation Method

We estimated the surface tension difference (designated as ΔΓ previously) of pure PTBSM, and poly(4-hydroxystyrene) (PHOST)) at 240°C using a method outlined in reference [27]. This method uses a combination of correlations to obtain estimates for the molar volume and molar parachor. These two quantities are then used to estimate the surface tension of the polymer according to the following equation:

$$\gamma = \left(\frac{P_s}{V}\right)^4 . \tag{6.13}$$

Here, γ is the surface tension and is a function of temperature. V is the polymer molar volume and is temperature dependent, whereas P_s is the molar parachor and is temperature independent. The fourth-power dependence of γ on P_s and V greatly amplifies any errors from estimating P_s and V. Using different combinations of correlations used in predicting V, several estimates of surface tension were obtained. These estimates are provided here in Table S6.1 and are labeled as method 1, method 2, etc.

Note that the smallest magnitude difference in surface tension, ΔΓ, is about 1.7 mN/m whereas the largest difference is about 13.9 mN/m. Augsburg *et al.* determined the solid surface energy of PHOST and poly(4-*tert*-butylestyrene) to be 44.1 and 22.0 mN/m, respectively [66]. This combination is similar to the copolymer system reported here and shows a room temperature ΔΓ of roughly 22 mN/m. Given the large uncertainty in ΔΓ, we probe a range of ΔΓ values in simulations, ranging from 0 to 20 mN/m.

Table S6.1 Summary of homopolymer surface tension estimates at 240°C obtained through different combinations of correlations. ΔΓ values for each method are provided.

Estimation Method	γ_{PTBSM} (mN/m)	γ_{PHOST} (mN/m)	ΔΓ (mN/m)
1	28.9	30.9	-2.0
2	28.5	31.3	-2.8
3	29.2	30.9	-1.7
4	28.7	31.1	-2.5
5	20.9	34.0	-13.2
6	20.5	34.4	-13.9
7	21.0	33.9	-12.9
8	20.7	34.3	-13.6

S6.4 Thickness reduction for pure PTBSM vs. PS-co-PTBSM

Fig. S6.3 provides thickness data measured at 225 °C for samples of pure PTBSM and 1:1 PS:PTBSM copolymer. The pure PTBSM shows both a faster thinning time and greater relative shrinkage because there are more subunits available for deprotection. The shrinkage for the pure PTBSM is roughly 50%, whereas it is roughly 25% for the 1:1 PS:PTBSM copolymer.

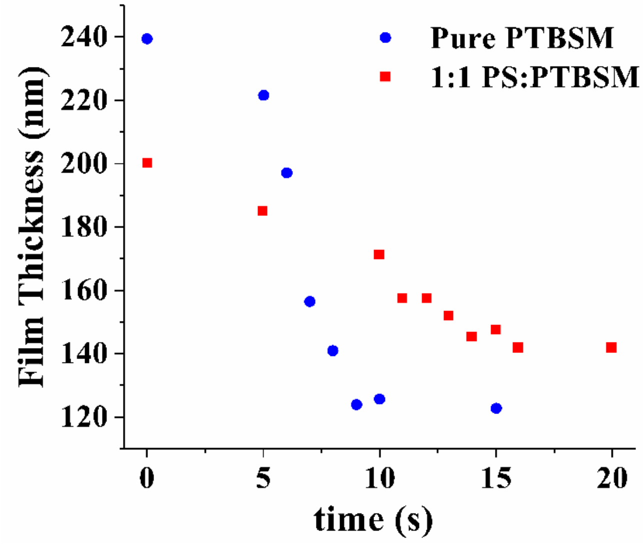

Figure S6.3 Thickness over time for pure PTBSM and PS-co-PTBSM annealed at 225°C on a silicon substrate.

The co-polymer has a $M_n = 4{,}624$ and $M_w = 7{,}412$ and was synthesized in a manner similar to that outlined in reference [17]. The pure PTBSM in the above experiment had a $M_n = 4{,}922$ and $M_w = 7{,}812$. It was synthesized by adding all of the reagents except styrene.

Chapter 7: Summary, Outlook, and Future Work

7.1 SUMMARY

In this work, we analytically and numerically determined the physical limits of equal line-space Marangoni-driven patterning (MDP). An estimate of 0.5 was provided as the upper limit of MDP and the minimum pitch was shown to be fundamentally limited by optical and engineering constraints. We also determined the conditions necessary to trigger dewetting events through MDP which could further push the inherent limits of the method beyond the 0.5 predicted aspect ratio. We also explored the use of photoexposure optimization techniques to improve two-dimensional patterning capabilities and we experimentally demonstrated the effectiveness of the optimization to more closely achieve desired structures on surfaces.

Finally, we examined the possible origins of the bias reversal process first observed by Zhong et al. [17]. It was shown through simulations that a reaction accelerated in the trench regions could be responsible for a Marangoni force driving bias reversal. To further confirm this, future work will involve ruling out solvent effects by performing a post-apply bake to drive off residual solvent. Furthermore, different sized trenches could be used to understand the effect of available substrate surface area on the bias reversal.

7.2 OUTLOOK FOR MARANGONI-DRIVEN PATTERNING

The practical applicability to MDP rests on its ability to control the pattern shape and achieve sufficiently high aspect ratios and small enough features. It is also important to bear in mind the processing advantages MDP has over entrenched patterning techniques.

A distinguishing characteristic of MDP is that it only requires a heating step to develop the patterns. Relative to optical lithography, MDP can therefore avoid the solvent development step which often employs toxic chemicals. At the wafer scale, this is not an issue, as the industry has been dealing with developing solvents for decades. However, at the roll-to-roll scale, the distinguishing characteristics of MDP may be advantageous. A web used in roll-to-roll MDP would only require a heating step in an annealing oven to develop the pattern, whereas when using optical lithography, the web would need to be pulled through a solvent bath to develop, which may not be ideal. If a breakthrough etch is required, this would add some complexity to the process, but this could be overcome by inducing dewetting.

The estimated maximum aspect ratio of 0.5 is small relative to current methods but may be suitable for some applications. A study by Davis et al. examined how wrinkled patterns could improve adhesion properties [15]. In their study, the aspect ratio of the wrinkles ranged from roughly 0.16 to 0.26, which is above the current capabilities of MDP but within the estimated range of possible aspect ratios. In a different study, Kim et al. examined the effects of using wrinkled polymer films to improve the light absorption capabilities of solar cells [14].[‡‡‡] The wrinkle patterns had a reported aspect ratio of 0.2, again within the predicted capabilities of MDP. These and other potential applications could be served by MDP if the maximum aspect ratio were made larger through improved patterning chemistries.

[‡‡‡] Note that we have calculated the aspect ratio from references [14,15] as $2\Delta h/\lambda$ to be consistent with how the aspect ratio is calculated in our studies.

To extend MDP to more applications still, it is essential to continue investigating MDP as a means to induce dewetting in thin polymer films. The dewetting event can serve both to increase the aspect ratio beyond the maximum 0.5 and also avoid the breakthrough etch step. This would greatly increase the value proposition of MDP.

7.3 FUTURE WORK

To make possible the previously mentioned advancements, future work should include developing new polymer chemistries that can generate very large surface tension differences when exposed to UV light while simultaneously ensuring miscibility and minimizing the species diffusion. Future work should also include experimentally demonstrating dewetting through MDP and validating the predicted conditions necessary to induce dewetting. These experiments could be done using previously demonstrated polymer systems with different substrates that allow for favorable dewetting conditions. Additionally, the model employed in this work does not account for the post-dewetting dynamics where more advanced models could allow for simulation beyond the dewetting point and add further insight to the process.

Regarding two-dimensional patterning advancements, optimization techniques could be developed to simultaneously design different sized features that cannot be easily formed in a single exposure and annealing sequence. As the flow and diffusion time scales change for different sized features, a single, binary exposure step would result in smaller features decaying faster than larger ones. To compensate for this, one might employ variable-intensity pixels rather than a binary pattern of exposed and unexposed pixels. This could offer more control over the surface tension gradient, where smaller features would receive more exposure and decay slower, thereby keeping pace with the larger features.

References

[1] J.M. Katzenstein, D.W. Janes, J.D. Cushen, N.B. Hira, D.L. McGuffin, N.A. Prisco, C.J. Ellison, Patterning by photochemically directing the Marangoni effect, ACS Macro Lett. 1 (2012) 1150–1154. https://doi.org/10.1021/mz300400p.

[2] D.W. Janes, J.M. Katzenstein, K. Shanmuganathan, C.J. Ellison, Directing convection to pattern thin polymer films, J. Polym. Sci. Part B Polym. Phys. 51 (2013) 535–545. https://doi.org/10.1002/polb.23262.

[3] C. Bin Kim, D.W. Janes, D.L. McGuffin, C.J. Ellison, Surface energy gradient driven convection for generating nanoscale and microscale patterned polymer films using photosensitizers, J. Polym. Sci. Part B Polym. Phys. 52 (2014) 1195–1202. https://doi.org/10.1002/polb.23546.

[4] J.M. Katzenstein, C. Bin Kim, N.A. Prisco, R. Katsumata, Z. Li, D.W. Janes, G. Blachut, C.J. Ellison, A photochemical approach to directing flow and stabilizing topography in polymer films, Macromolecules. 47 (2014) 6804–6812. https://doi.org/10.1021/ma5010698.

[5] C. Bin Kim, D.W. Janes, S.X. Zhou, A.R. Dulaney, C.J. Ellison, Bidirectional control of flow in thin polymer films by photochemically manipulating surface tension, Chem. Mater. 27 (2015) 4538–4545. https://doi.org/10.1021/acs.chemmater.5b01744.

[6] A.R. Jones, C. Bin Kim, S.X. Zhou, H. Ha, R. Katsumata, G. Blachut, R.T. Bonnecaze, C.J. Ellison, Generating large thermally stable Marangoni-driven topography in polymer films by stabilizing the surface energy gradient, Macromolecules. 50 (2017) 4588–4596. https://doi.org/10.1021/acs.macromol.7b00055.

[7] T.A. Arshad, C. Bin Kim, N.A. Prisco, J.M. Katzenstein, D.W. Janes, R.T. Bonnecaze, C.J. Ellison, Precision Marangoni-driven patterning, Soft Matter. 10 (2014) 8043–8050. https://doi.org/10.1039/c4sm01284d.

[8] S.K. Stanley, C.J. Ellison, R.T. Bonnecaze, Control of Marangoni-driven patterning by an optimized distribution of surface energy, J. Appl. Phys. 127 (2020) 065304. https://doi.org/10.1063/1.5132360.

[9] H. Ito, R. Schwalm, Thermally developable, positive resist systems with high sensitivity, J. Electrochem. Soc. 136 (1989) 241–245. https://doi.org/10.1149/1.2096594.

[10] A.P. Lane, Patternable materials for next-generation lithography, The University of Texas at Austin, 2017. https://doi.org/http://dx.doi.org/10.26153/tsw/2236.

[11] R. Menon, A. Patel, D. Gil, H.I. Smith, Maskless lithography, Mater. Today. 8 (2005) 26–33. https://doi.org/10.1016/s1369-7021(05)00699-1.

[12] R. Melik, E. Unal, N. Kosku Perkgoz, C. Puttlitz, H.V. Demir, Flexible metamaterials for wireless strain sensing, 95 (2009) 181105. https://doi.org/10.1063/1.3250175.

[13] I.E. Khodasevych, C.M. Shah, S. Sriram, M. Bhaskaran, W. Withayachumnankul,

B.S.Y.Y. Ung, H. Lin, W.S.T.T. Rowe, D. Abbott, A. Mitchell, Elastomeric silicone substrates for terahertz fishnet metamaterials, Appl. Phys. Lett. 100 (2012) 61101. https://doi.org/10.1063/1.3665180.

[14] J.B. Kim, P. Kim, N.C. Ṕgard, S.J. Oh, C.R. Kagan, J.W. Fleischer, H.A. Stone, Y.L. Loo, Wrinkles and deep folds as photonic structures in photovoltaics, Nat. Photonics. 6 (2012) 327–332. https://doi.org/10.1038/nphoton.2012.70.

[15] C.S. Davis, D. Martina, C. Creton, A. Lindner, A.J. Crosby, Enhanced adhesion of elastic materials to small-scale wrinkles, Langmuir. 28 (2012) 14899–14908. https://doi.org/10.1021/la302314z.

[16] J.F. Schumacher, M.L. Carman, T.G. Estes, A.W. Feinberg, L.H. Wilson, M.E. Callow, J.A. Callow, J.A. Finlay, A.B. Brennan, Engineered antifouling microtopographies - Effect of feature size, geometry, and roughness on settlement of zoospores of the green alga Ulva, Biofouling. 23 (2007) 55–62. https://doi.org/10.1080/08927010601136957.

[17] X. Zhong, R. Huang, B. Zhang, Superplanarizing spin-on carbon materials, 20160372326 A1, 2016.

[18] L.E. Stillwagon, R.G. Larson, Leveling of thin films over uneven substrates during spin coating, Phys. Fluids A. 2 (1990) 1937–1944. https://doi.org/10.1063/1.857669.

[19] L.E. Stillwagon, R.G. Larson, Fundamentals of topographic substrate leveling, J. Appl. Phys. 63 (1988) 5251–5258. https://doi.org/10.1063/1.340388.

[20] T. Sandstrom, A. Bleeker, J. Hintersteiner, K. Troost, J. Freyer, K. van der Mast, OML: optical maskless lithography for economic design prototyping and small-volume production., Proc. SPIE. 5377 (2004).

[21] J.G. Ok, M.K. Kwak, C.M. Huard, H.S. Youn, L.J. Guo, Photo-Roll Lithography (PRL) for continuous and scalable patterning with application in flexible electronics, Adv. Mater. 25 (2013) 6554–6561. https://doi.org/10.1002/adma.201303514.

[22] M.K. Kwak, J.G. Ok, J.Y. Lee, L.J. Guo, Continuous phase-shift lithography with a roll-type mask and application to transparent conductor fabrication, Nanotechnology. 23 (2012) 344008. https://doi.org/10.1088/0957-4484/23/34/344008.

[23] A. Oron, S.H. Davis, S.G. Bankoff, Long-scale evolution of thin liquid films, Rev. Mod. Phys. 69 (1997) 931–980. https://doi.org/10.1103/RevModPhys.69.931.

[24] R. Seemann, S. Herminghaus, K. Jacobs, Dewetting patterns and molecular forces: A reconciliation, Phys. Rev. Lett. 86 (2001) 5534–5537. https://doi.org/10.1103/PhysRevLett.86.5534.

[25] F. Doumenc, B. Guerrier, Self-patterning induced by a solutal Marangoni effect in a receding drying meniscus, Epl. 103 (2013) 14001. https://doi.org/10.1209/0295-5075/103/14001.

[26] J. Muller, H.M.J.M. Wedershoven, A.A. Darhuber, Monitoring photochemical reactions using Marangoni flows, Langmuir. 33 (2017) 3647–3658.

https://doi.org/10.1021/acs.langmuir.7b00278.
[27] J. Bicerano, Prediction of Polymer Properties, 3rd ed., Marcel Dekker, Inc., 2002. https://doi.org/10.1201/9780203910115.
[28] J.D. Mcgraw, K. Jacobs, Controlling Wetting Properties of Polymers, in: Encycl. Polym. Nanomater., Springer Berlin Heidelberg, 2016: pp. 1–10. https://doi.org/10.1007/978-3-642-36199-9_369-2.
[29] A.C. Freeland, Mathematical modeling of the dynamics and production of biosensors, The University of Texas at Austin, 2000.
[30] N. Stoop, R. Lagrange, D. Terwagne, P.M. Reis, J. Dunkel, Curvature-induced symmetry breaking determines elastic surface patterns, Nat. Mater. 14 (2015) 337–342. https://doi.org/10.1038/nmat4202.
[31] ASML, TWINSCAN NXT:2000i, 2019.
[32] W. Sutherland, LXXV. A dynamical theory of diffusion for non-electrolytes and the molecular mass of albumin, London, Edinburgh, Dublin Philos. Mag. J. Sci. 9 (1905) 781–785. https://doi.org/10.1080/14786440509463331.
[33] O. Olabisi, L.M. Robeson, M.T. Shaw, Polymer-Polymer Miscibility, Academic Press, New York, 1979.
[34] J.P. Singer, P.-T. Lin, S.E. Kooi, L.C. Kimerling, J. Michel, E.L. Thomas, Direct-write thermocapillary dewetting of polymer thin films by a laser-induced thermal gradient, Adv. Mater. 25 (2013) 6100–6105. https://doi.org/10.1002/adma.201302777.
[35] J.P. Singer, S.E. Kooi, E.L. Thomas, Focused laser-induced marangoni dewetting for patterning polymer thin films., J. Polym. Sci. Part B Polym. Phys. 54 (2016) 225–236. https://doi.org/10.1002/polb.23906.
[36] A.R. Gamboa, M.P. Nitzsche, V. Saro-Cortes, T. Ma, L. Lei, J.P. Singer, Thermocapillary multidewetting of thin films, MRS Adv. 3 (2018) 977–982. https://doi.org/10.1557/adv.2018.327.
[37] J.P. Singer, Thermocapillary approaches to the deliberate patterning of polymers, J. Polym. Sci. Part B Polym. Phys. 55 (2017) 1649–1668. https://doi.org/10.1002/polb.24298.
[38] X. Wang, C.E. Weinell, V. Tobar, S.M. Olsen, S. Kiil, Leveling measurements of antifouling coatings using an optical profilometer: Effects of additives and solvent concentration and type, Prog. Org. Coatings. 132 (2019) 159–168. https://doi.org/10.1016/j.porgcoat.2019.03.037.
[39] D.J. Resnick, S.V. Sreenivasan, C.G. Willson, Step & flash imprint lithography, Mater. Today. 8 (2005) 34–42. https://doi.org/10.1016/S1369-7021(05)00700-5.
[40] S.K. Wilson, The levelling of paint films, IMA J. Appl. Math. 50 (1993) 149–166. https://doi.org/10.1093/imamat/50.2.149.
[41] L.W. Schwartz, R.R. Eley, Simulation of droplet motion on low-energy and heterogeneous surfaces, J. Colloid Interface Sci. 202 (1998) 173–188. https://doi.org/10.1006/jcis.1998.5448.
[42] J. Park, S. Kumar, Droplet sliding on an inclined substrate with a topographical

defect, Langmuir. 33 (2017) 7352–7363. https://doi.org/10.1021/acs.langmuir.7b01716.

[43] J.M. DeSimone, A. Ermoshkin, N. Ermoshkin, E.T. Samulski, Continuous liquid interface printing, US 2016/0311158 A1, 2016.

[44] K. Fan, X. Zhao, J. Zhang, K. Geng, G.R. Keiser, H.R. Seren, G.D. Metcalfe, M. Wraback, X. Zhang, R.D. Averitt, Optically tunable terahertz metamaterials on highly flexible substrates, IEEE Trans. Terahertz Sci. Technol. 3 (2013) 702–708. https://doi.org/10.1109/tthz.2013.2285619.

[45] M.C. Kemp, P.F. Taday, B.E. Cole, J.A. Cluff, A.J. Fitzgerald, W.R. Tribe, Security applications of terahertz technology, in: Terahertz Mil. Secur. Appl., 2003. https://doi.org/10.1117/12.500491.

[46] C. Jastrow, K. Mu, R. Piesiewicz, T. Ku, M. Koch, T. Kleine-Ostmann, 300 GHz transmission system, Electron. Lett. 44 (2008) 213–214.

[47] H. Tao, N.I. Landy, K. Fan, A.C. Strikwerda, W.J. Padilla, R.D. Averitt, X. Zhang, Flexible terahertz metamaterials: towards a terahertz metamaterial invisible cloak, in: 2008 IEEE Int. Electron Devices Meet., IEEE, 2008. https://doi.org/10.1109/iedm.2008.4796673.

[48] C. Mack, Fundamental Principles of Optical Lithography: The Science of Microfabrication, John Wiley & Sons, Inc., West Sussex, 2007.

[49] M.R.E.E. Warner, R. V. Craster, O.K. Matar, Unstable van der Waals driven line rupture in Marangoni driven thin viscous films, Phys. Fluids. 14 (2002) 1642–1654. https://doi.org/10.1063/1.1460878.

[50] T. Pham, X. Cheng, S. Kumar, Drying of multicomponent thin films on substrates with topography, J. Polym. Sci. Part B Polym. Phys. 55 (2016) 1681–1691. https://doi.org/10.1002/polb.24276.

[51] A.M.P. Valli, R.N. Elias, G.F. Carey, A.L.G.A. Coutinho, PID adaptive control of incremental and arclength continuation in nonlinear applications, Int. J. Numer. Methods Fluids. 61 (2009) 1181–1200. https://doi.org/10.1002/fld.1998.

[52] M. Kumar, M. Husian, N. Upreti, D. Gupta, Genetic Algorithm: Review and Application, Int. J. Inf. Technol. Knowl. Manag. 2 (2010) 451–454. http://www.csjournals.com/IJITKM/PDF 3-1/55.pdf.

[53] Mathworks, Mixed Integer Optimization, (n.d.). https://www.mathworks.com/help/gads/mixed-integer-optimization.html#bs1cifg (accessed March 22, 2019).

[54] S.K. Stanley, R.T. Bonnecaze, Fundamental limits of Marangoni-driven patterning, Colloids Surfaces A Physicochem. Eng. Asp. 603 (2020) 125217. https://doi.org/10.1016/j.colsurfa.2020.125217.

[55] J. D'Errico, fminsearchbnd, fminsearchcon, (2006). https://www.mathworks.com/matlabcentral/fileexchange/8277-fminsearchbnd-fminsearchcon (accessed March 2, 2020).

[56] M.J. Bottema, Circularity of objects in images, in: 2000 IEEE Int. Conf. Acoust. Speech, Signal Process. Proc. (Cat. No.00CH37100), IEEE, n.d.

https://doi.org/10.1109/icassp.2000.859286.

[57] A.G. Emslie, F.T. Bonner, L.G. Peck, Flow of a viscous liquid on a rotating disk, J. Appl. Phys. 29 (1958) 858–862. https://doi.org/10.1063/1.1723300.

[58] A. Acrivos, M.J. Shah, E.E. Petersen, On the flow of a non-Newtonian liquid on a rotating disk, J. Appl. Phys. 31 (1960) 963–968. https://doi.org/10.1063/1.1735785.

[59] S.A. Jenekhe, S.B. Scheldt, Coating flow of non-Newtonian fluids on a flat rotating disk, Ind. Eng. Chem. Fundam. 23 (1984) 432–436. https://doi.org/10.1021/i100016a009.

[60] X. Zhang, W. Hendro, M. Fujii, T. Tomimura, N. Imaishi, Measurement of the thermal conductivity and thermal diffusivity of polymer melts with the short-hot-wire method, Int. J. Thermophys. 23 (2002) 1077–1090. https://doi.org/10.1023/a:1016394104244.

[61] T.L. Bergman, A.S. Lavine, F.P. Incropera, D.P. Dewitt, Fundamentals of Heat and Mass Transfer, 7th ed., John Wiley & Sons, Inc., Jefferson City, 2001. https://doi.org/10.1109/TKDE.2004.30.

[62] C.W. Frank, V. Rao, M.M. Despotopoulou, R.F.W. Pease, W.D. Hinsberg, R.D. Miller, J.F. Rabolt, Structure in thin and ultrathin spin-cast polymer films, Science (80-.). 273 (1996) 912–915. https://doi.org/10.1126/science.273.5277.912.

[63] D.P. Birnie, A model for drying control cosolvent selection for spin-coating uniformity: The thin film limit, Langmuir. 29 (2013) 9072–9078. https://doi.org/10.1021/la401106z.

[64] DIPPR Chemical Database [Online], (n.d.).

[65] G. Fleischer, Temperature dependence of self diffusion of polystyrene and polyethylene in the melt an interpretation in terms of the free volume theory, Polym. Bull. 11 (1984) 75–80. https://doi.org/10.1007/BF00401718.

[66] A. Augsburg, K. Grundke, K. Pöschel, H.J. Jacobascii, A.W. Neumann, Determination of contact angles and solid surface tensions of poly(4-X-styrene) films, Acta Polym. 49 (1998) 417–426. https://doi.org/10.1002/(SICI)1521-4044(199808)49:8<417::AID-APOL417>3.0.CO;2-Q.